WIND POWER IN FORESTS II

REPORT 2018:499

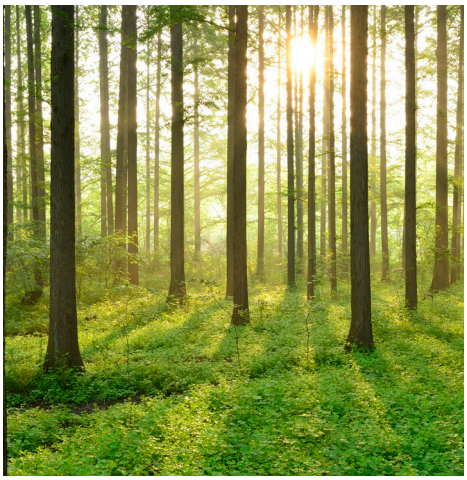

VINDFORSK

Energiforsk

Wind Power In Forests II

Forest wind

MATTHIAS MOHR, JOHAN ARNQVIST, HAMIDREZA ABEDI, HENRIK ALFREDSSON, MAGNUS BALTSCHEFFSKY, HANS BERGSTRÖM, INGEMAR CARLEN, LARS DAVIDSON, ANTONIO SEGALINI OCH STEFAN SÖDERBERG

*

ISBN 978-91-7673-499-5 | © Energiforsk November 2018

Energiforsk AB | Phone: 08-677 25 30 | E-mail: kontakt@energiforsk.se | www.energiforsk.se

Foreword

“Wind power in forests” är ett pojekt finansierat av Energiforsk och Energimyndigheten genom programmet Vindforsk IV.

Allt mer vindkraft byggs i skogsmiljö. Projektets syfte är att uppskatta skogens effekt på elproduktionen och lasterna. Resultaten kommer leda till mer pålitliga beräkningar av vinden över skog.

Tack vare praktiska mätningar i samarbete med OX2 från en 180 meter hög mätmast tillsammans med Sodar-mätningar, Lidar-mätningar och flygmätningar har projektet samlat in mätvärden under två års tid. Resultaten har analyserats och använts för att vidareutveckla och förbättra beräkningsmodellerna.

I och med att vindkraftverken blir allt större, med totalhöjder uppemot 250 meter i framtiden, blir det allt viktigare att förstå skogens inverkan på vindkraftverken. Vindskjuvningen och vindvridningen är kraftigare över skog än över andra vegetationstyper vilket och påverkar produktion och laster.

Samarbetet mellan akademi och projektör med praktiska mätningar kommer leda till värdefull kunskap och förbättrade modeller inför kommande utveckling av stora vindkraft projekt i skogsmiljö.

Projektet har genomförts av Matthias Mohr, som projektledare samt Johan Arnqvist och Hans Bergström på Uppsala Universitet, Hamidreza Abedio och Lars Davidson på Chalmers Tekniska Högskola, Henrik Alfredsson och Antonio Segalini på KTH, Magnus Baltscheffsky och Stefan Söderberg på Weathertech Scandinavia AB och Ingemar Carlen på Teknikgruppen AB.

Göran Dalén
Ordförande, Vindforsk IV

Sammanfattning

Sverige har goda förutsättningar för vindkraft, men stora delar (ca 70%) av Sveriges yta är täckt av skog. Skogen bromsar vinden och orsakar turbulens, något som inte är speciellt gynnsamt för vindkraft. Flera vindkarteringar har emellertid visat att skogsområdena i Norden kan vara bra lämpade för vindkraft (Bergström and Söderberg 2011, Byrkjedal and Åkervik 2009).

Samtidigt finns det en osäkerhet över hur vindförhållandena över skog är på mycket höga höjder (ca 150 m över marken och högre upp). Hur pass bra stämmer modellerna som används för resurskartering? Hur kommer vindkraftverk i skog att producera och vilka laster utsätts vindkraftverken för i skogen? Projektet har undersökt alla dessa frågor. Arbetet koncenterades i följande delar/arbetspaket (AP):

1. Vindresursen på mycket höga höjder
2. Turbulens- och vindmätningar på mycket höga höjder i skog
3. Analys av turbulensdata från skog
4. Modellsimuleringar med strömningsberäkningsmodeller
5. Modellsimuleringar med högupplösande väderprognosmodeller
6. Modellsimuleringar med Large Eddy Simuleringsmodeller (LES)
7. Förbättrad beräkning av så-kallad ”syntetisk turbulens” i skog
8. Analys av flygplansmätningar med lasers över skog
9. Skogens effekter på turbinernas energiproduktion
10. Lastsimuleringar för vindturbiner i skog

AP1 studerar hur vindhastigheten och -riktningen varierar med höjden över skog (upp till ca 150 m höjd över marken). Flera profilrelationer studeras här samtidigt som frekvensfördelningar av vindskjuvning och -vridning presenteras. AP2 beskriver turbulens- och vindmätningarna som utförts vid Hornamossen inom projektet. Dessutom beskrivs mätkampanjen som utförts i en linje tvärs över Hornamossen-kullen inom New European Wind Atlas projektet. AP3 analyserar turbulensdata från Hornamossen tillsammans med turbulensdata från Ryningsnäs. Av speciellt intresse är här turbulensintensitetens avtagande med höjden samt om IEC-standarden klass A, B eller C för vindturbiner uppfylls på de olika höjderna. AP4 beskriver den nyutvecklade linjäriserade strömningsmodellen ORFEUS med en dedikerad skogsbeskrivning. AP5 beskriver modellsimuleringar med WRF och MIUU-modellen, deras känslighet för skrovlighet och turbulensparameteriseringar. Medelvindprofiler från modellerna jämförs med mätningar från Hornamossen. AP6 beskriver LES-simuleringarna med Chalmers LES-modell och WRF-LES. LES-resultaten beror till stor del av hur de turbulenta virvlarna initialiseras vid inloppsränderna av LES-modellen. Flera olika metoder beskrivs här för att lösa detta. AP7 beskriver en ny turbulensmodell (Segalini & Arnqvist modellen) som tar hänsyn till atmosfärens stabilitet. Detta är en vidareutvecklingen av IEC-turbulensmodellen (=Mann-modellen). Koherensen av de turbulenta vindarna samt fasförskjutningen är andra förbättringar av IEC-modellen. AP8 beskriver en ny metod för att beräkna löv-/barrarealdensiteten från laserskanningar av den svenska skogen och hur man beräknar skrovligheten och

nollplansförskjutningen därifrån. Metoden jämförs med två andra metoder. Resultaten jämförs också med skoglig grunddata. Effekten på vindprofilen visas också. AP9 beskriver de nya metoderna för att estimera Annual Energy Production (AEP) från Power Curve Working Group och IEC-standarden för Power Performance Testing. Effekten på estimerad AEP visas. En ny enkel modell för att beräkna turbulensens effekter på energiproduktionen tas fram och jämförs med produktionsdata från en vindpark. Inom AP10 har en ny generisk open-source vindturbin tagits fram och använts för lastberäkningar via aero-elastiska simuleringar. Resultaten visar att den nya koherensmodellen för turbulens ger mindre laster än IEC-standardens turbulensmodell.

För mera information om projektets olika delar hänvisas det till rapportens introduktion, varje kapitels ”Summary and Conclusions” samt den övergripande sammanfattningen (”Executive Summary”) på slutet av rapporten.

Summary

Sweden has good conditions for wind power. However, most of Sweden (ca. 70%) is covered by forest. Forests decrease wind speeds and create turbulence, something which is not favourable for wind power. Several Swedish wind maps have shown that forests in Nordic countries can be well suited for wind power (e.g. Bergström and Söderberg 2011, Byrkjedal and Åkervik 2009).

At the same time, there is uncertainty over wind conditions over forests at very high altitudes (ca. 150 m above ground). How good do wind resource assessment models agree with measurements? How much energy is a wind turbine in forest going to produce and which loads will a wind turbine in forest experience?

This project has investigated all these issues. Work was concentrated in the following work packages:

1. Wind resource at very high heights
2. Turbulence- and wind measurements at very high heights above forest
3. Analysis of turbulence data from forests
4. Model simulations with wind flow models
5. Model simulations with very-high-resolution weather forecast models
6. Model simulations with Large Eddy Simulation (LES) models
7. Improved specification of so-called "synthetic turbulence" over forest
8. Analysis of airborne laser altimeter measurements over forest
9. Forest's effects on wind turbine energy production
10. Load simulations for wind turbines over forest

WP1 studies how wind speed and direction varies with height over forest (up to ca 150 m above ground and higher up). Several profile relations are studied here. Frequency distributions of wind shear and veer are presented. WP2 describes turbulence and wind measurements that have been carried out within the project at Hornamossen. Moreover, the measurement campaign that was carried out in a line over the Hornamossen-hill within the New European Wind Atlas project is described. WP3 analyses turbulence data from Hornamossen together with turbulence data from Ryningsnäs. Of special interest is how turbulence intensity decreases with height as well as if the IEC-standard class A, B or C for wind turbines is complied with at different heights. WP4 describes the newly developed linearised wind flow model ORFEUS with a dedicated forest module. WP5 describes model simulations with WRF and the MIUU model, their sensitivity for surface roughness and turbulence parameterisations. Mean wind profiles from the models are compared to Hornamossen. WP6 describes LES simulations with Chalmers LES model and WRF-LES. LES-resultats depend to a large degree on how the turbulent vortices are initialised at the inflow boundaries of the LES model. Several different methods for that are described. WP7 describes a new turbulence model (the Segalini & Arnqvist model) that includes atmospheric stability. This is a further development of the IEC turbulence model (=Mann model) for neutral stability. Coherence of turbulent winds as well as phase profiles are other improvements of the IEC model. WP8 describes a new method to compute leaf/needle/plant area density from laser scans of the Swedish forest and

how one estimates surface roughness and zero plane displacement from that. The new method is compared with two other methods. Results are also compared with official forest data (“skoglig grunddata”). The effect on the wind profile is also shown. WP9 describes the new methods for estimating AEP from the Power Curve Working Group and the IEC standard for Power Performance Testing. Effects on estimated AEP are shown. A new simple model for calculating turbulence effects on energy production is developed and compared with data from a wind farm. Within WP10 a new generic open-source wind turbine is developed and used for load simulations with aero-elastic simulations. Results show that the new coherence model for turbulence gives much smaller loads than the turbulence model of the IEC standard.

For more information on the different parts of the project the reader is referred to the report’s introduction, the ”Summary and Conclusions” of each chapter as well as the overall summary (”Executive Summary”) at the end of the report.

List of content

List of Symbols

U = mean wind speed at height z [m/s]
z = height above ground
U_1 = mean wind speed at lower level z_1 [m/s]
U_2 = mean wind speed at upper level z_2 [m/s]
α = wind shear exponent from power law
u_* = friction velocity [m/s]
κ = von Karman's constant = 0.4
d = zero plane displacement height [m]
z_0 = surface roughness length [m]
$z_{0,e}$ = effective surface roughness length [m]
h = height above ground [m]
L = Monin-Obukhov length [m]
z_r = reference height (above ground) [m]
β = parameter in log-linear wind profile
f = Coriolis parameter [1/s]
$\Psi\left(\frac{z}{L}\right)$=Integrated stability function for non-dimensional vertical wind gradient
TI = σ_U/U = Turbulence intensity [%]
$r_{\log}$ = correlation coefficient for fitted logarithmic wind profile
r_{power}= correlation coefficient for fitted power law
r_{lin} = correlation coefficient for fitted linear wind profile
$r_{\text{log-lin}}$= correlation coefficient for fitted log-linear wind profile
R = rotor diameter
H = wind turbine hub height
u = longitudinal velocity in turbulence measurements
v = lateral velocity in turbulence measurements
w = vertical velocity in turbulence measurements
$\bar{u}$ = time-average of u
$\bar{v}$ = time-average of v
$\bar{w}$ = time-average of w
S_{2D} = scalar wind speed from two dimensions
S_{3D} = scalar wind speed from three dimensions
u' = turbulent deviation of u from the mean value $\bar{u}$
α = wind direction
k = turbulent kinetic energy = $0.5 \cdot (\sigma_u^2 + \sigma_v^{2+} \sigma_w^2)$
β = wind direction relative to hub height

NB! This list is not complete. For information on further variables see text in each chapter.

List of Abbreviations

ABL	= Atmospheric Boundary Layer
TI	= Turbulence Intensity
REWS	= Rotor Equivalent Wind Speed
HHWS	= Hub height wind speed
NA	= Nacelle anemometer
AEP	= Annual Energy Production
IEC	= International Electrotechnical Commission
SNT	= Swedish Standard (=Normal) Time
LES	= Large Eddy Simulation
NTF	= Nacelle Transfer Function
CFD	= Computational Fluid Dynamics
WRF	= Weather Research & Forecasting model
MIUU	= Meteorological Insititute of Uppsala University
SGS	= SubGrid Scales
TKE	= Turbulent Kinetic Energy
BEM	= Blade Element Momentum theory
TSA	= Turbine Suitability Assessment
RDT	= Rapid Distortion Theory
ALS	= Airborne Laser Scans
PAI	= Plant Area Index
PAD	= Plant Area Desnity
LAI	= Leaf Area Index
LAD	= Leaf Area Density
WAsP	= Wind Atlas Analysis and Application Program
SCADA	= Supervisory Control And Data Acquisition

1 Introduction

Wind power in forest is growing strongly in Sweden. This is not surprising as ca. 70% of Sweden's land area is covered by forest. Several wind mapping efforts have shown that there is a good wind resources in Swedish forests (especially on forest covered hills and mountains) (e.g. Bergström and Söderberg ,2011; Byrkjedal and Åkervik, 2009). During the last couple of years wind power in Sweden was growing rapidly, most of all perhaps in Swedish forests.

The wind field above forests, however, is often characterised by high turbulence, strong wind increase with height (vertical wind shear) as well as strong wind veer with height (vertical wind veer). Optimum hub heights are not only determined by financials and other constraints, but winds have to comply with the IEC standard for turbulence (class A, B or C). Turbulence intensity is actually decreasing with height, even above forests, so higher hub heights are in general a good solution.

There was a certain fear in the industry of building wind farms in forest. Developers were afraid for big loads and underperformance. However, even though knowledge is growing rapidly, there is still not much knowledge about turbulence over forests. This project continued the work of the previous project "V-312 Wind Power in Forest" (Bergström et al., 2012) with additional turbulence measurements over forest at even higher heights (up to 180 m).

In the following, the work of each work package within the continuation project "Forestwind - Wind power in Forest II" is described briefly. Researchers from Uppsala University, WeatherTech Scandinavia, the Royal Institute of Technology (KTH), Chalmers University of Technology and Teknikgruppen have cooperated. Turbulence measurements with very high vertical and temporal resolution have been carried out on a typical Swedish forested hill ("Hornamossen"). Turbulence, wind speed & direction as well as temperature were measured down to 20 m height between the trees, to find better theoretical descriptions of the observed properties. Also remote sensing instruments were used, some in conjunction with a New European Wind Atlas (NEWA) intensive measurement campaign ().

In the following work from each section (corresponding to a work package) is outlined:

Section 2

The wind resource at very high heights was studied through measurements reaching up to at least 150 m above ground (a 140, 150 and 180 m high mast, Sodar data up to 250 m height as well as Lidar data up to 140 m height). Different profile relations for wind speed and direction were tested. Shear exponents were calculated for the lower and upper half of the profiles. Wind direction change with height (wind veer) was analysed.

Section 3

The set-up of turbulence and other measurements at Hornamossen/Hökensås in Southern Sweden is described. In addition to the long-term mast measurements, there was an intensive measurement campaign (within the NEWA project) in a line

across the Hornamossen hill from west to east (Mann et al., 2017). Turbulence instruments are compared to the other instruments (cup anemometers and wind vanes). Quality control and statistical treatment of the measurements are described. Mean wind and turbulence intensity profiles from the sonics, cups, two Lidars and one Sodar are compared.

Section 4

The analysis of the turbulence data is described. Data is compared to the previous site Ryningsnäs in Southern Sweden. Mean profiles (including wind speed, wind direction and turbulence intensity) for different stability classes are shown. Turbulence intensity is compared to the IEC standard class A, B and C for turbulence. Intermittent turbulence, which occurs during stable conditions (night time, winter) is studied.

Section 5

A new linearised wind flow model with a dedicated forest module (ORFEUS) is described. The model is compared to data from a LES and RANS model as well as to data from Ryningsnäs and Hornamossen. The model also includes effects of atmospheric stability.

Section 6

The mesoscale model simulations over Hornamossen are described. Both the WRF model and the MIUU model were used. Sensitivity studies are described. The quality of the mesoscale simulations strongly depends on input data, notably the surface data such as roughness length and displacement height. The choice of turbulence scheme is also very important. The possible use of mesoscale models as drivers for Large Eddy Simulation (LES) models is described. One can go either from the mesoscale model WRF directly to the LES model or via WRF-LES or use WRF-LES as the final LES model. Experiments with WRF-LES are described.

Section 7

Section 7 describes the LES simulations carried out within this project. A problem when carrying out LES simulations with real weather conditions is how to prescribe the turbulent winds (vortices) at the inflow boundaries. Two methods are described: One using fields from a separate LES simulation with periodic boundary conditions with the same LES model (a pre-cursor simulation) and one using fields from synthetic turbulence.

Section 8

This section describes the IEC turbulence model for synthetic turbulence from Mann (1994). Synthetic turbulence is used for aeroelastic simulations of wind turbines for load calculations. A new turbulence model including the effects of atmospheric stability (the Segalini & Arnqvist model) is described. The model is compared to data from Hornamossen. Turbulence coherence and phase lag is studied. Site specific model adaptations for forested areas are described.

Section 9

This section describes the use of Airborne Laser Scans (ALS) to compute tree height, surface roughness and displacement height as well as plant area density profiles. These parameters are routinely used as input data to CFD, wind flow or mesoscale models. A new method was developed and compared to existing methods. The derived data compares well to the official data on tree height and biomass from Skogsstyrelsen.

Section 10

Forest effects on wind turbine power production are described. The work of the Power Curve Working Group and the new IEC standard for Power Performance Testing (IEC 2017) are summarised. Rotor equivalent wind speeds (REWS) are calculated for the three masts available (Hornamossen, Ryningsnäs and the Östergötland site). Differences in AEP owing to REWS are analysed. A new simple model for the effects of turbulence on the power curve is described. Power production from an existing wind farm in forest is analysed for effects of turbulence on power production.

Section 11

Load simulations using an aeroelastic wind turbine model are described. A new generic open-source wind turbine is derived from several existing open source wind turbines. The improved standard of synthetic turbulence from section 8 is used here. A parameter study for tower and foundation loads is carried out. Short turbulent length scales during stable conditions (e.g. nighttime) and highly sheared wind gusts are also studied.

2 Wind resource at very high heights

2.1 THEORY

The Atmospheric Boundary Layer (ABL) is the layer of air closest to the earth's surface where the flow is always turbulent (e.g. Stull 1988). It is defined as the lowest part of the atmosphere that directly feels the effect of the earth's surface. Its depth ranges from just a few metres to several kilometres depending mostly on local factors.

The ABL can further be divided into:

- Surface Layer (approximately lowest 10% of the ABL): Here, turbulent fluxes of momentum and heat are assumed to be approximately constant with height. Hence, this layer often is called the constant-flux layer. The logarithmic wind law is valid in neutral stratification, otherwise profile functions (Monin-Obukhov similarity theory) can be used for non-neutral stratification. Also wind direction is assumed to be constant with height.
- Ekman Layer (upper 90% of the ABL): Here, turbulent fluxes of momentum and heat decrease to approach zero at the top of the ABL. Winds are increasing and turning in the form of an Ekman spiral. The logarithmic wind law is no longer valid.

A typical thickness of the ABL is 1000 m, yielding a typical thickness of the surface layer of 100 m (e.g. Emeis 2013). However, there is a strong diurnal and seasonal cycle. In Sweden, the ABL often is always stable (during day & night) in the midst of the winter. Clearly, this especially applies to Northern Sweden, where the sun barely rises over the horizon during the winter months.

Hence, with modern turbines - ranging from 150 to 250 m height above ground – the validity of the logarithmic as well as the power law are questionable. The following section explores wind profile relationships over forest at these heights.

Konow (2015) explored and compared modern above-surface-layer wind profile relationships to data from a 250 m high mast south-east of Hamburg. These include the logarithmic law (e.g. Stull 1988; Emeis 2013; Landberg 2015), the power law (e.g. Emeis 2013; Landberg 2015), a log-linear wind profile (Fiedler and Panofsky 1972), mixing layer wind profiles (e.g. Gryning et al. 2007; Pena et al. 2010) and a two-layer wind profile (e.g. Etling 2008).

In the following text only the logarithmic, power law and log-linear wind profile are investigated because of the mostly unknown parameters (friction velocity, boundary and surface layer height, etc.) that are needed for the other profiles.

Logarithmic Wind Law

The vertically displaced logarithmic wind profile is defined as:

$$U(z) = \frac{u_*}{\kappa}\left[\ln\left(\frac{z-d}{z_0}\right) - \Psi\left(\frac{z-d}{L}\right)\right] \quad (2\text{-}1)$$

where the stability function Ψ equals one for neutral stability. For non-neutral stability, if L is known the stability function can be calculated. However, this law is strictly only valid in the surface layer, which typically - under neutral conditions - extends up to 100 m height. Under stable conditions the surface layer often is shallower than that, whereas under unstable conditions it can be deeper than that. Despite these shortcomings, the logarithmic law is frequently used in the industry beyond the surface layer. In the text below, the goodness of fit of Equation (2-1) is described by the R-square values for the logarithmic wind law ($R^2_{\log}$). In all analyses in this chapter (chapter 2), the stability function was neglected, i.e. Ψ = 0.

Power Law

Over forest, the vertically displaced power law has to be used

$$U(z) = U(z_r)\left(\frac{z-d}{z_r-d}\right)^{\alpha} \quad (2\text{-}2)$$

The power law has the advantage of its simple formulation. However, it is strictly only valid for a small height range around the reference height z_r (Jacobsen, 2014). It also yields a simple wind shear parameter, the shear exponent. A scale factor was used in the fitting of the power law to take into account that the measured wind speed at the reference height does not always exactly agree to the fitted wind speed at the reference height. Hence, a modified version of the power law

$$U(z) = a \cdot U(z_r)\left(\frac{z-d}{z_r-d}\right)^{\alpha} \quad (2\text{-}2a)$$

was fitted to the profiles where a is the scale factor obtained from the fitting process.

For neutral stratification and homogeneous flat terrain, the shear exponent is related to the surface roughness through (e.g., Emeis 2013)

$$\alpha = \frac{1}{\ln\left(\frac{z_r-d}{z_0}\right)} \quad (2\text{-}3)$$

Emeis (2013), however, also proposed another (which he claimed better) relationship for the shear exponent

$$\alpha(\alpha-1) = -\frac{1}{\ln\left(\frac{z_r-d}{z_0}\right)} \quad (2\text{-}4)$$

However, equation 2-4 has no solution for low heights over rough surfaces with $z/z_o < 54.6$. For $z/z_o = 54.6$ it has one solution ($\alpha = 0.5$) and for $z/z_o > 54.6$ it has two solutions where the smaller one is chosen.

Jacobsen (2014) proposed the following relation

$$\alpha = \frac{(z_r - d)}{\mathrm{U}(z_r)} \frac{dU}{dz}\Big|_{z=z_r} \tag{2-5}$$

The logarithmic profile and the power law look very similar when plotted. However, while the former is based upon physical reasoning, the latter is based upon fitting mathematical expressions by engineers (Landberg 2015). Stangroom (2004) notes that there is no theoretical justification of the power law, but it is known to fit mean wind profiles well when suitable parameters are defined.

Wind shear exponents can be calculated from measurements at two heights as

$$\alpha = \frac{\ln\left(\frac{U_2}{U_1}\right)}{\ln\left(\frac{z_2 - d}{z_1 - d}\right)} \tag{2-6}$$

In this study, however, MATLABs curve fitting toolbox was used in conjunction with wind speeds from more than two vertical levels. The option "Non linear Least Squares" was used. In the text below, the goodness of fit of Equation 2-2a is described by the R-square values for the fitted power law (R^2_{power}).

Derrick et al. (2013) pointed out that a multi-point shear model (i.e. a multi-point power law fit) leads to lowest extrapolated wind speed errors. Also, the multi-point model was found to be least sensitive to canopy height errors, i.e. the estimation of d.

Log-Linear Wind Profile

The log-linear wind profile was proposed by Fiedler & Panofsky (1972) for heterogeneous terrain for profiles that extend above the surface layer. The effective roughness length ($z_{0,e}$) should be equal to the roughness length of homogeneous terrain reproducing the same momentum flux near ground. The log-linear wind profile reads

$$U(z) = \frac{u_*}{\kappa} \ln\left(\frac{z - d}{z_{0,e}}\right) + \beta(z - d) \tag{2-7}$$

where the parameter $\beta = 144\, f$. Our study, however, suggests that the parameter β is by far constant for individual wind profiles. Hence, the parameter β was fitted to the profile, i.e. not prescribed.

The log-linear wind profile was found to agree best with measured individual profiles, mainly as a consequence of the fact that three parameters (u*, β and $z_{0,e}$) can be fitted to the measured profile. The log-linear wind profile was found to be a good approximation by many researchers. It was found to extend well beyond the surface layer into the boundary layer for stable stratification (Skibin and Businger, 1985). In the text below, the goodness of fit of the log-linear wind profile is described by the R-square values for the log-linear wind profile ($R^2_{\text{log-lin}}$) obtained from the MATLAB curve fitting toolbox.

Wind Direction Profile

There are not many studies on the wind direction variation with height at typical heights of modern wind turbines (≈ 50 to 250 m height above ground). The vertical gradient of the wind direction can be calculated from two or more wind direction measurements.

Landberg (2016) simply states that, within the surface layer, wind direction is constant with height and the same as the wind direction at the surface. (Monin-Obukhov similarity theory states that the wind speed increases with height without a turning of the wind direction in the surface layer.) Above the surface layer, i.e. in the Ekman layer, however, wind direction changes considerably.

Lezaun Mas (2014) states that "If wind directions at different heights are measured, the wind direction relative to hub height wind direction can be approximated by a linear expression", namely

$$\beta(z) = \Psi \cdot (z - z_{hub}) \tag{2-8}$$

where $\beta(z)$ is the wind direction relative to hub height wind direction. Ψ is the vertical gradient of the wind direction. Moreover, he suggests that if only wind direction at hub height is measured, a constant representative value could be used for Ψ. CFD calculations or wind assessment tools might be used for determining a representative value of Ψ.

Certain very complex sites may, however, have non-linear vertical wind direction gradients (Lezau Mas, 2014). For those types of terrain, he recommends more thorough measurements of wind direction.

2.2 MEASUREMENTS

2.2.1 Mast measurements

Data from the Hornamossen mast, the Ryningsnäs mast and another forested site in Östergötland were analysed. Measurement periods, heights and number of analysed profiles are summarised in Table 2-1.

Table 2-1. Mast measurements from three forest sites in southern Sweden. For Ryningsnäs only sectors without wind turbine wakes were analysed. Heights in parentheses were excluded from the profile analysis.

Site	Measurement period	Measurement heights [m above ground]	Number of profiles	Number of analysed profiles	Wind direction sectors included
Hornamossen Mast	18 June 2015 - 12 June 2017	(21), (40), 60, 82, 100, 122, 152, 173	104 451 (= 100%)	56 908 (= 54.5%)	0-305° & 345-360°
Ryningsnäs Mast	2 Nov 2010 - 4 Feb 2012	(40), 59, 80, 98, 120, 138	64 219 (= 100%)	25 442 (= 39.6%)	0-30° & 100-120° & 220-305°
Östergötland Mast	24 Aug 2012 - 17 Nov 2014	50, 75, 100, 125, 150	100 925 (= 100%)	60 160 (= 59.6%)	All sectors

Data was filtered according to:

- Hornamossen: Only data with wind speeds ≥ 3 m/s at 152 m height was used.
- Ryningsnäs and Östergötland site: Only data with wind speed ≥ 3 m/s at the uppermost level (= 138 and 150 m height, respectively) was used.
- Hornamossen: Sectors influenced by tower shadows were excluded (see last column in Table 2-1).
- Hornamossen: Data from 17 December 2015 through 23 January 2016 was excluded due to poor quality.
- Ryningsnäs: Sectors influenced by tower shadows and wakes of the two nearby wind turbines were excluded (see last column in Table 2-1).
- Östergötland site: Anemometers from the windward side were always chosen for the analysis. (The same cup anemometers ("Thies First Class") were installed on booms at both sides of the tower.)
- Östergötland site: To avoid problems with instrument icing, only data was used where air temperatures were ≥ 3°C at all heights.

Data from Ryningsnäs and Hornamossen was not filtered for icing, as the sonics are believed to be free from icing.

Wind profiles

Four profile relations were tested for wind profile fitting, i.e.

- Logarithmic Wind Profile
- Power Law
- Linear Wind Profile
- Log-Linear Wind profile

At all sites, a displacement height of d = 15 m was used for all investigated sectors. It should be noted that these values only represent a good guess, whereas, for instance, Bergström et al. (2013) calculated displacement heights from mean profiles. However, the analysis presented below should not be very sensitive to the choice of a correct displacement height.

During almost all instances, the log-linear wind profile showed the best fit (Table 2-2). Second best performed the logarithmic wind profile or the power law, on average, depending on the site. Worst performed the linear profile.

This is not surprising as there are three parameters (z_0, u_* and β) that can be fitted in the log-linear wind profile instead of two (z_0 and u_*) in the logarithmic wind profile and two (slope and axis intercept) in the linear wind profile. In the modified power law, two parameters (α and a scale factor) can be fitted.

Table 2-2. Average of R^2 for different fitted wind profiles (from Section 2.1). Only full wind profiles were used. A displacement height of d = 15 m was used for all sites. The ranking of the different profile expressions is given in parentheses after the numbers.

Mean R-square value	Logarithmic	Power Law	Linear	Log-Linear
Hornamossen Mast	0.898 (2)	0.897 (3)	0.868 (4)	0.956 (1)
Ryningsnäs Mast	0.955 (3)	0.958 (2)	0.947 (4)	0.986 (1)
Östergötland Mast	0.935 (3)	0.942 (2)	0.924 (4)	0.984 (1)

Table 2-3 summarises the performance of the different wind profile expressions "logarithmic", "linear", "log-linear" and "power law" (Equations (2-1), (2-2) and (2-7)) in terms of R-square values. Somewhat arbitrarily, it was chosen that one profile relation performs better than the other when the R-square value of that profile relation was ≥ the R-square value of the other profile relation + 0.01.

It can be seen that at Hornamossen (the windiest site of all three), the logarithmic profile performs better than at the other two masts (1st, 2nd and last column of Table 2-3).

At all sites, the log-linear profile was the clear winner (performs better than log profile in around half of cases). This is perhaps not surprising as in 44% of the cases at the Östergötland site the linear profile outperformed the log profile. At the other two sites the linear profile only outperformed the log profile in 20%/31% of the cases, respectively.

The power law performed better than the log law during roughly half of the cases at the Östergötland site. At the other two sites, however, it performed better than the log profile in only 20-30% of the cases.

Table 2-3. Ranking of goodness of fit of wind profile expressions "logarithmic", "linear", "log-linear" and "power law" (Equations (2-1), (2-2) and (2-7)). R-square values for different fitted wind profiles were used. Only full wind profiles were considered. A displacement height of d = 15 m was used for all sites. Somewhat arbitrarily Δ = 0.01 was chosen.

	Log better than power	Log better than linear	Log-linear better than log	Linear better than log	Power better than log
	$R^2_{log} > R^2_{pow} + \Delta$	$R^2_{log} > R^2_{lin} + \Delta$	$R^2_{log\text{-}lin} > R^2_{log} + \Delta$	$R^2_{lin} > R^2_{log} + \Delta$	$R^2_{pow} > R^2_{log} + \Delta$
Hornamossen	25%	64%	50%	20%	19%
Ryningsnäs	13%	40%	46%	31%	29%
Östergötland site	17%	41%	69%	44%	46%

For sector-wise mean profiles, the log-linear wind profile again showed the best fit (Table 2-4), followed by the logarithmic wind profile or the power law depending on the site. The linear wind profile performed worst. A reason for that the logarithmic profile performed better than the power law at Hornamossen could be that Ryningsnäs and the Östergötland site are considerably less windy than

Hornamossen. Hence, the surface layer at Hornamossen should be deeper, on average, than the surface layer at the two other sites.

Table 2-4. Same as in Table 2-2, but for sector-wise averaged wind profiles. Wind direction sectors were 10° wide. This resulted in 32, 14 and 36 sectors for Hornamossen, Ryningsnäs and the Östergötland site, respectively. R-square values were averaged over all sectors. (Numbers in parenthesis indicate the range of correlation coefficients.) In each sector, Hornamossen had between 470 and 5841 profiles, Ryningsnäs between 723 and 2937 profiles and the Östergötland site between 658 and 3863 profiles. The ranking is given in parentheses after the numbers.

Mean correlation coefficient	Logarithmic R^2_{log}	Power Law R^2_{pow}	Linear R^2_{lin}	Log-Linear $R^2_{log\text{-}lin}$
Hornamossen Mast	0.9935 (2) (0.9815-0.9996)	0.9921 (3) (0.9630-0.9993)	0.9663 (4) (0.9086-0.9915)	0.9998 (1) (0.9892-0.9998)
Ryningsnäs Mast	0.9953 (3) (0.9917-0.9989)	0.9972 (2) (0.9857-1.0000)	0.9862 (4) (0.9585-0.9953)	0.9986 (1) (0.9936-1.0000)
Östergötland Mast	0.9898 (3) (0.9762-0.9990)	0.9947 (2) (0.9706-0.9997)	0.9799 (4) (0.9214-0.9970)	0.9994 (1) (0.9985-0.9999)

Wind shear

Shear exponents (α) for sector wise averaged wind profiles at Hornamossen ranged from 0.256 to 0.405, with a mean value of 0.327 and standard deviation of 0.036.

At Ryningsnäs the same shear exponents ranged from 0.340 to 0.454, with a mean value of 0.412 and standard deviation of 0.032. This corresponds well to the value of 0.41 reported by Dahlberg (2009).

At the Östergötland site the same shear exponents ranged from 0.250 to 0.426, with a mean value of 0.347 and standard deviation of 0.043.

Wind shear depends on wind speed as higher turbulence generally leads to less wind shear (Figure 2-1). There is large scatter for lower wind speeds owing to stability effects. At very high wind speeds, when neutral stratification can be assumed, the spread becomes very small and the shear exponents is almost constant.

No clear relationship between wind speed and shear exponent can be seen at all three masts (not shown). However, for all three masts, the variation of the shear exponent decreases with wind speed and the shear exponent becomes almost constant at high wind speeds (see Figure 2-1 for Hornamossen).

For that reason, average shear exponents were calculated for low wind speeds ($U_{100m} \leq 12$ m/s) as well as for high wind speeds ($U_{100m} > 12$ m/s). In the former case, stability effects have a strong impact on shear exponents. In the latter case, however, neutral stratification can be assumed with almost constant shear exponents. This is indeed the case as shown in Table 2-5.

Table 2-5. Average shear exponents from full profiles for low wind speeds (≤ 12 m/s at 100 m) and for high wind speeds (> 12 m/s at 100 m). The standard deviation of the average shear exponents is also given.

Site	Shear exponent α (U_{100m} ≤ 12 m/s)	Standard deviation of α (U_{100m} ≤ 12 m/s)	Shear exponent α (U_{100m} > 12 m/s)	Standard deviation of α (U_{100m} > 12 m/s)
Hornamossen	0.3071	0.1565	0.2952	0.0569
Ryningsnäs	0.4102	0.1642	0.3234	0.0534
Östergötland site	0.3536	0.1811	0.2719	0.0562

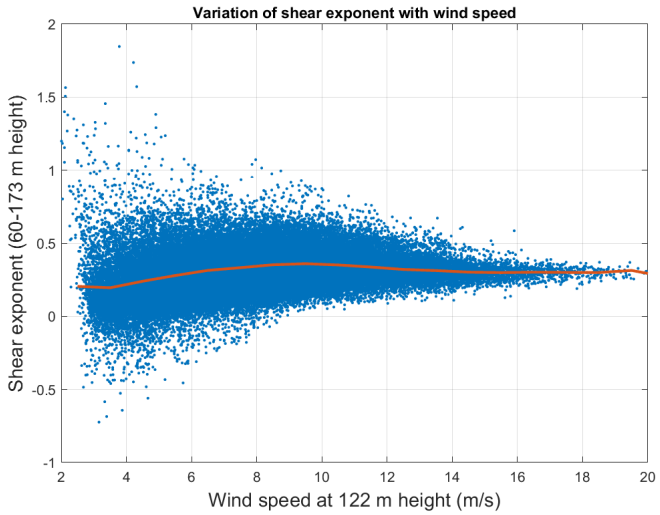

Figure 2-1 Dependence of wind shear exponent on wind speed at Hornamossen mast. Obtained between 60 and 173 m height. Only full wind profiles from sectors specified in Table 2-1 were used. Binned averages are shown in red.

Frequency distributions of wind shear exponents look pretty similar at all sites (Figure 2-2). The distribution at Hornamossen is much narrower than at the two other sites. This could be caused by lower surface roughness or orographic speed-up. The distributions resemble closely those from other studies (e.g. Kelly 2014). However, in contrast to Kelly, negative shear exponents are almost non-existent at the three forest masts studied herein.

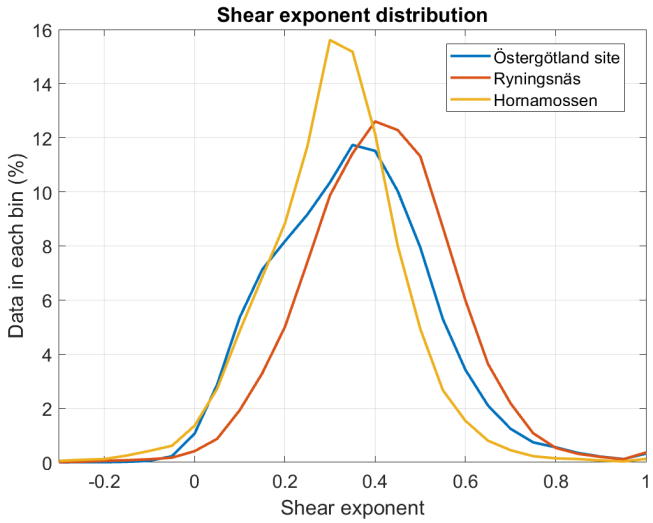

Figure 2-2 Histogram of shear exponents for Hornamossen, Ryningsnäs and the Östergötland site. Obtained between 60 and 173 m height for Hornamossen, between 59 and 138 m height for Ryningsnäs and between 50 and 150 m height for the Östergötland site. Only full wind direction profiles from sectors specified in Table 2-1 were used.

Wind shear over entire profile versus lower/upper half profile

Wind shear exponents were computed for the entire profiles as well as for the lower/upper half of the profiles for the following heights:

- Hornamossen: 60-173 m (full), 60-122 m (lower) and 122-173 m (upper)
- Ryningsnäs: 59-138 m (full), 59-98 m (lower) and 98-138 m (upper)
- Östergötland site: 50-150 m (full), 50-100 m(lower) and 100-150 m (upper)

Scatter plots for Hornamossen are shown in Figures 2-3 a-c. Figure 2-3d shows shear exponents obtained from two levels only versus shear exponents obtained by curve fitting. Scatter plots for the other two sites look very similar (not shown).

Figure 2-3 d shows that shear exponents from curve fitting of the lower profiles (60- 122 m) agree excellently with those based on two levels only (60 and 122 m). Shear exponents based on two heights only are, on average, 0.5% lower than those based upon curve fitting (Table 2-8). This difference, however, was not present at the other two sites and could be a result of the bad calibration of the sonics at Hornamossen.

Correlation is quite good when shear exponents from the lower and upper half of the profiles were compared to shear exponents from the entire profiles ("full profiles"). However, when shear exponents from the lower half of the profiles were compared to shear exponents from the upper half of the profiles correlation was virtually not existent (Table 2-6 and Figure 2-3).

Table 2-6. Shear exponents from upper/lower half of profile versus shear exponents from full profile. Correlation coefficients (not squared) are also given. For the lower half, shear exponents obtained from curve fitting ("cf") were also compared to shear exponents from two heights only ("simple"). Bold numbers indicate recommended ways to estimate shear of whole/parts of the profile (from x to y), whereas red numbers designate non-favourable ways to estimate shear of whole/parts of the profile.

Site	Comparison (y / x)	Slope (linear fit through origin)	Correlation coefficient R (linear fit through origin)	Slope (linear fit)	Y-axis intercept (linear fit)	Correlation coefficient R (linear fit)
Hornamossen	**Lower half / full profile**	**1.05**	**0.84**	0.90	0.06	0.86
	Full profile / lower half	0.90	0.85	0.82	0.03	0.86
	Upper half / full profile	0.94	0.86	1.15	-0.08	0.87
	Full profile / upper half	0.97	0.72	0.66	0.13	0.87
	Upper half / lower half	**0.78**	**0.50**	**0.65**	**0.05**	**0.52**
	Lower half / upper half	**0.94**	**0**	**0.41**	**0.22**	**0.52**
	simple / cf (lower half)	0.99	0.996	0.98	0.00	0.996
	cf / simple (lower half)	1.01	0.996	1.01	0.00	0.996
Ryningsnäs	**Lower half / full profile**	**1.00**	**0.83**	0.87	0.06	0.84
	Full profile / lower half	**0.96**	**0.82**	0.81	0.07	0.84
	Upper half / full profile	1.01	0.82	1.15	-0.06	0.83
	Full profile / upper half	0.91	0.67	0.60	0.17	0.83
	Upper half / lower half	**0.92**	**0.30**	**0.56**	**0.18**	**0.42**
	Lower half / upper half	**0.85**	**0**	**0.31**	**0.29**	**0.42**
	simple / cf (lower half)	1.00	0.998	1.00	-0.00	0.998
	cf / simple (lower half)	1.00	0.998	0.99	0.00	0.998
Östergötland site	**Lower half / full profile**	**0.97**	**0.84**	0.87	0.05	0.85
	Full profile / lower half	**0.96**	**0.83**	0.83	0.06	0.85
	Upper half / full profile	1.00	0.83	1.12	-0.05	0.83
	Full profile / upper half	0.89	0.71	0.62	0.14	0.83
	Upper half / lower half	**0.89**	**0.34**	**0.57**	**0.14**	**0.44**
	Lower half / upper half	**0.80**	**0**	**0.33**	**0.24**	**0.44**
	simple / cf (lower half)	1.00	0.996	1.00	0.00	0.996
	cf / simple (lower half)	1.00	0.996	1.00	0.00	0.996

Average shear exponents for Hornamossen, Ryningsnäs and the Östergötland site are given in Table 2-7. At all sites, shear decreased with height: At Hornamossen, the lower profiles showed shear exponents of, on average, 10% higher than those of the full profiles. Also, the upper profiles at Hornamossen have shear exponents of, on average, 10% lower than those of the full profiles (Figure 2-3 and Table 2-7). At the other two sites, average shear exponents were almost constant with height, with only a slight decrease with height. The reason for the discrepancy in between the sites is probably the orographic speed-up at Hornamossen. At the other two sites (Ryningsnäs and the Östergötland site) the orographic speed up is much less than at Hornamossen.

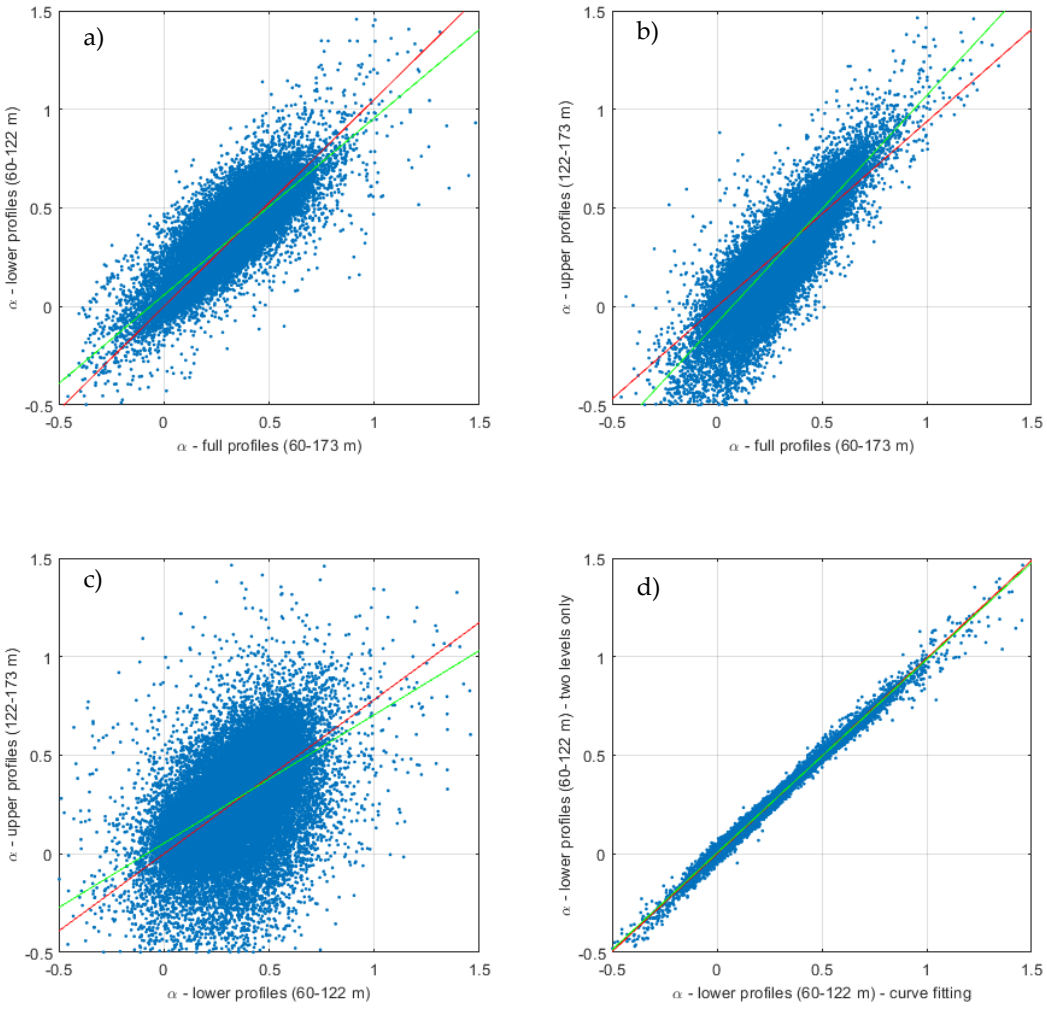

Figure 2-3. Relationship between shear exponents (α) at Hornamossen obtained from: a) Full profiles (60-173 m height) and lower profiles (60-122 m height), b) Full profiles (60-173 m height) and upper profiles (122-173 m height), c) Lower profiles (60-122 m height) and upper profiles (122 -173 m height), d) Lower profiles (60-122 m height) and two levels only (60 and 122 m height). Only full profiles were used.

Table 2-7. Average shear exponents from full profiles, lower and upper half of profiles for Hornamossen, Ryningsnäs and the Östergötland site. The number of profiles used is also given in the table.

Site	No of profiles	α (full profile)	α (lower half)	α (upper half)
Hornamossen	60308	0.309	0.334	0.267
Ryningsnäs	25442	0.409	0.415	0.406
Östergötland site	60160	0.353	0.352	0.345

Table 2-8. Average shear exponents for lower half of profiles from curve fitting using several heights and from simple method using two heights.

Site	No of profiles	α (lower half, curve fitting)	α (lower half, two points)	Difference
Hornamossen	60308	0.333	0.332	-0.5%
Ryningsnäs	25442	0.415	0.416	+0.1%
Östergötland site	60160	0.352	0.352	-0.1%

Wind direction

The linear wind direction profile of Equation 2-8 was fitted to all available wind direction profiles. The wind direction sectors given in Table 2-1 were used to avoid tower shadows and turbine wakes. Wind direction was computed from the sonic anemometers and is, hence, available at the same heights as the wind speeds at Hornamossen and Ryningsnäs. At the Östergötland site, only two measurement heights (73 and 146 m) were available for wind direction.

Average absolute correlation coefficients for wind direction profiles were 0.762 at Hornamossen and 0.901 at Ryningsnäs (from roughly 60 000 and 25 000 profiles, respectively). The low correlation at Hornamossen is a consequence of the poor quality of the wind direction values from the sonic anemometers. At the Östergötland site, no correlation coefficients for wind direction change with height could be computed, as only two heights with wind vanes were available. Here, roughly 60 000 values were available for the wind direction change with height.

Average values for wind direction change with height ("wind veer") were 4.8° per 100 m height difference for Hornamossen, 13.1° per 100 m height difference for Ryningsnäs and 14.8° per 100 m height difference at the Östergötland site. Standard deviations for wind direction change with height ("wind veer") were 8.0° per 100 m height difference, 8.4° per 100 m height difference and 13.7° per 100 m height difference, respectively. Frequency distributions are shown in Figure 2-4.

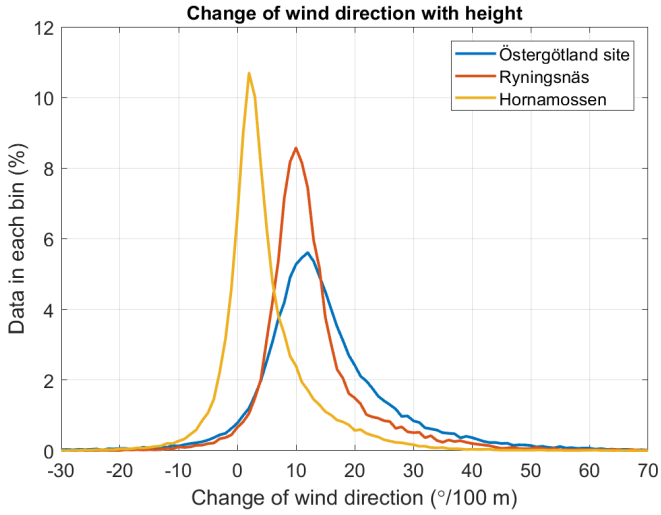

Figure 2-4 Change of wind direction with height for Hornamossen, Ryningsnäs and the Östergötland site. Obtained with linear fit between 60 and 173 m, 59 and 138 m and 73 and 146 m height, respectively. Only full wind direction profiles from sectors specified in Table 2-1 were used.

Also wind veer is a function of wind speed (see Figure 2-5 for Hornamossen). At higher wind speeds, binned averages of wind veer are generally smaller. Also the scatter becomes much smaller at higher wind speeds. Again, this is probably a factor of atmospheric stability that plays an important role at low wind speeds, but is negligible at higher wind speeds, when stratification is close to neutral.

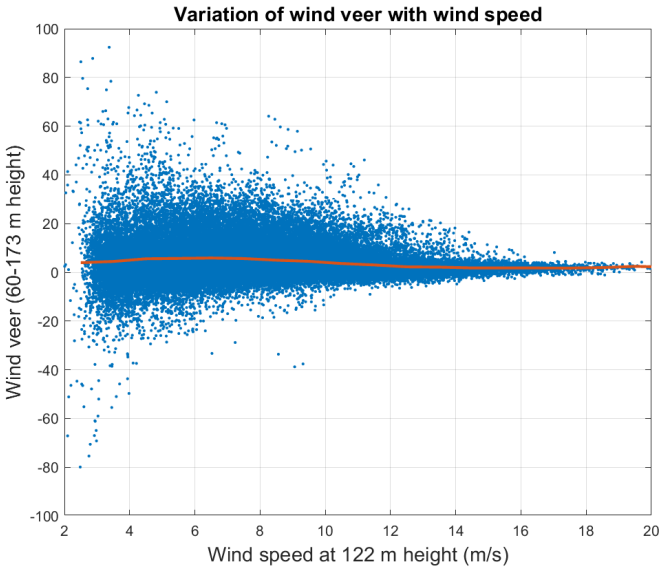

Figure 2-5. Dependence of wind veer on wind speed at Hornamossen mast. Obtained between 60 and 173 m height. Only full wind direction profiles from sectors specified in Table 2-1 were used. Binned averages shown in red.

2.2.2 Sodar & Lidar measurements

Sodar measurements

Sodar data from two airports from The Swedish Armed Forces (Luleå and Ronneby) were analysed. Luleå airport is situated in northern Sweden at the coast of the Baltic Sea, 2 km from the Baltic sea with a small archipelago in between the airport and the open sea. Ronneby airport is situated in southern Sweden roughly 10 km from the coast of the Baltic Sea with an irregular coast line and some small islands. Wind sectors were chosen to represent non-homogeneous forest terrain that is typical in Sweden (Table 2-9 and Figures 2-6 & 2-7). Wind profiles from roughly 4 years of measurements were analysed. All data with error codes was discarded and only full profiles from 70 to 250 m height above ground were used. The wind sectors were chosen to represent forest conditions and to avoid winds from the sea.

Table 2-9 Sodar measurements from Swedish Armed Forces (Metek Sodar PCS.2000-64 including RASS). Only sectors with relatively undisturbed patchy forest were used.

Site	Measurement period	Measurement heights [m above ground]	Number of records	Number of complete profiles	Number of analysed profiles	Wind direction sector
Luleå Sodar	11 Sep 2012 - 10 May 2016	70, 100, 130, 160, 190, 220, 250	154324 (= 100%)	110247 (= 71.4%)	14109 (= 9.1%)	260-320° (= 60°)
Ronneby Sodar	10 Sep 2014 - 31 Oct 2017	70, 100, 130, 160, 190, 220, 250	106007 (= 100%)	94780 (= 89.4%)	40273 (=38.0%)	270-90° (= 180°)

Remarkable is that the Sodar performed relatively poorly at Luleå Airport. This is also evident in the error codes that show a large amount of probably fixed echoes. Also, civilian air traffic at Luleå airport is much greater than at Ronneby airport, which could induce some noise-related disturbances. For more detail see Mohr (2018).

Sodar locations are outlined in Figures 2-6 & 2-7. A Metek PCS.2000-64 64-speaker phased-array Sodar was used together with a Radio Accoustic Sounding System (RASS) for temperature profiles. The Sodar measures up to ca 700 m height in ideal conditions. However, in this report only data up to 250 m height above ground was used. The quality of the temperature data from the Radio Acoustic Sounding System (RASS), however, was so poor that it could not be used at all.

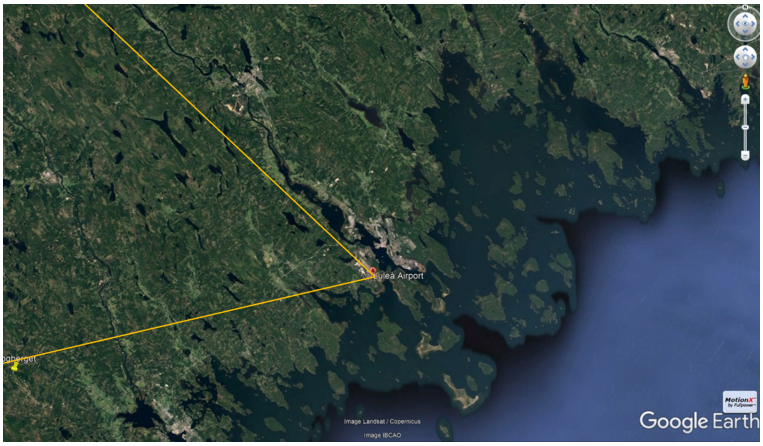

Figure 2-6. Location of Sodar at Luleå Airport and surroundings. The wind direction sector 260° to 320° (representing relatively undisturbed patchy forest) was used in the analysis. Sector is indicated by yellow lines.

Figure 2-7. Same as in Figure 2-6, but location of Sodar at Ronneby Airport. The wind direction sector 270° to 90° was used in the analysis.

Lidar measurements

Long-term Lidar measurements from Havsnäs wind farm were analysed (Figure 2-8). The Lidar was located at 64.113°N and 15.709°E. Data comprised a period of 10 months (Table 2-10). The Lidar was installed for power performance testing. Hence, only wake-free sectors were analysed (Table 2-10). The Lidar (a WINDCUBE V1) was located 51 m to the north of a co-located fixed power performance mast (Derick et al., 2013).

A broken wiper unit was replaced in November 2011, clearly improving data capture. Operational availability of the Lidar before and after wiper replacement was 91% and 99.9%, respectively. However, data quality was still poor due to low aerosol density at the site. Qualified data capture increased dramatically when the number of pulses per line of site was increased by a factor of four. Derrick et al. (2013) compared Lidar wind speeds to wind speeds from the power performance mast and the agreement was found to be good.

Table 2-10. Lidar mesaurements from Havsnäs wind farm. Only sectors with no wind turbine wakes were used.

Site	Measurement period	Measurement heights [m above ground]	Number of records	Number of complete profiles	Number of analysed profiles	Wind direction sector
Havsnäs	16 Sep 2011 - 24 Jul 2012	52, 67, 77, 87, 97, 107, 117, 127, 137, 142	39451 (=100%)	19481 (=50%)	4 892 (= 25%)	297 - 85° (=148°)

Of the roughly 20 000 profiles only 273 (roughly 1%) were incomplete.

Figure 2-8. Location of Lidar at Havsnäs Wind Farm and surroundings. The wind direction sector 297° to 85° (representing patchy forest and lakes) was used in the analysis. The sector (free from turbine wakes and tower shadows) is indicated by yellow lines.

Wind profiles

The same four profile relations as for the met masts were tested using data from the Sodars and the Lidar. At Luleå Airport, a displacement height of $d = 10$ m was used for all investigated sectors, whereas $d = 15$ m was used at Ronneby Airport. At Havsnäs, a displacement height of $d = 7.5$ m was used. It should be noted that these values only represent a good guess, whereas, for instance, Bergström et al. (2013) calculated displacement heights from mean profiles.

For almost all 15-minute average profiles from the Sodar, the log-linear wind profile showed the best fit (Table 2-11). This is not surprising as there are three parameters (z_0, u_* and β) that can be fitted in the log-linear wind profile instead of two (z_0 and u_*) in the logarithmic wind profile, two (slope and axis intercept) in the linear wind profile and two (α and scale factor) in the power law. (The scale factor in the power law was used to take into account that the measured wind speed at the reference height does not always exactly agree to the fitted wind speed at the reference height.)

Second best performed the linear profile/ the power law at Luleå/Ronneby airport. At Havsnäs, the power law performed second best. Surprisingly, the logarithmic

profile performed worst at Luleå airport whereas, at Ronneby airport and Havsnäs, the linear profile performed worst (Table 2-11).

Table 2-11. Average of R^2 for different fitted wind profiles (see Section 2.1). Only full wind profiles from 70 to 250 m height above ground (for Havsnäs from 52 to 142 m height above ground) were used. Values of d = 10 m and d = 15 m were used for Luleå and Ronneby, respectively. For Havsnäs, d = 7.5 m was used. The ranking is given in parentheses after the numbers.

Mean correlation coefficient	Logarithmic	Power Law	Linear	Log-Linear
Luleå Sodar	0.844 (4)	0.852 (3)	0.855 (2)	0.956 (1)
Ronneby Sodar	0.889 (3)	0.893 (2)	0.883 (4)	0.970 (1)
Havsnäs Lidar	0.888 (3)	0.893 (2)	0.883 (4)	0.959 (1)

Table 2-12 ranks the performance of the different wind profile expressions "logarithmic", "linear", "log-linear" and "power law" (Equations (2-1), (2-2) and (2-7)) in terms of R-square values. Somewhat arbitrarily, it was chosen that one profile relation performs better than the other when the R-square value of the profile relation was ≥ the R-square value of the other profile relation + 0.01.

It can be seen that at Luleå, the power law performs better than the logarithmic profile in 42% of the cases. At Ronneby and Havsnäs, this happens in roughly one third of the cases (36% and 30%, respectively). The logarithmic profile performs better than the power law in less than 20% of the cases (2nd column of Table 2-12).

The log-linear profile was the clear winner at all three sites (performed better than log profile in 77%, 67% and 57%, respectively, of the cases). This is perhaps not surprising as in the log-linear profile three parameters can be fitted to the measured profile as compared to two in the other profile expressions.

Table 2-12. Ranking of goodness of fit of wind profile expressions "logarithmic", "linear", "log-linear" and "power law" (Equations (2-1), (2-2a) and (2-7)). Only full wind profiles were considered. A displacement height of d = 10 m, d = 15 m and d = 7.5 m was used for Luleå, Ronneby and Havsnäs, respectively. Somewhat arbitrarily Δ = 0.01 was chosen. Values in table denote number of profiles where one profile relation performed better than the other as fraction of total number of profiles.

	Power better than log	Log better than power	Log better than linear	Linear better than log	Log-linear better than power
	$R^2_{pow} > R^2_{log} + \Delta$	$R^2_{log} > R^2_{pow} + \Delta$	$R^2_{log} > R^2_{lin} + \Delta$	$R^2_{lin} > R^2_{log} + \Delta$	$R_{log\text{-}lin} > R^2_{log} + \Delta$
Luleå	42%	18%	33%	56%	77%
Ronneby	36%	17%	43%	43%	67%
Havsnäs	30%	10%	40%	45%	57%

For sector-wise mean profiles, the log-linear wind profile again showed the best fit (Table 2-13), followed, however, by the power law. The logarithmic wind profile performed almost as well as the power law, whereas the linear wind profile performed worst.

Table 2-13. Same as in Table 2-11, but for sector-wise averaged wind profiles. Wind direction sectors were 10° wide from 270° to 90° at Ronneby and from 260° to 320° at Luleå Airport, as well as from 295° to 85° at Havsnäs windfarm. R-square values were averaged over all sectors. (Numbers in parenthesis indicate the range of correlation coefficients.) The ranking is given in parentheses after the numbers.

Mean correlation coefficient	Logarithmic	Power Law	Linear	Log-Linear
Luleå Sodar	0.992 (3) (0.986-0.998)	0.998 (2) (0.996-1.000)	0.985 (4) (0.978-0.993)	1.000 (1) (0.999-1.000)
Ronneby Sodar	0.994 (3) (0.984-1.000)	0.998 (2) (0.995-0.999)	0.976 (4) (0.959-0.992)	0.999 (1) (0.998-1.000)
Havsnäs Lidar	0.995 (3) (0.987-1.000)	0.996 (2) (0.981-1.000)	0.980 (4) (0.938- 0.998)	0.999 (1) (0.996-1.000)

Wind shear

Shear exponents (α) for sector wise averaged wind profiles at Ronneby Airport ranged from 0.249 to 0.316, with a mean value and standard deviation of 0.279 and 0.017, respectively.

Shear exponents (α) for sector wise averaged wind profiles at Luleå Airport ranged from 0.186 to 0.287, with a mean value and standard deviation of 0.247 and 0.040. For the sectors 260-270°, 270-280°, 280-290°, 290-300°, 300-310°, and 310-320°, α was 0.2781, 0.2867, 0.2729, 0.2455, 0.2159, 0.1855, respectively. This indicates that only the first three sectors represent undisturbed forest terrain.

Shear exponents (α) for sector wise averaged wind profiles at Havsnäs ranged from 0.220 to 0.385, with a mean value and standard deviation of 0.268 and 0.041. The number of profiles in each sector was between 36 and 1556. Clearly longer data sets are required to get reliable mean wind profiles in the least frequent sectors.

Wind shear depends on wind speed as higher turbulence generally leads to less wind shear (see Figure 2-9 for Ronneby airport). Owing to stability effects, there is large scatter for lower wind speeds. At very high wind speeds, when neutral stratification can be assumed, the spread becomes very small and the shear exponents is almost constant. Figures looked similar for the other two sites (not shown). At Havsnäs, however, the number of profiles at high wind speeds was too low to draw any conclusion.

Frequency distributions of wind shear exponents look pretty similar at both sites (Figure 2-10). The distribution at Ronneby airport is a bit narrower than at Luleå airport. This could be caused by the fact that not all sectors used at Luleå airport resembled shear exponents for forested areas. The distributions resemble closely those from Figure 2-2 for the three met masts studied herein. However, both Sodar

locations showed a higher prevalence of negative wind shear exponents than the met masts. The distribution at Havsnäs seems a bit narrower than at the two other sites (Figure 2-10). This could be caused by lower surface roughness or orographic speed-up.

Average shear exponents were calculated for low wind speeds ($U_{100m} \leq 12$ m/s) as well as for high wind speeds ($U_{100m} > 12$ m/s). In the former case, stability effects have a strong impact on shear exponents. In the latter case, however, neutral stratification can be assumed with almost constant shear exponents. This is indeed the case as shown in Table 2-14.

Table 2-14. Average shear exponents from full profiles for low wind speeds (≤ 12 m/s at 100 m) and for high wind speeds (> 12 m/s at 100 m). The standard deviations of the average shear exponents are also given.

Site	Shear exponent α ($U_{100m} \leq 12$ m/s)	Standard deviation of α ($U_{100m} \leq 12$ m/s)	Shear exponent α ($U_{100m} > 12$ m/s)	Standard deviation of α ($U_{100m} > 12$ m/s)
Luleå Sodar	0.255	0.204	0.212	0.094
Ronneby Sodar	0.284	0.161	0.159	0.076
Havsnäs Lidar	0.268	0.188	0.121	0.048

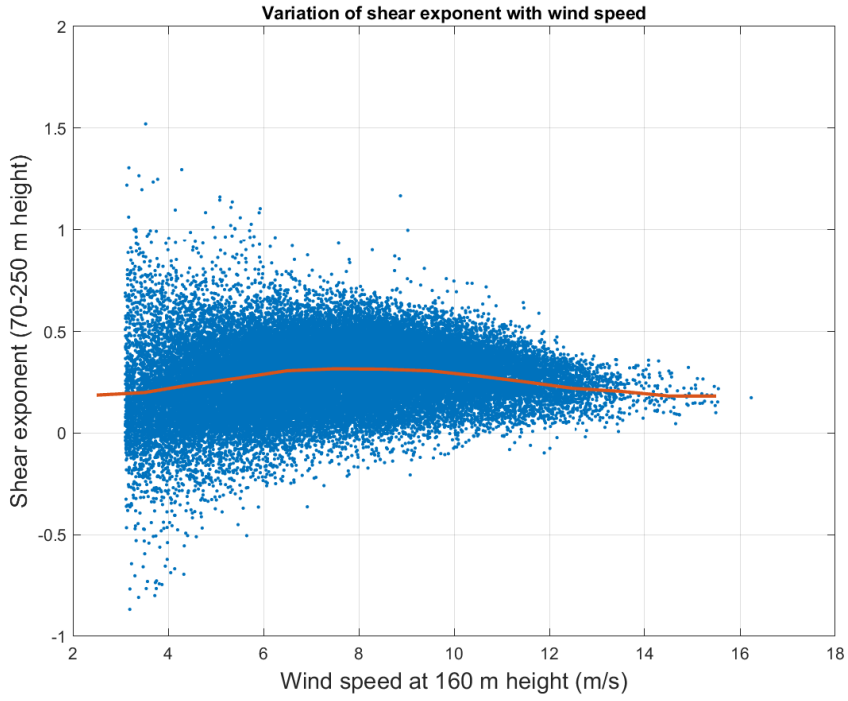

Figure 2-9. Dependence of wind shear exponent on wind speed for Ronneby Airport. Obtained between 70 and 250 m height. Only full wind direction profiles from sectors specified in Table 2-6 were used. Binned averages shown in red.

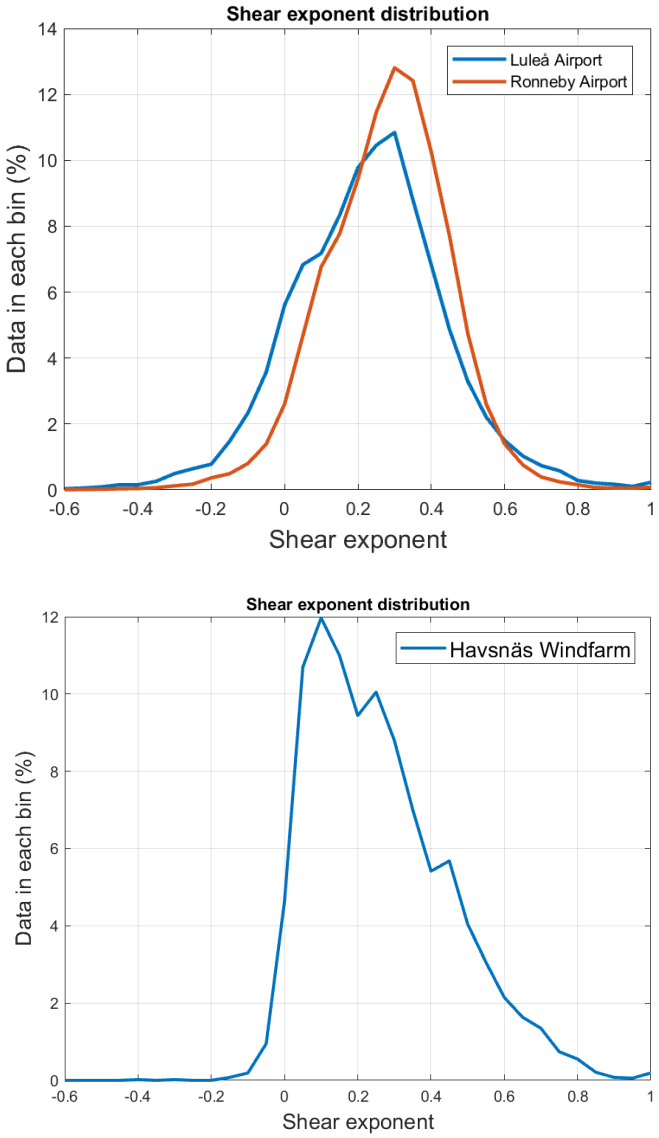

Figure 2-10. Histogram of shear exponents for Luleå and Ronneby Airport (upper) as well as Havsnäs (lower). Obtained between 70 and 250 m height (upper) and 52 and 142 m height (lower). Only full wind direction profiles from sectors specified in Table 2-12 were used.

Wind shear over entire profile versus lower/upper half profile

Wind shear exponents were computed for the entire profiles (70-250 m height) as well as for the lower/upper half of the profiles (70-160 m/160-250 m height). At Havsnäs, wind shear exponents were computed for the entire profiles (52-142 m height) as well as for the lower/upper half of the profiles (52-97 m/107-142 m height). Correlation is quite good when shear exponents from the lower and upper half of the profiles were compared to shear exponents from the full profiles. However, when shear exponents from the lower half of the profiles were compared to shear exponents from the upper half of the profiles correlation was not existent (Table 2-15).

Table 2-15. Shear exponents from upper/lower half of profile versus shear exponent from full profile. Correlation coefficients (not squared) are also given. For the lower half, shear exponents obtained from curve fitting ("cf") were also compared to shear exponents from two heights only ("simple"). Bold numbers indicate recommended ways to estimate shear of whole/parts of the profile (from x to y), whereas red numbers designate non-favourable ways to estimate shear of whole/parts of the profile.

Site	Comparison (y / x)	Slope (linear fit through origin)	Correlation coefficient R (linear fit through origin)	Slope (linear fit)	Y-axis intercept (linear fit)	Correlation coefficient R (linear fit)
Luleå	**Lower half / full profile**	0.90	0.88	0.81	0.04	0.89
	Full profile / lower half	**1.01**	**0.88**	**0.97**	**0.02**	**0.89**
	Upper half / full profile	1.17	0.84	1.38	-0.10	0.86
	Full profile / upper half	**0.71**	**0.74**	**0.54**	**0.11**	**0.86**
	Upper half / lower half	**1.03**	**0.54**	**0.95**	**0.03**	**0.54**
	Lower half / upper half	**0.55**	**0**	**0.31**	**0.16**	**0.54**
	simple / cf (lower half)	**1.02**	**1.00**	**1.03**	**0.0**	**1.00**
	cf / simple (lower half)	**0.98**	**1.00**	**0.96**	**0.0**	**1.00**
Ronneby	**Lower half / full profile**	**0.97**	**0.88**	0.88	0.0	0.89
	Full profile / lower half	**0.98**	**0.88**	0.90	0.03	0.89
	Upper half / full profile	1.11	0.78	1.27	-0.10	0.85
	Full profile / upper half	**0.80**	**0.70**	**0.56**	**0.12**	**0.85**
	Upper half / lower half	**0.97**	**0.50**	**0.79**	**0.10**	**0.52**
	Lower half / upper half	**0.71**	**0**	**0.34**	**0.18**	**0.52**
	Simple / cf (lower half)	**1.03**	**1.00**	**1.05**	**0.0**	**1.00**
	cf / simple (lower half)	**0.97**	**1.00**	**0.95**	**0.0**	**1.00**
Havsnäs	**Lower half / full profile**	0.94	0.88	0.87	0.0	0.89
	Full profile/ lower half	**0.99**	**0.88**	0.90	0.0	0.89
	Upper half / full profile	1.04	0.82	1.04	0.0	0.82
	Full profile / upper half	**0.82**	**0.76**	**0.64**	**0.09**	**0.82**
	Upper half / lower half	**0.93**	**0.43**	**0.65**	**0.1**	**0.50**
	Lower half / upper half	**0.69**	**0**	**0.39**	**0.15**	**0.50**
	simple /cf (lower half)	**0.98**	**1.00**	**0.98**	**0.0**	**1.00**
	cf / simple (lower half)	**1.01**	**1.00**	**1.02**	**0.0**	**1.00**

Average shear exponents for Luleå, Ronneby and Havsnäs are summarised in Table 2-16. In contrast to the three masts investigated herein, average shear exponents for the lower half of the profiles are lower than average shear exponents for the full profiles which, in turn, are lower than average shear exponents for the upper half of the profiles. At Ronneby Airport, however, the differences are very small. Somewhat surprisingly, shear seems to increase with height at all three sites. However, this increase seems to be very small at Ronneby (Table 2-16).

Table 2-17 shows average shear exponents for the lower half of the profiles estimated from curve fitting (based upon several data points) and the simple method (based upon two points only). In the latter case Equation 2-2 was used whereas in the former case the Curve Fitting Toolbox in MATLAB was used together with an additional scale factor (Equation 2-2a). Differences in mean shear exponents from both methods are very small and correlations are very good (Table 2-15 and Table 2-17).

Table 2-16. Average shear exponents from full profiles, lower and upper half of profiles for Luleå Airport, Ronneby Airport and Havsnäs windfarm. The number of profiles used is also given in the table.

Site	No of profiles	α (full profile)	α (lower half)	α (upper half)
Luleå	13518	0.253	0.243	0.263
Ronneby	40185	0.284	0.282	0.291
Havsnäs	5264	0.257	0.249	0.267

Table 2-17. Average shear exponents for lower half of profiles from curve fitting using several heights and from simple method using two heights.

Site	No of profiles	α (lower half, curve fitting)	α (lower half, two points)	Difference
Luleå	13518	0.243	0.246	+1
Ronneby	40185	0.282	0.288	+2%
Havsnäs	5264	0.249	0.249	0%

Wind direction profile

Wind direction change across the rotor is important for energy yield (through REWS) as well as for load estimations.

For the wind direction profiles a linear fit seems to agree excellently (as suggested by Lezaun Mas 2014). Again only full profiles between 70 and 250 m height above ground were used.

Average absolute correlation coefficients are 0.849 for Ronneby and 0.884 for Luleå from roughly 40 000 and 14 000 profiles, respectively. Average values for vertical wind direction gradients are 4.0° per 100 m height difference for Ronneby and 6.2° per 100 m height difference for Luleå. Standard deviations of these gradients are 6.4° per 100 m height difference and 8.4° per 100 m height difference, respectively. Frequency distributions are shown in Figure 2-11.

It seems that wind direction generally changes more with height at Luleå airport than at Ronneby airport. Probably, the higher occurrence of stable conditions at Luleå Airport leads to a slightly higher veer, on average.

At Havsnäs, wind direction profiles between 52 and 142 m height above ground were used. Average absolute correlation coefficients were 0.961 from roughly 5 000 profiles. Average wind direction change with height was 4.5° per 100 m height difference for Havsnäs. The standard deviation of the vertical wind direction gradient was 7.8° per 100 m height difference. Distributions are shown in Figure 2-11.

As already shown in Figure 2-5, wind veer depends on wind speed as higher turbulence generally leads to less wind veer. This can clearly be seen at all three sites (not shown). However, the number of profiles at high wind speeds is very low. Surprisingly, wind veer was zero at Havsnäs for very high wind speeds.

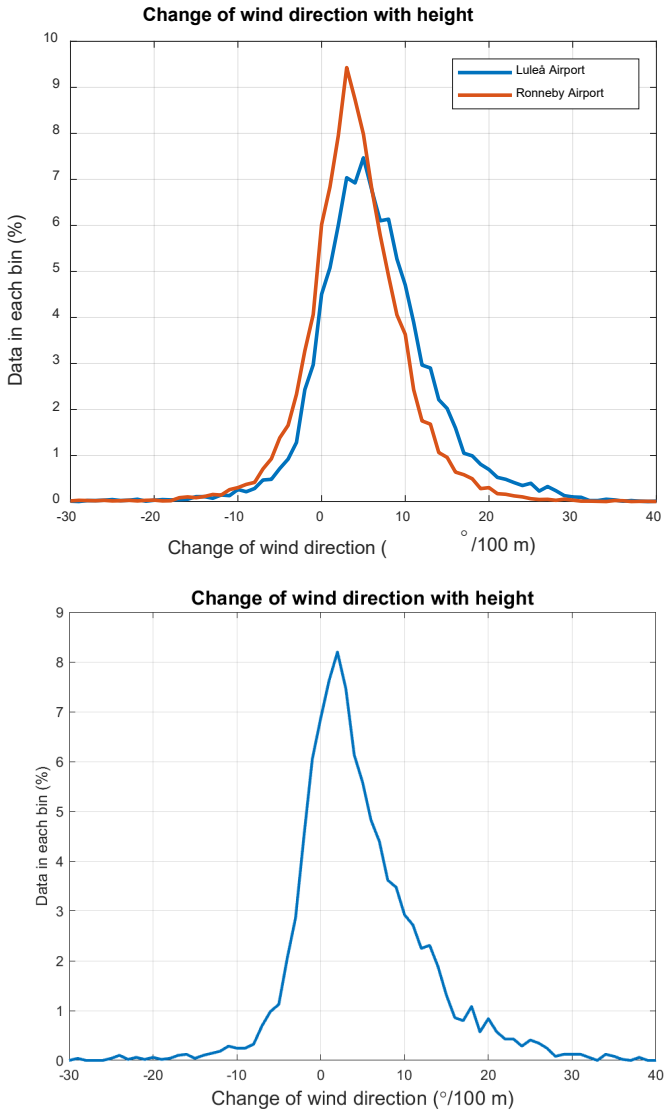

Figure 2-11. Change of wind direction with height for Luleå and Ronneby Airport (upper) as well as Havsnäs wind farm (lower). Obtained with linear fit between 70 and 250 m height (for Havsnäs between 52 and 142 m height). Only full wind direction profiles from sectors specified in Table 2-9 and Table 2-10 were used.

2.3 SUMMARY & CONCLUSIONS

The wind resource at very high heights was studied using measurements from three tall masts (Hornamossen, Ryningsnäs and a site in Östergötland) as well as two Sodars (Luleå and Ronneby airport) and one Lidar (Havsnäs wind farm). For the wind profile ("wind shear"), the following expressions were tested in conjunction with a pre-estimated (first-guess) displacement height:

- Logarithmic wind profile
- Power law
- Linear wind profile
- Log-linear wind profile

For the wind direction profile ("wind veer"), a linear fit was used. Both 10/15-minute averages as well as wind direction sector averages were analysed.

Altogether, roughly 400 days of data from Hornamossen and the Östergötland site as well as roughly 180 days worth of data from Ryningsnäs were used. Wind speed and direction profiles reached up to 180 m height at Hornamossen, 140 m height at Ryningsnäs and 150 m height at the Östergötland site. Sodar data reached up to 250 m height and Lidar data up to 143 m height.

Not surprisingly, the log-linear profile outperformed, on average, the remaining expressions as there are three parameters that can be fitted to the profile compared to two in the remaining expressions. The Power law slightly outperformed the logarithmic wind law, on average, except for Hornamossen where both performed approximately equally well. At Luleå, the linear wind profile slightly outperformed the power law, on average.

For roughly 50-70% of the profiles, the log-linear profile performed better than the logarithmic profile. For roughly 30-50% of the profiles, the linear profile performed better than the logarithmic profile. However, for only roughly 10% of the profiles the linear profile performed better than the power law. For roughly one third of the profiles, the power law performed significantly better than the logarithmic profile. For less than 20% of the profiles, however, the logarithmic profile performed significantly better than the power law.

For sector-wise mean profiles, the log-linear profile again performed best, followed by the power law (except for Hornamossen where the power law and the logarithmic profile performed approximately equally well).

For Ryningsnäs and the Östergötland site, wind shear, on average, decreased slightly with height from the lower half of the profiles to the upper half of the profiles. At Luleå, Ronneby and Havsnäs wind shear increased slightly with height. At Hornamossen, on the other hand, shear exponents decreased strongly (by about 10%) with height.

There is a lot of variation in wind shear exponents up to about 12, 13, 14 m/s, or so, when shear exponents are plotted against 10-minute average wind speed. This is due to stability effects. Above that, where neutral stratification can be assumed, wind shear exponents are almost constant with little variation.

Wind shear exponent frequency distributions look very similar to normal distributions. Hornamossen, which has more speed-up than the other two sites, shows a wind shear frequency distribution that is narrower. Negative shear exponents are pretty rare at all three measurement masts as well as at Ronneby and Havsnäs, except for Luleå where they seem to occur quite frequently.

Wind shear exponents from the lower half of the profiles correlate well with wind shear exponents from the full profiles, deviating only about a couple of percent (except for Hornamossen where wind shear seems to decrease by 10% from the lower half of the profiles to the upper half of the profiles). However, wind shear exponents from the lower half of the profiles do not correlate at all with wind shear exponents from the upper half of the profiles.

Wind shear exponents calculated from two points only agree excellently with wind shear exponents from curve fitting using multiple points. However, as Derrick et al. (2013) pointed out the multi-point curve fitting method should be less dependent on a correct estimation of the displacement height.

Wind direction profiles follow a linear expression very well. Most of the time wind direction (in degrees) increases with height. Wind direction changes with height were on average roughly 5°, 13° and 15° per 100 m height difference at Hornamossen, Ryningsnäs and the Östergötland site. At Ronneby, Luleå and Havsnäs, this was 4°, 6° and 5° respectively, per 100 m height difference. Standard deviations of wind direction changes with height seem to be around 8° per 100 m height difference (except for the Östergötland site where this was 14° per 100 m height difference).

Wind veer with height shows a large variation up to 10-minute average wind speeds of say 12, 13 or 14 m/s. Above that, when neutral stratification can be assumed, wind veer with height is nearly constant.

It can be concluded that at very high heights the power law seems to work very well for both 10-minute average and sector-average wind profiles at very high heights, Even though the log-linear profile performs even better, it is probably going to be impractical to use. For the 10-minute average wind direction profiles a linear profile seems to work very well.

3 Turbulence and wind measurements

3.1 HORNAMOSSEN SITE DESCRIPTION

Much of the work within the project revolves around the tower measurements performed in southern Sweden. The measurements were taken in a 180 m high meteorological mast equipped with sensors to measure the conditions in the atmosphere. The project partners collaborated with OX2 Wind AB who co-financed the measurements and made it possible to carry out these unique measurements. The site is called Hornamossen and is located in southern Sweden (57.981° N, 13.942° E) on the top of a hill as part of the ridge Hökensås.

Figure 3-1. Location of the measurement site. The red box marks the area of Figure 3-2 (upper figures).

The location of the site can be seen in Figure 3-1, where the red box indicates the area of the outmost zoom in Figure 3-2 a) and b), which shows the elevation and tree height deduced from airborne laser scans. The forest consists predominately of spruce, but is mixed with pine and some deciduous forest types. The site includes a variety of heterogeneities in both topography and land cover. The forest itself is also heterogeneous with patches of trees of different densities, height and age. The site is typical for wind energy exploration in Sweden and offers many possibilities to investigate heterogeneities in the wind field due to vegetation and elevation.

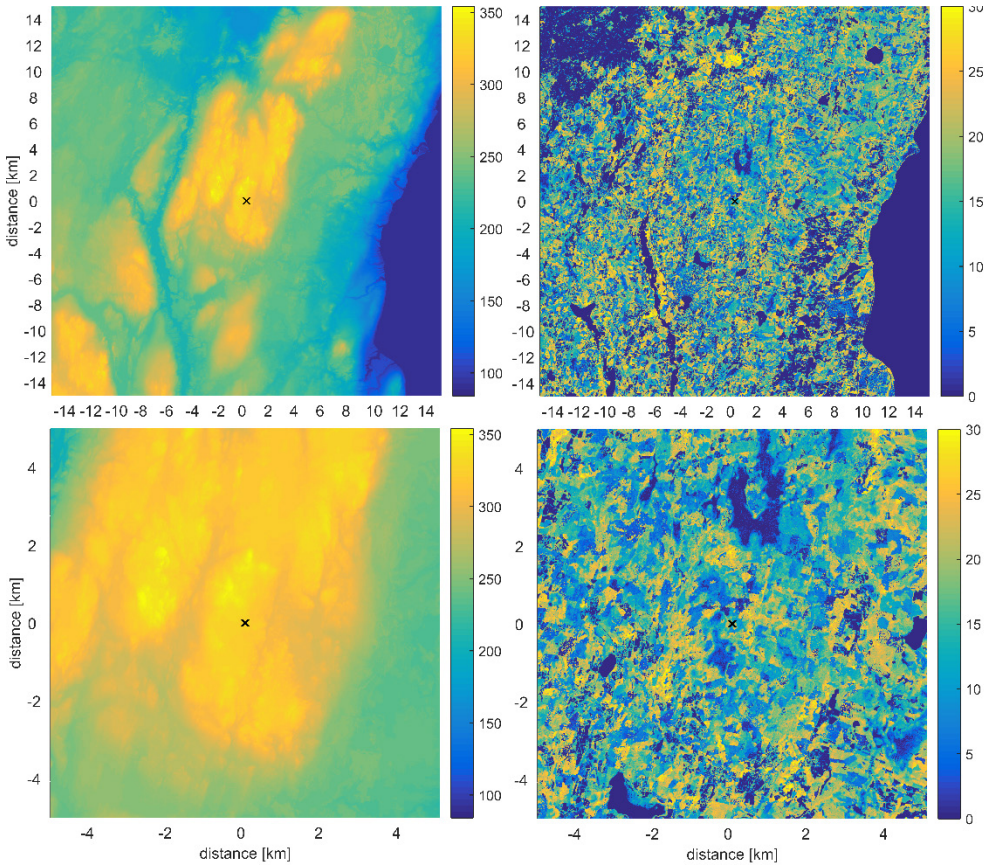

Figure 3-2. Elevation (left panels) and tree height (right panels) for the area surrounding the measurement tower. The location of the tower is marked by x. Lower figures show zoomed-in images of upper figures.

3.2 MEASUREMENTS TAKEN WITHIN THE PROJECT

The met mast was operational between May 2015 and June 2017, giving two full years of data. The mast was triangular with sides of 1.2 m and tethered at the levels 30, 53, 76, 100, 147 and 170 m above ground in the directions 41°, 161° and 281°. An overview of the main instrumentation is found in Table 3-1. The anemometers were placed at the end of 6 m long booms that extended 5 m out from the tower and were supported by 4 m long support booms. Apart from the instruments listed in the table, atmospheric pressure measurements were taken at 7 m and relative humidity at 173 m.

The sonic anemometers where sampled and stored at the frequency of 20 Hz. The levels 40, 100, 151.9 and 173 m included instrument heating.

The temperature measurements originally consisted of a thermocouple system, but after considerable measurement problems during the first year, most probably caused by disturbances from the currents to the other instruments, the lantern and the fans, the system was replaced by platinum resistance sensors that are less sensitive. That system was operational during the second year of the tower measurements. All the temperature measurements were ventilated using Young aspirated ventilation shields.

In addition to the measurements in the tower, AQSystem contributed to the project by placing an AQ510 sodar 400 m northwest of the tower from Oct 13 2015 to Jan 13 2016. Meventus contributed to the project by placing a Leosphere Windcube V2 at the tower between June 28 and July 31 2016.

Table 3-1. Hornamossen tower instrumentation.

Instrument	Measurement heights (m)	Boom directions
Metek uSonic-3	20.8, 40.0, 60.2, 82.1, 100.0, 121.9, 151.9, 173.0	131°
Vaisala cup	77.6, 117.9, 147.7	311°
Thies 1st class cup	40.0, 60.0, 82.1, 100.0, 122.0, 152.0, 179.8	311°
Wind vane	77.5, 122.9, 147.7	131°
Temperature sensors	9, 18.7, 39.2, 58.3, 80.9, 98.9, 120.9, 150.8, 172.3	N/A

3.3 MEASUREMENTS TAKEN WITHIN THE NEWA CAMPAIGN

Apart from the measurements taken within the ForestWind project, additional measurements were taken within the NEWA project. These included measurements by remote sensing at eight additional locations as well as at the site of the tower. The location of the remote sensing instruments is best seen in Figure 3-3 where they are indicated by their model name. At the tower site there was a Zephir 300 lidar measuring at the same heights as the tower, but recording raw data in order to validate the lidar performance and provide redundancy to the tower measurements. Also at the tower site 2 Kipp and Zonen 4-way radiation sensors at the heights 1 and 30.5 m were installed. An additional Zephir 300 was deployed at the westernmost location, measuring the wind speed up to 300 m and also recording raw data.

One of the remote sensing points was equipped with a Leosphere V1 lidar (40-200 m), a Leosphere WLS70 lidar (100-1500 m) and a Vaisala ceilometer backscatter lidar, with the aim of covering the wind profile in the whole boundary layer, and using the ceilometer backscatter information to monitor the boundary layer height. The other measurement points consisted of AQSystem AQ510 sodar profilers. They measure the wind profile between 40 and 200 m with 5 m resolution. Raw data was recorded to enable additional analysis on turbulence and boundary layer height.

In addition to the wind measurements, a system of Digiquartz 6000-16B-IS microbarometers was deployed in a square with around 3 km sides in an attempt to measure the static pressure gradient of the atmosphere.

The remote sensing campaign ran between April and October 2016, but some of the instruments were removed in August.

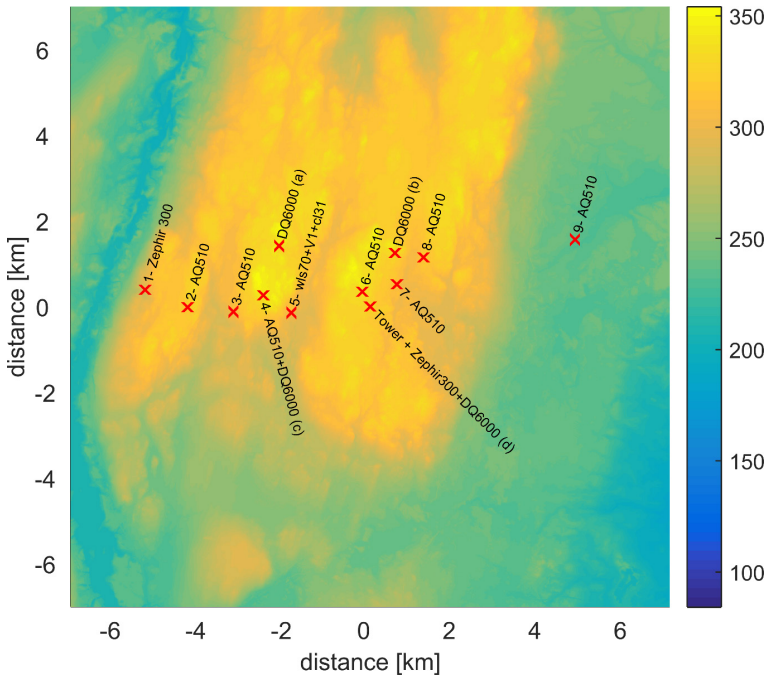

Figure 3-3. Locations of instruments during the extended measurement campaign taken within the NEWA project.

3.4 POST PROCESSING AND QUALITY CONTROL

3.4.1 Cup anemometers

Cup anemometer measurements were transformed into 10-minute averages before logging, yielding statistics of mean value, standard deviation, minimum and maximum value within each 10-minute interval. When comparing the cup anemometers to the other anemometers it became apparent that the Thies cups, even though heated in the bearing, were affected by icing. An example of how an icing event affects the Thies cups but not the Vaisala cups is illustrated in Figure 3-4. Due to this the Thies cups quality was flagged when the temperature was below zero.

3.4.2 Sonic anemometers

The sonic anemometers were sampled and stored at 20 Hz. Icing on unheated Metek uSonic-3 may cause errors in the form of large unphysical values in the time series. To assess quality and correct for spikes data quality control was performed as in Arnqvist et al (2015), which involves searching for and correcting for unphysical spikes in the original coordinate system of the instrument. If the number of spikes was more than 60 during a 30-minute period (36 000 values) a bad-quality flag was raised.

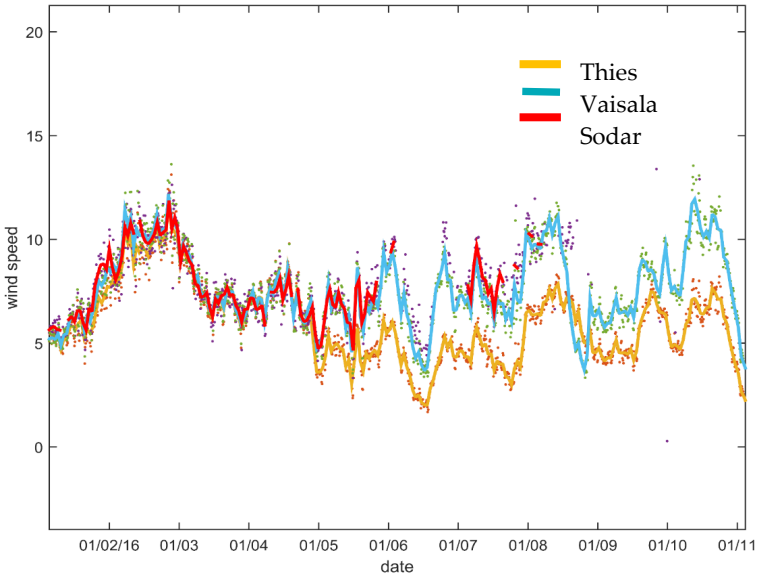

Figure 3-4. Time series of the wind speeds from cups and sodar during an icing event. The full lines represent hourly average and the dots 10-minute averages.

Out of the 20 Hz time series statistics were computed for 5, 10 and 30 minute averages. The coordinate system of the sonic was turned in the direction of the mean wind, $\bar{u}$, where the overbar denotes time average and the three velocity components are u, v and w, representing longitudinal, lateral and vertical velocity. Scalar wind speed s was also computed, both using 2D ($s_{2D} = \sqrt{\overline{u^2 + v^2}}$) and 3D ($s_{3D} = \sqrt{\overline{u^2 + v^2 + w^2}}$). Instantaneous fluctuations around the mean value are denoted with a prime, as in u'=u-$\bar{u}$. From the time series, averages of all the first and second order moments were computed as well as the isotropic third order moments. In addition to that, the sonic anemometer was resampled using a length constant of 3 m in order to mimic the measurement of a cup anemometer, and the average 2D as well as 3D wind speed were computed. To assess the stratification, the Obukhov length, L, was determined as:

$$L = \frac{-u_*^3}{\kappa \overline{w't'}} \frac{T_0}{g}, \qquad (3\text{-}1)$$

were $u_* = (\overline{u'w'}^2 + \overline{v'w'}^2)^{1/4}$ is the friction velocity, T_0 is virtual air temperature in Kelvin, g is the gravitational acceleration, κ is the von Karman constant (κ=0.4), and $\overline{w't'}$ is the virtual kinematic heat flux. T_0 is the mean temperature at the same level. L and u_* were determined both using a 2D and 3D rotation of the velocity field, but if not otherwise is mentioned, the 2D rotation was used. u_* and L were calculated at all levels, but if not otherwise mentioned the 40 m level is used.

When studying the wind speed from both sonics and cups it became apparent that the sonic anemometers were measuring slightly too low or slightly too high values (Figure 3-5). The sonic anemometers were not wind tunnel calibrated when purchased, which the cup anemometers were. Since wind tunnel calibration was not possible while the sonics were in the tower, a first correction was calculated with the process described below:

- Data were selected by ensuring neutral conditions (z/L>-0.1 and z/L<0.07), the data quality was good, and the data was stationary.
- The lowest wind speed was greater than 3 ms^{-1}.
- The temperature was > 5 °C.
- The wind direction was perpendicular to the boom direction within ± 10°.

For each height with both a sonic and a cup anemometer, a linear regression coefficient k, as in $y=kx$, was then calculated and used to correct the sonic mean winds. In order to account for errors (statistical and other) in both cups and sonics, the problem was solved by least square minimisation using both cups and sonics as the dependent variable (x) and the final k was calculated by geometric average of the two estimates as $k=(k_1/k_2)^{1/2}$. The wind profile before and after this procedure can be seen in Figure 3-5. Individual scatterplots with linear fits can be seen in Figure 3-6. The coefficients were used to correct both the mean scalar and vector wind.

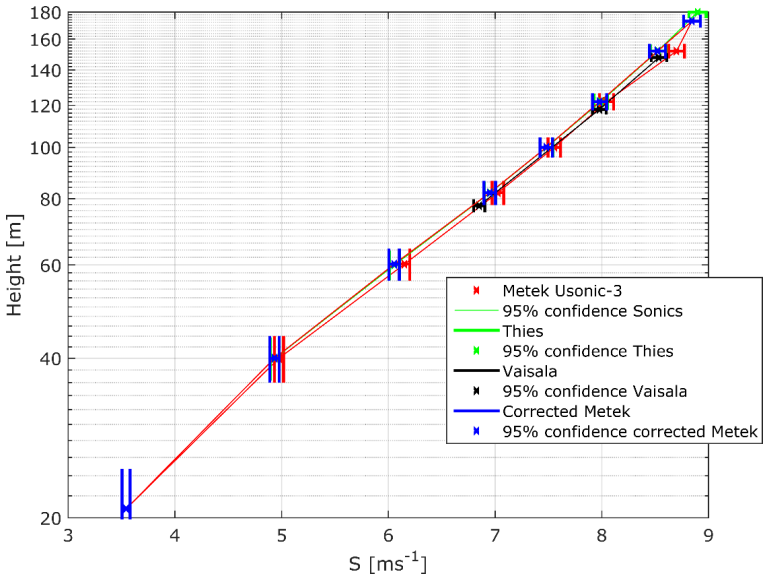

Figure 3-5. Wind profile before and after the correction of the Metek sonics.

When installing the Metek sonics on the booms the technicians were not able to align the instruments exactly along the booms, which meant that the wind direction had an individual offset for each height. Unfortunately, not enough care was directed to measuring this offset when the tower was taken down. Instead, in order to correct the wind directions from the sonic, remote sensing instruments were used. These included the Zephir and the Windcube V2 that were placed at the tower site. Linear offsets were found from scatterplots and the wind directions were corrected accordingly. See Figure 3-7 for a comparison of the wind veer profile before and after application of the offsets.

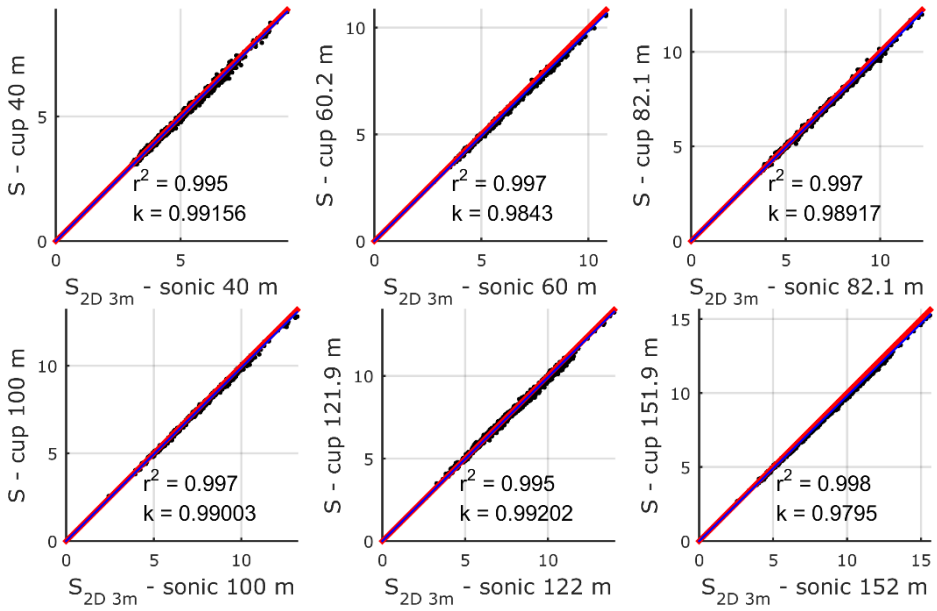

Figure 3-6. Scatterplots of the uncorrected wind speed from the sonics as well as from the cups. The red line shows the 1:1 line, the blue line is the regression *y=kx* and the individual measurements are shown by blue dots.

3.4.3 Flow distortion assessment

The centre of the flow distortion was found by studying the ratio of the anemometers on each side of the tower at the same height and seeing when the maximum difference occurred. This was done since the booms are placed on one side of the tower and thus the direction of maximum flow distortion is not the same as the direction of the booms. The centre of flow distortion was found to be 137° for the cups and 325° for the sonics, as opposed to the boom directions of 131° and 311° respectively.

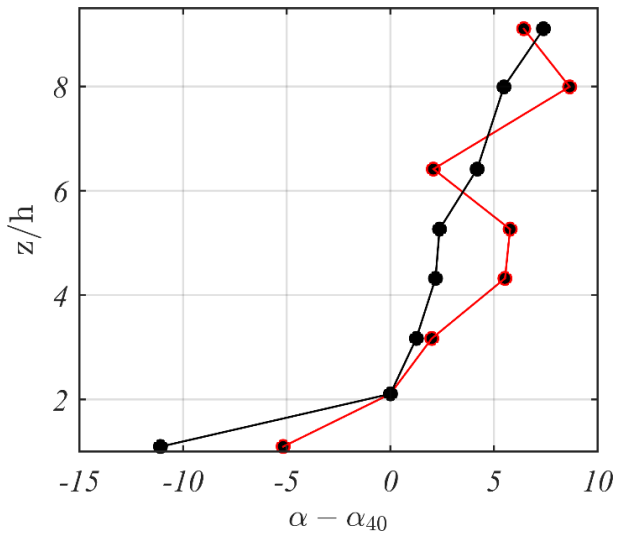

Figure 3-7. Wind veer profile before (red) and after (black) offsets to the wind direction deduced from remote sensing comparison had been applied.

3.4.4 Temperature measurements

The cups, vanes and temperature sensors were all sampled at 1 Hz and 10 minute statistics were produced by the logger including, among other things, the temporal mean, maximum/minimum value and standard deviation.

Considerable time was spent on trying to filter the thermocouple measurements by removing spikes from the high frequency time series, studying correlation patterns with possible disturbances, filtering, etc., but finally it was deemed that the data was of too poor quality to give reliable estimates of the temperature gradient.

It was therefore decided to replace the thermocouples with platinum wires. Instead of measuring temperature differences between two levels, the platinum wire sensors were configured to measure the absolute temperature at each level. Hence, the accuracy of the temperature differences is not as high as with a thermocouple system. Before mounting, calibration of the sensors was made in ice water, but an examination of the field data still showed some inconsistencies in the profile. In order to correct for that, the following procedure was used:

- Stationary and quality controlled statistics from the sonic anemometers were used to find neutral conditions.
- Neutral conditions were defined by ensuring each height, z, satisfies the criteria $z/L > -0.1$ and $z/L < 0.07$.
- A linear regression line was fitted to the average temperature fulfilling the above conditions.
- Offset constants were derived based on the difference between the line and the measurements.

Figure 3-8 a) shows the mean temperature before and after correction following the above procedure (only showing neutral data). The figure also shows the potential temperature, indicating that even though neutral conditions were sought for, the data was biased towards stable stratification. The dry-adiabatic lapse rate is included as a reference as well. Figure 3-8 b) shows the average temperature during day (12-16) and night (00-04) as well as for neutral conditions after the correction factors were applied. From Figure 3-8 b) the curves look smooth without any suspicious wiggle. The lower measurement level is taken below the forest height and hence a different gradient is expected there.

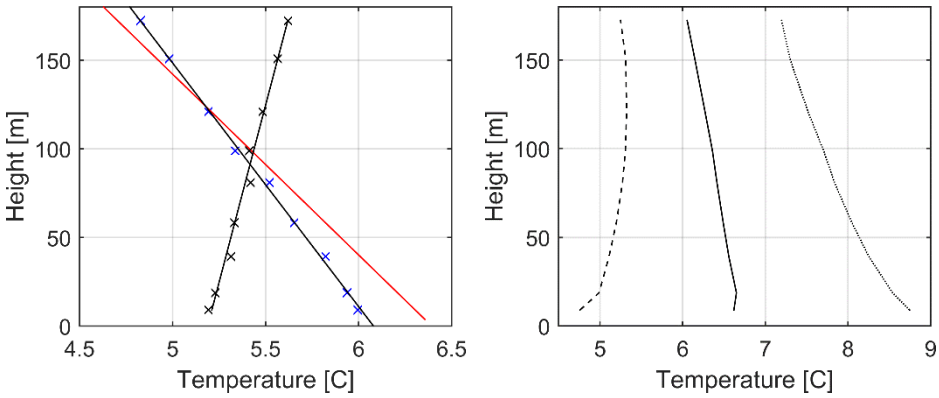

Figure 3-8. Linear correction of the temperature measurements. In a) the blue x-marks show the uncorrected regular temperature, the black x-marks the uncorrected potential temperature, the black lines are curve fits and the red line is the dry-adiabatic lapse rate. In b) the day (dotted), night (dashed) and neutrally stratified (full line) average is shown after correction.

3.5 INSTRUMENT COMPARISONS

As previously mentioned, the NEWA campaign meant that during a shorter period of time the site was instrumented with remote sensing instruments as well. During the period from June 28 to July 31 2016 a total of 6 different measurement systems were measuring at the tower site or nearby. These include the two brands of cup anemometers, the sonic anemometer, the Leosphere WindCube V2 lidar, the Zephir 300 lidar and an AQ510 sodar. The sodar was placed 400 m northwest of the tower and hence does not directly compare to the other instruments. Comparisons were made with the instruments when all instruments showed concurrent good data quality. Data from the tower were omitted when the wind direction was within ±20° of the centre of the flow distortion. The availability of the instruments was not assessed since the period was only one month and the conditions were in the middle of the summer, and hence not representative for long term wind measurements. The wind profile can be seen in Figure 3-9 and the turbulence profile in Figure 3-10. Both wind speed and turbulence have been scaled by the friction velocity taken from the sonic at 40 m. The friction velocity is the same for all instruments and is only acting as a scaling factor and does not affect the relative differences between the curves.

The wind profile is well estimated by all instruments, and well within the confidence level. It is worth noting that the relatively short period contributes to the wide confidence level, and it would be important to measure for a full year in order to assess smaller, but still meaningful differences between the instruments. For example, the deviation of the 152 m sonic anemometer (see Figure 3-5 for the correction) is still well within the confidence level.

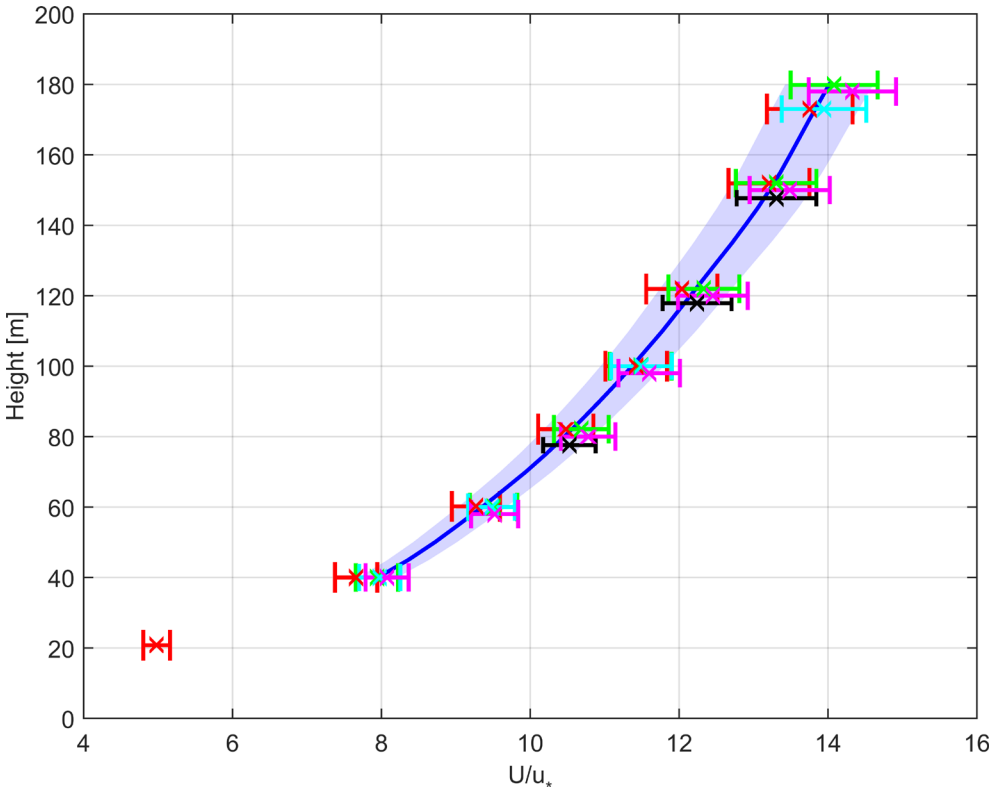

Figure 3-9 Wind profile from the comparison of July 2016. Thies cup (green), Vasila cup (black), Metek sonics (red), Windcube V2 lidar (purple), Zephir 300 lidar (light blue) and AQ510 sodar (dark blue). The error bars and shaded region represent the 95% confidence interval for the mean value based on an assumed Gaussian distribution.

The turbulence level is not well predicted by the instruments and there are differences much larger than the confidence levels (Figure 3-10). As expected, the sonic anemometers capture the high frequency turbulence better than the cups. This leads to higher turbulence level values from the sonics, especially closer to the ground, where the turbulence scales are smaller. The Zephir 300 follows the cup turbulence levels up to 100 m, which is expected since the instrument was probably developed to match the cup turbulence levels. Above 100 m the turbulence level does not decrease as much as in the in-situ instruments which could be a sign of too large measurement volumes or decreasing levels of the signal to noise ratio. The turbulence level from the WindCube V2 is much higher than the other instruments, and while a very good correlation was found, the magnitude is overestimated. The turbulence form the AQ510 agrees with the sonic anemometers in the upper part of the profile, but has much lower levels in the lower part of the profile. This may partly be due to the fact that the sodar was placed in a large clearing, which could affect the turbulence level at the lower heights.

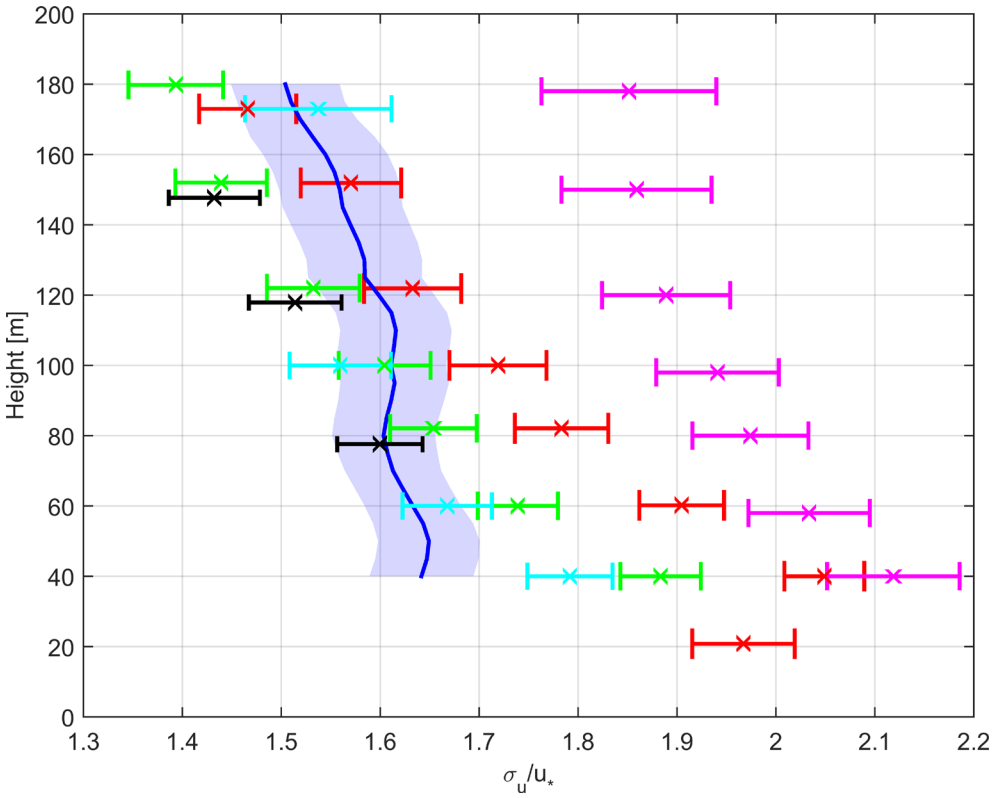

Figure 3-10 Profile of the wind speed standard deviation from the comparison of July 2016. Thies cup (green), Vasila cup (black), Metek sonics (red), Windcube V2 lidar (purple), Zephir 300 lidar (light blue) and AQ510 sodar (dark blue). The error bars and shaded region represent the 95% confidence interval for the mean value based on an assumed Gaussian distribution.

3.6 SUMMARY AND CONCLUSIONS

The chapter describes the measurement campaign at Hornamossen, Hökensås in Southern Sweden. The campaign centered around a 180 m met mast with measurements of wind profile (10 cup and 8 sonic anemometers) as well as the temperature profile (9 levels).

A site description is included using airborne laser scans to characterize the forest and measure the ground elevation.

The measurements are described in two parts, first the measurements taken within the project, which include the tower measurements, and a second part describing the extensive campaign with remote sensing instruments carried out as part of the New European Wind Atlas program.

Quality control and statistical treatment of the measurements are described and include flow distortion, assessment of icing disturbances and correction to the sonic anemometers in terms of wind speed magnitude and wind direction offset, something that proved necessary due to inadequate calibration and mounting precision. The quality control also includes correction for the temperature calibration.

As a concluding section an instrument comparison is presented that shows the wind and turbulence profile measured with 6 systems concurrently for one month. The comparison shows that all of the measurement systems agree in terms of the mean wind profile when conditions have been filtered to only include data of high quality (as flagged by each system), but that the turbulence profile differs between the different systems. The reasons for the different turbulence magnitudes are likely linked to instrumental design, such as response time for the cups and measurement volume for the remote sensing instruments.

4 Analysis of turbulence data

4.1 WIND STATISTICS

Long term statistics of the wind speed over forests was one of the main outcomes of the previous Vindforsk forest project (Bergström et al 2013). The first to third order turbulence moments were reported in Arnqvist et al (2015). In the following section we present an update to the most important parameters for wind energy.

In order to evaluate the different conditions turbines encounter, the data have been split into different atmospheric stabilities by the ratio h/L (Table 4-1). In addition to atmospheric stability, the data have furthermore been split into night and day, by using the local time. Even though there is only an indirect physical connection between turbulence and the hour of the day it is still interesting to see how the *average night* is different from the *average day*. A class representing all the data is also included.

The data in the profile plots represent 30-minute averages. Selection for Ryningsnäs was done as in Arnqvist (2015) and the selection in Hornamossen has been the same, but all wind directions except for $305° < \alpha < 345°$, which were deemed to be flow distorted, have been used.

Table 4-1. Selection criteria for the different atmospheric stability classes.

Name	Selection criteria	Marker
Very stable	*h/L<100*	⋆
Stable	*100<h/L<400*	■
Stable near neutral	*400<h/L<1000*	▲
Neutral	$\|h\|$>1000	X
Unstable near neutral	*-1000<h/L<-400*	Δ
Unstable	*-400<h/L<-100*	□
Night	Between 00:00 and 04:00	●
Day	Between 12:00 and 16:00	○
All data	All data	*

4.1.1 First order moments

Mean wind speed and mean wind veer, α - $\alpha_{\text{reference}}$, can be seen in Figure 4-1. The scaled mean wind speed is larger for all classes at Hornamossen compared to Ryningsnäs which indicates either a lower overall roughness (a lower tree height) or effects of the rolling landscape. Since the topography is relatively mild, most of the effect is likely a lower roughness.

The neutral wind class and the class with all data are considerably different for both sites, reflecting that there is a bias towards stable stratification in the long term mean value. Furthermore, there are large differences between night and day, night having a much larger shear, with weaker turbulence. The effect of the limited boundary layer depth is clearly seen in the very stable class at Hornamossen, with

shear decreasing considerably with height, and almost vanishing above 120 m. This is not seen in Ryningsnäs and may also be an effect of higher roughness.

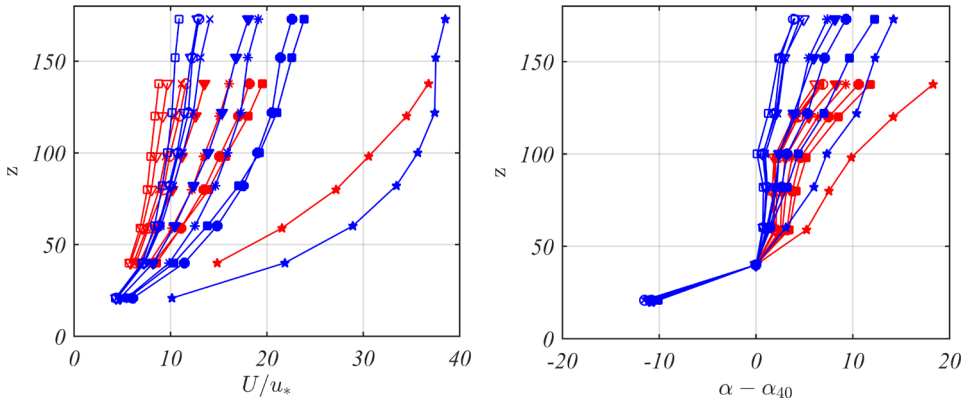

Figure 4-1 Mean wind speed and mean wind veer from Hornamossen (blue) and Ryningsnäs (red). Symbols as in Table 4-1.

The wind veer is weaker at Hornamossen, but still considerable, with an average of more than 6° between 50 and 150 m height above ground for night conditions.

4.1.2 Higher order statistics

The most commonly used higher order turbulence statistics in wind energy is the turbulence intensity. As seen in Figure 4-2, the turbulence intensity is a strong function of atmospheric stability, but also of roughness, and hence Hornamossen has lower values than Ryningsnäs. There is again a large difference between day and night, with night conditions generally below 10% above 100 m while during the day the average values range between 17% and 15% for Hornamossen.

In general the second order moments decrease more quickly with height at Hornamossen than at Ryningsnäs. Also, they show a larger variation with atmospheric stability. The values of standard deviations to friction velocity seem to follow a universal behaviour, $\sigma_u \approx 2u_*$, $\sigma_v \approx 1.6u_*$ and $\sigma_w \approx 1.4u_*$. However, the values decrease more rapidly with height at Hornamossen than at Ryningsnäs and since the friction velocity is defined at 40 m height that is the level for which the ratios are the same at both sites. See chapter 8 for a comparison of the measurements to the IEC standard turbulence.

The skewness of the longitudinal velocity shows a typical roughness sublayer characteristic in the lower part of the profile, with larger positive values closer to the forest height. For unstable stratification the skewness is lower than in stable stratification, taking mostly negative values at rotor heights. This is expected because of the dominance of updrafts in unstable conditions.

Turbulence intensity is often modelled as a function of wind speed, as for example in the IEC standard. The standard formulates 90-percentile values (the value that is only exceeded 10% of the time) for the turbulence intensity. These are defined in three classes A, B and C as function of the wind speed (IEC 2005).

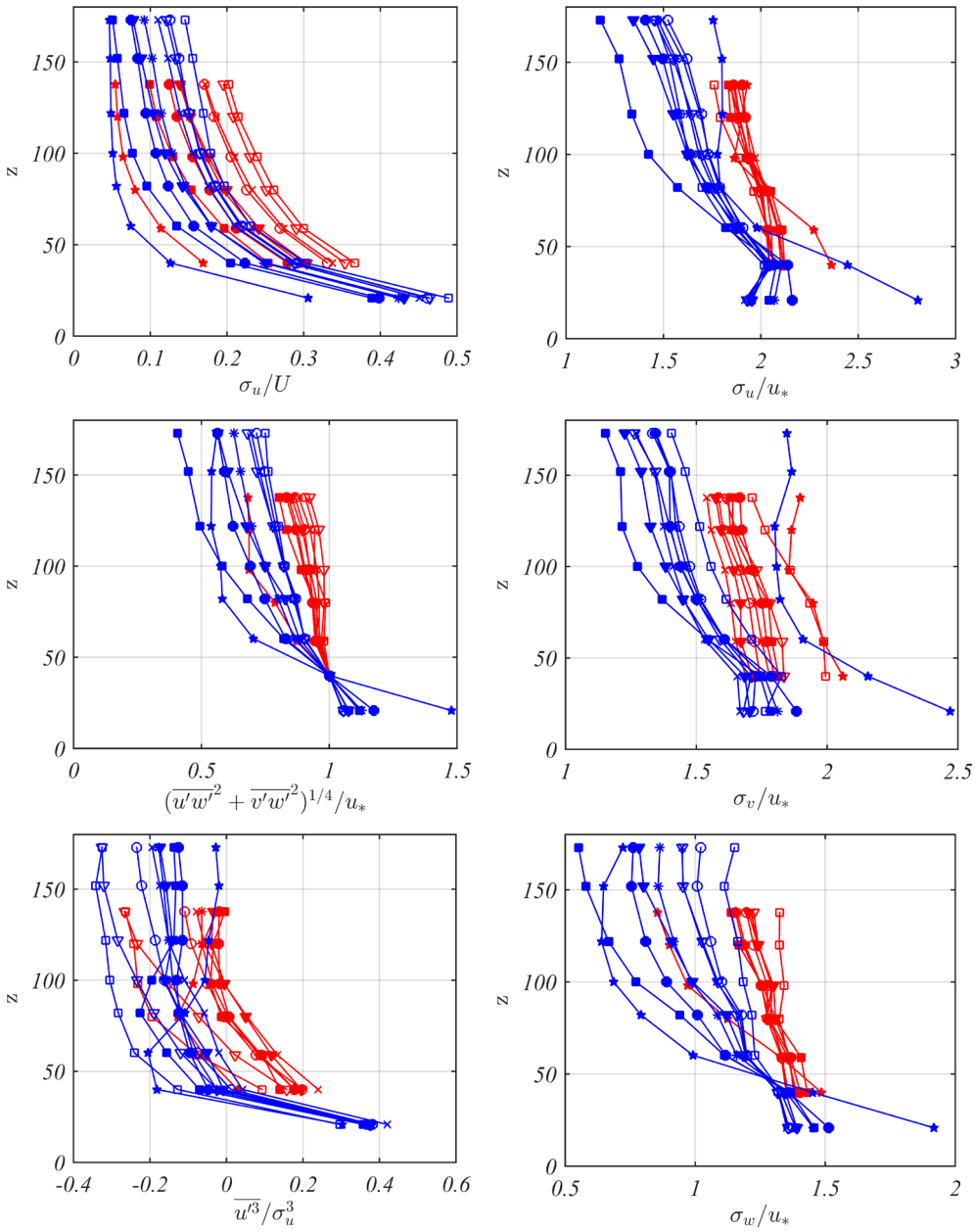

Figure 4-2 Higher order turbulence moments from Hornamossen (blue) and Ryningsnäs (red). Symbols as in Table 4-1.

In Figure 4-3 the IEC model is compared to measurements of 10-minute average σ_u/U from Hornamossen. As can be seen here as well, turbulence intensity is a strong function of stratification, with stable conditions showing much less turbulence intensity than neutral. There is also a large difference between daytime and nighttime values. Also included in the plot is the turbulence intensity from the measurements in strictly neutral conditions, defined as $-0.1 < 173\ \mathrm{m}/L < 0.07$. The strictly neutral conditions could be thought of as the conditions inside the vast majority of CFD models (running strictly neutral conditions). It can be observed that the strictly neutral data show almost constant turbulence intensity with increasing wind speed, something that is not seen when considering all the data.

Compared to conditions representing the norm at the site, the turbulence intensity is around 1.5 times higher in strictly neutral conditions (black and green lines in Figure 4-3, respectively).

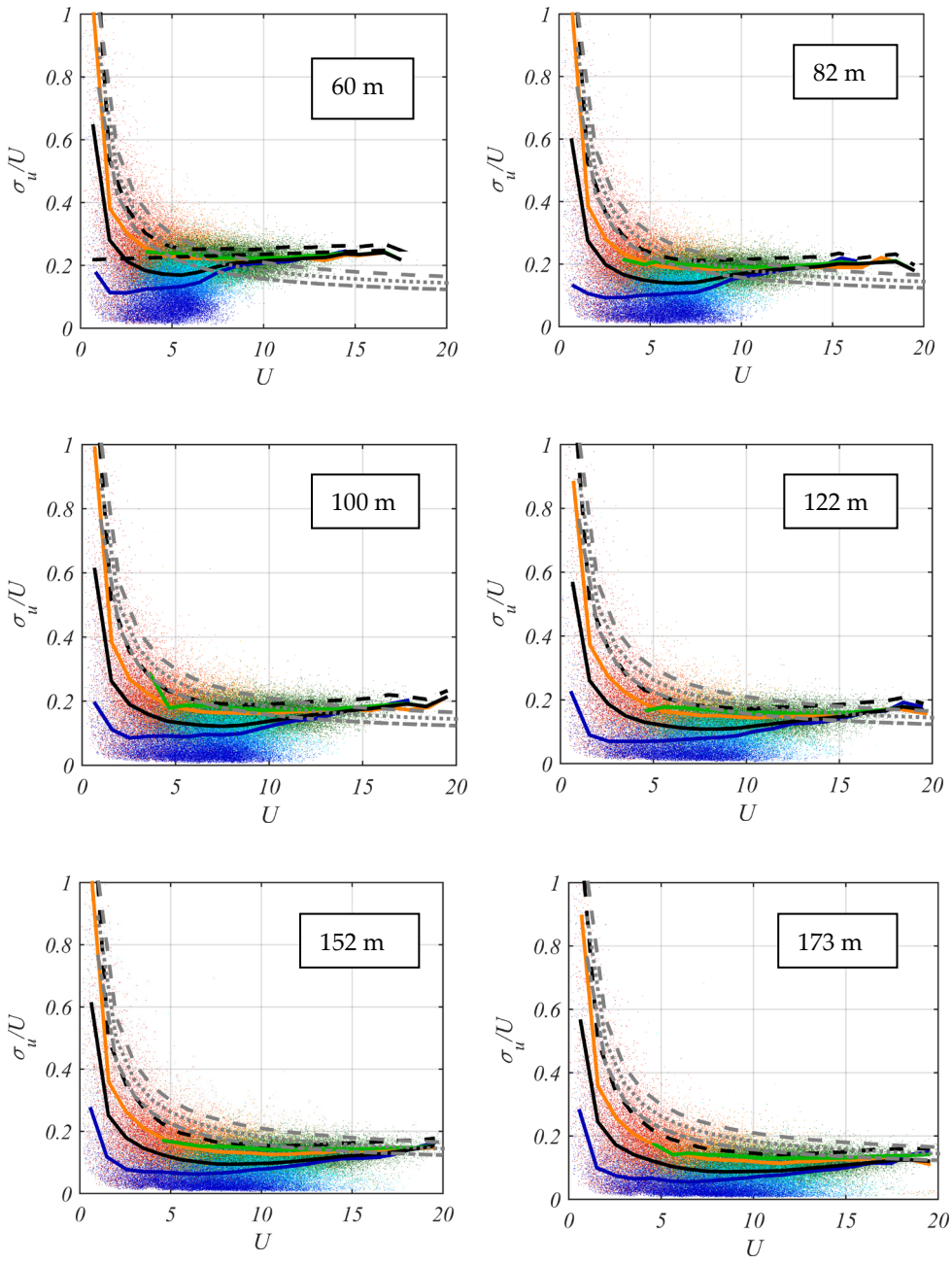

Figure 4-3. Turbulence intensities from Hornamossen. The colour represents the atmospheric stability, with blue as stable, green as neutral and red as unstable. The grey lines represent IEC turbulence model A (dashed), B (dotted), and C (dash-dotted). The dashed black line is the 90% percentile of the measurements. The full lines represent bin averages of nighttime (blue), all data (black), daytime (orange) and strictly neutral (green).

4.2 INTERMITTENT TURBULENCE

During the work of the previous project *Wind power in forests I* (Bergström et al., 2013) it was noted that during nights the turbulence level was mostly very low (see Figure 4-3), but that sometimes bursts of turbulence would occur that suddenly increased the turbulence level sharply. This has earlier been studied in connection with surface fluxes or gravity waves, but not in the context of wind energy. Van de Wiel et al. (2002) developed a model that predicted that such intermittency of turbulence in stable stratification would be more pronounced if the roughness of the surface was high and thus it is very interesting in the context of wind energy above forests to investigate the matter.

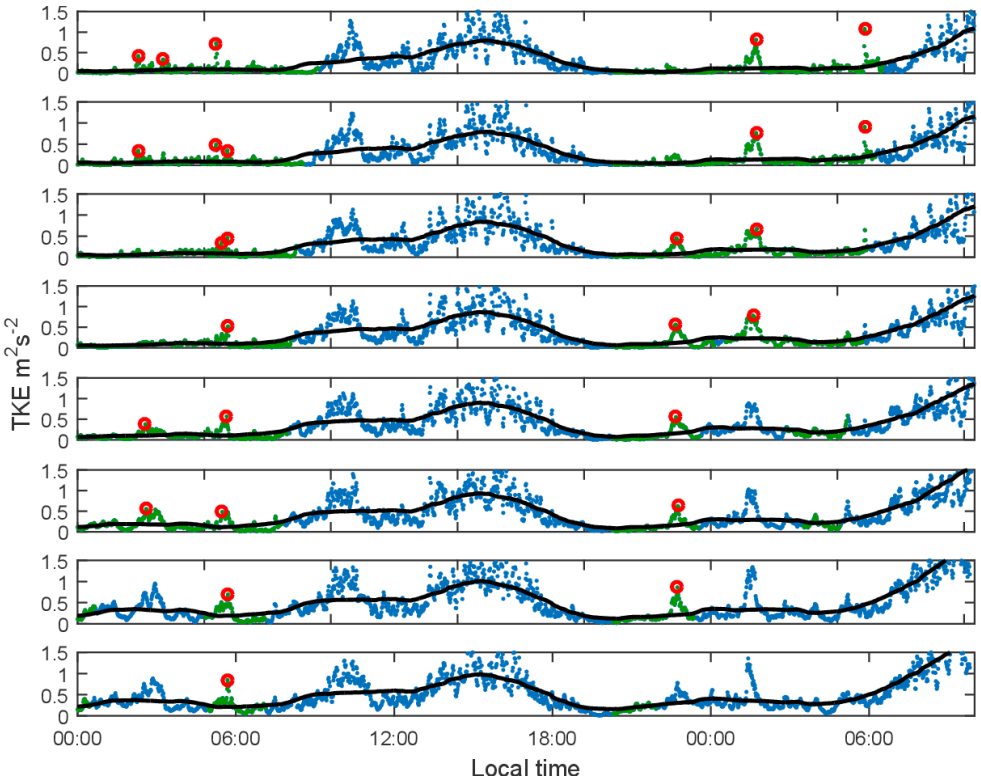

Figure 4-4. Example of the detection of turbulence bursts. The dots represent individual 5-minute means, with green colour showing stable calm periods. Detected bursts are marked by red circles.

To investigate the prevalence of intermittent turbulence, periods with stable conditions and low turbulence were identified, Stable Calm Periods (SCPs). The criteria for selection was $L > 0$ and $k_{4h} < 0.25$ m²s⁻², where k is the turbulence kinetic energy $k = (\sigma_u^2+\sigma_v^2+\sigma_w^2)/2$ and the subscript 4h indicates four-hour average. To detect bursts of turbulence a time series of k was constructed, with a 5 minute moving average for every single minute. A burst of turbulence, B, was defined when $k > 0.3$ m²s⁻² and $k > 3k_{4h}$ occurred. The dimensional threshold of 0.3 m²s⁻² was added to provide some relevance of the turbulence bursts to wind energy and thus disregards the smallest turbulence levels. If several adjacent times were marked as bursts only the one with the largest k was saved in order to avoid having a single

broad burst being detected as many small bursts. The width of the burst was defined as the shortest time between the crossing of k and k_{4h} before and after an identified burst. An example that shows the detection algorithm can be seen in Figure 4-4. The idea behind the selection criteria was not to provide something that covers all the turbulent bursts, but rather to get an indication of the prevalence of intermittent turbulence during otherwise calm periods.

After SCP and *B* had been identified the number of bursts at each height, the width of the burst and the ratio of SCPs containing bursts were collected (Table 4-2). The results show that both the number of SCPs as well as the number of bursts increase with height. The number of bursts is however a much stronger function of height, with the number of bursts per year being approximately the same as for the height above ground. The probability of having a SCPs is slightly less than one per day, which reflects the fact that some stable periods are too windy to pass the $k_{4h} < 0.25$ m^2s^{-2} criterion. In total a SCP is a common condition occurring roughly 10% of the time at the lowest heights and 25% of the time at the highest heights.

The number of bursts approach the number of SCP with height, though it should be noted that the probability of a burst occurring during a SCP only reaches about 50% as a maximum. This in turn reflects the fact that some conditions are more favourable for intermittent turbulence than others and may then have a higher frequency of bursts. The distribution of wind speeds for cases with intermittent turbulence largely followed the overall distribution of wind speeds, but was slightly narrower, reflecting that at too low or too high wind speeds bursts are less likely to be found.

Table 4-2. Statistical properties of turbulence bursts. Days is the number of days with data collected, SCP is the number of Stable Calm Periods, p(SCP) is the probability of SCP occurring considering all conditions, p(*B*) is the probability of at least one turbulence burst appearing in a SCP. The last column shows the median length of the turbulence bursts in minutes.

Site	z AGL [m]	Days	SCP	p(SCP)	p(*B*)	Total nr of *B*	Length of *B*
Hornamossen	21	298	112	0.08	0.12	15	28
Hornamossen	40	298	131	0.10	0.16	25	26
Hornamossen	60	298	153	0.14	0.24	46	26
Hornamossen	82	298	166	0.17	0.33	72	26
Hornamossen	100	298	173	0.19	0.42	102	24
Hornamossen	122	298	182	0.21	0.45	138	18
Hornamossen	152	298	194	0.24	0.47	152	19
Hornamossen	173	298	200	0.25	0.52	182	17
Ryningsnäs	40	399	230	0.12	0.30	93	28
Ryningsnäs	59	399	267	0.15	0.26	102	22
Ryningsnäs	80	399	252	0.15	0.35	151	20
Ryningsnäs	98	399	282	0.17	0.37	174	18
Ryningsnäs	120	399	303	0.19	0.42	244	18
Ryningsnäs	138	399	297	0.20	0.46	238	18

4.3 SUMMARY AND CONCLUSION

The chapter contains analysis of the turbulence measurements from Hornamossen and Ryningsnäs. The data was split into different bins of atmospheric stratification to investigate the sensitivity of the turbulence to atmospheric stratification. Data selection was furthermore done for night conditions (00:00-04:00 SNT), day conditions (12:00-16:00 SNT) and all data.

Investigation of the average wind profile shows that the long term mean is biased to stable stratification (neutral condition is not a good approximation). Also, there is a large difference between day and night and the wind veer is considerable at nighttime and in stable stratification.

The second order turbulence moments (variances and covariances) decrease more rapidly with height at Hornamossen than at Ryningsnäs but the qualitative behavior with stratification is the same (also for skewness). Scaled with the friction velocity the standard deviation follows roughly $\sigma_u \approx 2u_*$, $\sigma_v \approx 1.6u_*$ and $\sigma_w \approx 1.4u_*$ for both sites.

It was shown that the turbulence intensity is generally much larger during the day than during the night, apart from during the very highest wind speeds. As a function of wind speed the long term averaged turbulence intensity did not follow the IEC standard but instead showed lower than expected values below rated wind speed and higher than expected values above rated wind speed. The analysis showed that the turbulence intensity in strictly neutral conditions is constant with respect to wind speed.

A study into intermittence of turbulence was presented and it was shown that intermittence of turbulence during otherwise calm periods is common. Above 100 m calm periods were found during roughly 20 % of the time and above 150 m, calm periods were found during 25 % of the time. During such conditions sudden bursts of turbulence were found to be quite common and the number of sudden turbulence bursts was found to be around 100 per year. The median length of the bursts was found to be around 20 minutes, after which the conditions settled back into almost laminar again. This is potentially very interesting since the conditions of suddenly increasing turbulence are something that is usually not taken into account and could have considerable influence on the operation and loads of wind turbines.

5 New linear wind-flow model ORFEUS

5.1 MODEL DESCRIPTION

A new linearized flow model (ORFEUS = On Resource optimization For Energy USage) has been developed at KTH to simulate wind farms placed in complex terrain, with particular focus on forestry and moderately complex terrains. The linearization implies that the flow equations are approximated and made simpler, with the advantage that the needed computational time decreases drastically of at least two orders of magnitude without loosing too much accuracy. Consequently, ORFEUS has the potential to become a useful tool for site assessment even for companies that do not have large computational power, complementing more computationally-demanding simulation tools.

The basic idea of ORFEUS is similar to other linearized codes: the flow is subdivided into an undisturbed atmospheric boundary layer, $U_0(z)$, and a perturbation, $U_1(x,y,z)$, due to the presence of terrain, roughness, forest and wind turbines. If the perturbation is small compared to the atmospheric wind velocity, non-linear terms involving multiplication of perturbative terms can be neglected when compared to linear terms. This implies that the equations can be solved with fast and numerically accurate methods available for linear equations, reducing the computational cost of the simulations. A detailed description of the model is reported in Segalini (2017) together with some validation cases involving terrain, forestry and wind turbines. The focus in the present report will be given to the forested cases.

5.2 MODEL SET-UP

The computational domain is composed by a structured Cartesian grid determined by the starting and final location and by the number of grid points in the horizontal directions (that are uniformly discretised) and in the vertical (that is logarithmically mapped). The topography is introduced as a shift of the vertical coordinate, so that different areas or wind directions do not need a new grid. The code automatically rotates the domain for the different wind directions, requiring minimal input from the user.

The Navier-Stokes equations are then linearized around the incoming boundary layer, obtaining a set of linear equations that can be written in matricial form as

$$\begin{pmatrix} U_0\frac{\partial}{\partial x}-\nu\nabla^2 & 0 & U_0' & \frac{\partial}{\partial x} \\ U_0\frac{\partial}{\partial x} & -\nu\nabla^2 & 0 & \frac{\partial}{\partial y} \\ U_0\frac{\partial}{\partial x} & 0 & -\nu\nabla^2 & \frac{\partial}{\partial z} \\ \frac{\partial}{\partial x} & \frac{\partial}{\partial y} & \frac{\partial}{\partial z} & 0 \end{pmatrix} \begin{pmatrix} U_1 \\ V_1 \\ W_1 \\ P_1/\rho \end{pmatrix} + \begin{pmatrix} \nabla\cdot\overline{\mathbf{u}'\cdot\mathbf{u}'} \\ 0 \end{pmatrix} = \frac{1}{\rho}\begin{pmatrix} F_x \\ F_y \\ F_z \\ 0 \end{pmatrix} \qquad (5\text{-}1)$$

with ν indicating the kinematic viscosity. The first term is given by the advective and viscous terms together with the pressure terms, while the second one provides turbulent transport of momentum. The right-hand side is the source term associated to the thrust of the turbines, the drag of a forest or the displacement

imposed by terrain. The equations remain unclosed (namely with more unknowns than equations) as long as a model for the Reynolds stress tensor is not provided.

A zero-equation turbulence model is introduced to provide a simple closure scheme for the Reynolds stress tensor, determining the diffusivity of momentum due to the turbulent activity. The model assumes a simple Boussinesq model with a height-dependent eddy viscosity of the form

$$-\overline{u_i' u_j'} = \nu_t \left(\frac{\partial U_i}{\partial x_j} + \frac{\partial U_j}{\partial x_i} \right) - \frac{2}{3}\delta_{ij} k \qquad , \qquad \nu_t = \kappa u_* z \tag{5-2}$$

where k is the turbulent kinetic energy (TKE), κ=0.4 is the von Kármán constant and u^* is the friction velocity. The knowledge of the TKE is not required because it will be merged with the pressure contribution. Alternative formulations have been attempted as well: the most promising is to implement a k-ε model to estimate the eddy viscosity, thereby accounting for the modification of the eddy viscosity due to the presence of the body forces as well. However, such a model (with its fast implementation) is still to be validated and will not be discussed further here since good results are already obtained over forests with the simplest model. For the wind farm case, where the turbulent diffusivity is expected to become more important to determine the wake recover, it is expected that the turbulence model will play a more crucial role.

The turbines, if present, are modelled with a simple actuator-disk model, where the only information needed is the thrust coefficient, here assumed to be 0.8 for Ryningsnäs only (the only site with two turbines), while wind turbines were not simulated for Hornamossen. More details about the turbine implementation can be found in Segalini (2017).

5.3 FOREST MODELLING

The forest was introduced as a body force of the form

$$F=-C_d*PAD*(U_0+U_1)^2 \tag{5-3}$$

according to the plant area density (*PAD*) distribution in space provided by the aerial scans available within the project, while the drag coefficient of the trees, C_d, was assumed to be 0.2. This approach differs from the traditional ones where forests are treated as a boundary condition, since here the forest in added as a body force inside the domain and does not necessitate of an a priori estimation of the roughness length z_0. Indeed, the roughness-lngth variation in the simulation has been neglected since its contribution is minimal when compared to the forest effect.

Given the *PAD* distribution, the vertical structure of the forest is also known. In the special case where only the Leaf-Area Index (LAI) is known (namely the vertical integral of the PAD), a homogeneous distribution is assumed up to the local tree height.

Since the velocity perturbation, U_1, is unknown, an iterative scheme is adopted to determine the force that the flow has to face. This needs some careful relaxation of

the iterative scheme to avoid that the strong force of the forest would lead to excessive back-flow regions, making the iterative scheme unstable. The tuning implied a ramping of the forest intensity, *PAD*, from nearly zero (very weak forest) to the actual intensity. This ramping and over-relaxation increased the number of iterations needed to convergence but at the same time increased the robustness of the code.

5.4 BOUNDARY CONDITIONS

Since ORFEUS uses the Fourier transform in the horizontal directions, periodicity is required at the inlet/outlet and at the lateral boundaries. There is however a problem at the inlet and outlet boundaries since the forest is absorbing momentum and the outlet profile cannot match the inlet one unless an artificial pressure gradient is introduced. To cope with this problem, in the last part of the domain a buffer (fringe) region is introduced as an artificial body force aimed at annihilating the perturbation and recover the inflow boundary layer, ensuring periodicity of the inlet/outlet. At the ground and at the top of the domain, the velocity perturbation is simply assumed to vanish. More details about the fringe implementation can be found in Ebenhoch et al. (2016).

5.5 RESULTS AND COMPARISON WITH MEASUREMENTS

A set of simulations was first performed to assess the predictive capability of ORFEUS over forested terrain under controlled conditions. The simulation focused on a statistical two-dimensional case (Segalini, et al., 2016) where a short forest was simulated. The forest was $40h_c$ long, with h_c indicating the forest height, with Leaf-Area Index (LAI) equal to 2 and known vertical forest intensity. Large-eddy simulation (LES) data was available for comparison together with non-linear RANS data computed with OpenFOAM. Since the case was two-dimensional, only few minutes were necessary to achieve convergence in a domain composed by 1024 x 80 grid points in the horizontal and vertical directions, respectively. Figure 5-1 shows the comparison between the LES, the RANS and the ORFEUS computations. Despite the approximations done to develop the code and the very low computational cost, the computation performed by ORFEUS is not far from much more expensive methods.

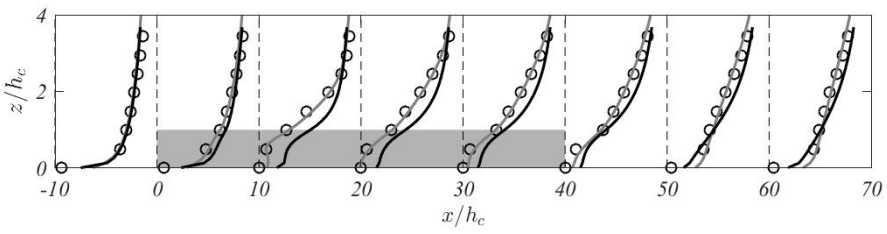

Figure 5-1. Comparison between the ORFEUS simulation (first order in black, second order in red) and LES data (circles). RANS data (grey lines).

The next step was the simulation of the forests in Ryningsnäs (with the two turbines) and Hornamossen for several wind directions. In both cases, the computational domain was 12 km x 3.6 km x 4.5 km in the streamwise, spanwise and vertical directions, respectively, discretized with 512 x 256 x 80 grid points. The mast was located 4.5 km downstream of the inlet in the middle of the spanwise domain. Due to the iteration scheme, several iterations were necessary, with a computational time of around 20 minutes for every wind direction. No tuning was performed in the model parameters and the only information available a priori was the terrain topography, the tree height and the *PAD* as well as the position of the turbines for Ryningsnäs. The atmospheric boundary layer was assumed to be the one proposed by Harman and Finnigan (2007) as function of the height, tree height h_c and leaf area index, while neutral stratification was assumed.

Figure 5-2 shows a comparison of the wind profile computed by ORFEUS against mast measurements for the wind direction 270 degrees, free of turbines upstream of the mast, while figure 5-3 shows the comparison for 45 degrees, namely with one turbine upstream. The agreement is remarkable for the 270 degrees case and still reasonably good for the 45 degrees case, despite of the crude modelling of the turbine.

A similar plot is reported in figure 5-4 for Hornamossen for the wind direction 270 degrees: interestingly, while the near-forest region seems well characterized, the region above $5h_c$ appears under predicted, probably due to an incorrect inflow boundary layer (here assumed to be logarithmic up to the top of the domain) while the measured profile has a lower boundary-layer top. The same trend is observed for all wind directions in Hornamossen.

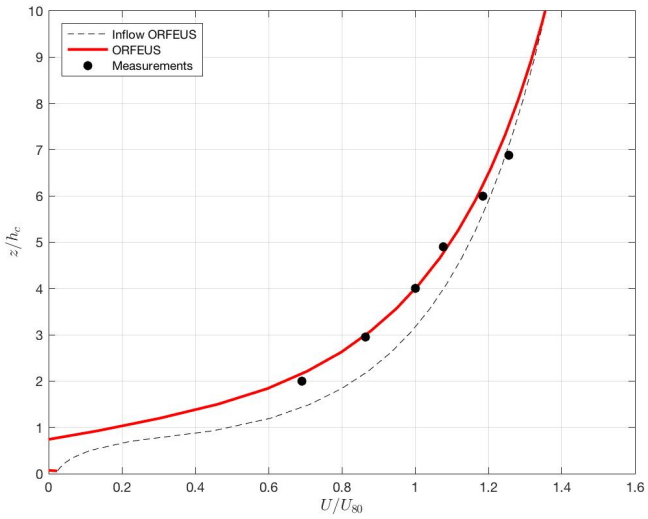

Figure 5-2. Comparison between the ORFEUS simulation and mast measurements at Ryningsnäs for neutral stratification and wind direction 270 degrees. For the sake of comparison, the unperturbed (inlet) boundary layer is also reported.

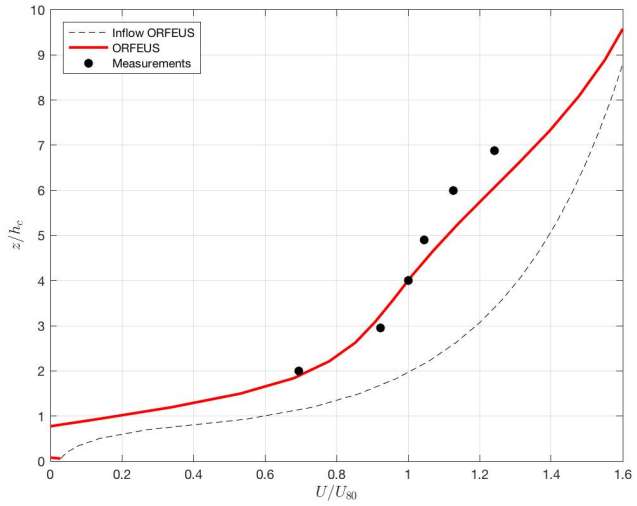

Figure 5-3. Comparison between the ORFEUS simulation and mast measurements at Ryningsnäs for neutral stratification and wind direction 45º, namely in the wake of a wind turbine with hub height at $5h_c$.

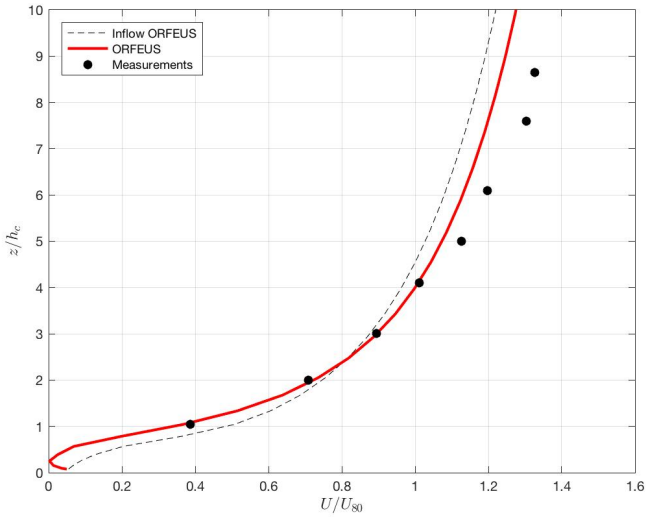

Figure 5-4. Comparison between the ORFEUS simulation and mast measurements at Hornamossen for neutral stratification and wind direction 270 degrees.

Stratification effects are also accounted in the computations done by ORFEUS through a change in the incoming velocity profile and the eddy viscosity according to Monin-Obukhov similarity theory. Figure 5-5 shows the comparison of the simulated and measured velocity profile when the Obukhov length is L=200 m, namely for a strongly stratified case. The agreement is very good, despite of the fact that no heat flux is introduced by the forest and only the turbulence model is modified following scalings developed over flat terrain without forest, supporting even more ORFEUS as a tool to perform wind-resource assessment over complex terrains.

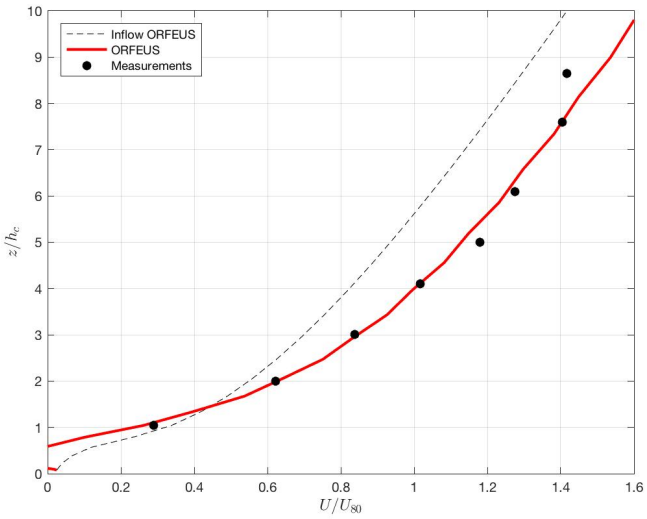

Figure 5-5 Comparison between the ORFEUS simulation and mast measurements at Hornamossen for stable stratification (L=200 m) and wind direction 270 degrees.

5.6 SUMMARY AND CONCLUSIONS

A new tool called ORFEUS was developed to estimate the wind resource over complex forested terrains and it was validated in the present project against mast measurements from the forests of Ryningsnäs and Hornamossen. ORFEUS is not a standard CFD code, although the outputs and capabilities are similar. The code is based on a linearization of the flow equations and is characterised by a high computational speed when compared to traditional CFD who solves for the non-linear flow equations. The linearization is here chosen because it allows for fast and feasible simulations even for actors that do not have significant computational resources to run CFD.

Differently from other linearised solvers like WAsP, ORFEUS solves for body forces inside the domain, so that wind turbines and forests can be directly accounted for, improving the simulation accuracy near forests, for instance. The forest model coupled with a linearised solver is new in the wind community, since other linearised solvers account for forestry only through the boundary conditions, and the forest is introduced through the roughness-length parameter, z_0, which is generally unknown or estimated by proxies, as it depends on the amount of momentum absorbed by the forest. Sometimes z_0 is even treated as a parameter to change arbitrarily to improve the simulation quality in validation efforts, underlining how uncertain the approach is that replaces a forest with a boundary condition. This uncertainty is removed by simulating the forest through body forces as ORFEUS (or traditional CFD with a forest module) does. In practice, it is often easier to quantify the PAD through, for instance, the amount of vegetation than to quantify the roughness length. This implies that ORFEUS is able to simulate forested terrains better than other linearised solvers (like WAsP), providing results two orders of magnitude faster than traditional CFD, with a similar accuracy. The validation performed in the present report indicates that results from ORFEUS simulations agree reasonably well with measurements under

neutral and stably-stratified conditions, namely the conditions of interest for the wind industry. The only required inputs are the forest-density distribution and the terrain height. Linear solvers are indeed sufficient to characterise forest flows (at least for what concerns the mean velocity distribution) even in presence of stable density stratification. The non-linearity of the forest drag force (which goes quadratically with the wind speed inside the forest) must be anyway accounted for to avoid unphysical solutions for sufficiently long forests, similarly to what was proposed by Belcher et al. (2003).

The comparison between measurements with a wind-turbine wake in Ryningsnäs and ORFEUS indicates an acceptable agreement, although the wake from ORFEUS appeared to recover more slowly than what is pointed out by the measurements, a phenomenon already observed in other validation tests, which suggests that the code needs a better modelling of the actuator disk and turbulence with the inclusion of a high-order turbulence model (most likely a k-ε turbulence model).

The implications of this research point out that linearised solvers can be used with confidence for wind-resource assessment and micro-meteorology studies. Furthermore, due to the high computational speed, parametric studies of forest density, forest configurations, clearings and forest/wind turbine interactions are feasible for future investigations.

6 Mesoscale model simulations

The use of mesoscale models for wind resource assessments has increased during recent decades. Especially in complex terrain, the need for more advanced models than has earlier been used is often obvious. The use of the Weather Research and Forecasting (WRF) model is now wide spread within the wind industry, but other mesoscale models are also put to use. One such model is the MIUU model, which has previously been used to map the wind resource over the whole of Sweden. First with 1 km x 1 km horizontal resolution (Bergström and Söderberg, 2009), and later with a 500 m x 500 m resolution (Bergström and Söderberg, 2011).

The quality of the mesoscale simulations strongly depends on the input to the models, notably the surface data such as roughness length and displacement height and for both the WRF model and the MIUU model sensitivity studies have been carried out to investigate various surface data options.

Besides using the mesoscale models for long term wind resource assessment another use is to provide boundary conditions for microscale modelling. An advantage of using mesoscale models for such purpose is that the non-stationary and varying atmospheric conditions are taken into account. When bridging the gap between micro and mesoscale modelling, finer and finer resolution is used. A recently available option for such a downscaling process is to use the LES version of the WRF model, and an investigation into that possibility is presented in the chapter.

6.1 WRF MODEL

6.1.1 Model description

The atmospheric model Weather Research and Forecasting (WRF) model is a community model with a large group of worldwide users. The development is supervised by the National Centers for Environmental Prediction (NCEP) and the National Center for Atmospheric Research (NCAR) in the US. WRF is a state-of-the-art mesoscale numerical weather prediction model suitable for running high-resolution simulations. For a detailed description, see Skamarock et al. (2008) and https://www.mmm.ucar.edu/wrf-model-general.

Two dynamical solvers are currently available: the Advanced Research WRF (ARW) and the Nonhydrostatic Mesoscale Model (NMM). In the sensitivity experiments (section 6.2) WRF ARW v3.8 was used. In all other sections WRF ARW v3.8.1 was used. The dynamical solver in WRF consists of a set of Eulerian equations that is fully compressible, non-hydrostatic and conservative for scalar variables. Prognostic variables are horizontal and vertical velocity components, perturbation potential temperature, perturbation geopotential, and perturbation surface pressure of dry air.

Physical processes important for the atmosphere, but not explicitly resolved in space and time on the numerical grid used by the model, are parameterized as a functions of the resolved scale variables. Examples of such processes are radiation, clouds, and vertical tendencies of temperature, moisture, and horizontal momentum.

6.1.2 Sensitivity experiments

Several physical parameterization schemes are available with the ARW-solver. WRF can be set up in numerous ways and depending on how WRF is applied, some setups are chosen for speed while others are more physically sound but computationally heavy. WRF should therefore not be viewed as "a model", it is more correct to view WRF as "a model system", which result depend on the model setup.

For wind resource applications the choice of Planetary Boundary Layer (PBL) scheme computing vertical tendencies of temperature, moisture, and horizontal momentum and the accompanying Surface Layer (SFC) schemes are important. To assess the impact of different planetary boundary layer and surface layer schemes a number of sensitivity experiments were carried out. The different schemes are briefly described in Table 6-1 and the experiment names and setups are summarized in Table 6-2.

Table 6-1. Description of schemes used in the sensitivity experiments. PBL: Planetary Boundary Layer. SFC: Surface Layer. TKE: Turbulent Kinetic Energy.

	Full name	Category	Description
MYNN	Mellor-Yamada Nakanishi and Niino Level 2.5 PBL.	PBL	Predicts sub-grid TKE terms.
MYJ	Mellor-Yamada-Janjic scheme.	PBL	Eta operational scheme. One-dimensional prognostic turbulent kinetic energy scheme with local vertical mixing.
YSU	Yonsei University scheme.	PBL	Non-local-K scheme with explicit entrainment layer and parabolic K profile in unstable mixed layer.
Shin-Hong	Shin-Hong scheme.	PBL	Include scale dependency for vertical transport in convective PBL. Vertical mixing in the stable PBL and free atmosphere follows YSU. This scheme also has diagnosed TKE and mixing length output.
MYNN_sfc	MYNN surface layer.	SFC	Nakanishi and Niino PBL's surface layer scheme.
MM5	MM5 similarity.	SFC	Based on Monin-Obukhov with Carslon-Boland viscous sub-layer and standard similarity functions from look-up tables
ETA	Eta similarity.	SFC	Used in Eta model. Based on Monin-Obukhov with Zilitinkevich thermal roughness length and standard similarity functions from look-up tables.

Data for surface characteristics was extracted from several sources. Landuse data was taken from the Corine database (http://dataservice.eea.europa.eu/). Data from Lantmäteriet was used for topography information. Other terrestrial data was extracted from the standard WRF source package.

In the sensitivity experiments 5 nesting levels were used: An outer domain with 27km model grid resolution and within that, 4 nests with 9km, 3km, 1km, and 333m model grid resolution. Initial and lateral boundary conditions were taken from the ERA Interim reanalysis provided by ECMWF.

The time period covered is 1 Jan 2016 to 31 December 2016. For the results presented here, model data intersecting with observations from the Hornamossen met mast (section 3.1) make up more than 6 months of hourly data distributed over the year.

Table 6-2. Experiment names and model setup used in the sensitivity experiments.

	PBL	SFC	Other
MYNN1	MYNN	MYNN_sfc	
MYNN2	MYNN	MYNN_sfc	scale aware
MYNN3	MYNN	MM5	
MYNN4	MYNN	MM5	scale aware
MYJ	MYJ	ETA	
YSU	YSU	MM5	
Shin-Hong	Shin-Hong	MM5	

Vertical profiles of normalized wind speed from the sensitivity experiments and observations from the Hornamossen met mast are shown in Figure 6-1. The model grid resolution is from top to bottom 3000 x 3000m^2, 1000 x 1000m^2, and 333 x 333m^2. The model setups grouping closest to the observed profile are the scale aware MYNN experiments (MYNN2 and MYNN4), MYJ, and YSU. Profiles of bias and correlation coefficient *R* are plotted in Figure 6-2. For the Hornamossen site the wind speed bias decreases with height and with increased model grid resolution. For R the spread among the experiments increases and R decreases slightly with model grid resolution. A slight decrease in R with an increased model grid resolution is often seen and can to some extent be explained with the timing problem that comes with an increased variability in the modelled wind speed. These results motivate to further investigate and develop a better representation of forests in WRF in order to improve model performance in typical Scandinavian conditions.

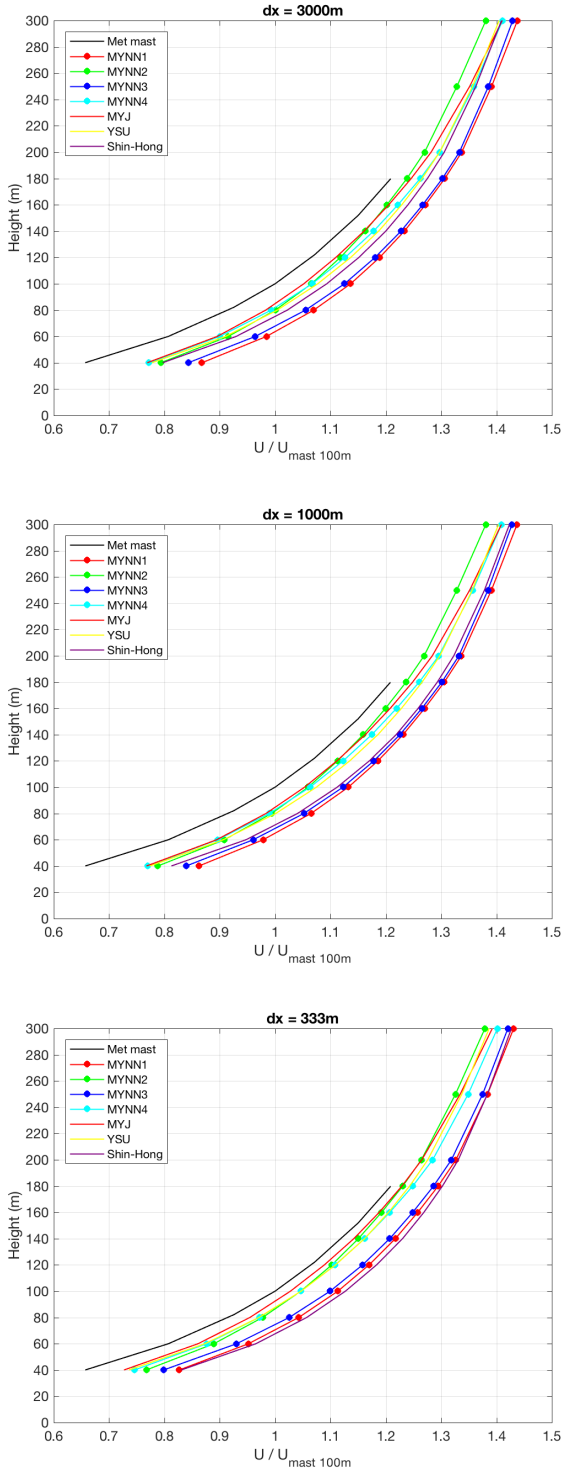

Figure 6-1. Vertical profiles of normalized wind speed (m/s) from the Hornamossen met mast and model sensitivity experiments. All profiles have been scaled with the wind speed at 100m from the met mast. Model grid resolutions are 3000x3000m², 1000x1000m², and 333x333m².

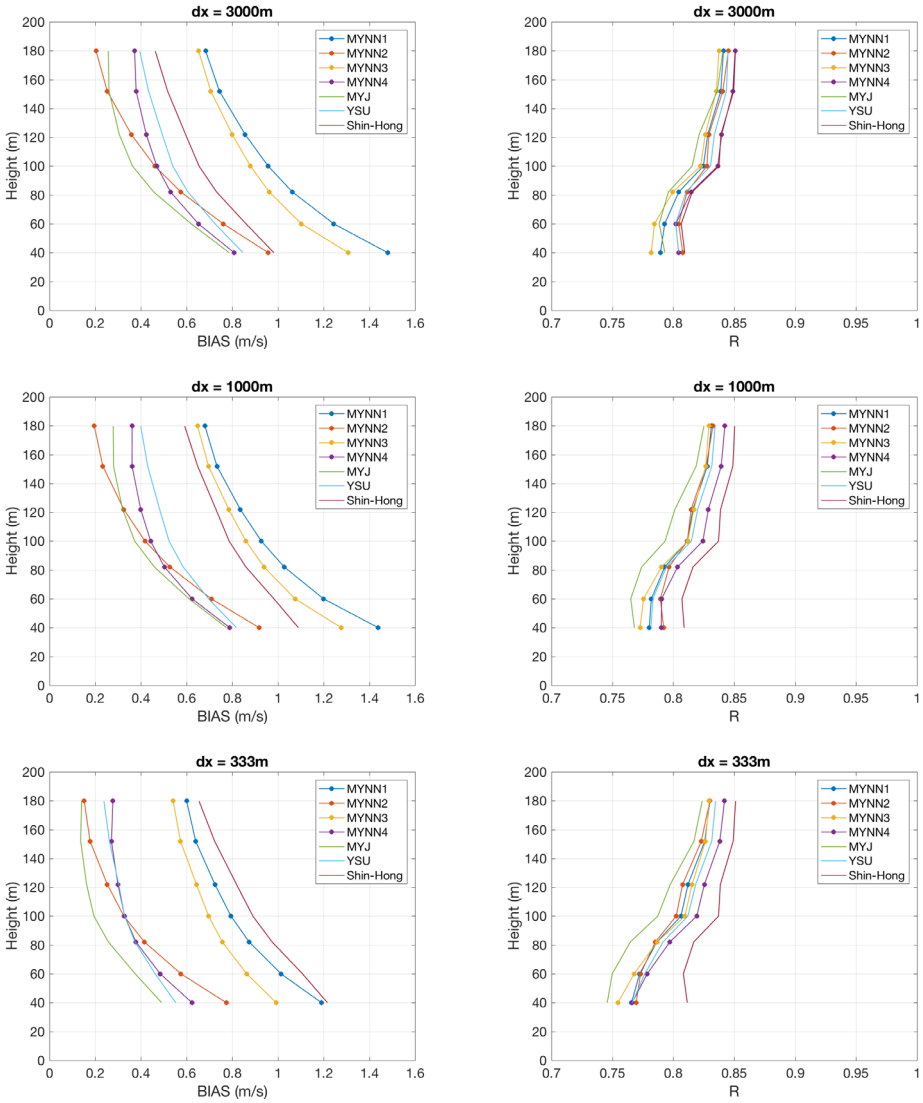

Figure 6-2. Vertical profiles of wind speed bias (m/s) and correlation coefficient *R* from the Hornamossen sensitivity experiments with 3000 x 3000 m², 1000 x 1000 m², and 333 x 333 m² model grid resolution.

6.1.3 Model and observation comparison

WRF model runs have been carried out for a full year with concurrent measurement data from the Hornamossen met mast. Here a model setup similar to the suggested WRF model setup for the NEWA wind atlas model runs has been used (final NEWA model setup will be published in 2019).

The NEWA production runs will have a model grid resolution of 3000m. For this experiment the model has been setup up with an outer domain with 27km model grid resolution and within that, 4 nests with 9km, 3km, 1km, and 333m model grid resolution. Landuse data was taken from the Corine database (http://dataservice.eea.europa.eu/) for all nests but the outer domain. Data from Lantmäteriet was used for topography information for the 1km and 333m model

domains. Other terrestrial data was extracted from the standard WRF source package.

The MYNN planetary boundary scheme and surface layer scheme were used for these WRF model runs. The surface layer scheme was slightly modified to match the behaviour that was default in WRF versions previous to v3.7 since the newer versions have shown some erratic behaviour at certain sites.

Initial and lateral boundary conditions were taken from the ERA Interim reanalysis provided by ECMWF. Spectral nudging was applied to the outer domain. The reason for constraining the model by applying nudging is to keep the model runs more consistent with the forcing data. The setup also includes Sea Surface Temperature (SST) and sea ice data from OSTIA (Operational Sea Surface Temperature and Sea Ice Analysis, Donlon et al. 2012), a high-resolution analysis of the current SST for the global ocean. The OSTIA system uses satellite data together with in-situ observations and to produce a daily analysis at a resolution of 1/20° (approximately 5km).

The objective for these model runs was to create a database with WRF model data that can be used for detailed studies of the vertical structure of the atmosphere over an area covering the Hornamossen site. Examples of variables in the database are wind speed, wind direction, air temperature, potential temperature, TKE, turbulent exchange coefficients, pressure, and relative humidity. Friction velocity and surface fluxes are also included in the database. Data is given on 23 levels from 10m to 3000m with 30-minutes interval from 1 May 2016 to 30 April 2017.

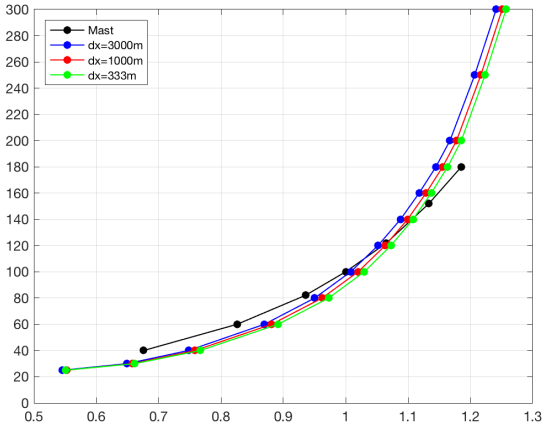

Figure 6-3. Vertical profiles of normalized wind speed (m/s) from the Hornamossen met mast and WRF model runs with model grid resolutions 3000 x 3000 m², 1000 x 1000 m², and 333 x 333 m². All profiles have been scaled with the wind speed at 100 m from the met mast.

In Figure 6-3 profiles of normalized wind speed from the met mast and WRF model runs with model grid resolutions 3000 x 3000 m², 1000 x 1000 m², and 333 x 333 m² are shown. The nest with the highest model grid resolution gives a slightly lower wind speed than the other two. But, all model resolutions yield a profile with a wind shear that does not agree with the observed one. In particular the modelled wind speeds just above the forest are too high. Statistics for all

measurement heights with a Thies cup anemometers and for each model grid resolution are presented in Table 6-3 to Table 6-5.

Table 6-3. Statistics for WRF 3000 x 3000 m² model run and Thies cup anemometers. Here R is the correlation coefficient, MAE the mead average error, RSME the root-mean-square error and nsamp the number of hours used in the comparison.

z (m)	R	bias (m/s)	MAE (m/s)	RMSE (m/s)	nsamp
179.8	0.84	-0.26	1.53	1.99	8481
152	0.83	-0.18	1.48	1.91	8481
122	0.81	-0.06	1.42	1.83	8481
100	0.80	0.05	1.37	1.76	8481
82.1	0.80	0.13	1.30	1.66	8481
60	0.79	0.28	1.19	1.52	8481
40	0.78	0.46	1.07	1.36	8481

Table 6-4. Statistics for WRF 1000 x 1000 m² model run and Thies cup anemometers.

z (m)	R	bias (m/s)	MAE (m/s)	RMSE (m/s)	nsamp
179.8	0.83	-0.19	1.53	2.00	8481
152	0.83	-0.11	1.49	1.93	8481
122	0.81	0.01	1.43	1.85	8481
100	0.80	0.13	1.38	1.78	8481
82.1	0.79	0.21	1.32	1.69	8481
60	0.78	0.36	1.22	1.55	8481
40	0.77	0.53	1.09	1.39	8481

Table 6-5. Statistics for WRF 333 x 333 m² model run and Thies cup anemometers.

z (m)	R	bias (m/s)	MAE (m/s)	RMSE (m/s)	nsamp
179.8	0.83	-0.14	1.54	2.00	8481
152	0.83	-0.05	1.49	1.94	8481
122	0.81	0.07	1.44	1.86	8481
100	0.80	0.19	1.40	1.79	8481
82.1	0.79	0.28	1.34	1.71	8481
60	0.79	0.42	1.24	1.58	8481
40	0.78	0.59	1.12	1.42	8481

6.1.4 Forest and roughness effects

Forest canopies are generally represented in mesoscale model as a rough surface. The default roughness length for typical Swedish forests in the WRF model is 0.5m but for many sites in Sweden the true roughness length is considerably higher. There is also a large variation in roughness length within each categorical type of forest depending on how patchy the forest is, its density and the tree height. To test the WRF model's sensitivity concerning how the forest is represented in the model a few model experiments have been carried out.

To facilitate these experiments the tree height and biomass, from which PAI was derived, databases from Skogsstyrelsen have been pre-processed and ingested in the WRF model system. These datasets are based on ALS of Sweden and have a horizontal resolution of 12.5m.

Two experiments were carried out with a homogeneous forest with a roughness length of 1.3m and 0.9m respectively. To simulate an inhomogeneous forest two experiments were made were the roughness length was calculated as either a function of PAI and tree height or only tree height. Finally, one experiment was made were the forest was represented as an elevated drag force instead of roughness from a flat surface. A summary of these five experiments can be found in Table 6-6 and an illustration of the resulting model roughness for each method is shown in Figure 6-4.

Table 6-6. Description of the forest roughness experiments.

Name	Forest roughness function	Avg. forest roughness in model domain
t6.0.2	z0 = 1.3m	1.3m
t6.0.3	z0 from tree height and PAI	0.37m
t6.0.4	z0 = 0.1 x tree height	1.36m
t6.0.5	z0 = 0.9 (as in NEWA)	0.9m
t6.0.7	Canopy drag force	N/A

The model runs for these experiments were only made to cover 1 day so the time period is too short in order to assess the model's performance in general. It is however possible to use these runs to say something about how model runs with different forest canopy representation compare to each other. The model results are plotted in Figure 6-5 against some of the Sodar measurements made during the NEWA measurement campaign. It is clear from Figure 6-5 that the experiments with a higher average surface roughness matched the observed profiles more closely. We can also see that the test where the roughness length is a function of both tree height and PAI is an outlier with very high wind speeds. This is due to the low average roughness length in this test, which is unrealistic, and a result from errors made in the preprocessing. The results were kept in the analysis as an extreme example of the effects from underestimating the roughness length.

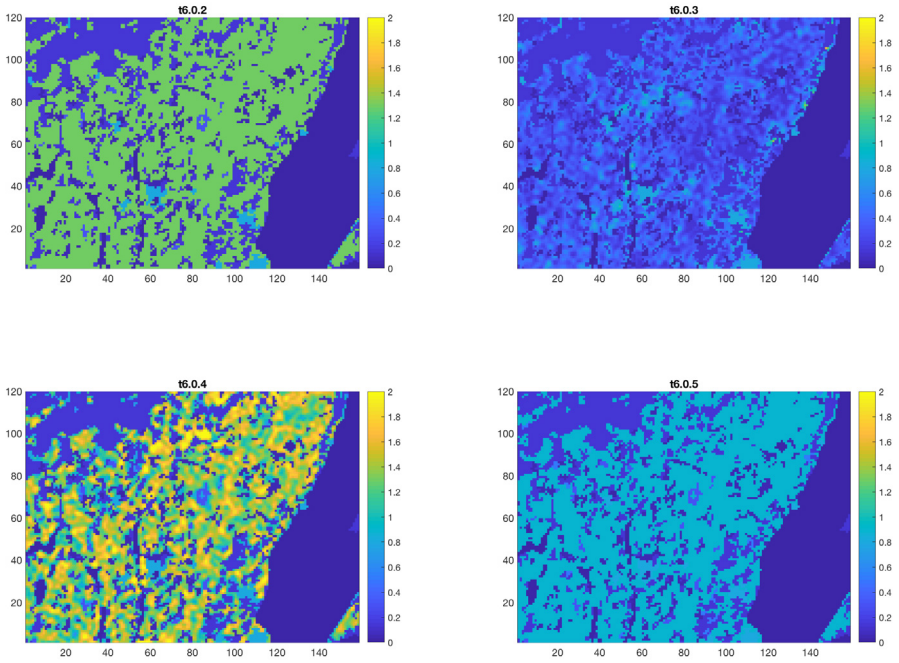

Figure 6-4. Model roughness for the four experiments using different forest roughness functions. See Table 6-6 for description of the runs/calculations.

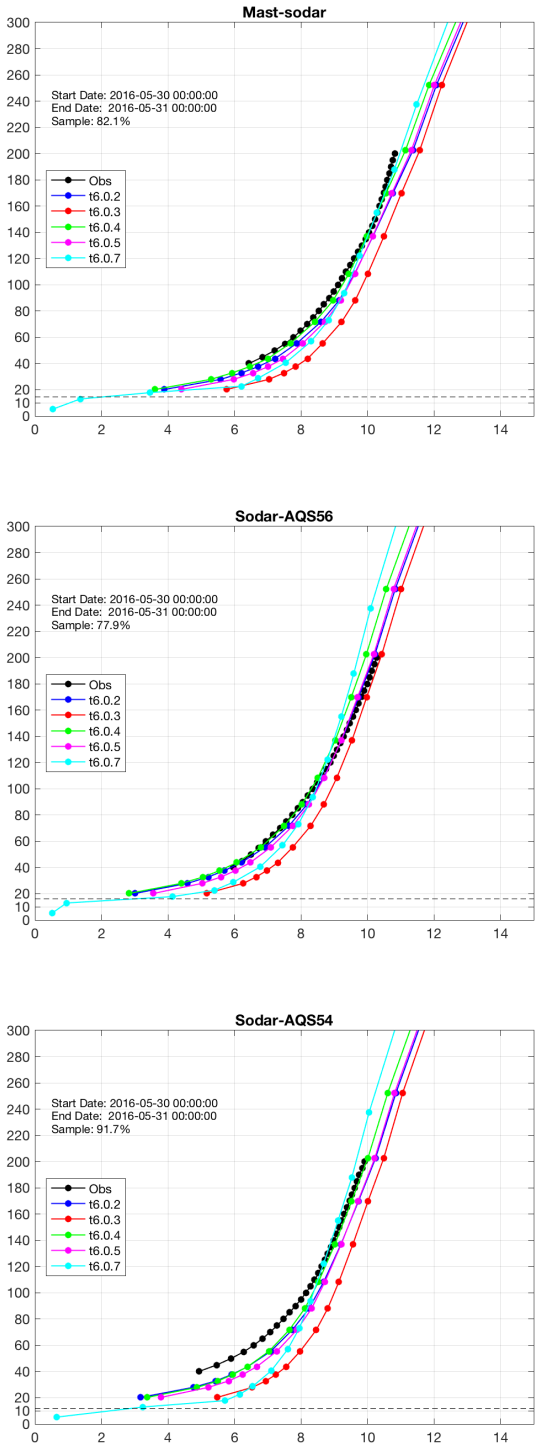

Figure 6-5. Example profiles of observed wind speed and model wind speed using different forest roughness functions.

To investigate the difference between using a homogeneous and an inhomogeneous forest representation in the model, experiment t6.0.2 and t6.0.4 were studied in more detail since they have a similar average roughness length in the model domain. Figure 6-6 shows the average wind speed in both experiments at 20m height and it is hard to see any large differences between the two. However, in Figure 6-7 where the differences are plotted it is clear that locally at low vertical levels there are differences of the order of 0.5 m/s. These differences gradually decrease towards an asymptotic level as we move upwards in the vertical showing how the fetch is longer at higher levels. This is further corroborated by the decreasing correlation between wind speed difference and local surface roughness difference at higher levels, which is also shown in Figure 6-7.

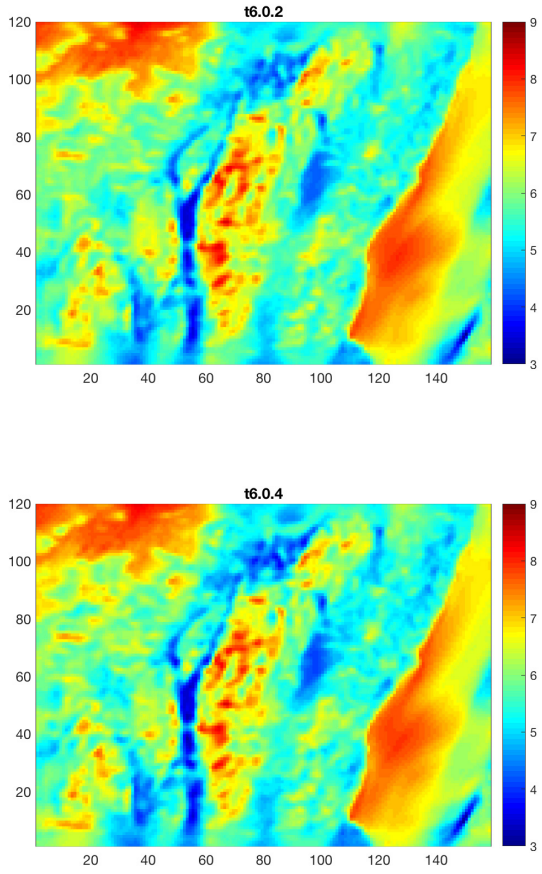

Figure 6-6. Average wind speed at 20m height 2016-05-30 00 to 2016-05-31 00 for experiment t6.0.2 (top) and t6.0.4 (bottom).

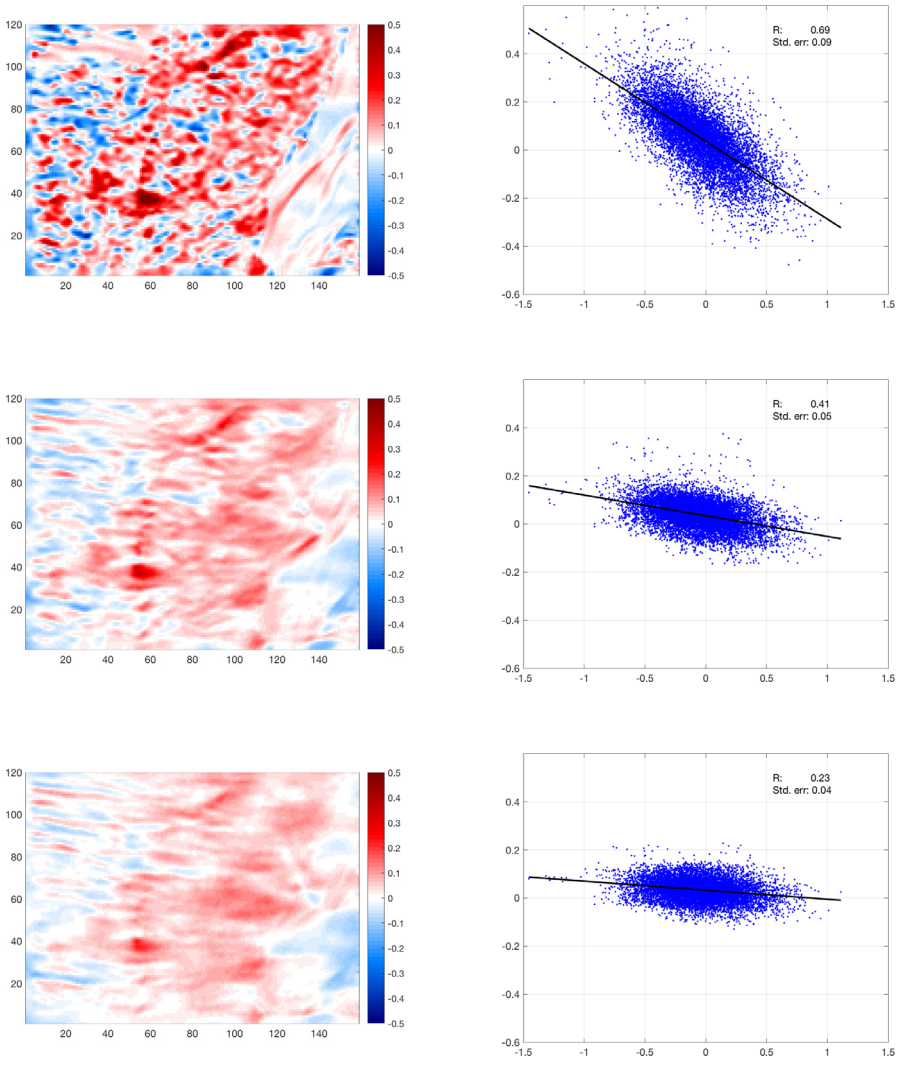

Figure 6-7. Differences in wind speed between experiment t6.0.2 and t6.0.4 (left) and scatter plot of wind speed difference as function of differences in roughness lengths (right) for three heights; 20m (top), 60m (middle) and 100m (bottom).

6.1.5 LES forcing output

Some of the LES runs described in section 7 were initialized with mesoscale data from the WRF model. In order to initialize the LES model properly vertical profiles of heat and momentum flux were needed. These variables are not output by a default WRF setup since it is not a turbulence-resolving model. However, the PBL parameterization, which handles vertical diffusion, calculates and outputs the exchange coefficients for heat and momentum. These exchange coefficients were used together with the vertical profiles of wind and temperature to diagnostically calculate the vertical profiles of heat and momentum flux.

6.1.6 WRF multiscale modelling

An LES mode was added to the WRF model some time ago and research concerning how to nest an LES domain in a mesoscale domain has been fairly active during recent years (e.g. Mirocha et al. 2014, Muñoz-Esparza et al. 2015, Liu et al. 2011 and Talbot et al. 2012). In this project we have implemented the generalized cell perturbation method following Muñoz-Esparza et al. (2015). The reasoning behind this method is that turbulence in the LES domain can be spun up efficiently by introducing small theta perturbations on the inflow boundary.

The development and testing of our implementation of the cell perturbation method was made in conjunction with a number of idealized WRF runs were an LES nested in a mesoscale domain was compared to a standalone periodic LES. The horizontal resolution was 90m and the runs were initialized with a neutral temperature profile. The objective for the nested LES is to reach a solution that is similar to the standalone LES after as short a spin-up distance as possible. The results of the final batch of idealized runs are shown in Figure 6-8 and Figure 6-9.

In Figure 6-8 we can see that when running WRF LES nested in a mesoscale domain without modifying the boundary conditions (middle plot) there are almost no turbulent structures at all. But when we add theta perturbations (lower plot) we do spin up turbulence that looks reasonable when comparing with the standalone run (top plot) where there are no spin-up issues since periodic boundary conditions are used.

Figure 6-9 shows frequency spectra for the three idealized runs. Comparing the frequency where there is a drop in energy gives further evidence that the nested WRF LES with theta perturbations has indeed resolved turbulence on a time scale similar to the standalone WRF LES while the unperturbed nested WRF LES has a drop in energy at a much lower frequency.

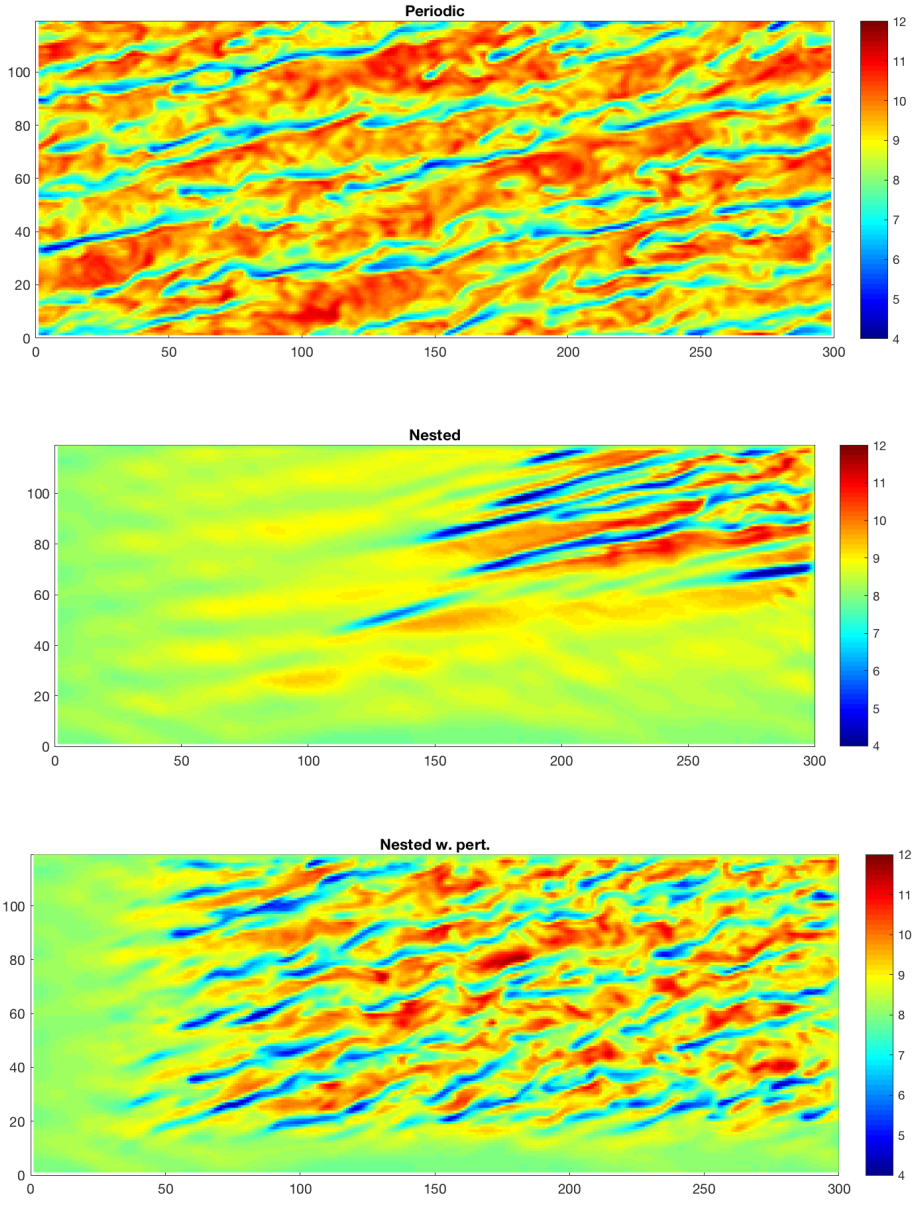

Figure 6-8. Snapshot of the wind speed at 120m height for the three idealized runs.

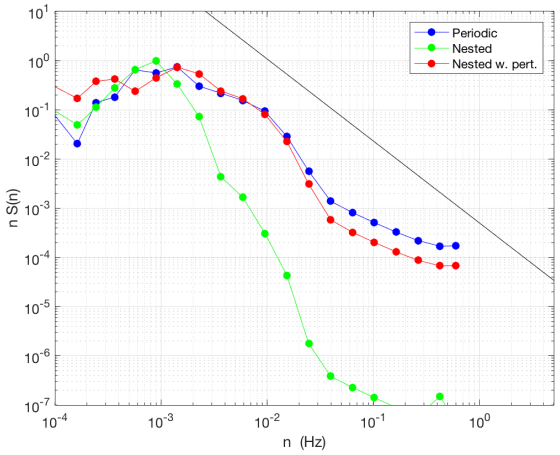

Figure 6-9. Frequency spectra for the three idealized runs.

The biggest upside of being able to nest an LES in the WRF model is that it makes it simple to do LES runs forced with real weather and geographical data. We found that getting optimal performance from LES nests with cell perturbations probably demands some tuning and manual modifications to our implementation. But even without any such tuning the improvement over using unperturbed boundary conditions is evident as shown in Figure 6-10.

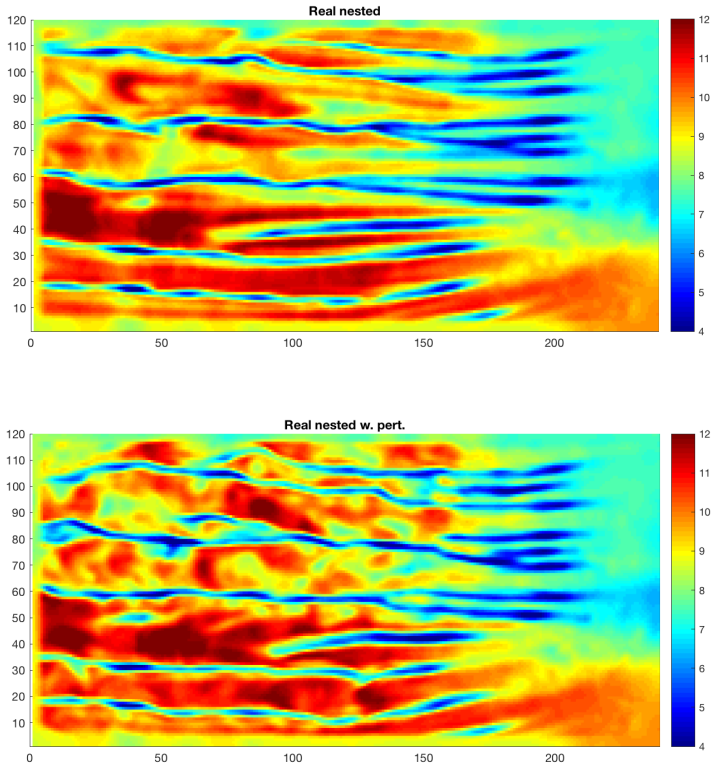

Figure 6-10. Snapshot of the wind speed at 120m height in a real weather run.

6.2 MIUU MODEL

Here the MIUU-model developed at Uppsala University has been used to map the wind climate at two forested sites in southern Sweden in order to investigate differences in model results due to different input data for topography and land use.

6.2.1 Wind climate modelling

In an ideal climate study, model runs should be made representing all weather conditions. But this would require a large number of simulations. Since the MIUU-model is rather computer-time consuming to run, a method was developed where only the variables of greatest importance to the flow is varied in order to cover an as wide range of atmospheric conditions as needed in order to get an accurate description of the wind climatology (Bergström and Söderberg 2009; Bergström and Söderberg 2011). The parameters judged to be of most importance to the wind field are: The horizontal air pressure gradient (i.e. geostrophic wind, strength and direction), thermal stratification (through the daily temperature variation), surface roughness, topography, and land-sea/lake temperature differences (Bergström, 2002).

In short, for each season, runs were made with three values of the geostrophic wind speed, and with 16 wind direction sectors, summing up to 192 model runs to cover the most important parameters determining the boundary layer wind climate.

The annual mean wind speed has been calculated according to the method of Bersgström and Söderberg (2011), by weighting the four individual months (January, April, July and October) together. Thus, the result from a study of the climatological wind field may be presented as the mean wind speed (annual or seasonal), or wind energy potential, at different heights. The wind speed distribution and the corresponding Weibull parameters may also be determined. It should be pointed out that the MIUU model uses no local wind measurements as input, but it is of course important to validate the results against observations.

6.2.2 Model domains

Here the results of the 1 km model runs made in the Swedish national wind resource mapping (Bergström and Söderberg,, 2009) have been used to further downscale in two steps. First from 1 km to 300 m resolution, then from 300 m to 100 m resolution. This was done for two forested sites with wind measurements on high towers: Hornamossen with a 180 m high tower, and Ryningsnäs with a 140 m high tower.

Two versions of model runs were made. In the first version topography and land use were taken from Lantmäteriet (Swedish Land Survey). The second version was based on laser scanning from airplanes, also available from Lantmäteriet. The laser data was processed to give topography and land use according to the PAI method described in Chapter 9. Tree height and plant area density were thus used to estimate the roughness length and zero-plane displacement needed when modelling the wind resource.

6.2.3 Hornamossen

This site is a hilly area mainly covered with forests. A site description can be found in Chapter 3. The roughness length estimated from the laser scanning data following the procedure given in Chapter 9 is shown in Figure 6-11. Typical values are between 1 and 2 m for forested areas. Following the previously used techniques to determine the roughness length from land use data, the laser estimates gives larger values of the roughness length. Figure 6-12 shows a histogram of the differences between laser scan roughness length values and values estimated from land use data provided by Lantmäteriet. These roughness length values are similar to the values used in the previous Swedish wind resource mapping. It is obvious that at least for this site, the values estimated from the laser scanning typically result in a roughness length about 1 m higher.

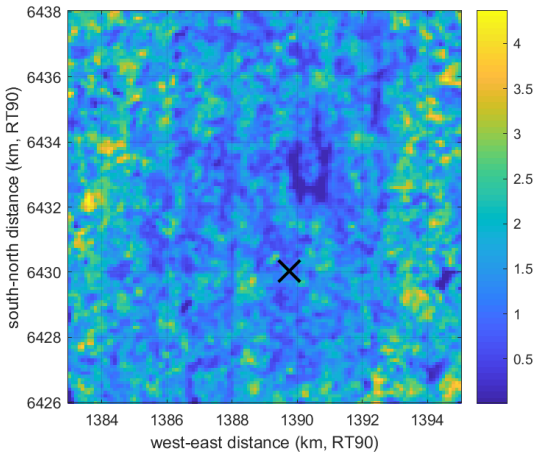

Figure 6-11 Roughness length z_0 in the 12 km x 12 km modelled area around the Hornamossen site estimated from the laser scanning. Scale shows z_0 in metres. The cross marks the location of the Hornamossen mast.

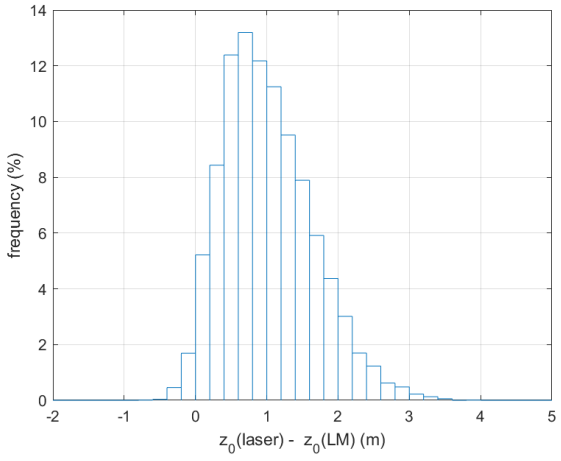

Figure 6-12 Histogram showing the difference in roughness length between values estimated from laser scanning and values estimated from Lantmäteriet's land use data over the Hornamossen site.

Model calculations were done using three setups. All used the Swedish national wind resource mapping on a 1 km x 1 km horizontal scale as primary input (Bergström and Söderberg, 2009). A first downscaling to 300 m horizontal resolution was made, followed by a second downscaling from 300 m to 100 m horizontal resolution, both using:

1. Terrain height and roughness length based on the laser scanning data.
2. Terrain height and roughness length taken from Lantmäteriet data.
3. Terrain height taken from Lantmäteriet data together with roughness length based on laser scanning data.

The third version was made in order to get some knowledge about the relative importance of the data source for terrain height and roughness length. As the terrain height from the two sources didn't differ very much other than in details, it was not judged necessary to make a model setup using terrain height from laser data and roughness length from the Lantmäteriet land use data.

Comparisons were made with wind observations taken in the 180 m high tower at Hornamossen.. Due to confidentiality, the wind results are not given in m/s, but as the ratio between the local wind speed and the measured wind speed taken on the tower during the two year period June 2015 to May 2017. All results presented are at 100 m height above local ground. As the model results are originally given at heights above zero-plane displacement, this was also needed. This was done from laser scanning estimates of tree height. The resulting zero-plane displacement is shown in Figure 6-13. Typical numbers are 10 to 20 m for the forested areas.

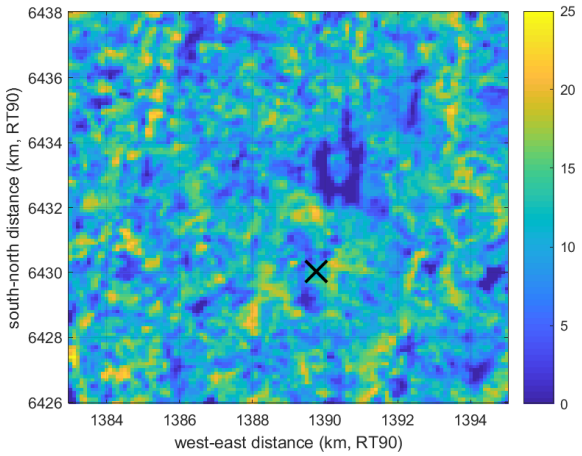

Figure 6-13. Zero-plane displacement d in the 12 km x 12 km modelled area around the Hornamossen site estimated from the laser scanning data of tree height. Scale show d in metres. The cross marks the location of the measurement tower.

Comparisons between the modelled and measured normalized wind profiles at the locations of the measurement towers are shown in Figure 6-14 to 6-16.

Using laser scanning data to determine both terrain height and roughness length the modelled wind profile shows good agreement with the observed wind profile

(Figure 6-14), with only some tendency for the modelled profile to increase somewhat slower with height above 100 m.

Using the Lantmäteriet data for topography and land use as model input, the modelled normalized wind profile is about 3 % above the observed one (Figure 6-15). Keeping Lantmäteriet data for terrain height but using roughness length determined from laser scanning data, the agreement between modelled and observed normalized wind profile is again good. This indicates that the important difference are the results of the larger roughness lengths from the laser scanning, while the minor differences as regards terrain height are of less importance yielding differences less than 0.5 % in the normalized wind profile.

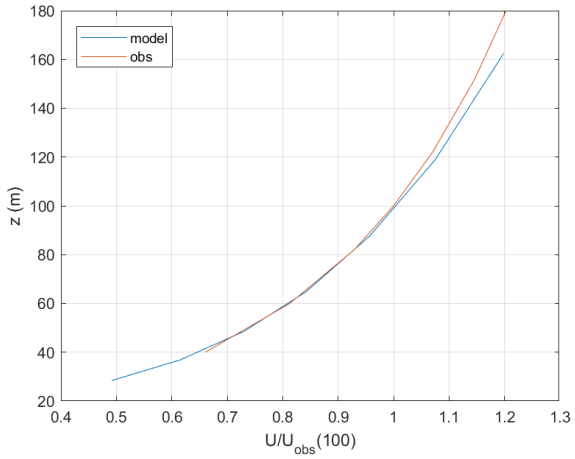

Figure 6-14 Modelled and observed normalized wind profile at the Hornamossen measurement tower. Height is above ground. Model runs using terrain height and surface roughness based on laser scanning data.

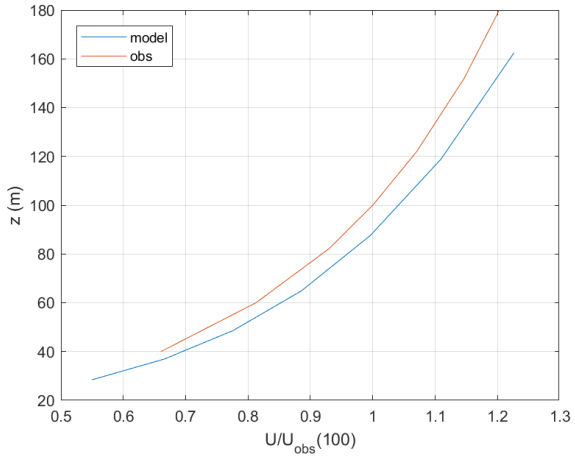

Figure 6-15. Same as in Figure 6-14, but from model runs using terrain height and surface roughness based on Lantmäteriet data.

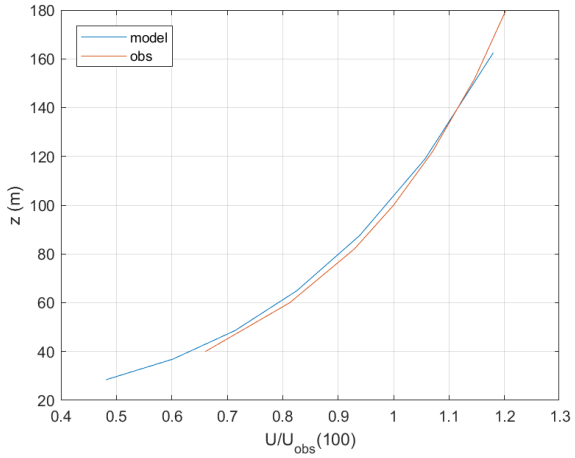

Figure 6-16. Same as in Figure 6-14, but from model runs using terrain height based on Lantmäteriet data and roughness length using laser scanning data.

Maps showing the normalized wind speed at 100 m height above ground are shown in Figure 6-17 to 6-19, while differences between normalized wind speed using the different sources for terrain height and roughness length are shown in Figure 6-20 and Figure 6-21. As already seen comparing modelled and observed wind profiles at the location of the Hornamossen tower, it is clear that the smaller values of roughness length using land use data from Lantmäteriet not surprisingly result in a higher wind speed compared to the larger values of roughness length determined from laser scanning data. Also the differences in wind speed are mainly caused by the differences in roughness length, while differences in terrain height have smaller impacts in the modelled wind speed.

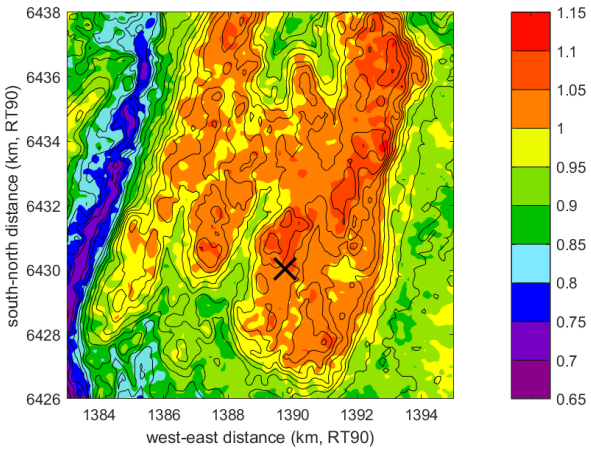

Figure 6-17. Modelled normalized annual wind speed, $U/U_{obs}(100)$, at 100 m height above ground in the area with 100 m horizontal resolution around Hornamossen. The cross marks the location of the measurement tower. The observed average wind speed at 100 m from the tower was used for the normalization. Model runs using terrain height and roughness length determined from laser scanning data.

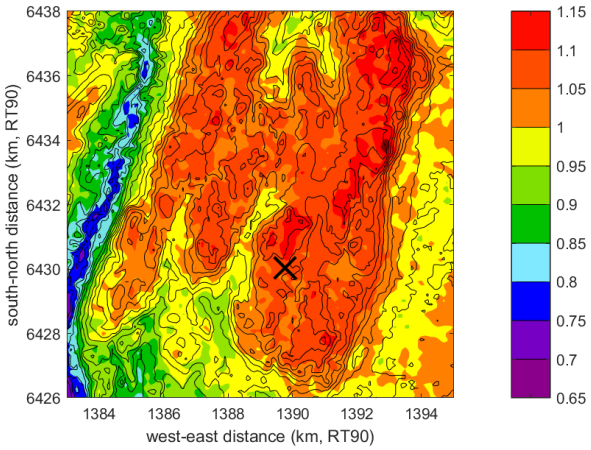

Figure 6-18. Same as in Figure 6-17, but from model runs using terrain height and roughness length from Lantmäteriet data.

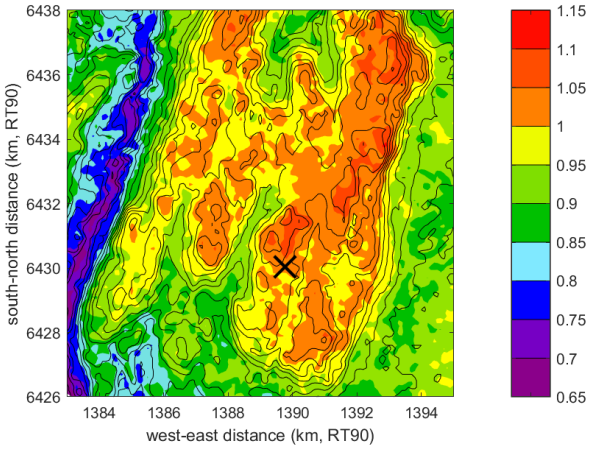

Figure 6-19. Same as in Figure 6-17, but from model runs using terrain height from Lantmäteriet data and roughness length using laser scanning data.

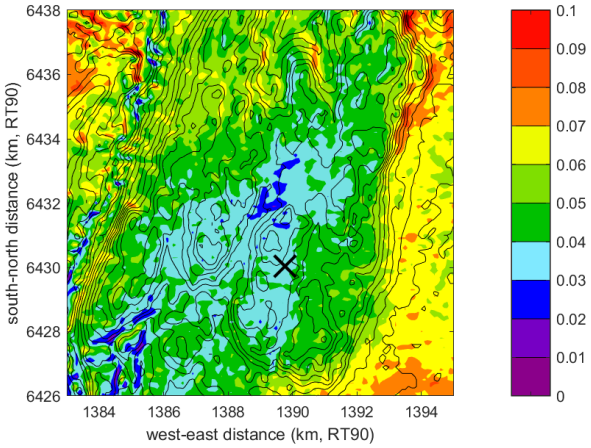

Figure 6-20. Difference between modelled normalized annual wind speed at 100 m height above ground using Lantmäteriet data for terrain height and roughness length and using laser scanning data.

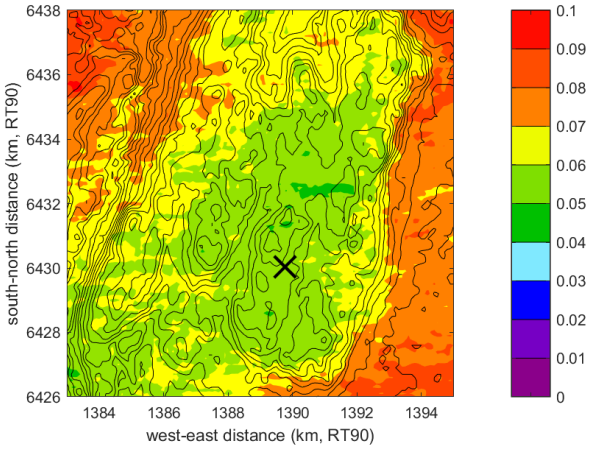

Figure6-21. Same as in Figure 6-20, but differences using Lantmäteriet data for terrain height and roughness length and using laser scanning data for roughness length while keeping Lantmäteriet data for terrain height.

6.2.4 Ryningsnäs

This site is also mainly covered with forest, but has smaller differences in terrain height than Hornamossen. The topography is shown in Figure 6-22 estimated from the laser scanning. The highest areas reach about 140 m above sea level, while the surrounding terrain is typically 90-100 m lower. Height differences within the 8 x 8 km area are about 40-50 m as compared to more than 200 m at the Hornamossen site. Differences between laser scan data and terrain height data from Lantmäteriet are typically small around Ryningsnäs, but can locally be about 10 m.

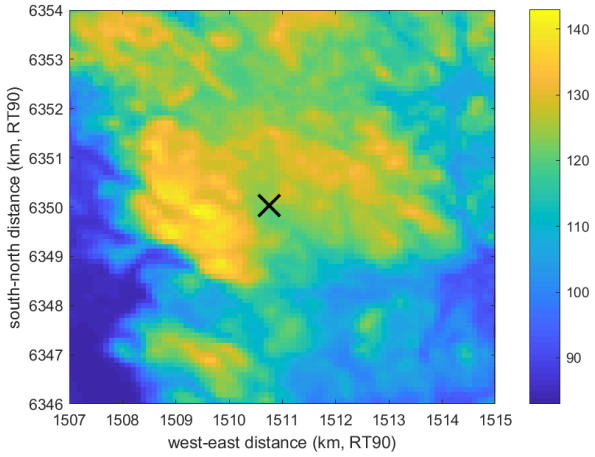

Figure 6-22. Topography in the 8 km x 8 km modelled area around the Ryningsnäs site estimated from the laser scanning. Scale shows m above sea level. The cross marks the location of the measurement tower. Horizontal resolution is 100 m x 100 m.

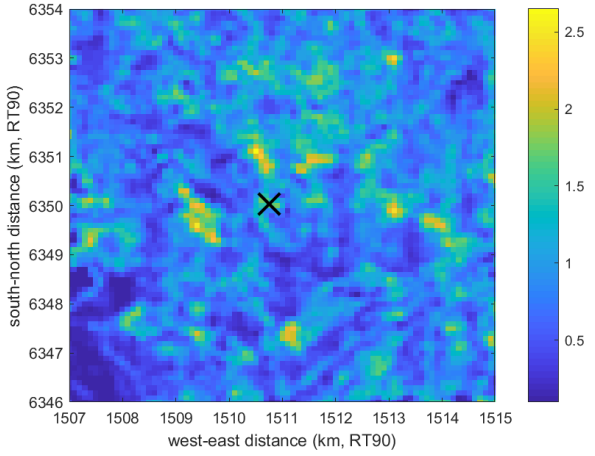

Figure 6-23. Same as in Figure 6-22, but for roughness length z_0 in meters.

The roughness length has also been estimated from the laser scanning data following the procedure given in Chapter 9, and is shown in Figure 6-23. Typical values are around 1 m for forested areas, with smaller areas reaching 2 m. Following the previously used techniques to determine the roughness length from land use data, the laser estimates give larger values of the roughness length. Figure 6-24 shows a histogram of the differences between laser scan roughness length values and values estimated from land use data provided by Lantmäteriet. These roughness length values are similar to the values used in the previous Swedish wind resource mapping. It is obvious that the data estimated through the laser scanning typically results in a roughness length, which is higher. But differences at the Ryningsnäs site are not as large as at the Hornamossen site.

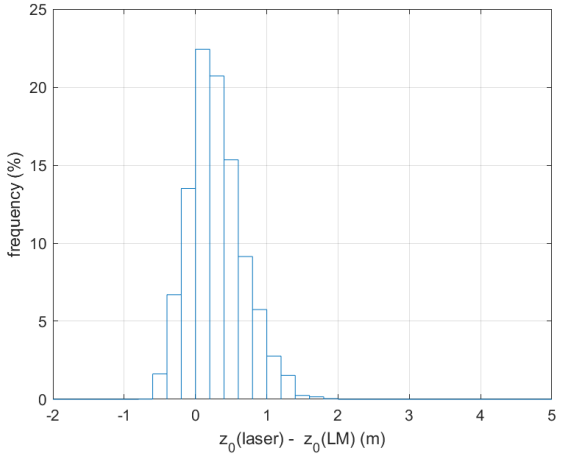

Figure6-24. Histogram showing the differences in roughness length between values estimated from laser scanning and values taken from Lantmäteriet's land use data over the Ryningsnäs site.

Model calculations over the Ryningsnäs area were done using two setups. Again all simulations used the Swedish national wind resource mapping on a 1 km x 1 km horizontal scale as primary input (Bergström and Söderberg, 2009). A first downscaling to 300 m horizontal resolution was made, followed by a second downscaling from 300 m to 100 m horizontal resolution, both using:

1. Terrain height and roughness length based on the laser scanning data.
2. Terrain height and roughness length taken from Lantmäteriet data.

Comparisons were made with wind observations from the 140 m high tower at Ryningsnäs, marked with a cross in Figure 6-23 and Figure 6-25, and in the graphs showing wind data below. As for Hornamossen, results are given as the ratio between the local wind speed and the measured wind speed taken from a reference period. All results presented are at 100 m height above local ground. Zero plane displacement adjustment was done as at Hornamossen. The resulting zero-plane displacement is shown in Figure 6-25. Typical numbers are 10 to 20 m for the forested areas.

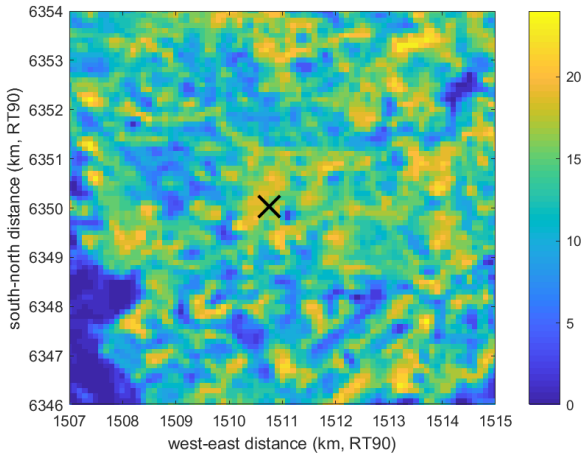

Figure 6-25. Zero-plane displacement d in the 8 km x 8 km modelled area around the Ryningsnäs site estimated from the laser scanning data of tree height. Scale shows d in metres. The cross marks the location of the measurement tower.

Comparisons between the modelled and observed normalized wind profiles at the location of the measurement tower are shown in Figure 6-26. The normalization was made using the observed wind speed at 100 m height.

Using laser scanning data to determine both terrain height and roughness length the modelled normalized wind profile shows higher winds than the observed wind profile. About 20 % at heights of 80-140 m. As seen above the Hornamossen wind profile modelled using laser scanning data for both terrain height and roughness length showed good agreement with the observations. Much better than using Lantmäteriet data. A reason to why this is not the case at the Ryningsnäs site may be that the differences in roughness length using different data sources (laser scanning or land used from Lantmäteriet) are much smaller at Ryningsnäs than at Hornamossen. As the same technique was used for both sites when determining roughness length from laser scanning data, it seems reasonable to assume that this is somehow a result of different forest properties. This was not investigated in any detail here, why more research is needed to find the explanation.

Maps showing the normalized wind speed at 100 m height above ground are shown in Figures 6-28 and 6-29, while differences between normalized wind speed using the different sources for terrain height and roughness length are shown in Figure 6-30. As already seen comparing modelled and observed wind profiles at the location of the Ryningsnäs tower, it is clear that the small differences in roughness length using land use data from Lantmäteriet or laser scanning data not surprisingly result in small wind speed differences.

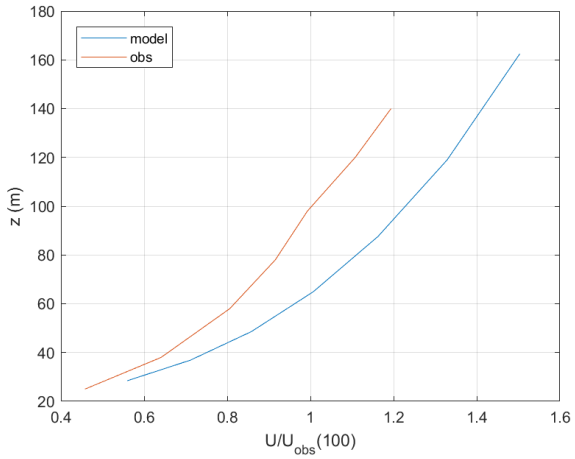

Figure 6-26. Modelled and observed normalized wind profile at the Ryningsnäs measurement tower. Height is above ground. Model runs were made using terrain height and surface roughness based on laser scanning data.

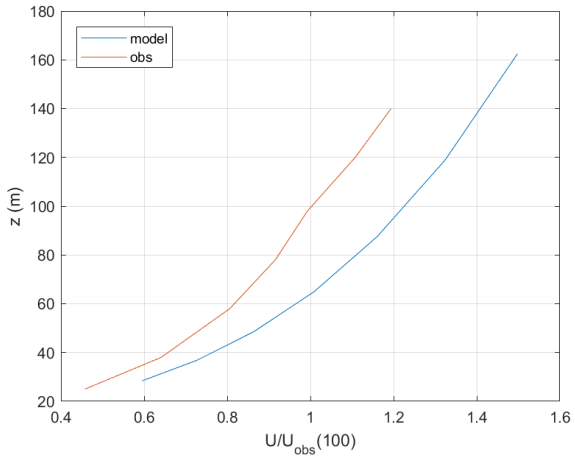

Figure 6-27. Same as in Figure 6-26, but from model runs made using terrain height and surface roughness based on Lantmäteriet data.

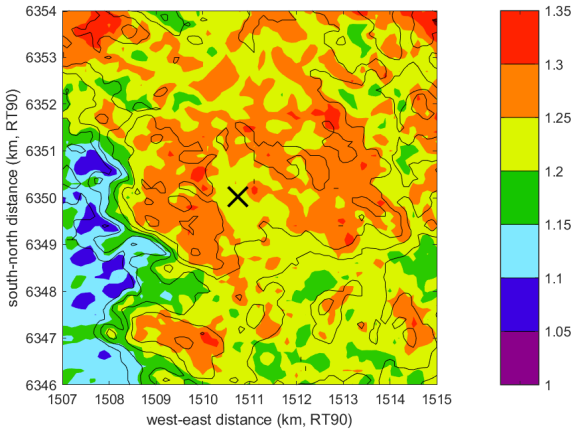

Figure 6-28. Modelled normalized annual wind speed, $U/U_{obs}(100)$, at 100 m height above ground in the area with 100 m horizontal resolution around Ryningsnäs. The cross marks the location of the measurement tower. The observed average wind speed at 100 m from the tower was used for the normalization. Model runs were made using terrain height and roughness length determined from laser scanning data.

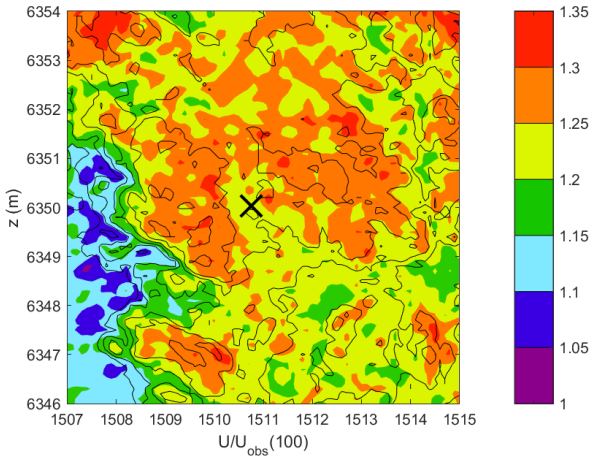

Figure 6-29. Same as in Figure 6-28, but based upon model runs using terrain height and roughness length from Lantmäteriet data.

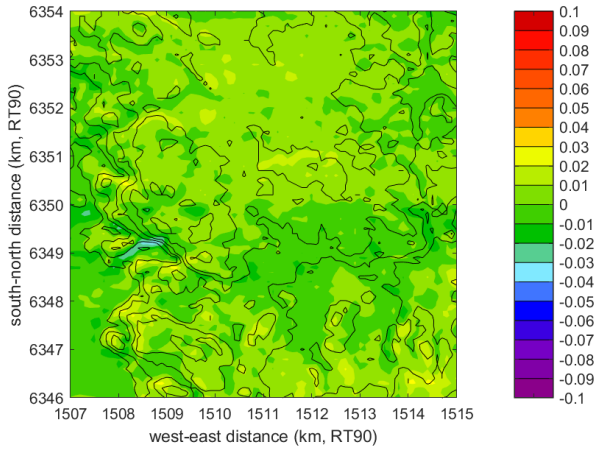

Figure 6-30. Differences between modelled normalized annual wind speeds at 100 m height above ground using Lantmäteriet data for both terrain height and roughness length and using laser scanning data.

6.3 SUMMARY AND CONCLUSIONS

In forested areas, both with and without larger or smaller topographical differences, additional complications when modelling the wind resource arise as a result of differences in forest properties, such as tree height, tree density, and plant area density. These differences become important when modelling the wind resource since they affect the roughness length and the zero-plane displacement. Previously these parameters have most often been estimated from available land use data, e.g. from Lantmäteriet.

During recent years detailed laser scanning has been carried out by flight measurements, and techniques are being developed to use the laser scanning data to determine roughness length and zero-plane displacement, in addition to new detailed estimates of terrain height, tree height, and plant area densities (see Chapter 9).

We have used the MIUU-model together with the MIUU-method to estimate the wind resource at two forested sites in Sweden using different sources for roughness length and zero-plane displacement. The results show that at one site the laser scanning data gives a modelled wind in good agreement with observations, while the modelled wind at the other site is higher than given by the observations. Generally the roughness lengths estimated from laser scanning data are higher than what is estimated from land use data following generally used look-up tables. But the differences were found to be much larger at the site where the modelled wind resource was in good agreement with observations, while at the other site the differences were much smaller.

The reason for this is presently not clear. It seems at least not directly to be due to differences in tree height, which are about the same at both sites. At both sites the maximum tree heights are about 20-25 m, only seldom reaching 30 m. Typical tree heights for both forest areas are 15-25 m. More research is thus needed on how to estimate the surface roughness from the laser scanning data.

7 LES model simulations

7.1 MODEL DESCRIPTION

In Large Eddy Simulations (LES), the large turbulent eddies are resolved and the small, subgrid scales (SGS) are modelled with a sub-grid scale model. The distinction between large and small scales is done implicitly by the grid and is referred to as grid filtering.

An incompressible finite volume method is used which is based on the pressure-velocity coupling treated with fractional step. A second-order central differencing scheme is used for the momentum equations. For modelling the SGS turbulence, we employ a one-equation turbulence model which predicts the SGS turbulent kinetic energy. This equation is discretized with the hybrid method (first order upwind combined with second-order central scheme). The second-order Crank-Nicholson scheme is employed for time discretization. For more detail, see Davidson & Peng (2003).

7.2 MODEL SET-UP AND BOUNDARY CONDITIONS

The domain is a cube with sides of 1000 m. A grid with N_x = 98 (streamwise), N_y = 98 (lateral) and N_z = 194 (vertical) cells is used. The flow is either neutral (h/L = 0) or weakly stable (h/L = −0.045). A time step of 0.2 s is used.

Symmetry boundary conditions are used at the top of the domain. A surface roughness of z_0 = 0.02 m is prescribed everywhere. Two different methods for prescribing the inlet boundary conditions are used.

1. In weakly stable flow, a pre-cursor LES is carried out using periodic boundary conditions in streamwise (x) and lateral (y) directions. The velocity at hub height and the surface heat flux are prescribed from WRF (Weather Research and Forecasting) simulations (see Chapter 6 for a description of the WRF simulations). At each time step, the velocity field in a y − z plane is stored on the disk.
2. In the neutral flow case, the inlet boundary conditions are
   - either taken from a pre-cursor LES (same as in 1.)
   - or the mean inlet velocity profile is taken from WRF and synthetic fluctuations are superimposed on the mean profile. The method for generating the synthetic fluctuations (see Chapter 8 for details) was developed by Segalini and Arnqvist (2015). A MATLAB script for generating the synthetic fluctuations was provided by the project partners Uppsala University and KTH. The synthetic velocity inlet fluctuations are scaled by:

$$\left(\frac{u_*^2(1-z/\delta)^{3/2}}{uw_{synt}}\right)^{1/2} \tag{7-1}$$

where uw_{synt} is the magnitude of the original synthetic shear stress, u_* is the friction velocity and δ is the boundary layer thickness (= height of the domain).

LES simulations are then carried out using one of the inlet boundary conditions described above (LES or synthetic fluctuations).

7.3 MODELLING OF FOREST

The height of the forest is 20 m. The effects of the forest on the flow field are modelled by adding a drag term in the x momentum equation (Nebenführ and Davidson, 2015). An additional source term in the TKE equation (Shaw and Patton, 2003) is employed for modelling the effect of the forest on the SGS turbulence.

7.4 RESULTS

First, we will look at the results for neutral conditions using option 1 (synthetic fluctuations) for inlet boundary conditions. The inlet mean velocity is taken from WRF. The velocity, Reynolds stresses are shown at three positions: inlet, 250 and 900 m downstream of the inlet. Figure 7-1 presents velocity profiles at 250 and 900 m downstream the inlet compared with WRF (recall that the WRF velocity profile is set as mean inlet profile). As can be seen the velocity profile does not change at all from the inlet to 900 m downstream the inlet.

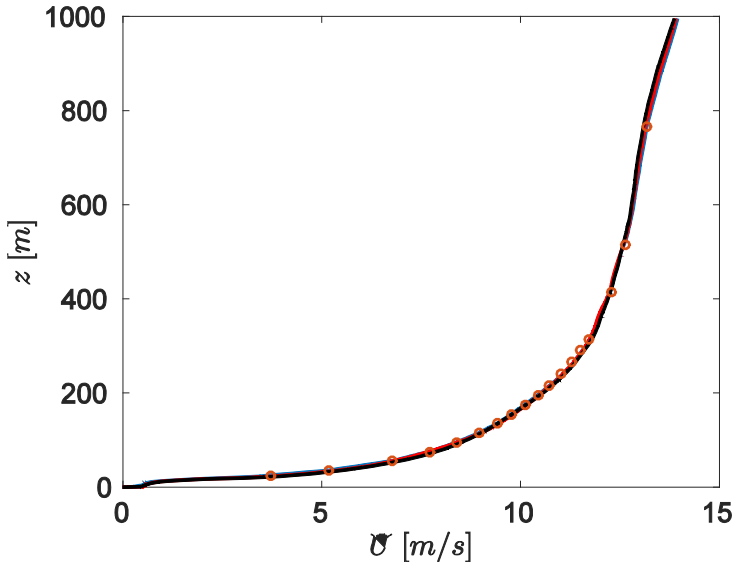

Figure 7-1. Neutral conditions. Synthetic inlet fluctuations. Streamwise mean velocity. Solid blue line: inlet; red dashed line: x=250m; black dash-dotted line: x=900m; markers: WRF.

The turbulent stresses in Figures 7-2 and 7-3 show that the turbulence quickly becomes fully developed. The peak of streamwise fluctuations has increased by 50% at 250m, but has decreased again towards the outlet (900m). This is also seen in Figure 7- 4, which shows the peak values versus the streamwise direction x.

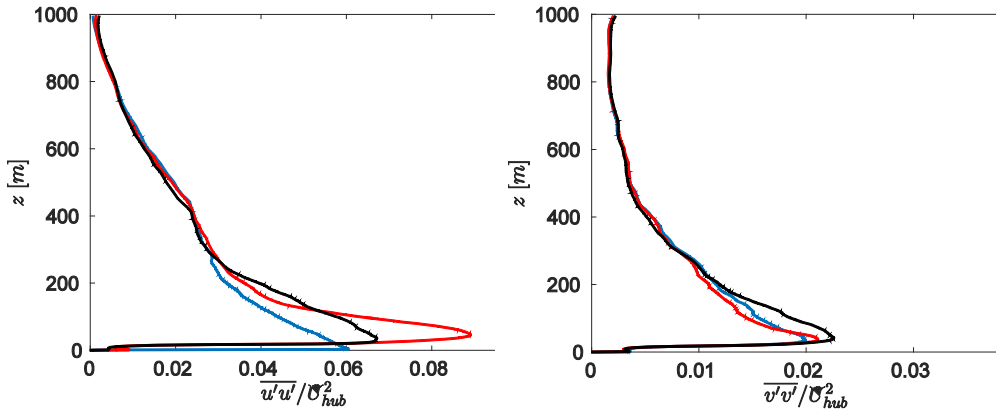

Figure 7-2. Neutral conditions. Synthetic inlet fluctuations. Streamwise (left) and vertical (right) fluctuations. Solid blue line: inlet; red dashed line: x=250m; black dash-dotted line: x=900m.

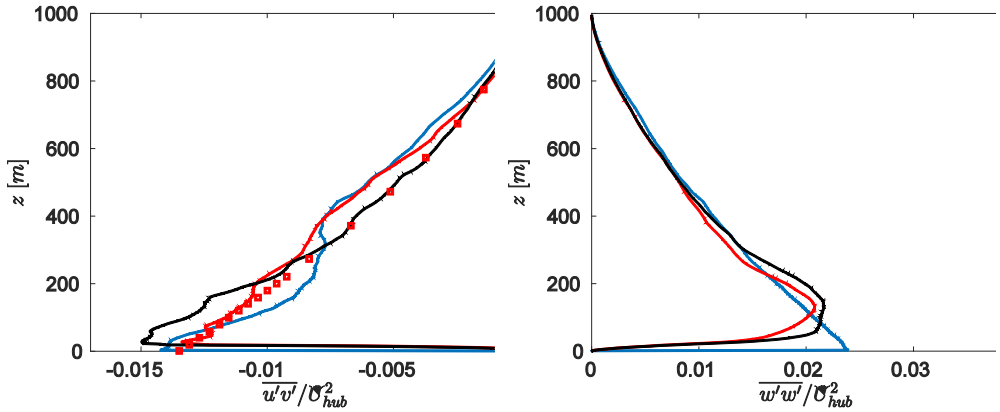

Figure 7-3. Neutral conditions. Synthetic inlet fluctuations. Shear stress (left) and lateral (right) fluctuations. Solid blue line: inlet; red dashed line: x=250m; black dash-dotted line: x=900m; markers: WRF.

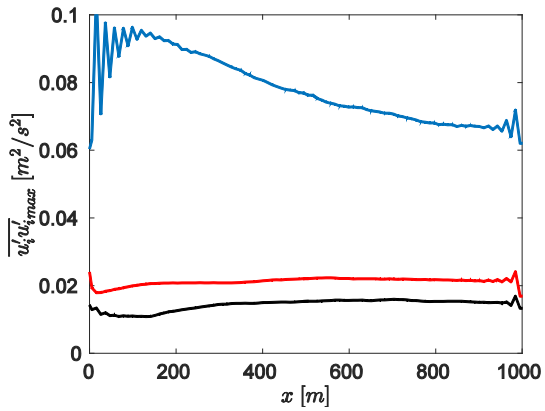

Figure 7-4. Neutral conditions. Synthetic inlet fluctuations. Maximal fluctuations versus x. Solid blue line: streamwise fluctuations; red dashed line: lateral fluctuations; black dash-dotted line: vertical fluctuations.

Next, we use inlet fluctuations from a periodic pre-cursor LES (option 2) in which the mean LES velocity at hub height (90 m) is taken from WRF. Figure 7-5 presents the velocity profiles, which are rather different from the WRF profile (if the domain in Figure 7-1 were made much longer, the velocity profiles in Figure 7-5 and at the end of the domain in Figure 7-1 would be identical). The main reasons why the LES and the WRF velocity profiles in Figure 7-5 differ are that the LES has a much finer grid and the WRF profile includes the effects of topography. The Reynolds stresses in Figures 7-6, 7-7 and 7-8 do not change much downstream the inlet. The reason is, of course, that the inlet velocity field is taken from a fully-developed pre-cursor LES. But the magnitudes of the stresses are much larger in Figures 7-6 and 7-7 than in Figures 7-2 and 7-3. The reason for the latter is that the inlet profiles are different. In Figure 7-1 the WRF profile is prescribed as inlet boundary condition whereas in Figure 7-5 the WRF velocity is prescribed only in one point (at hub height). The velocity gradient becomes much smaller in the latter case and hence the smaller Reynolds stresses. Which one is more correct? That depends on the effect of the topology. If it is small, then WRF and LES should predict the same boundary layer, but LES is using a much finer mesh. In this case, the results in Figures 7-5, 7-6 and 7-7 should be correct. If the effect of the topology is strong, the results in Figures 7-1, 7-2 and 7-3 are probably more correct. In this case we could consider using the LES fluctuations rather than the LES velocities as inlet conditions and use the WRF velocity profile as mean inlet velocity.

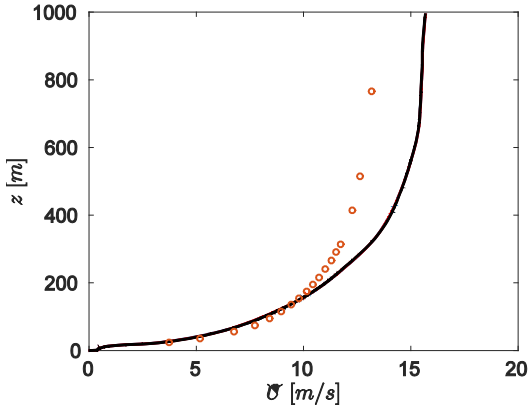

Figure 7-5. Neutral conditions. LES inlet fluctuations. Streamwise mean velocity. Solid blue line: inlet; red dashed line: x=250m; black dash-dotted line: x=900m; markers: WRF.

The final case we will analyse is weakly stable flow. Figure 7-9 shows the velocity and the temperature profiles. As in the previous case, the LES velocity profile does not agree with the WRF profile. The Reynolds stresses become quickly fully developed, see Figures 7-10 and 7-11. The heat fluxes in Figure 7-12 are not yet fully developed and the reason is probably two-fold. First, the temperature decreases slowly downstream the domain due to the heat sink in the forest. Second, the buoyancy term in the vertical momentum is related to the plane-averaged temperature, and it is not the same in the pre-cursor simulations and in the inlet-outlet simulations. Figure 7-13 shows the maximum stresses and vertical

heat flux versus x. Again, it can be seen that the stresses become quickly fully developed.

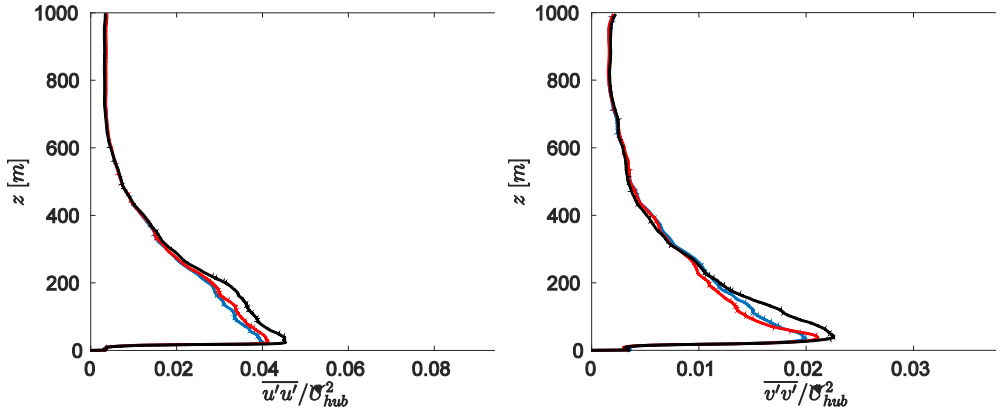

Figure 7-6. Neutral conditions. LES inlet fluctuations. Streamwise (left) and vertical (right) fluctuations. Solid blue line: inlet; red dashed line: x=250m; black dash-dotted line: x=900m.

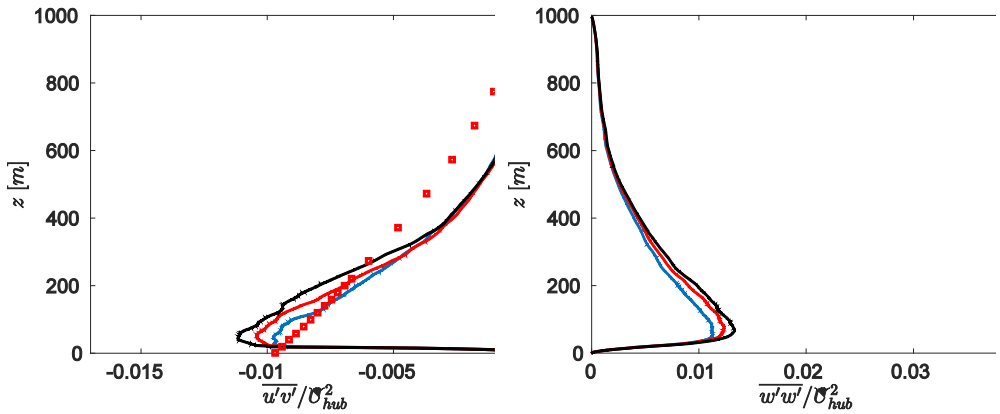

Figure 7-7. Neutral conditions. LES inlet fluctuations. Shear stress (left) and lateral (right) fluctuations. Solid blue line: inlet; red dashed line: x=250m; black dash-dotted line: x=900m; markers: WRF.

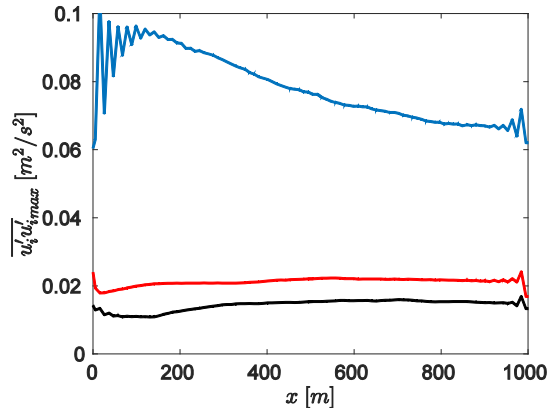

Figure 7-8. Neutral conditions. LES inlet fluctuations. Maximal fluctuations versus x. Solid blue line: streamwise fluctuations; red dashed line: lateral fluctuations; black dash-dotted line: vertical fluctuations.

7.5 SUMMARY AND CONCLUSIONS

The wind in a forest region is predicted using advanced CFD simulations (CFD = Computational Fluid Dynamics). The method that is used is called Large Eddy Simulations (LES). First, weather conditions at the site are computed using WRF (Weather research and forecasting model). The WRF predictions are made by WeatherTech Scandinavia AB. In the next step LES is used in the region surrounding the site of the wind turbines (no wind turbines are included in the LES simulations). Inlet boundary conditions of the mean flow for the LES are taken from WRF. However, the LES also needs small-scale turbulent fluctuations. These fluctuations are taken either from a synthetic fluctuation generator (synthetic turbulence) or from a pre-cursor LES using period boundary conditions (i.e. no inlet boundary conditions are required). A MATLAB code for creating the synthetic fluctuations was provided by Uppsala University and KTH. Both neutral and weakly stable conditions have been simulated.

It is found that both the pre-cursor LES and the MATLAB code create physical and reasonable inlet fluctuations. However, for neutral conditions it is found that the synthetic fluctuation generator and the pre-cursor LES give rather different results. The reason is that the WRF velocity is prescribed in a different way. When synthetic fluctuations are used, the entire WRF velocity profile is used. When inlet fluctuations from the pre-cursor LES are employed, the velocity from WRF is prescribed only at one point (at hub height) but the velocity profile is taken from the pre-cursor LES. Which method is more accurate depends probably on how important the effect of the topology are.

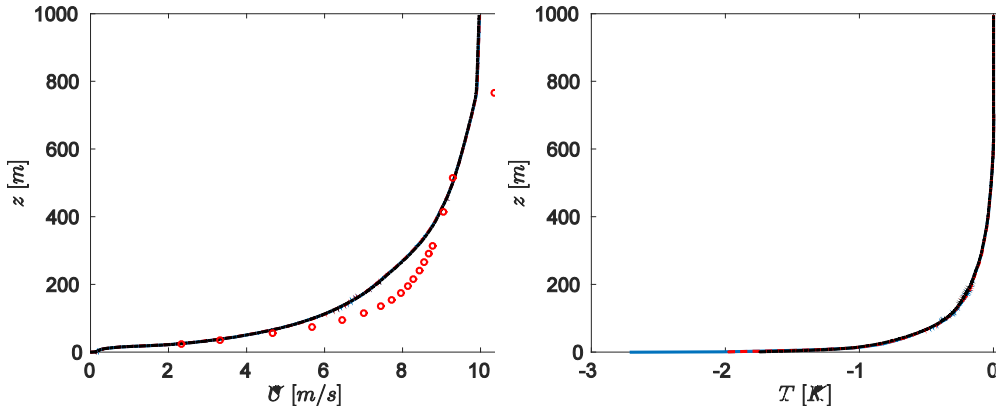

Figure 7-9. Stable. LES inlet fluctuations. Streamwise mean velocity (left) and temperature (right). Solid blue line: inlet; red dashed line: x=250m; black dash-dotted line: x=900m; markers: WRF.

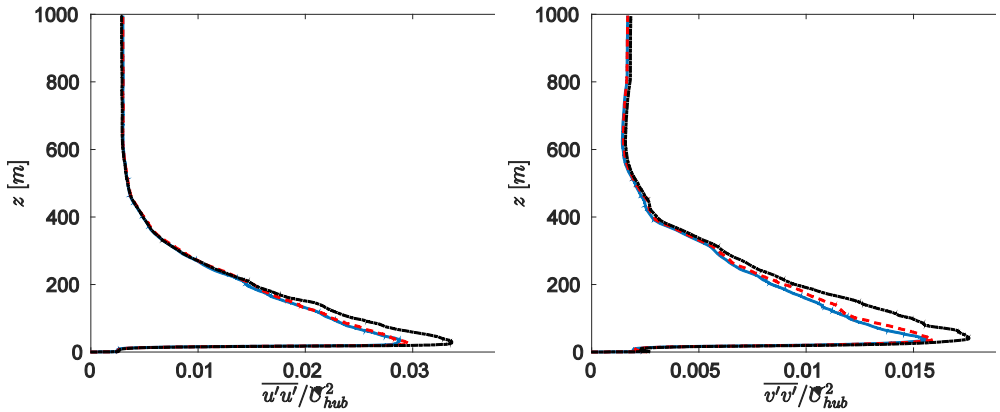

Figure 7-10. Stable conditions. LES inlet fluctuations. Streamwise (left) and vertical (right) fluctuations. Solid blue line: inlet; red dashed line: x=250m; black dash-dotted line: x=900m.

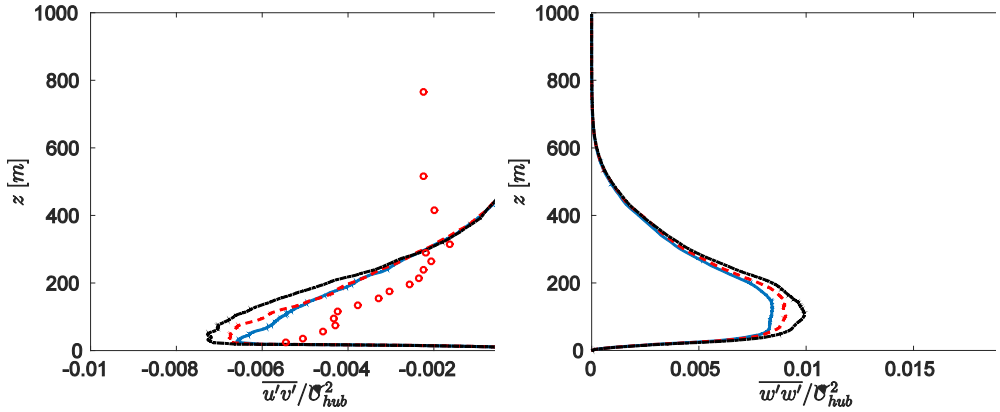

Figure 7-11. Stable conditions. LES inlet fluctuations. Shear stress (left) and lateral (right) fluctuations. Solid blue line: inlet; red dashed line: x=250m; black dash-dotted line: x=900m; markers: WRF.

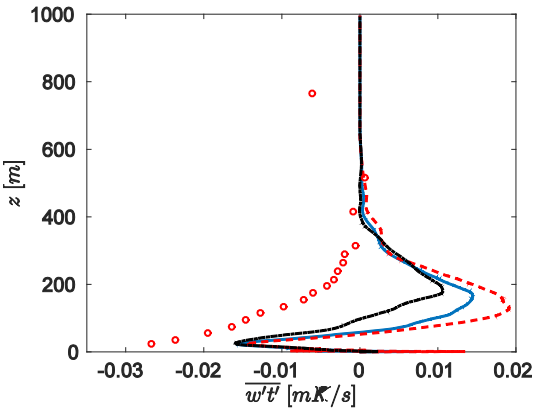

Figure 7.12. Stable conditions. LES inlet fluctuations. Vertical heat flux. Solid blue line: inlet; red dashed line: x=250m; black dash-dotted line: x=900m; markers: WRF.

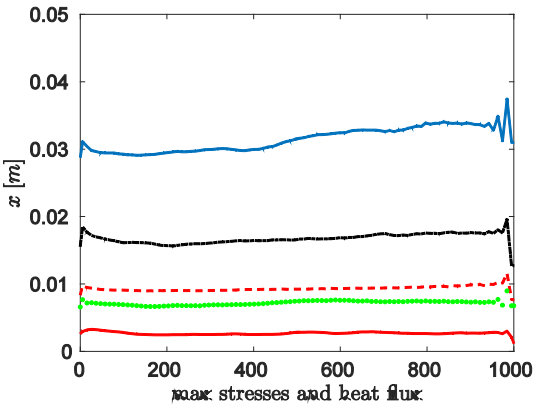

Figure 7.13. Stable conditions. LES inlet fluctuations. Maximal fluctuations versus x. Solid blue line: streamwise fluctuations; red dashed line: lateral fluctuations; black dash-dotted line: vertical fluctuations: green blue line: negative shear stress; solid red line: negative vertical heat flux (multiplied by five).

8 Synthetic turbulence

In the mid-1990s time domain aeroelastic simulation became the state-of-the art choice of modelling for wind turbine load analysis and control design, in the wind industry as well as within the major R&D communities. Here the rotor aerodynamics was described by Blade Element Momentum theory (BEM), and the wind input was usually stochastic 3D wind fields generated from a target statistical description of the inflow in space and time. The time series of wind velocity were *synthesized* from correlated random harmonic components using some type of Fourier transform, and the resulting meteorology then usually referred to as *synthetic turbulence simulation*. Despite huge efforts put into the development of more advanced models for rotor aerodynamics and turbulence modelling, such as *Vortex models* and *Large Eddy Simulation*, the 25 year old semi analytical approach is still the most commonly used.

For wind turbine certification, it is clearly specified in the governing international standards how the turbulence shall be modelled, and corresponding model parameter values for different wind turbine classes are prescribed. When trying to fit a turbine model to a specific site, a Turbine Suitability Assessment (TSA) usually has to be performed. In the TSA a new load analysis is carried out, considering the specific flow conditions on the site. Here the turbulence is usually characterised only by turbulence intensity for the longitudinal wind speed and a single wind shear parameter. In the following, it is outlined how knowledge about typical turbulence characteristics over the Scandinavian inland can be used to achieve improvements to site-specific synthetic turbulence modelling.

8.1 INTRODUCTION TO THE SEGALINI AND ARNQVIST (2015) TURBULENCE MODEL

In the atmospheric community, the Mann model (Mann 1994) is one of the most used models, it is also one to the two turbulence models described within the IEC standard.: The approach is based on the decomposition of atmospheric turbulence in spatial waves (so that Fourier methods can be introduced) and determines the waves complex amplitude so that the overall spectrum (namely the energy for every wave) is equal to the one observed in nature. Since three velocity components must be considered, the amount of complex amplitudes is very large, making the problem a fitting exercise with an almost impossible generalization. Mann (1994) formulated a model to determine the velocity spectra with homogeneous shear (namely assuming that the local velocity gradient is constant) based on the Rapid Distortion Theory (RDT) approach, a well-known technique in theoretical turbulence. The key idea of the work was to let the velocity spectra evolve from an initially isotropic condition (where the spectrum is analytically known) for a certain characteristic time according to a simplified set of flow equations (the RDT equations). This reduced the number of free parameters to three (two to determine the initial isotropic spectrum and one to quantify the evolution time). Since the model determines the spectrum in space, it is also possible to quantify two-point correlations, key quantities in synthetic-turbulence generation.

The model equations of the Mann model was developed for neutral stratification (namely when the air temperature has a vertical gradient of -0.1°C/km) and lack any coupling between velocity and temperature (or density) that is required to account for non-neutral stratification. Noting the large impact of stratification on turbulence statistics (Bergström et al 2013, Arnqvist et al 2015) Segalini and Arnqvist (2015) have recently extended the Mann approach to the stably-stratified case by means of an analytical solution of the stratified RDT equations.

This allowed for the determination of the spectra evolution at any given time starting from a known initial condition. Following the same approach adopted by Mann, a model for the velocity spectral tensor in the atmospheric surface layer was obtained, with very good agreement between model predictions and atmospheric measurements over forests.

The determination of the spectra is analytical, and hence it is very fast to calculate. When the spectra are translated into velocity fluctuations in physical space, the projection of them is made through numerical integration, but this integration is very efficient. The whole turbulence-generation process is considered computationally effective when compared to other approaches used to obtain physically-consistent turbulence fields.

8.2 VALIDATION OF THE SEGALINI AND ARNQVIST (2015) TURBULENCE MODEL

The model was originally adopted to the turbulence measured at Ryningsnäs (Segalini and Arnqvist 2015, Segalini et al 2016), but to investigate how the model compared to measured spectra at another site, a validation study with the data from Hornamossen is presented here. Data from the 180 m tower was selected based on the selection criteria described in Chapter 4. The selection included 6 m/s < U_{100} < 8 m/s, stationarity, non-flow distorted and division into stratification bins. In order to facilitate easier reading of the plots a subset of the stratification bins are shown in the figures, including stable, stable near neutral, neutral, unstable near neutral and unstable.

The variables needed to run the model are:

1. The shear $d\bar{u}/dz$
2. The spectral length scale L_s
3. The velocity scale u_τ
4. The Brunt-Vaisala frequency N
5. The ratio of the initial energy of density fluctuations to velocity fluctuations Q_ρ/Q_u.

However, both N and Q_ρ/Q_u can be estimated from the other parameters as shown below.

The shear $d\bar{u}/dz$ was taken directly from the measurements by means of the linear gradient between 80 and 120 m. N was estimated by $N = \sqrt{Ri/(d\bar{u}/dz)^2}$, where Ri, the Richardsson number was taken from

$$Ri = Ri_f \frac{\phi_m}{\phi_h} \tag{8-1}$$

where Ri_f is the flux Richardsson number, taken from the measurements at 100 m and φ_m and φ_h are the Monin Obokhov similarity expression of momentum and heat respectively (Högström 1996).

Length scale of the spectra, L_s, was set to $L_s=\kappa(z-d)$ for all the stability classes. This is done in contrast to the work of Segalini and Arnqvist (2015) and Chougule et al (2017 and 2018) who used length scales that varied with stability. But since the RDT solution does in fact modify the Fourier components by decreasing spectral kinetic energy in stable stratification and increasing it in unstable stratification, there is no need to change the initial isotropic spectral length scale provided that the integration time of the solution is right.

The ratio of the energy in the isotropic velocity spectra to the temperature spectra was hypothesized in Arnqvist and Segalin (2015) to be

$$\left(\frac{Q_\rho}{Q_u}\right)_{\text{est}} = \frac{\beta}{\alpha}\left(\frac{NL_s}{u_\tau}\right)^2 \frac{Ri_f}{1-Ri_f} = \frac{18}{55\alpha_1}\frac{10\beta_1}{6}\left(\frac{NL_s}{u_\tau}\right)^2 \frac{Ri_f}{1-Ri_f} \tag{8-2}$$

where α and β are the Kolmogorov constants for three-dimensional velocity and temperature spectra and α_1 and β_1 are the Kolmogorov constants for one-dimensional spectra evaluated in the longitudinal direction. This number does however reflect the ratio of temperature spectral energy to velocity spectral energy in the final stationary state of turbulence. Since we seek the ratio of the spectral energies in the isotropic state, before the time integration of the RDT solution, this ratio will provide too large values (since the presence of buoyancy will produce additional energy in the temperature spectral component during the time integration). A correction for this fact that give reasonable agreement with the measurements is:

$$\frac{Q_\rho}{Q_u} \approx \left(\frac{Q_\rho}{Q_u}\right)_{\text{est}} (1-|Ri_f|)^2 \tag{8-3}$$

The velocity scale u_τ was taken from

$$u_\tau = (3k + \kappa(z-d)\mathrm{d}\bar{u}/\mathrm{d}z)/4 \tag{8-4}$$

where k is the turbulence kinetic energy of the measurements and the second term is the shear production of the logarithmic (neutral) wind profile. The last term is present due to the fact that the RDT solution will enhance the velocity components in unstable stratification and reduce the velocity components in stable stratification and hence u_τ must always be closer to the neutral value than k. The relative weight of ¼ of the neutral velocity scale was not optimized but gave results that agreed well with the measured spectra over a large range of stratifications.

After the variables u_τ, L_s, N and Q_ρ/Q_u were determined the model was run at 100 m height with the vertical separation of -60, -17.9, 0, 21.9 and 73 m corresponding to the heights in the tower.

Since the model is itself non-dimensional, the spectral densities were made dimensional by multiplication of u_τ for velocity and by $-T_0 u_\tau^2/(gL_s)$ for temperature. The wavenumber k_0 was converted to frequency by $f=k_0\bar{u}/(2\pi)$.

The resulting power spectra are shown in Figure 8-1. The model fits the measured spectra reasonably well both in terms of magnitude and peak frequency for all stratifications apart from the unstable which over predicts the vertical component and thus also the momentum flux.

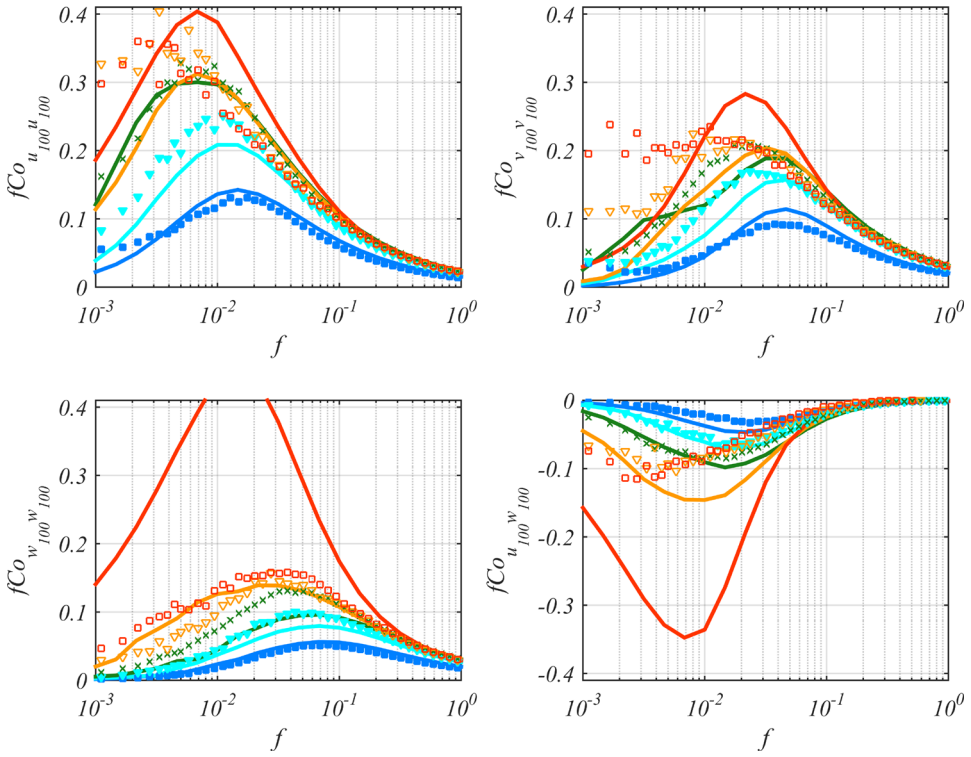

Figure 8-1. Auto spectra and Co spectra from Hornamossen (symbols) and modeled through the Segalini and Arnqvist RDT model (full lines). The markers indicate atmospheric stability from unstable (red) via neutral (green) to stable (blue). See Table 4-1 for the symbols and details of the classes.

One advantage of using an RDT model is that it provides information of the spatial and temporal correlation of the Fourier components. One way of validating the spatial and temporal correlations is through the root coherence

$$Coh_{i,j}(f) = \frac{|C_{i,j}(f)|}{\sqrt{C_{i,i}(f)C_{j,j}(f)}} \quad (8\text{-}5)$$

Where C is the cross spectra of variable i and j, and the phase lag,

$$\Delta\phi_{i,j}(f) = \arctan\frac{\Im C_{i,j}(f)}{\Re C_{i,j}(f)} \quad (8\text{-}6)$$

As the results for small separations are more or less the same for negative and positive separation distances, we here show results only for upward separation.

The prediction of root coherence and phase lag for the heights 100 and 121.9 m can be seen in Figure 8-2 and 8-3, respectively. The coherence is over predicted for almost all stability classes and frequencies, but the tendency with stratification is rather well captured. The phase lag is over predicted for high frequencies, indicating that either the integration time might need to be adjusted or that the wind shear is over predicted, or both.

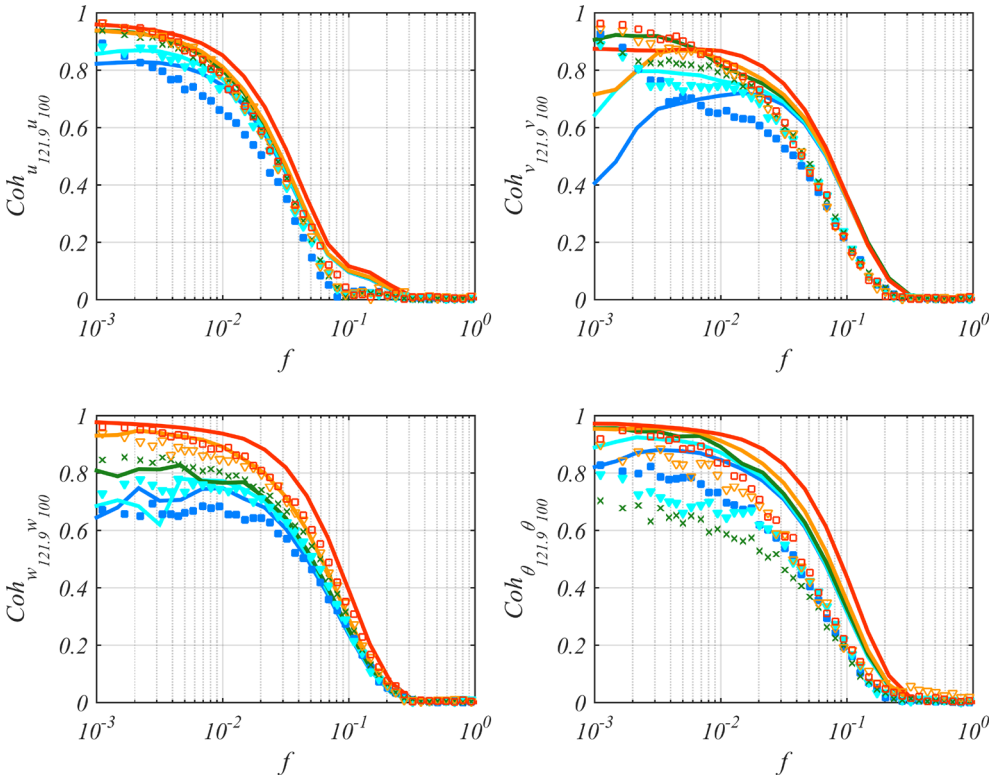

Figure 8-2. Root coherence between 100 and 122 m from measurements (symbols) and predicted by the RDT model (full lines). The symbols indicate atmospheric stability from unstable (red) via neutral (green) to stable (blue). See Table 4-1 for the symbols and details of the classes.

Over large distances, the approximations of the model naturally becomes rather unsuitable, since neither wind shear, variances nor length scale can be said to be constant with height. Despite that, the model still produces coherences and phase shifts that largely agree with the measured values. As with smaller separations, the model overpredicts coherences but the change with stratification is rather well predicted. The fact that in reality the shear is larger in the lower parts of the profile, manifests itself as an underprediction of the phase lag for large negative vertical separations, see the difference between 40 to 100 m and 100 to 173 m in Figures 8-4 and 8-5.

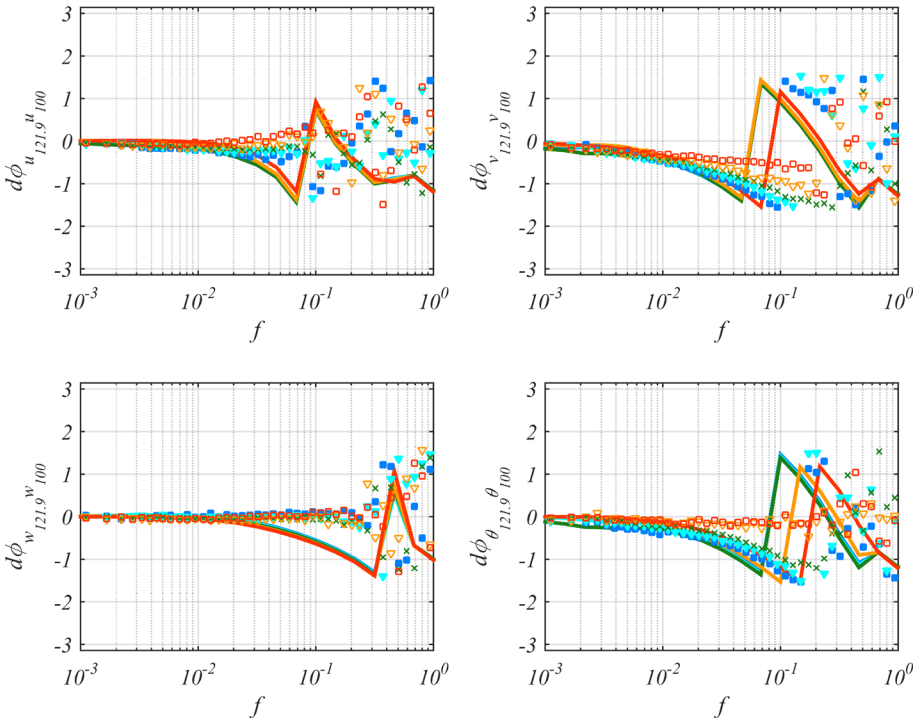

Figure 8-3. Phase lag from measurements (symbols) and predicted by the RDT model (full lines) between 100 and 122 m. The symbols indicate atmospheric stability from unstable (red) via neutral (green) to stable (blue). See Table 4-1 for the symbols and details of the classes.

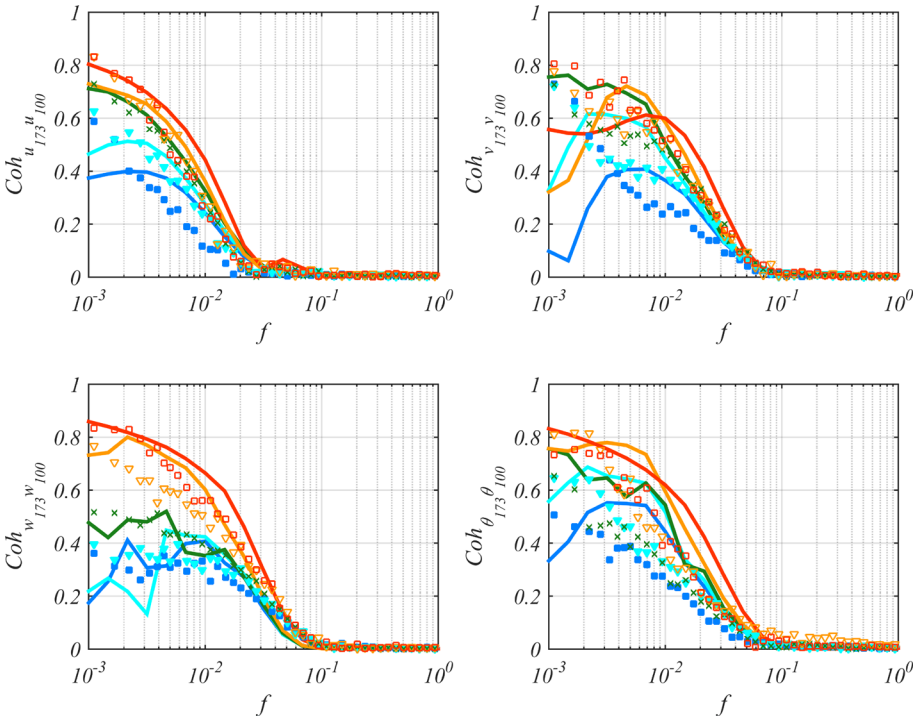

Figure 8-4. Root coherence between 100 and 173 m from measurements (symbols) and predicted by the RDT model (full lines) The symbols indicate atmospheric stability from unstable (red) via neutral (green) to stable (blue). See Table 4-1 for the symbols and details of the classes.

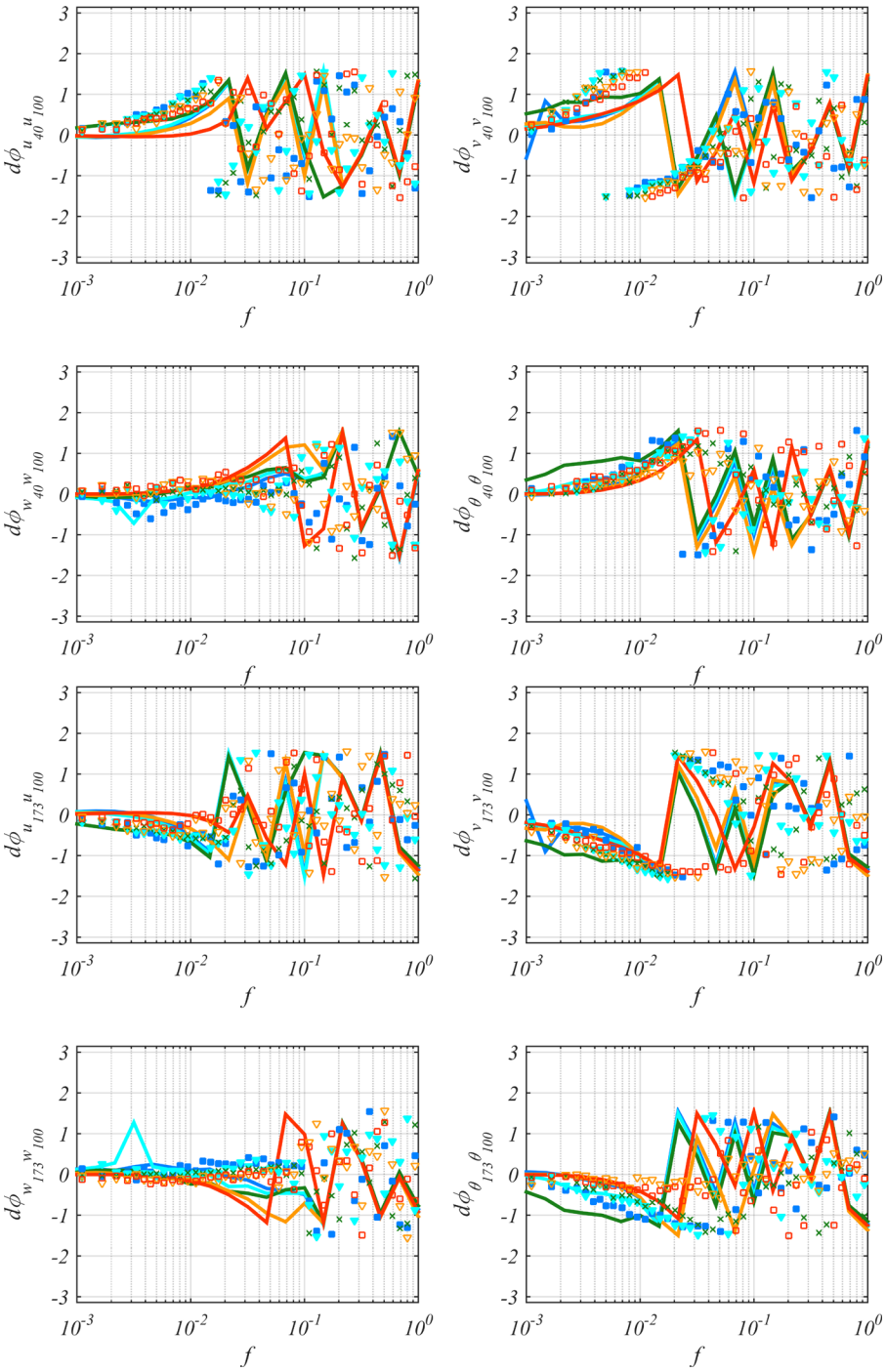

Figure 8-5. Phase lag from measurements (symbols) and predicted by the RDT model (full lines) between 100 and 40 m (upper four panels) and 100 and 173 m (lower four panels). The symbols indicate atmospheric stability from unstable (red) via neutral (green) to stable (blue). See Table 4-1 for the symbols and details of the classes.

8.3 WIND SIMULATION FROM TURBULENCE TENSOR

The generation of time series that have some resemblance with real measured time series is an important branch of fluid dynamics, especially for what concerns numerical simulations that require "realistic" turbulent inflows in order to avoid the simulation of a long domain (to create natural turbulence) or a precursive simulation (namely a simulation where the flow is assumed to be parallel). Synthetic turbulence represents indeed an engineering shortcut to reduce the computational cost since the computational time to generate it is negligible when compared with the cost of running a LES. The standard approach to generate synthetic time series in wind energy from time/spatial spectra was developed by Shinozuka & Jan (1972): given the spectrum in space, $\Phi_{ij}(\boldsymbol{k})$, the estimated time series are obtained from a superposition of sines and cosines with a known amplitude (given by the spectra) for a given wavenumber, $\boldsymbol{k}$, and randomly-distributed phases. Since the signal is obtained as a superposition of waves of different wavelengths, the distribution of the final signal is Gaussian according to the Central Limit Theorem, so that the phases themselves are chosen as Gaussian for the sake of simplicity.

The approach adopted here to simulate synthetic time series is equivalent with the model of Shinozuka & Jan (1972) and Mann (1998), but here it is extended to account for a fourth signal, namely the temperature. The time series of a generic velocity component (u_i with $i=1,2,3$) temperature (indicated as u_4) is given by

$$u_i(\mathbf{x}) = \sum_{\mathbf{k}} e^{i\mathbf{x}\cdot\mathbf{k}} C_{ij}(\mathbf{k}) n_j(\mathbf{k}) \tag{8-7}$$

where $n_j(\boldsymbol{k})$ are random signals (here assumed to follow a standard distribution), while the coefficients $C_{ij}(\boldsymbol{k})$ are computed from the formula

$$C_{ij}(\mathbf{k}) = \frac{(2\pi)^{3/2}}{L_x L_y L_z} A_{ij}(\mathbf{k}) \tag{8-8}$$

ith L_x, L_y, L_z indicating the size of the domain in space, while $A_{ij}(\boldsymbol{k})$ is a Cholesky decomposition of the spectral tensor, so that

$$A^{*T} A = \Phi \tag{8-9}$$

The method is subdivided in two steps. In the first, the spectral tensor is computed from the available parameters (velocity shear, length scale, Brunt-Väisäla frequency, etc.). Then the coefficients $C_{ij}(\boldsymbol{k})$ are calculated from the spectral tensor and 4 independent Guassian random signals are generated for $n_j(\boldsymbol{k})$. The velocity/temperature field is however distributed in space, so that the Taylor hypothesis must be used to convert the x streamwise direction into time. This step provides the highest uncertainty in the approach as Taylor hypothesis is not correct if shear is present, but represents a viable option to obtain synthetic turbulence: this is probably associated to the sudden decay of turbulent fluctuations after the inlet in LES where synthetic-turbulence methods are used.

8.4 WIND SIMULATION FROM CROSS SPECTRA

Turbulent wind velocity inflow in 3 dimensions may also be simulated from a description of cross-spectra. The most common approach is here to generate the time series of wind vector component as independent between the longitudinal, lateral and vertical directions, but it is possible to include also e.g. the uw-correlation.

In section 8.3 it was described how simulated snapshots of turbulent wind velocity in the grid-points of a cartesian domain, can be translated to time series and used as a description of rotor inflow through the use of *Taylor's hypothesis*.

Stochastic wind inflow in 3 dimensions may also be simulated from a model of cross-spectra, an approach that is less numerically efficient but allows for more model tuning using field measurements. The most common approach is here to generate the time series of wind vector components as independent between the longitudinal, lateral and vertical directions, but it is possible to include also e.g. the *uw*-correlation. An outline of the method was originally presented by Shinozuka & Jan (1972), and useful extensions can be found in Veers (1988) and Winkelaar (1991). The synthesis of time histories of longitudinal wind velocity fluctuations can here be formulated as

$$u_j(t) \sim \sqrt{2\Delta_\omega} \sum_{l=1}^{M} \exp\left(i\theta_{jl}\right) \sum_{k=1}^{N} \left|H_{jk}(\omega_l)\right| \exp\left(i\left(\omega_l t + \phi_{kl}\right)\right) \tag{8-10}$$

where N is the number of grid-points in an arbitrary grid layout, M is the number of frequency components included, and phase angles ϕ are independent and uniformly distributed [0,2π]. Typically equation xx is evaluated as a *Discrete Fourier Transform* (DFT). The amplitude filter matrix **H** here satisfies the condition

$$\mathbf{H}\,\mathbf{H}^T = \mathbf{S} \tag{8-11}$$

where **S** is the spectral matrix with entries

$$S_{jk}(\omega) = \int_{-\infty}^{\infty} R_{jk}(\tau) e^{i\omega\tau} d\tau = \int_{-\infty}^{\infty} u_j(t) u_k(t+\tau) e^{i\omega\tau} d\tau \tag{8-12}$$

The spectral matrix is usually decomposed as

$$\left|S_{jk}(\omega)\right| = Coh\left(\omega, U_m, z_m, \Delta_y, \Delta_z\right) \sqrt{S_{jj}(\omega) S_{kk}(\omega)} \ , \ \arg\left(S_{jk}\right) = \theta_{jk} \tag{8-13}$$

where *Coh* denotes the coherence function to be interpreted as the spatial correlation coefficient in frequency space. It is also assumed that U_m is the mean velocity, z_m is the mean height of grid-points j and k, and that the lateral and vertical separation is Δ_y and Δ_z respectively. The phase angle θ in eq (8-10) and (8-13) describes a vertical profile that can be chosen to describe the *eddy slope* typically observed in snapshots of shear turbulence. When using the simulation method described in the previous section, the underlying theory will produce a linear phase profile based on a uniform shear assumption, but here the mean phase can be chosen arbitrarily. Engineering models and observed phase profiles from Hornamossen, will be further discussed in section 8.5.

8.5 SITE SPECIFIC MODEL ADAPTATIONS FOR FORESTED AREAS

In the IEC 61400-1 standard (IEC 2005) there are two options for generating turbulent wind input for load calculations during design or site assessment. The two alternatives basically follow the ideas outlined in sections 8.3 and 8.4 above. In case the chosen simulation model is based on a description of cross-spectra, then there are more possibilities to adapt the turbulence structure to measured site characteristics. The most important part is then here the velocity spectra, which in the IEC 61400-1 standard (Kaimal model) has the form

$$\frac{f\,S_m(f)}{\sigma_m^2} = \frac{4L_m/U}{\left(1+6\,f\,L_m/U\right)^{5/3}} \qquad (8\text{-}14)$$

where index m denotes the velocity component [u,v,w], and the turbulent length scales for modern size turbines is a prescribed as L_u = 340.2 m, L_v = 113.4 m and L_w = 27.7 m respectively. During site assessment the spectra are scaled with characteristic values of component standard deviations σ_m, but the length scales are usually left unchanged. In Figure 8-6 the IEC model (8-14) is compared with measured spectra from Hornamossen at 122 m. In general the model corresponds well with the measurements for neutral and daytime data. During night, when the boundary layer usually is characterized by stable stratification, the length scales of turbulence are significantly smaller (50-65%). It is also seen in Figure 8-6 that for the w component, the IEC length scale is considerably smaller than what is observed in the measurements. This is the case for all stratifications and heights up to 173 m.

Apart from the length scales, the magnitudes of the turbulence in each of the three directions is an important modelling parameter. The ratio of the standard deviations is assumed in the IEC model to be σ_v/σ_u=0.8 and σ_w/σ_u=0.5. The values for both Hornamossen and Ryningsnäs indicate higher values of both ratios. There is also a systematic change with height: σ_v/σ_u is increasing with height for both sites while σ_w/σ_u is decreasing with height. Both sites have the values close to σ_v/σ_u=0.84 and σ_w/σ_u=0.65 at 40 m height and at 100 m height the values are σ_v/σ_u=0.89, σ_v/σ_u=0.88 for Hornamossen and Ryningsnäs respectively while both sites have σ_w/σ_u=0.59 at 100 m. At greater heights both sites seem to indicate a ratio of 1 for longitudinal and lateral components while σ_w/σ_u stays at close to 0.6, with smaller values in stable stratification and larger values in unstable stratification.

It has previously been reported that models for spectral coherence fail to produce a reasonable fit with field measurements when evaluating separations > 10-30 m (Segalini and Arnqvist 2015). Initial processing of the high frequency wind data from Hornamossen immediately verified these assumptions, and different modifications to the engineering models discussed in section 8.5 where explored. A reasonable fit was here achieved by adding a parameter β to the IEC coherence model, thus resulting in

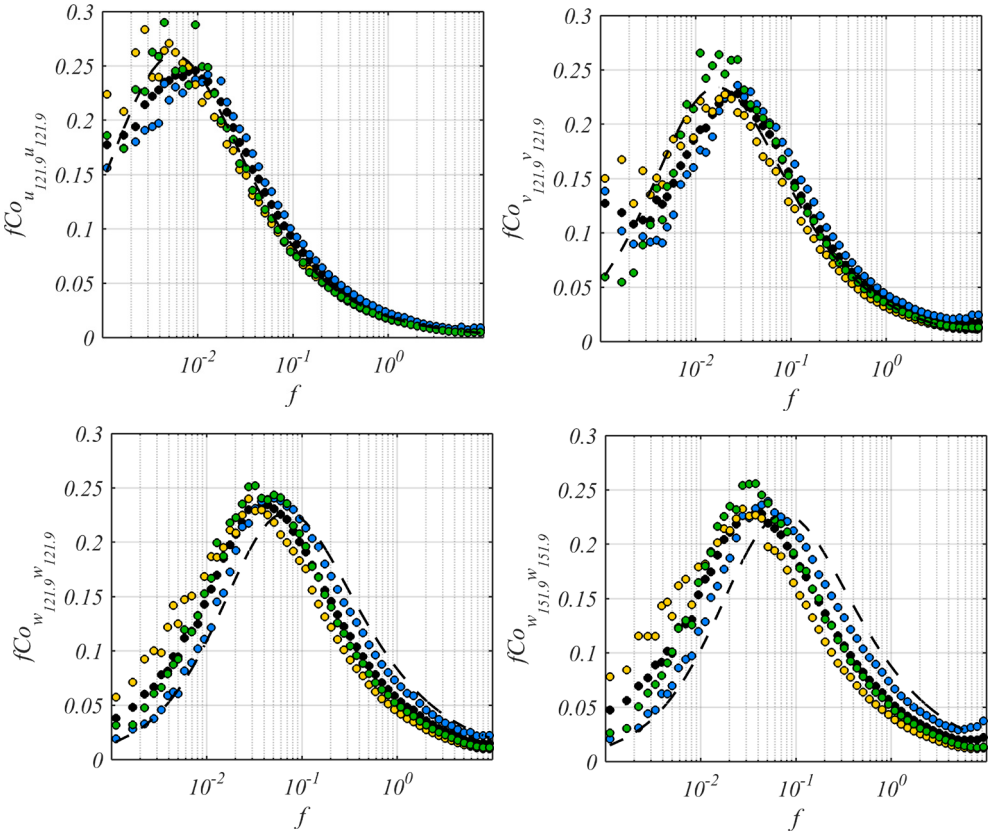

Figure 8-6. Wind velocity spectra at 122 m from Hornamossen for *u*, *v* and *w* components respectively. Dotted lines show the measurements filtered for all conditions (black), night conditions (blue), day conditions (yellow) and strictly neutral conditions (green). The dashed line here represent the IEC spectra with length scales as given above. In the lower right corner w-spectra are shown also for 152 m.

$$Coh_{jk} = \exp\left[-12\left(\left(\frac{r_{jk}^{\beta} f}{U_m}\right)^2 + \left(\frac{0.12\, r_{jk}^{\beta}}{L_c}\right)^2\right)^{1/2}\right] \quad , \quad U_m = \frac{U_j + U_k}{2} \tag{8-15}$$

where the relation between the coherence length scale L_c and the length scale of the longitudinal velocity L_u was kept as in the original form. It was finally decided that choosing $\beta = 1.24$ results in a reasonable fit to Hornamossen data. A comparison between the modified model and measured spectral coherence is shown in Figures 8-7 and 8-8 for a mean wind speed of 7 m/s and 12 m/s, respectively. Here all data was used, and no binning for sectors, stability, daylight etc. was done. It should be noted that for lateral separations, the two-point correlation is not expected to deviate from theory and textbook models to the same extent as for vertical separation.

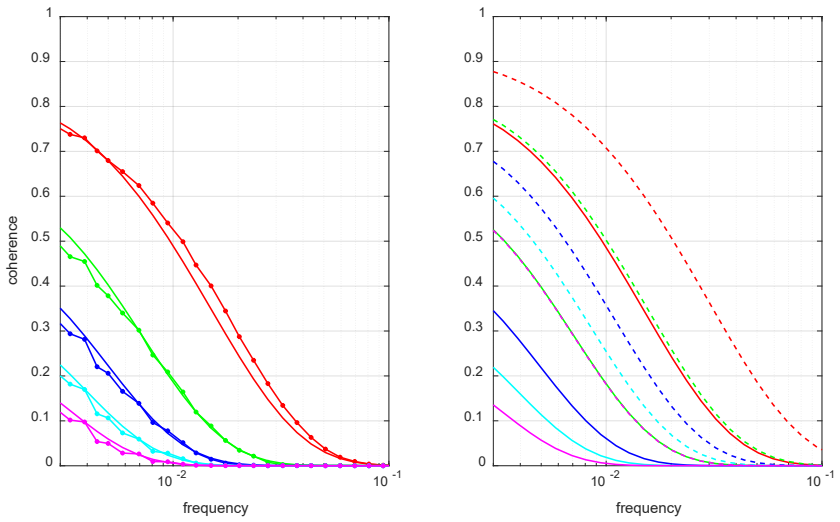

Figure 8-7. Left: Proposed coherence model (dots) fitted to Hornamossen data (solid) for available separations at 7 m/s mean wind speed at 100 m height above ground. Right: New model (solid) compared to the original IEC version (dashed).

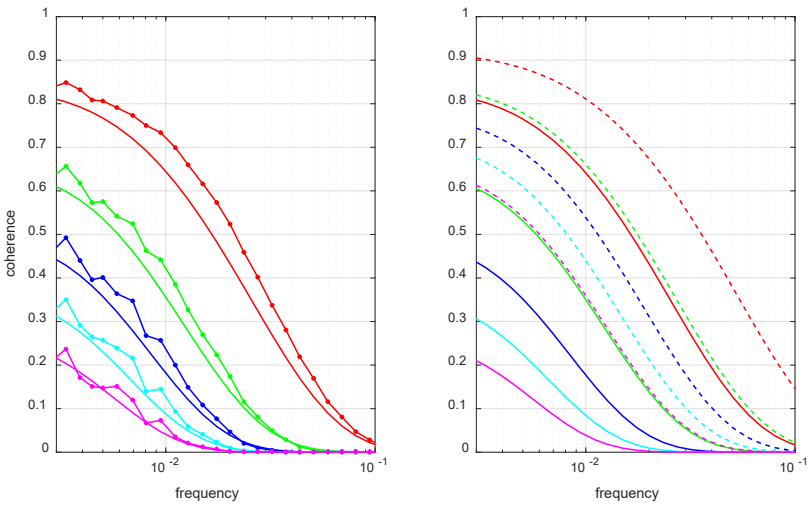

Figure 8-8. Same as Figure 8.7 but for mean wind speed 12 m/s at 100 m height.

As mentioned in section 8.5, the phase profile is seldom included when synthetic turbulence is simulated from cross-spectra. One reason may here be the lack of engineering models in the literature. A model proposed in Panofsky (1984) gives unreasonable results for heights above ≈ 30 m, and in ESDU (1982) the presented relations are somewhat complex to implement in a simulation code. In order to facilitate an investigation of the importance of the phase profile for loads and power production, a modification of the relation in Panofsky (1984) was here fitted to the Hornamossen data in a similar manner as for the spectral coherence. The modified relation for a phase shift between two heights within ≈ 10 - 20 m is given by

$$\Delta\theta\left(f,U_j,U_k,z_j,z_k\right)=K\frac{2\pi f(z_k-z_j)}{(U_k+U_j)(z_k+z_j)}\quad,\quad K=260 \tag{8-16}$$

This form makes it possible to construct a phase profile by successively adding increments from a reference value for the lowest height considered. Phase profiles evaluated from Hornamossen data are compared with the proposed model in Figure 8-9 for 100 m height and mean wind speeds of 8, 9, 10, 11, 12 m/s as well as frequencies of 0.005 and 0.02 Hz.

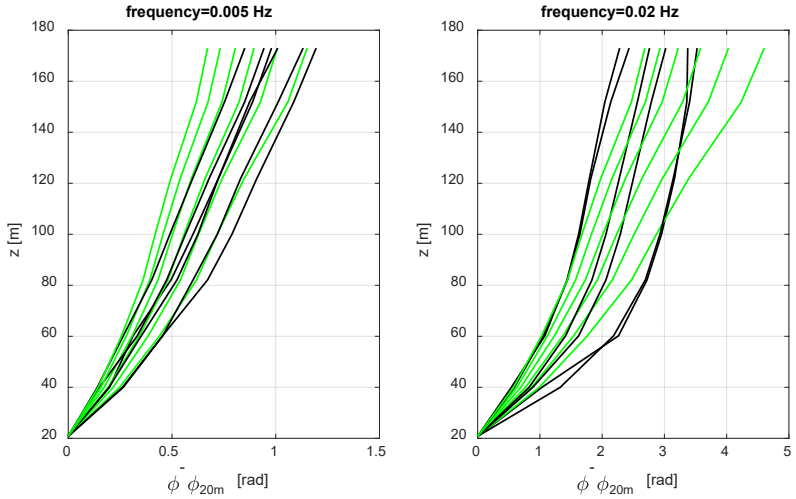

Figure 8-9. Constructed phase profiles from 20 to 173 m. Proposed model (green), and Hornamossen data (black).

An example of a time-space snapshot of simulated turbulent wind speed based on the proposed models above is shown in Figure 8-10. The *eddy slope* is here clearly visible through a time shift from top to bottom.

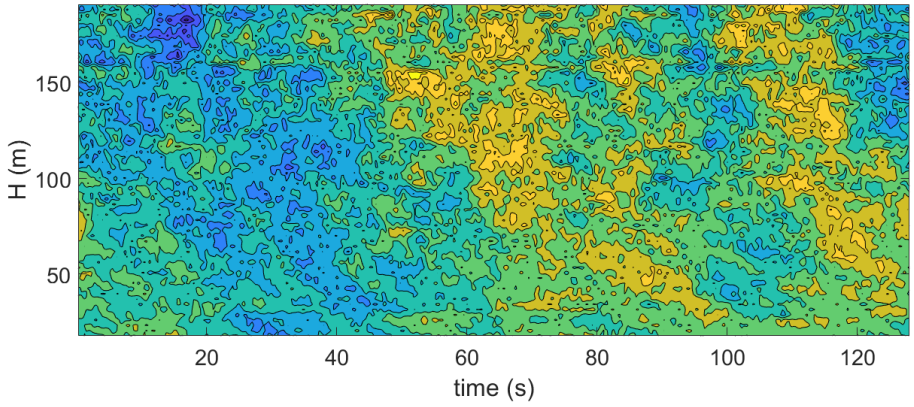

Figure 8-10. Example of a time-space snapshot (contours) of simulated longitudinal wind velocity where the models for coherence and phase proposed in the present study were implemented in a prototype simulation code.

8.6 SUMMARY AND CONCLUSIONS

Based on analysis of wind measurements from the Hornamossen 180 m met-mast, it has been shown how high-resolution site data can be used to describe the turbulence characteristics over the rotor in detail. Improved site-specific wind descriptions will in many cases mean better possibilities for site optimization, and help to reduce uncertainties in the suitability assessment. It was here demonstrated how the spectral models given in the international standard IEC 61400-1 (IEC 2005) can be adjusted to reach reasonable correspondence with measured data. In particular, the problem with the turbulence description within IEC 61400-1 is not foremost a lack of adaptation to forest turbulence but rather the general lack of effects of atmospheric stratification. It has been shown that the models fit the neutral and daytime data from Hornamossen rather well, but during nights and even when considering the average of all the lack of stratification effects in the models become apparent. Due to this it seems like a big step forward to use the model adaptations presented in this chapter for the Kaimal turbulence model and to use the extension of the Mann model published by Segalini and Arnqvist 2015 or the numerical equivalent presented by Chougule (2013) where the effects of stratification are included.

Another conclusion of the work presented in this chapter is the over estimation of the vertical two point coherence, and it would likely be an improvement to use the updated constants presented in chapter 8-5 when modelling turbulence for forested sites in the future.

9 Analysis of airborne laser data

9.1 BACKGROUND

Following technological advancements the mapping of areas with Airborne Laser Scans (ALS) has become a standard procedure. For example, Lantmäteriet scanned the entire Sweden (Lantmäteriet 2018). The data consist of a so called point cloud, which include lidar backscatter points with coordinates x,y and z in a geographical coordinate system. The database of Lantmäteriet (2018) furthermore has labelled the points with classes, determining if the return is from land or water.

The procedure of collecting the data consists of flying the aircraft at a height of around 2000 m and scanning the ground back and forth with the lidar beam. The footprint of the beam is around 0.5 m^2 large when it reaches the ground. The scan is performed in pulses, so that one pulse returns a number of reflections, the first one being of the first order, the second one (from lower height) being the second order, etc. Each reflection is associated with a return intensity, stating how much of the outgoing beam is reflected on the object.

The backscatter from the airborne Lidar can be used to determine the density of the vegetation. The density is often given as PAD, Plant Area Density, which is the frontal area per vertical meter of forest. Another measure is the PAI, Plant Area Index, which is the integrated PAD from the ground to the forest top. Sometimes LAI/LAD (Leaf Area Index/Leaf Area Density) is used, but since the wind is disturbed also by branches, the PAI/PAD notation will be adopted here.

In a pioneering study Boudreault et al. (2015) used airborne laser scans to determine the PAD of the forest and used it as input to a CFD model. Earlier work, Jarvis (1976), Jackson (1981), Raupach (1994) to mention a few, have sought to find a relationship between the density of the forest and the roughness length and displacement height.

The possibility of using remote sensing measurements to determine the roughness length and displacement height has thus emerged, and it is certainly an appealing option for the wind energy community considering the substantial uncertainty that would otherwise be present in determining the roughness and displacement height.

9.2 FROM AIRBORNE LASER SCANS TO PLANT AREA DENSITIES

The method used by Boudreault et al. (2015) is based on examining the number of returns within a certain layer of the canopy as compared to the number of returns from the ground and the vegetation layers below the layer of interest. In order to do so they defined a grid cell and evaluated the number of returns at different heights in the grid cell. The mathematical model is the so-called Beer-Lambert law, first introduced in the field of ALS by Monsi and Saeki (1953)

$$I = I_0 e^{-k\int_{z_1}^{z_2} a(z)\mathrm{d}z} \tag{9-1}$$

which states how much intensity (I) of incoming radiation (I_0) is transmitted through the canopy between layer z_1 and z_2. The extinction coefficient is defined as $k = 0.5/\cos(\theta_l)$, where θ_l is the zenith angle of the lidar (assuming that the leaves are reflecting equally well in all directions). The density of the canopy $a(z)$ is the same as PAD. By reversing the Beer-Lambert law, PAD can be determined as

$$\mathrm{PAD} = -2\cos\theta_l \ln\frac{I_2}{I_1} \tag{9-2}$$

By comparing the number of reflections from each layer the intensity can be determined. In Boudreault et al (2015) that was done by counting the number of first reflections (higher order reflections were omitted) at each level in the grid cell so that

$$I_k = 1 - \sum_{i=1}^{k} r_i/r_0 \tag{9-3}$$

where r_i is the number of (first order) reflections of a particular layer and r_0 is the total number of (first order) reflections inside the grid cell and the summation is from the canopy top, i=1, to the k^{th} level.

Hopkinson et al. (2007) proposed that instead of using only the first reflection one can take into account also the higher order reflections by summing the return intensity, *RI*, from all reflections (both first and higher order) within a certain layer, giving

$$I_k = 1 - \sum_{i=1}^{k} RI_k/RI_t \tag{9-4}$$

A problem with using the method of Boudreault et al (2015) is that if the canopy density is high compared to the scanning density, no first order reflections from the ground may be recorded and the routine gives infinite density for all the layers below the lowermost first order reflection. That problem is mostly solved when instead using also the higher order reflections since the probability of some part of the laser beam reaching the ground is much higher than the probability of the entire laser beam reaching the ground without being intercepted. A drawback of the method is that it assumes that the intensities of all the pulses within a grid box can be put together. This may give problems when the grid cell contains a forest edge, since the reflections from the part of the cell that does not contain forest will have a very high *RI* leading to an underestimation of the PAD.

To overcome the problems of the two methods described above, a routine was developed that sums the intensity of the individual pulse and scales the return intensity of a specific reflection with the total return intensity from that pulse. In that way, a weak return from a single pine needle, for instance, will be less important than a strong return from a branch. After this scaling is performed on the reflections of every single pulse, the scaled returns can be summed up like in Boudreault et al (2015), but now including the higher order returns, which can be written

$$I_k = 1 - \sum_{i=1}^{k} r_{s_k}/r_{s_0} \tag{9-5}$$

where the s subscript indicates that the reflection has been scaled with the total reflection of its pulse. Depending on the brand and version of the scanning device, the number of reflections may be limited, and in the case where only one reflection is reported the method would give the same results as in Boudreault et al (2015).

In a M.Sc thesis Freier (2017) tested all three of the above methods and found that the individually scaled one gives values of the PAD that lie between the estimates of the Hopkinson(2007) method, which gives the lowest estimates, and the Boudreault et al. routine that gives the highest PAD estimates.

In the following work, the method of individual pulse scaling has been used, if not otherwise mentioned.

The ground height has been determined in each grid cell as the median of the returns classified as ground in the grid cell. The tree height in a grid cell has been determined as the highest reflection minus the ground height and thus represents the tallest trees in each cell.

9.3 FROM PLANT AREA DENSITIES TO ROUGHNESS AND DISPLACEMENT

Even though some flow models have successfully implemented forest drag by directly using the forest densities, the vast majority of models still rely on displacement height and roughness length to model the effect of the forest.

The literature is rich in attempts of calculating these parameters from the forest densities, with contributions from Inue (1963), Jackson (1981), Raupach (1994) being some of the more cited. Often the calculations are based on matching a logarithmic layer above the forest to an exponential layer within the forest. By such a procedure, Raupach (1994) reached the following expressions:

$$\frac{d}{h} = 1 - \frac{1 - \exp(-\sqrt{c_{d_1}\Lambda})}{\sqrt{2c_{d_1}\Lambda)}} \tag{9-6}$$

where c_{d_1} is a constant with value 7.5 and Λ is 2 times the PAI,

$$\frac{z_0}{h} = \left(1 - \frac{d}{h}\right) \exp(-\kappa \bar{u}_h/u_* - \Psi_h) \tag{9-7}$$

where the subscript h denotes the canopy top and Ψ_h is a correction factor for the roughness sublayer effect. Raupach (1994) recommended using $u_h/\ u_*$=0.3 and Ψ_h=0.193.

The expressions do however include some tuning constants, which leave room for uncertainty in the application to any given forest. An attempt to improve on this is put forward below. The derivations of Inoue (1963) and Jackson (1981) are combined, which leads to new expressions for z_0 and d.

The basic assumption is that the forest drag can be modelled by introducing a drag coefficient (where u = mean wind speed in x direction) as

$$\frac{\partial \tau}{\partial z} = \rho C_d a u^2 \tag{9-8}$$

where τ is the shear stress, a is a constant and C_d is the drag coefficient and ρ the density of air. Furthermore the shear stress is modelled through a mixing length l_m

$$\tau = \rho l_m^2 \frac{\partial u}{\partial z}\left|\frac{\partial u}{\partial z}\right| \tag{9-9}$$

We assume that the shape of the wind profile within the forest is

$$u = u_h e^{\alpha(z/h-1)} \tag{9-10}$$

where α is a constant related to the forest density and subscript h indicates the value at the height of the forest top, h. Combining the above expressions with the (large) approximation that C_d and a are constant with height yields

$$\alpha = \sqrt[3]{\frac{C_d a h^3}{2 l_m^2}} \tag{9-11}$$

which is the result of Inoue (1963). Thom (1971) hypothesized that the displacement height is equal to the centroid of the momentum absorption by the canopy, and this was later put in a theoretical foundation by Jackson (1981). Thus,

$$d = \frac{1}{\tau_h}\int_0^h (\tau_h - \tau) dz \tag{9-12}$$

Combining this with the shear stress profile one gets from integrating Equation (9-8) with the expression of u from Equation (9-10)

$$d = \frac{1}{\tau_h}\int_0^h (\tau_h - \frac{h C_d a u^2}{2\alpha} e^{2\alpha(z/h-1)}) dz \tag{9-13}$$

which simplifies to

$$d = h\left(1 - \frac{1 - e^{-2\alpha}}{2\alpha}\right) \tag{9-14}$$

To close the equation for d one needs to assume the mixing length at the canopy top. Inoue (1963) assumed that the mixing length was $\kappa(h\text{-}d)$. Arnqvist and Bergström (2014) also found support for $\kappa(h\text{-}d)$, and if that holds, Equations (9-13) and (9-14) can be combined to give

$$2Ax^{1/3} = 1 - e^{-2Ax^{2/3}} \tag{9-15}$$

where $A = \sqrt[3]{\frac{hC_d a}{2\kappa^2}}$ and $x = h/(h-d)$. Equation (9-15) does not have a straight forward solution and has to be solved iteratively, but the expression

$$d \approx \left(\frac{1}{4h^2 a} + \frac{1}{h}\right)^{-1} \tag{9-16}$$

is a good approximation. The value of z_0 is found by merging the solution within the forest to the solution in the logarithmic layer, giving

$$z_0 = (h-d)e^{-\left|\frac{\kappa h}{\alpha l_m}\right|} \tag{9-17}$$

An approximation for dense forests may be found by observing that the exponent in Equation (9-17) goes to zero for large α (dense forests), and the equation simplifies to

$$d \approx h\left(1 - \frac{1}{2\alpha}\right) \tag{9-18}$$

which can be used to close Equation (9-11), giving

$$d \approx h\left(1 - \frac{\kappa^2}{4C_d a h}\right) \tag{9-19}$$

while requiring $d > 0$, and

$$z_0 \approx (h-d)e^{-2} \tag{9-20}$$

Equations (9-14) and (9-17), as well as the approximations (9-19) and (9-20) give means of estimating z_0 and d as function of the leaf area density only using previously well-defined constants C_d and κ. Still, they require matching a wind profile within the trees to a wind profile above the trees, even though the constants themselves, z_0 and d only apply to the wind profile above the trees. Furthermore the derivation requires a (the PAD) to be constant in the whole canopy, something that is not true for real forests. It would thus be attractive to estimate z_0 and d from the forest density wind profile above the trees only. While we have not found such a derivation, from dimensional grounds one may argue that the appropriate length scale for the roughness length must include the forest density, and not the tree height, but rather h-d which is the effective distance that the upper wind profile is subjected to drag. Such a length scale is

$$l_d = (h-d)\int_d^h a \mathrm{d}z \tag{9-21}$$

which connects the length scale of the upper wind profile, h-d, to the integrated frontal area of that length scale. In the simple case where a is constant and there is a proportionality constant, C_l, between l_d and z_0 the expression simplifies to

$$z_0 = C_l l_d = C_l (h-d)^2 a \tag{9-22}$$

With these assumptions there is a simple relation between z_0, d and a, which can be found by dividing the wind speed and the wind shear in the logarithmic layer

$$\frac{u}{\frac{\partial u}{\partial z}} = \ln\left(\frac{z-d}{z_0}\right)(z-d) \tag{9-23}$$

At the forest top, the vorticity thickness $u/(\partial u/\partial z)$, can be set equal to $2\,(h\text{-}d)$, as shown in Arnqvist and Bergström (2014). Inserting that in Equation (9-23) together with Equation (9-22) gives

$$d = h\left(1 - \frac{e^{-2}}{C_1 a h}\right) \tag{9-24}$$

It can be seen that, for low densities, d will become negative. Hence, it is appropriate to require $d > 0$.

The three pairs of equations, Equations (9-6) and (9-7) (from Raupach 1994), Equations (9-14) and (9-17) (from the centroid method), as well as Equations (9-22) and (9-24) (from PAI formulations) are shown in Figures 9-1 and 9-2. As can be seen the values of Raupach (1994) are much higher for the roughness length, which in large part is due to including roughness sublayer effects. In order to adjust for roughness sublayer effects, a version of the centroid method, and the PAI method where l_m was modified to $l_m = 0.6(h\text{-}d)$ instead of $l_m = \kappa(h\text{-}d)$ is also shown. Interesting to note is also that all the methods are functions of PAI and not h, which means that the density per vertical meter is not affecting z_0 and d, but rather the total integrated density from ground to h, the PAI. This means that, as long as the PAI is the same, the roughness length and displacement height will be the same independent of the forest height (e.g. the trees could be 30 m high or 0.3 m high). In spite of this, constant values of $d=0.75h$ and $z_0=0.1h$ are often used for real forest.

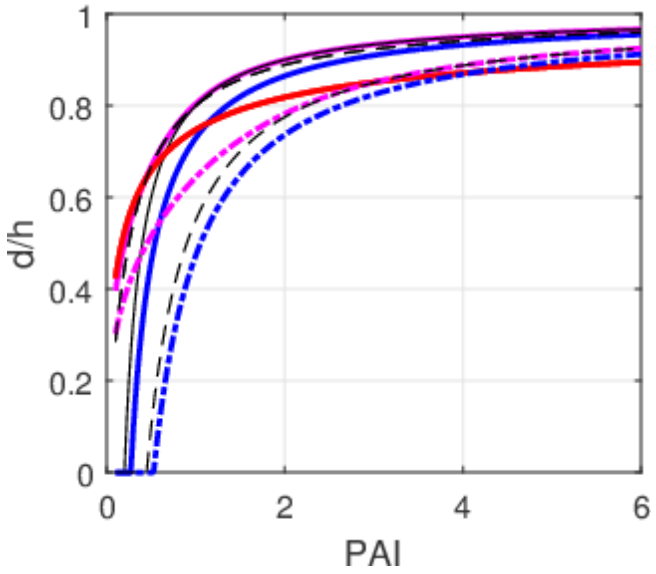

Figure 9-1. Displacement height normalized with tree height as a function of PAI. Red curve from Raupach (1994), Purple curves from the centroid method, Equation (9-17) and blue curves from the PAI method, Equation (9-22). The black thin lines are the approximations of Equation (9-16) and Equation (9-19). For the centroid and the PAI method, dash-dotted lines show the roughness sublayer correction l_m=0.6(h-d) while the full lines are made with l_m=κ(h-d).

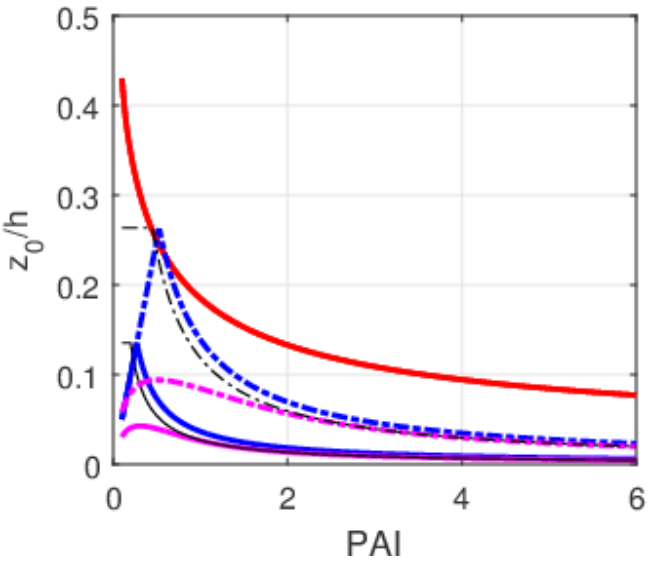

Figure 9-2. Roughness length normalized with the tree height as a function of the PAI. Red curve from Raupach (1994), Purple curves from the centroid method, Equation (9-17) and blue curves from the PAI method, Equation (9-22). The black thin lines are from the approximation Equation (9-20). For the centroid and the PAI method, dash-dotted lines show the roughness sublayer correction $l_m=0.6(h-d)$ while the full lines are made with $l_m=\kappa(h-d)$.

In Figures 9-3 and 9-4 the resulting logarithmic wind profiles from Ryningsnäs and Hornamossen are shown respectively. The curves were made using the Raupach (1994) method, the centroid method (Equation 9-17) and the PAI method (Equation 9-22) with $C_l=0.5$. Measurements are taken from strictly neutral conditions. Also included is the wind profile assuming $d=0.75h$ and $z_0=0.1h$. It should be noted that Hornamossen is placed on a hill, so speed-up effects could influence the shape of the wind profile.

Aggregating roughness is still very much an open question and hence the curves were produced in two different ways:

1. By averaging the PAI within 15 km, $\overline{PAI}$, and calculating z_0 and d based on the curves in Figures 9-1 and 9-2.
2. By calculating $\overline{z_0}$ and $\overline{d}$ by making separate estimates of z_0 and d for each 10x10 m PAI grid box within 15 km for z_0 and 0.2 km for d, and performing the averaging.

The values of z_0 and d can be seen in Table 1.

As seen in Figures 9-3 and 9-4 the wind profiles without roughness sublayer effects are overestimating the wind speed for both sites, and hence it seems necessary to include roughness sublayer effects. As the forests for both sites are very patchy, see Figure 9-5, the effective roughness is expected to be influenced to a large degree by forest edges. As has been shown (Silva Lopes et al. 2015) clearings often contribute to a higher effective roughness and since the above expressions apply for homogenous forests an overestimation of the wind speed is expected.

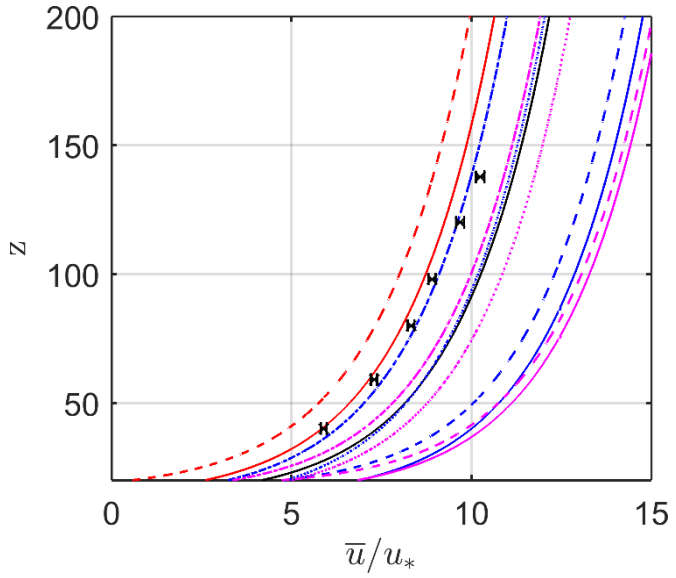

Figure 9-3. Logarithmic wind profiles from Ryningsnäs. Red curve from Raupach (1994), Purple curves from the centroid method, Equation (9-17), and blue curves from the PAI method, Equation (9-22). Full lines are made by calculating z_0 and d for each grid cell within 15 km and 0.2 km respectively and then applying an arithmetic mean giving $\overline{z_0}$ and $\overline{d}$. The dotted lines are also from $\overline{z_0}$ and $\overline{d}$ but with the roughness sublayer correction l_m=0.6(h-d). The dashed lines are made from $\overline{PAI}$ within 15 km, as well as the dash-dotted, which are made with the roughness sublayer correction $\overline{z_0}$ and $\overline{d}$. The black full line is made from $\overline{h}$ within 0.2 km for d and 15 km for z_0. The measurements for neutral conditions are shown in black x with the error bars showing 95 % confidence levels.

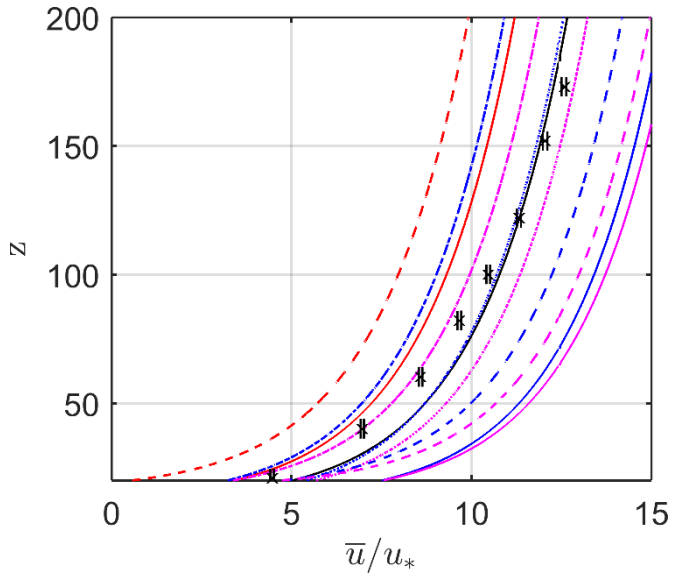

Figure 9-4. Same as in Figure 9-3, but for Hornamossen.

If the flow model cannot handle high resolution PAI data, one has to make the choice of whether to average the PAI or the roughness lengths. Based on the results shown here, Raupach (1994) underestimates the wind speed when the average PAI is used. The centroid method seems to give reasonable estimates for the averaged PAI and could hence be a good method if the resolution is low, if the forest is very homogenous or if the averaging is done on PAI, provided that roughness sublayer effects are considered.

Despite the uncertainties involved in estimating roughness and displacement from ALS data, work done partly within this project showed that even by using the simple relations $d = 0.75h$ and $z_0 = 0.1h$ an improvement is seen from using high resolution data (Floors et al. 2018).

Table 9-1. Roughness lengths and displacement heights calculated from PAI for Ryningsnäs and Hornamossen. The calculations are based on arithmetic averages within 15 km for z_0 and 0.2 km for *d*. The average PAI within 15 km was 1.22 for Ryningsnäs and 1.19 for Hornamossen. The calculations are based on a forest height of *h=20* m for both sites.

	Ryningsnäs z_0	**Ryningsnäs *d***	**Hornamossen z_0**	**Hornamossen *d***
From $\bar{h}$	1.19 (=0.1$\bar{h}$)	11.1(=0.75$\bar{h}$)	1.44 (=0.1$\bar{h}$)	12.3 (=0.75$\bar{h}$)
$\overline{PAI}$ Raupach (1994)	3.43	15.7	3.48	15.5
$\overline{PAI}$ Centroid	0.45	17.0	0.46	16.9
$\overline{PAI}$ PAI-method	0.61	15.8	0.63	15.7
$\overline{PAI}$ Centroid, l_m=0.6(*h*-*d*)	1.58	13.9	1.61	13.8
$\overline{PAI}$ PAI-method, l_m=0.6(*h*-*d*)	2.32	11.6	2.40	11.3
$\bar{z_0}$ and $\bar{d}$ Raupach (1994)	2.66	12.5	2.13	11.6
$\bar{z_0}$ and $\bar{d}$ Centroid	0.79	13.4	0.69	12.6
$\bar{z_0}$ and $\bar{d}$ PAI-method	0.51	12.0	0.41	11.6
$\bar{z_0}$ and $\bar{d}$ Centroid, l_m=0.6(*h*-*d*)	1.15	11.5	0.95	10.7
$\bar{z_0}$ and $\bar{d}$ PAI-method, l_m=0.6(*h*-*d*)	1.54	9.2	1.26	9.0

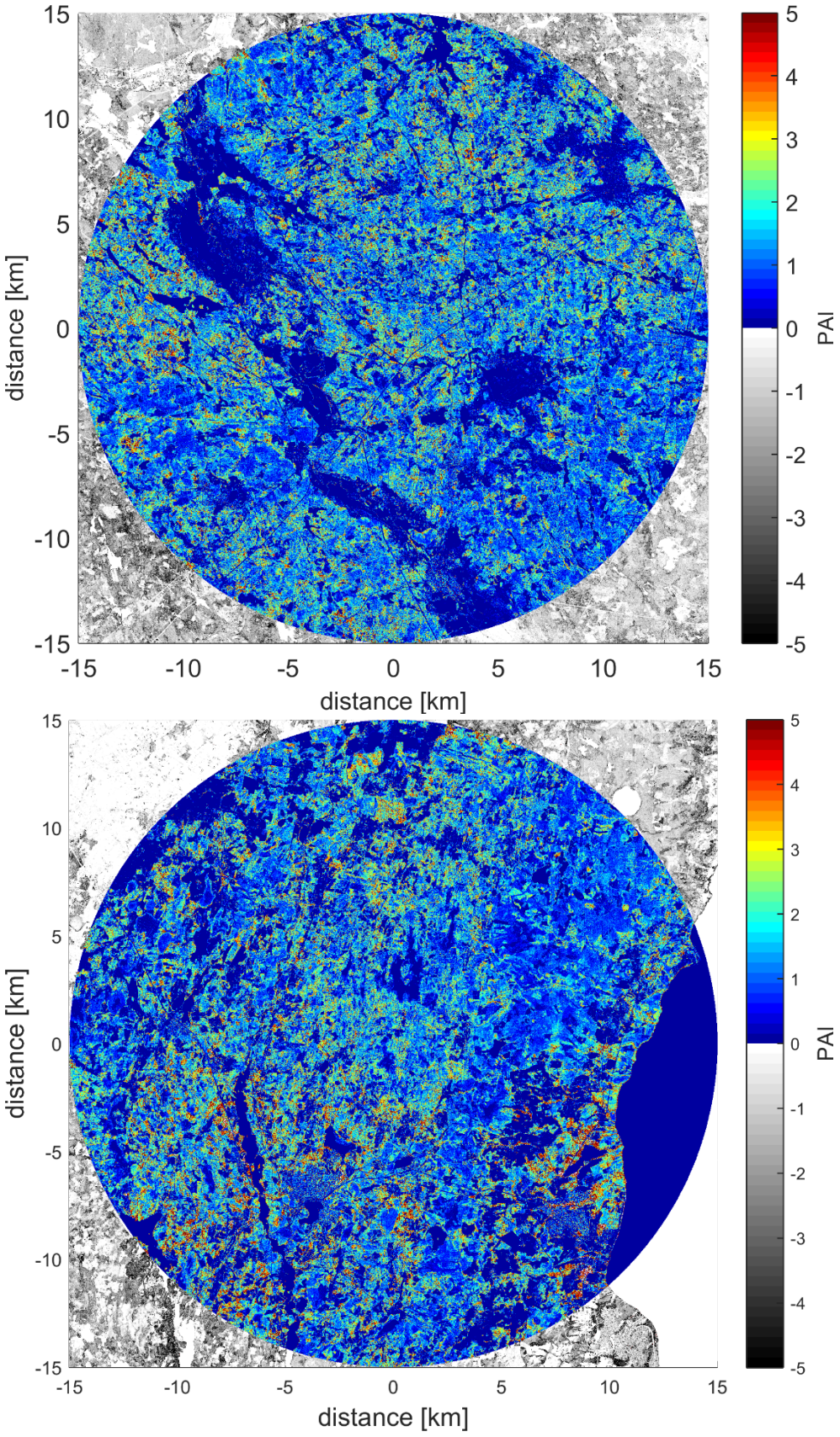

Figure 9-5. PAI from Ryningsnäs (top) and Hornamossen (bottom). The areas within 15 km of the measurement towers have been colored.

9.4 OVERVIEW OF DATASETS

Extensive work on the topic of comparing performance of different data sets compared to ALS data was done within the project and the study was published in Wind Energy Science Discussion (Floors et al. 2018). The main conclusion was that even though the flow model (WAsP) did not use much of the detail of the roughness maps, the better representation and more realistic values provided by ALS still made an improvement compared to using CORINE Global Land Cover Classification (GLCC), Modis Vegetation Continuous Field and ESA GLOBCOVER as implemented into WindPro software. The study showed a 50% reduction in the risk of making errors of power production larger than 25% but also a general improvement on the average power production estimate.

A data set missing from Floors et al (2018) is the data set of Skogsstyrelsen, consisting of forest metrics. It is also based on ALS but is updated with forest management as opposed to the ALS data from Lantmäteriet that is a single scan. The Skogsstyrelsen data set with 12.5 m x 12.5 m resolution consists of average forest heights and densities in the form of volume, stem diameter and biomass.

The forest height from Skogsstyrelsen is averaged forest height within the grid box, as opposed to the forest height used in Floors et al (2018) as well as herein. By comparing the forest heights in a 40 x 40 km area surrounding the Hornamossen tower, a conversion factor of 1.049 is recommended. That is, the forest heights from Skogsstyrelsen should be increased with 4.9% in order to be comparable to the ones used in Floors et al (2018).

When it comes to forest densities the most promising is using the biomass, since the other volumetric is based on the brown wood content, or stems, and as such much of the surface area of leaves and branches may be missed. A conversion factor between the PAI from ALS and the biomass from Skogsstyrelsen was found to be 0.0172. That conversion includes the conversion from ha to m^2 and from density to surface area. PAI from ALS as compared to PAI from biomass can be seen in
Figure 9-6.

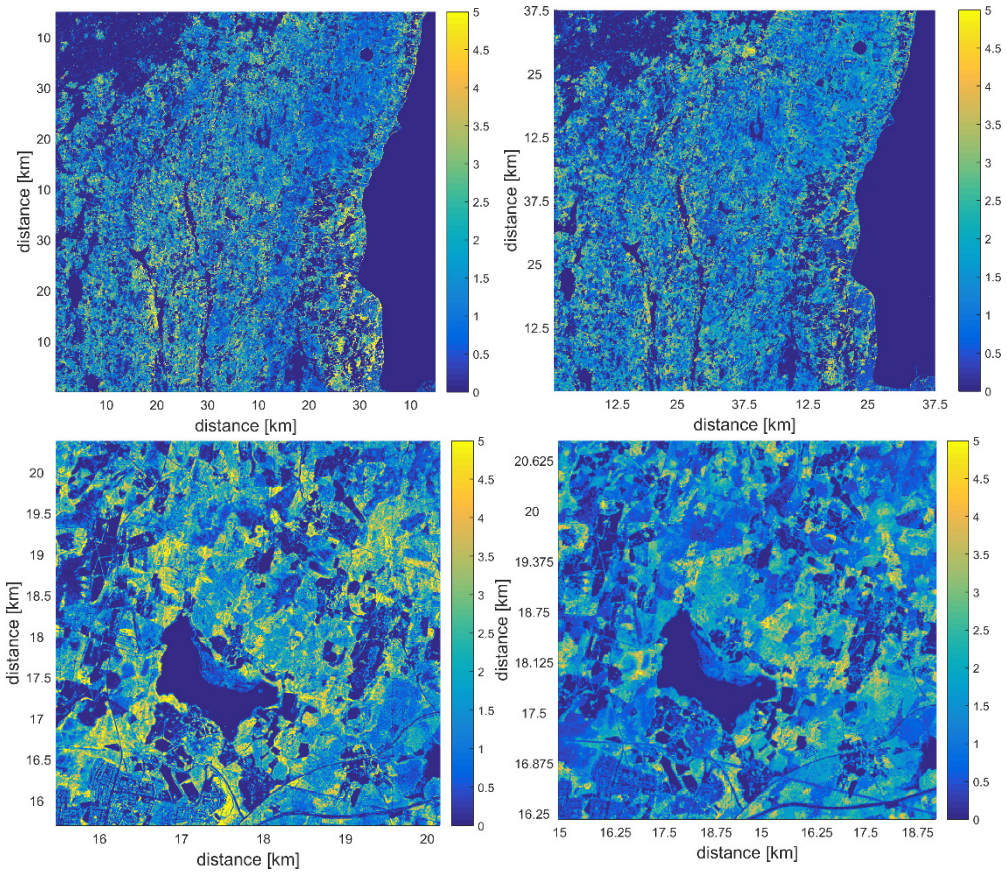

Figure 9-6. PAI from ALS, left panel and from biomass from Skogsstyrelsen, right panel. A conversion of 0.0172 was used on the original biomass values from Skogsstyrelsen. Lower figures show zoomed-in images of upper figures.

9.5 SUMMARY AND CONCLUSIONS

The chapter includes a description of three methods to derive forest densities from airborne laser scans. Two of the methods already existed and one of the methods was developed within the project to improve the two earlier methods. The improvement is that the backscatter intensity of each laser pulse is being taken into account, which improves the estimate around forest heterogeneities and in very dense forests.

Several methods of converting forest densities into roughness length and displacement height has been described. Two of the formulations are new. It was found that roughness sublayer effects are important to find estimates that agree with the measured wind profiles from Ryningsnäs and Hornamossen. To summarize the results, the method of Raupach (1994) works best when the estimation of roughness and displacement is made on a fine grid and subsequently averaged, while for the other methods it was better to first average the forest densities and then compute the roughness and displacement from the average forest density. It was found that a suitable roughness sublayer correction is to increase the length scale at the forest top from 0.4(h-d) to 0.6(h-d). Approximations to the newly developed models were derived which conform to the exact expressions for medium and high forest densities and since they represent a

simplification leading up to single equations for both roughness and displacement. The new models should be an attractive option for calculation based on the forest density.

Work within the project on this topic also includes the publication of Floors et al (2018) which is described in the chapter. The main conclusion from that work was that using the WAsP simulation tool, surface data fields from ALS improved the estimation compared to standard surface data sets and minimized the risk of making large prediction errors. Here, roughness length was calculated as 0.1h and displacement as 0.75h which seemed to give reasonable estimates, but omits the effect forest density has on the parameters.

Finally, forest heights and PAI from ALS, using the newly developed model, were compared to estimates of forest height and volume from Skogsstyrelsen, which is freely available. It was concluded that the forest heights are very similar from the two methods, with the forest heights from Skogsstyrelsen being 5% lower. The best estimation of forest density was found using the biomass from Skogsstyrelsen, which gave, on average, the same PAI as the new ALS method when multiplied with a conversion factor 0.0172.

Since the data from Skogsstyrelsen are freely available, continuously updated, of high spatial resolution and correlates well with the estimates derived directly from ALS it is recommended for use when estimating the wind resource at a site.

If the method presented in Floors et al. (2018) is used, the conversion factor for forest height is 1.049. A further improvement may be to take into account the PAI which is found by multiplying the biomass by 0.0172 and using the simplified PAI-based methods to derive roughness and displacement (including roughness sublayer effects): $d=h(1-2e^{-2(0.4/0.6)}/PAI)$ and $z_o=0.5(h-d)^2PAI/h$. It should be noted though, that the possible improvements of using a density based approach have not yet fully been investigated.

10 Forest effects on power production

Manufacturers, developers and owners want to ensure that the wind turbine power curve is met during real conditions. This is done through power performance measurements and power curve certifications. Power curves are usually also warranted by the manufacturer given that certain conditions at the site are met (e.g. wind shear exponent and turbulence intensity in a certain range).

The power of a wind turbine is calculated as

$$P = \frac{1}{2} \cdot c_p \cdot A \cdot \rho \cdot U^3 \tag{10-1}$$

where U is the horizontal wind speed at hub height (averaged over 10 minutes), A is the rotor swept area, ρ is the air density at hub height (averaged over 10 minutes) and c_p is the turbine-specific power coefficient, which is a function of U.

Air density has a considerable effect on power production. Therefore, wind turbine output power has to be corrected for actual density when carrying out power performance studies. According to IEC (2017), air density normalisation should be applied to the wind speed at hub height using

$$U_{norm} = U \cdot \left(\frac{\rho}{\rho_0}\right)^{1/3} \tag{10-2}$$

where U_{norm} is the normalised wind speed after the density correction. As reference density ρ_0= 1.225 kg/m^3 is used.

Power curves depend on the hardware and software of the turbine as well as on the climatic conditions experienced by the turbine, i.e.

- wind speed
- air density
- vertical wind shear
- vertical wind veer
- turbulence intensity (*TI*)
- inflow angle

(e.g. Tüxen, 2014; Ormel, 2015). Also, wind direction standard deviation is a very important factor influencing power curve variations (Clerc, 2013). However, wind direction standard deviation is highly correlated to *TI* (Clerc found R = 0.77 for one site, whereas the Östergötland site studied herein yields R = 0.66). Therfore, Clerc argued that the inclusion of *TI* as a factor influencing power curve variations is enough. In complex terrain inflow angle should be measured as power curves are not warranted for large inflow angles (e.g. Højstrup 2014).

Hence, the Power Curve Working Group (https://pcwg.org/) identified the six factors from the list above as main influencing factors on wind turbine power output (Figure 10-1). In addition to these factors, rotor aerodynamics and controller behaviour are important (Baylis et al. 2014).

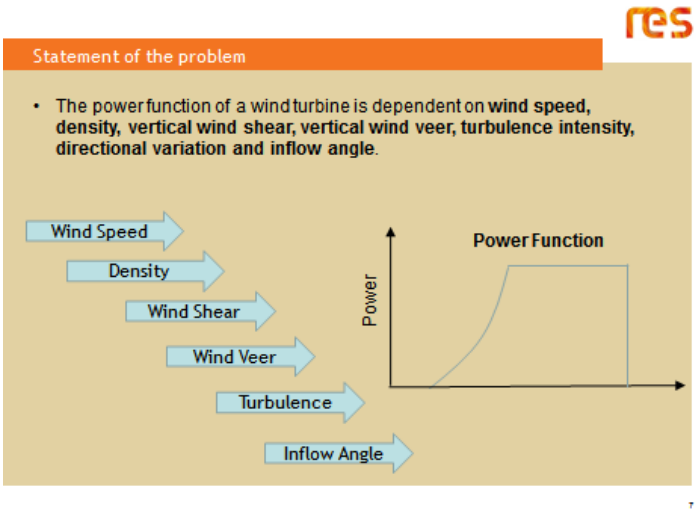

Figure 10-1: Dependence of wind turbine power curve on external factors. Power curve shown in figure is typical for laminar flow. Over forest, wind shear and veer as well as turbulence are enhanced. Figure adopted from Stuart (2014b).

Several authors claim that, in real world conditions, turbines generally underperform between about 0% and 4% compared to the warranted, or sales, power curve (e.g. Geer 2015, Bernadett 2016). Bernadett (2016) suggested that power curves are the primary reason that actual performance falls below predicted levels, therefore advocating site-specific power curve loss adjustments. (If there is insufficient information on the turbine model or on the site, Bernadett proposes a standard loss factor of 2.4%, corresponding to average historical underperformance.) Also, he recommended calculating AEP using both advertised and measured power curves. Moreover, he claimed that prototype turbines produce 0.6% more, on average, than production turbines.

In the following, factors that could influence wind turbine power curves in forests are summarised and power output of one wind farm in forest is investigated.

10.1 SUMMARY OF NEW IEC STANDARD FOR POWER PERFORMANCE

Wind turbine power performance is determined by measured power curves and estimated annual energy production (AEP). The measured power curve is defined as the relationship between the wind speed and the wind turbine power output (usually obtained at coastal wind turbine test sites in Denmark, Germany or the Netherlands with relatively low turbulence intensity, i.e. *TI* of order of 10%).

The new IEC standard (IEC, 2017) states: "Measured power curves are obtained from simultaneous measurements of meteorological variables (wind speed, direction, pressure, temperature & humidity) at one or several levels, as well as wind power output during a long enough period to represent different wind regimes and atmospheric stabilities."

The new IEC standard for power performance testing (IEC, 2017) describes methods to correct wind turbine power curves for the effects of

- wind shear
- wind veer
- turbulence

It is well known from boundary-layer meteorology that these phenomena are either correlated or inversely correlated with each other.

Both wind shear and veer are included in the Rotor-Equivalent Wind Speed (REWS) – see description below. For turbulence, a turbulence renormalisation method is suggested in the IEC standard (IEC, 2017, Appendix M). The standard claims that it doesn't matter which correction is carried out first.

Wind turbine power output has to be corrected for actual density using Equation (10-2). Air density also varies over the height of the rotor. However, this variation is small and the use of air density only at hub height should be sufficient. If humidity is not measured, a relative humdity of 50% should be used for density calculations at all times (IEC, 2017).

The standard further recommends that hub height wind speed measurements are supplemented with wind shear measurements in the lower half of the rotor to reduce wind speed uncertainty. To further reduce uncertainty REWS should be used as input to the power curve. More than three measuring heights are required for obtaining REWS values. However, it is recommended to use as many heights as possible. For complex terrain, the IEC standard recommends using met masts covering heights of at least hub height + 2/3 rotor diameter (IEC, 2017).

Remote sensing devices that usually assume horizontal flow uniformity through the scanned volume are only allowed in non-complex terrain. These devices have to be verified either before the measurement campaign or in-situ. The remote sensing device can be used to measure hub height wind speed, wind shear, wind veer and/or REWS. However, the standard requires that remote sensing devices have to be simultaneously compared with a top-mounted anemometer on a met mast higher than the lower tip-height of the rotor (IEC, 2017).

If wind speed is only measured at hub height, an additional uncertainty term has to be be added in the power performance test. For uncertainty analysis, an estimated wind shear or wind veer based on site characteristics (e.g. roughness) or modelling (e.g. resource assessment) have to be used. If wind veer is only measured across the half rotor, wind veer across the full rotor can be estimated as 2.5 times that value for uncertainty analysis (IEC, 2017).

Whilst there is broad agreement on existing correction methods (air density, REWS and turbulence renormalisation) they do not fully explain all the available observations (Stuart, 2014a). In the low wind speed and low turbulence case the methods suggested by IEC (2017) still yield large deviations of produced power from calculated power (Stuart 2014b).

10.1.1 Rotor-Equivalent Wind Speed (REWS)

Large wind turbines experience highly varying wind conditions across the rotor-swept area, a factor being even more important over forests. Over forests, we can expect larger wind shear and veer and higher turbulence than at the sites where the warranted power curve was measured. In order to take wind speed and direction variations across the rotor into account, the concept of Rotor Equivalent Wind Speed (REWS) was developed.

Common practice is to measure wind shear only over the lower half of the rotor. Whilst state-of-the-art remote sensing devices can measure wind shear over the entire rotor diameter, they are less frequently used due to various reasons. Wind shear, wind veer, and turbulence are a function of atmospheric stability and influence the relationship between hub height wind speed and rotor-equivalent wind speed (REWS).

REWS is defined as wind speed corresponding to the kinetic energy flux through the swept rotor area when accounting for the variation of the wind speed with height over the entire rotor diameter. REWS from several sites are presented and compared with hub height wind speeds below.

According to IEC (2017), the segments (with areas A_i) shall be chosen in the way that the horizontal separation line between two segments lies in the middle of two measurement points. Figure 10-2 shows an example of a wind turbine and a met mast with five segments A_i and five wind speeds U_i.

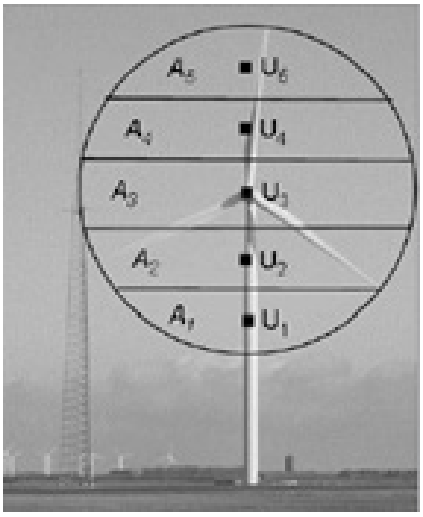

Figure 10.2 Concept of areal segments A_i that are used in calculation of Rotor Equivalent Wind Speeds. Each wind speed U_i is assumed to be representative for segment A_i. REWS is calculated using equation 10-3.

In the case of large wind turbine rotors, it is recommended to apply the extended definition of equivalent wind speed including wind veer. This reads (IEC 2017):

$$U_{equiv} = \left(\sum_i (U_i \cos(\phi_i))^3 \cdot \frac{A_i}{A} \right)^{1/3} \quad (10\text{-}3)$$

where A_i are the areal segments of the wind turbine rotor, and U_i the wind speeds (measured at the central height of each areal segment A_i). The wind speeds are assumed assumed to be representative for segment A_i. φ_i is the difference in wind direction from the hub height wind direction.

Wind speeds and directions must be given at the centre elevations of the segments with areas A_i. The areas of the segments are calculated as (IEC 2017):

$$A_i = \int_{z_i}^{z_{i+1}} 2\sqrt{R^2 - (z-H)^2}\, dz = g(z_{i+1}) - g(z_i) \quad (10\text{-}4)$$

where z_i is the height of the i-th segment lower separation line. The integrated function is

$$g(z) = (z-H)\sqrt{R^2 - (z-H)^2} + R^2 \arctan\left(\frac{z-H}{\sqrt{R^2-(z-H)^2}} \right) \quad (10\text{-}5)$$

10.1.2 Turbulence Effects

Wind turbine power curves are used to calculate wind turbine energy output depending on 10-minute mean wind speed at hub height. In the IEC standard for power performance testing, it was noted that wind turbine power curve measurements are influenced by *TI*. A significant part of the *TI* effect is caused by the averaging of the measured power output over 10 minutes as well as the averaging of the measured wind speed over 10 minutes. The standard recommended method to remove this effect from the measurements is to normalise the power curve data to a reference *TI*. A reference *TI* of 10 % might be applied (IEC, 2017).

The IEC standard for power performance testing (IEC, 2017) suggests to construct a zero-order turbulence power curve from the manufacturer power curve. It states, however, that this *TI* normalisation procedure is a strongly simplified approach for characterising short term wind speed fluctuations. Furthermore, there remains uncertainty of the evaluated power curve due to possible turbulence effects, even after applying this normalisation procedure. The standard explicitly states that the method only removes about half of the observed *TI* effect on wind turbine power curves. Hence, there remains a strong need for improvement.

The procedure for constructing a laminar (= zero turbulence) power curve is suggested in the IEC standard for power performance testing Annex M (IEC, 2017). However, the method is still in development. Therefore, we chose to use the laminar power curve from a re-scaled generic open-source benchmark turbine (Section 10.5.1) in the studies presented below.

10.2 SUMMARY OF RESULTS FROM POWER CURVE WORKING GROUP

This section contains a short summary of the results of the Power Curve Working Group (PCWG). For a more comprehensive summary see Mohr (2018).

Tindal (2013b) divided power curve corrections into type A and B, namely:

- Type A: Adjustments made to reflect changes in the kinetic energy available for conversion across the rotor in a ten minute period due to 'non-standard conditions'.
- Type B: Adjustments made to reflect changes in the conversion efficiency due to 'non-standard conditions'.

Tüxen (2014) pointed out that the kinetic power related to a certain area (i.e. the rotor area) and to a certain averaging time (typically 10 minutes) is determined by the flow. Considering the factors influencing the kinetic power could be done by means of "proxies" such as a shear, veer and turbulence intensity. However, it could also be done by direct analysis (using very high resolution in space and time).

The Power Curve Working Group (PCWG) was formed to investigate these issues (Stuart, 2014b). Central questions were:

- What power does a wind turbine generate in the full range of atmospheric conditions seen in the "real world"?
- More specifically: Is a power curve based on just wind speed and air density the "whole truth"?

While owners want site specific power curves, suppliers have problems warranting site specific power curves due to unknown site conditions (Albers, 2012).

Moriarty (2012) recommended further analysis with highly instrumented test sites. Turbulence, turbulence coherence, momentum flux and wind veer were identified as critical variables for power loss and loads.

Tindal (2013a) recommended to design pre-construction measurement campaigns with power curve issues in mind, e.g. measure wind speed up to tip height with for instance remote sensing. In complex terrain inflow angle should be measured in addition. Also he recommended to carry out modelling, in order to prepare inputs for power curve assessment.

Clifton (2013) proposed multivariate power curves depending on *TI*, shear and power curve region (below rated, rated, above rated). Atkinson et al. (2015) mentioned that the blades' lift-to-drag ratio is dependent on variations in turbulence, angle of attack and wind speed.

Power curves should be referenced to either hub height, rotor equivalent wind speed or both. It was suggested that a "power matrix" could be adopted to express a similar concept by showing turbine efficiency (electrical power normalised to kinetic power) as a function of wind speed and turbulence (Stuart, 2014a). It was suggested that this could be done using currently available 'open–source' rotors (e.g. the NREL rotor) and BEM (blade element momentum) models.

The PCWG concluded that the density correction reduces variations associated with air pressure and temperature (Stuart, 2014a). The *TI* correction deals with *TI* and the standard deviation of the wind direction. (Variations in produced power associated with *TI* and wind direction standard deviation were significantly reduced by this correction.) Instead of calculating wind shear, veer and flow inclinaton angle, Lezaun Mas (2014) suggested that ratios or linear adjustments could be used. So far there is little experience in this field but previous cases suggest that this approach could be good enough.

Kelly (2014) recommended to update shear exponents α that are used in normal turbulence load cases (depending on the effective surface roughness). For operational load cases near rated wind speed over large rotors (> 100 m diameter), a wind veer of 5-10° should be applied.

Stevens (2013) mentioned that remote sensing is only permitted if the terrain meets the requirements of Annex B (i.e. no site calibration required) and if the device meets the accuracy requirements of IEC (2017).

Baylis et al. (2014) suggested a 3D power performance matrix (instead of the usual power curve) dependent on hub height wind speed, *TI* and rotor wind speed ratio (= wind shear).

Ormel (2015) pointed out that there is a correlation between turbulence and shear/veer. Also, the pitch/yaw time constant should be included in the definition of turbulence (de-trending). Moreover, non-roughness shear often does not follow the power law (e.g. low level jets, katabatic winds).

Ormel (2015) suggested to address the variation of climatic variables (shear, veer and turbulence) including

- Better tools to characterise these variables in the field
- Establish 'default' distributions for these variables
- Match field data and power curve models
- Agree on AEP influences for classes of these variables

All in all, there was broad agreement on existing correction methods (air density, REWS and turbulence renormalisation) in the PCWG. However, the methods still do not fully explain all the available observations (Stuart, 2014a).

10.3 INNER/OUTER RANGE MODEL

Often hub height wind speeds do not accurately describe the wind profile. State of the art is that power curves are warranted for an inner range, close to the conditions where the power curve was measured. This **inner range** is typically defined as (Stevens, 2013)

1. Shear exponent $\alpha = 0 – 0.35$
2. $TI = 5 – 15\%$
3. Inflow angle smaller than ±8°

Conditions at each site are divided into an inner and outer range. The inner range corresponds to conditions found at wind turbine test sites, such as in coastal

Denmark, Germany or the Netherlands (i.e. low wind shear combined with low turbulence). Also, calculated power curves apply a particular set of inner range conditions (i.e. shear, turbulence, etc.).

For neutral conditions and in the surface layer, *TI* is a function of roughness length and height above ground only as

$$TI = \frac{1}{\ln\left(\frac{z-d}{z_0}\right)} \tag{10-6}$$

assuming $\sigma_U = 2.5\, u_*$ and using the logarithmic wind profile (Pena et al., 2016).

For the **outer range** beyond those conditions, the actual power curve can be different to the warranted power curve. Whiting (2014) found for one hypothetical turbine, which he simulated with the model BLADED, that almost 2/3 of the time and half of energy produced falls in 'outer' range. He suggested using actual measured profiles together with the model BLADED to simulate power production.

Rivera Lamata and Pollack (2014) and Stuart (2013) stated that the inner range is the range of conditions for which one can expect to achieve a performance equal to the performance using traditional power curves based upon hub height wind speed only. The outer range, on the other hand, is the range of conditions for which one can expect to achieve a performance of less than 100% compared to the performance expected using traditional power curves based upon hub height wind speed only (Figure 10-3).

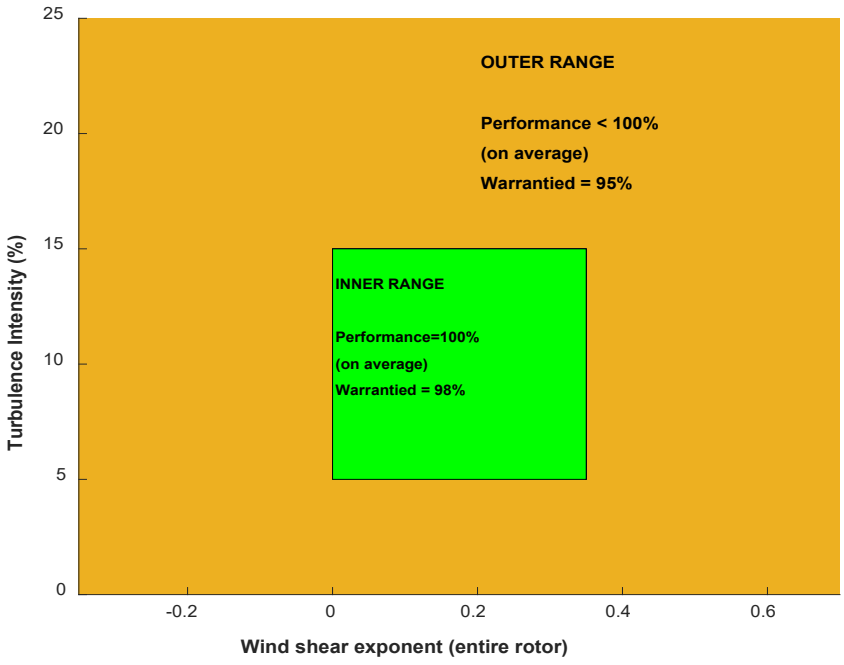

Figure 10.3 Inner and Outer Range for wind turbine power performance. In the outer range a performance < 100% can be expected, whereas in the inner range performance ≈ 100% can be expected. Here, performance is based upon theoretical performance using traditional power curves based upon hub height wind speed only. Figure adopted from Rivera Lamata & Pollack (2014).

Real world conditions are composed of both inner and outer range wind conditions. In the outer range Stevens (2014) proposed to reduce the contractual guaranteed warranty level from 98% to 95%, i.e. a reduction of three percentage points.

Theoretical AEP can then be calculated from traditional power curves based upon hub height wind speed only. Total AEP (both theoretical and measured) is sum of inner and outer range AEP:

$$AEP = AEP_{inner\text{-}range} + AEP_{outer\text{-}range} \quad (10\text{-}7)$$

Hence, if outer range conditions occur a lot, an annual performance of < 100% (compared to theoretical AEP) can be expected.

Hence, not the number of hours in the inner/outer range is of interest, but the energy produced in the inner/outer range. For the four sites studied herein where TI was measured, this is summarised in Table 10-1.

Table 10-1 shows that most of the energy produced is indeed in the outer range (expect for Havsnäs where inner/outer range comprise about 50% each). It seems that more of the energy can be found in the inner range the windier the site is and the lower the surface roughness. Time in the inner/outer range seems to agree pretty well with the energy produced in the inner/outer range.

The results seem to indicate that wind speed at hub height is not enough as a proxy for wind turbine power production, but that other factors (REWS and turbulence effects) are important over the forested Swedish sites studied herein.

Table 10-1. Energy produced during inner/outer range conditions. Energy is based upon a Enercon E-141 EP4 (4.2MW) power curve using 150 m hub height. Expected energy is calculated using this traditional power curve based upon hub height wind speed only. Wind shear and TI at 150 m hub height were used to determine if respective 10-minute interval belongs to inner/outer range. At Ryningsnäs 138 m hub height is used instead.

Site	Energy (inner range)	Time (inner range)	Energy (outer range)	Time (outer range)
Hornamossen	35.1%	32.7%	64.9%	67.2%
Ryningsnäs	8.4%	10.5%	91.6%	89.4%
Östergötland site	23.5%	23.9%	76.5%	76.1%
Havsnäs	52.1%	43.6%	47.8%	56.3%

10.4 MEASURED ROTOR-EQUIVALENT WIND SPEEDS

We use a turbine with 126 m diameter to calculate REWS from measurements at several Swedish sites with forest. This could be either the new open-source benchmark turbine presented herein (see section 11.1). However, as no measured power curve is available for this turbine, we chose the Enercon E-126 EP4 4.2 MW turbine for our study (see Appendix for power curve). The Enercon turbine is designed for sites with medium wind conditions, i.e. typical Swedish sites. The results presented in this section are believed not to be dependent on the chosen wind turbine, but this has still to be proven.

Rotor Equivalent Wind Speed (REWS) versus Hub Height Wind Speed (HHWS)

Figure 10-4 shows calculated REWS vs hub height wind speeds for Hornamossen. The turbine hub height was chosen at 100 m height above ground (coincident with one of the sonic anemometers). Hence, the rotor ranges from 37 to 163 m above ground, i.e. very close to the forest top. Correlation between REWS and HHWS is excellent and differences are quite small. Figures for the other two sites are very similar with very similar correlation coefficients and linear fits (not shown).

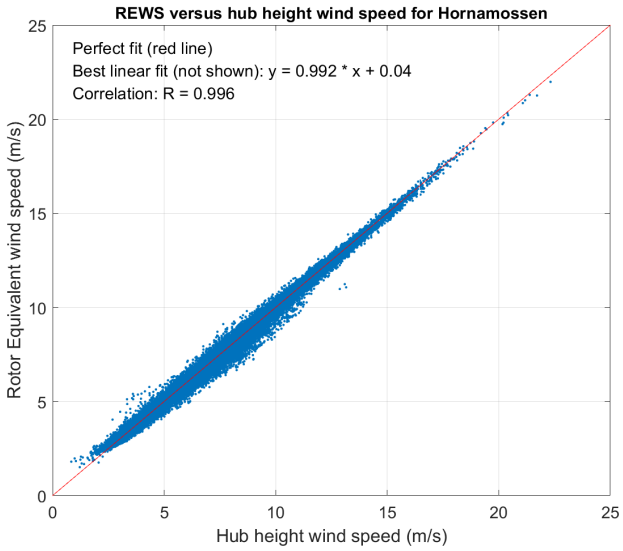

Figure 10-4 REWS versus hub height wind speed at Hornamossen for hypothetical turbine with 126 m rotor diameter. Hub height was chosen at 100 m above ground. Based upon roughly 60000 wind profiles (10-minute averages) corresponding to 410 days.

A frequency distribution of the differences is shown in Figure 10-5 for all three sites. Again differences are quite small; however, the distribution is slightly skewed to the right, resulting in a slightly higher REWS than hub height wind speed, on average at Ryningsnäs. At Hornamossen, the distribution is slightly skewed to the left, resulting in a slightly lower REWS than hub height wind speed, on average (not shown). At the Östergötland site, HHWS and REWS were almost identical.

The calculated REWS were used with the power curve of an Enercon E-126 EP4 4.2 MW machine, to compute hypothetical AEP values (Table 10-2). Actually, another power curve is meant to be used with REWS values (rather than HHWS values) should be used in conjunction with REWS. However, still the AEP differences from Table 10-2 are believed to represent the magnitude of difference in AEP (either positive or negative) that can be expected when using the different methods (HHWS versus REWS).

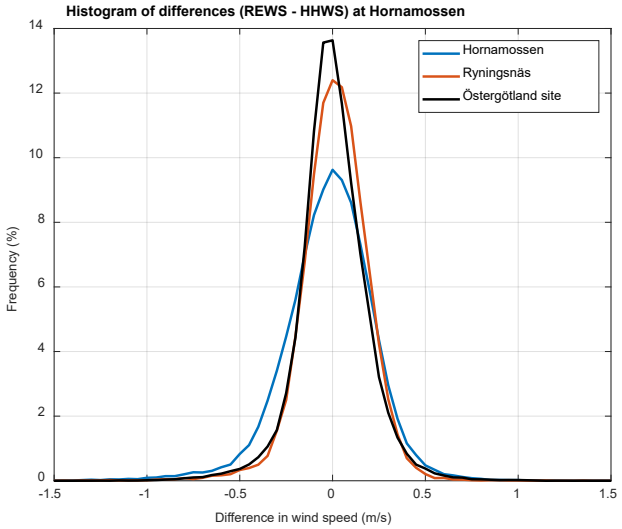

Figure 10-5 Same as in Figure 10-4, but histogram of differences between REWS and hub height wind speed for all three sites.

Table 10-2. Difference in estimated AEP when using HHWS and REWS as input to the power curve of an Enercon E-126 EP4 4.2 MW machine. HHWS = hub height wind speed; REWS = rotor-equivalent wind speed.

Site	Hub height	Anemo-meter heights	No. of profiles	AEP based upon HHWS	AEP based upon REWS	Differenc e in AEP
Ryningsnäs	98 m	40 - 138 m	23 124 (=161 days)	100%	100.8%	+0.8%
Hornamossen	100 m	21 - 173 m	59 006 (=410 days)	100%	99.3%	-0.7%
Östergötland site	100 m	50 - 151 m	58 843 (=408 days)	100%	100.3%	+0.3%

10.5 EFFECTS OF TURBULENCE

St. Martin et al. (2016) studied power curves for different *TI* regimes. They found that turbulence undermines power production at wind speeds near rated, but increases power production at lower wind speeds. Vanderwende and Lundquist (2012) found underperformance during stable regimes (with little turbulence) and overperformance during convective regimes (with considerable turbulence) at moderate wind speeds from 8 to 12 m/s. The Power Curve Working Group found strong influences of TI on the power curve (e.g. Moriarty, 2012).

In the following a simple statistical model for simulating the effects of turbulence is described. The model still has to be validated. However, a comparison of the statistical simple model against aeroelastic simulations of an open-source generic wind turbine shows very good agreement (not shown).

10.5.1 TI dependent power curves

We start with the laminar power curve (Figure 10-6). The laminar power curve is obtained from aeroelastic simulations using data from re-scaled open-source generic turbines (see Section 11.1). A laminar power curve might also be constructed based upon the assumption that the manufacturer power curve is valid for say 10% *TI* at all hub height wind speeds. However, this seems to be a rather complicated process (e.g. IEC 2017, Appendix M).

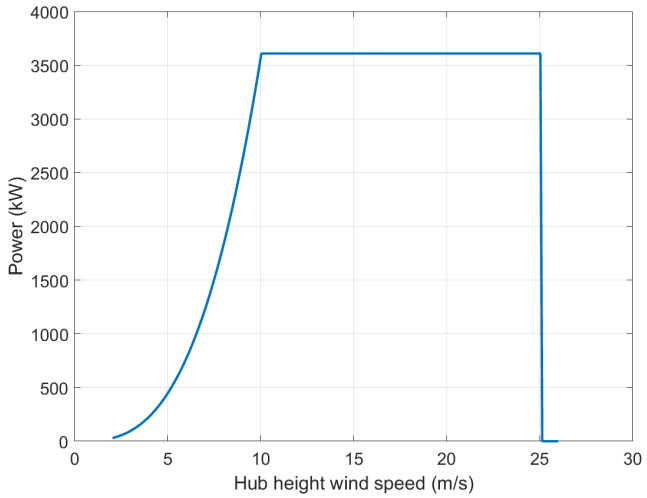

Figure 10-6. Power curve from generic IEC126/3.6MW IEC class IIB wind turbine. Turbine data is based upon re-scaling of several open-source wind turbines (see Section 11.1).

To estimate turbulence effects, we assume Gaussian turbulence around the 10-minute mean wind speed at hub height (U), i.e.

$$U_{momentaneous} = U_{10-minute\ average} + U' \tag{10-8}$$

Figure 10-7 shows an example of a frequency distribution of the turbulent wind speed U' described by a simple Gaussian model as well as an example distribution from measurements at Hornamossen. The Gaussian distribution for U' is defined by

$$\sigma_U = TI \cdot U \tag{10-9}$$

centered around the mean wind $U_{10\text{-}minute\ \mathrm{average}}$.

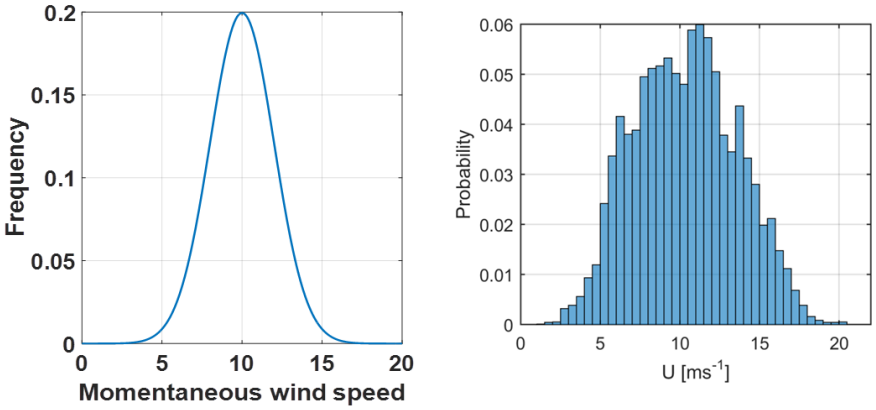

Figure 10-7. Distribution of momentaneous wind speed at hub height using theoretical Gaussian distribution (left) and measurements (right). Wind speed varies in any given 10-minute interval according to that distribution.

We use this distribution together with the laminar power curve from Figure 10-6 for different 10-minute- average wind speeds $U_{10-minute-average}$ and different *TI*s to obtain Figure 10-8. Based upon Segalini et al. (2015)

$$U'_{rotor-average} = 0.5 \cdot U' \qquad (10\text{-}10)$$

was used as a first guess. It should be pointed out that this is a first guess only and that further research is needed to estimate $U'_{rotor\text{-}average}$ based upon typical horizontal and vertical turbulence coherence functions for each 10-minute average hub height wind speed.

Figure 10-8 shows that for HHWS below ≈ 9 m/s, high turbulence leads to higher power output, whereas at HHWS above ≈ 9 m/s, high turbulence leads to lower power output (Figure 10-8). In nature both situations will occur.

In the calculations presented below, the power curve with *TI* = 8% was used as a hypothetical manufacturer power curve.

10.5.2 AEP based on TI dependent power curves

From the simple model above AEP was calculated at each site for a power curve using 8% TI at all hub height wind speeds as well as for a power curve using actual TI values at hub height (see Figure 10-8).

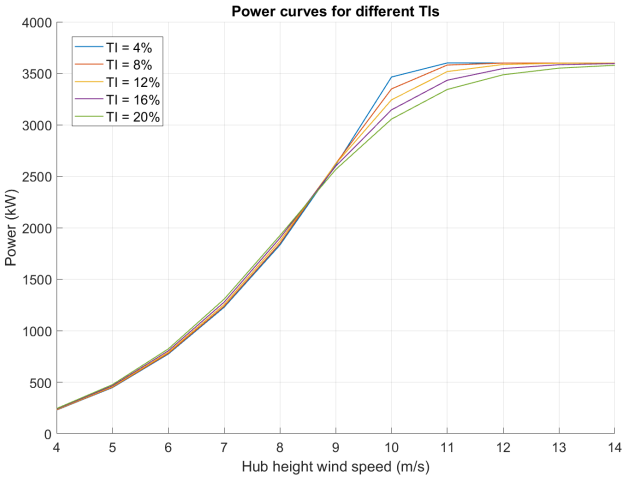

Figure 10-8. Power curves of generic IEC126/3.6MW IEC class IIB turbine for different turbulent intensities (*TI* values). A Gaussian distribution was used for the turbulent wind that the entire rotor experiences.

Table 10-2a shows that the resulting AEP values differ less than ±1% from the reference AEP values obtained from a power curve for 8% TI at all hub height wind speeds. Differences are even lower for higher hub heights (not shown).

Table 10-2a. Difference in estimated AEP when using TI dependent power curve as compared to power curve with reference TI of 8%. Hub height wind speed (HHWS) only was used in the power curve. The generic IEC126/3.6MW IEC class IIB turbine from section 11.1 was used. TI dependent power curves are shown in Figure 10-8.

Site	Hub height	No. of records (10 minute averages)	AEP based upon TI-dependent power curve	AEP based upon 8% TI power curve	Difference in AEP
Ryningsnäs	98 m	25 442 (=177 days)	100.4%	100%	**+0.4%**
Hornamossen	100 m	82 681 (=574 days)	99.3%	100%	**-0.7%**
Östergötland site	100 m	66 264 (=460 days)	100.5%	100%	**+0.5%**

10.6 POWER PRODUCTION OF EXISTING WIND FARMS IN FORESTS

The analysis of production data from operating wind farms is still a relatively unstudied field within wind power research (Turkyilmaz et al., 2016; Khatab, 2017). In the study presented herein, an analysis of power production data from a wind farm in forest in southern Sweden is presented.

10.6.1 Wind farm location, outline and data

The wind farm is located in moderately complex terrain and experiences rather long and harsh winters. Average elevation at the site is 430 m above sea level. The minimum distance between neighbouring turbines varies from 3.5 to 10.8 rotor diameters with an average of 5.2 rotor diameters. The turbine layout consists of in total 17 turbines; five 2.0 MW turbines with 80 m hub height and twelve 2.0 MW turbines with 105 m hub height.

The wind farm was built in two stages: Five turbines with 80 m hub height were erected in 2006 and twelve turbines with 105 m hub height were erected in 2008. All turbines have 90 m rotor diameter. Turkyilmaz et al. (2016) studied two wind turbines of the older part of the wind farm (WTG02 and WTG03) with nacelle mounted Lidar (see below).

SCADA data from four years of operation (2013 to 2016) was analysed. The data consists of

- Average ambient wind speed
- Standard deviation of ambient wind speed
- Absolute average of ambient wind direction
- Average ambient temperature
- Average total active power produced

All data represents averages over 10 minutes. In order to avoid icing effects, only data with Average ambient temperatures ≥ 3°C was analysed. Also data with negative power production as well as with power production ≥ 2005 kW was discarded. Furthermore, data with power production ≤ 75% of the theoretical power production according to the manufacturer power curve (using Average ambient wind speed from the SCADA data) was discarded. This should be sufficient to remove occasions when the turbine was not operating in full performance (i.e. standing still or curtailed through e.g. icing).

10.6.2 Accuracy of nacelle mounted instruments

St. Martin et al. (2016) noted that Nacelle Anemometers (NAs) do not observe ambient wind speeds that rotor disks experience because winds that flow through rotor disks and along the nacelle during operation are modified by the blades and nacelle. In many cases, however, operators calculate power curves based upon NAs due to lack of other data (St. Martin et al., 2016).

Göçmen and Giebel (2016) found that NA *TI* overestimates atmospheric *TI* by up to 3.7%. In their study, *TI* estimated from rotor effective wind speed at Lillgrund and Horns Rev-I offshore wind farms agreed better with met mast *TI* as compared to NA *TI*. In contrast to our findings, Liu (2011) claimed that *TI* did not significantly impact the NA based power curve from a 1.8 MW test turbine.

NA wind directions from all 17 wind turbines of the wind farm were compared to a nearby SMHI station on a hill (roughly 30 km north-northwest of the wind farm) as well as to the NA wind directions of the other turbines of the wind farm. There are slight deviations from true North in NA wind directions at most turbines (Table 10-3). At four wind turbines (WTG06, WTG09, WTG13 and WTG19),

however, wind directions were off more than 10° with respect to the SMHI station (bold numbers in Table 10-3). These four turbines were neglected in the analysis below.

Table 10-3. Wind direction differences between different turbines and reference mast/reference turbine (= SMHI station or wind turbine WTG04). Nacelle-measured wind directions (from SCADA data) have been used. Values represent all wind directions. Using wake-free sectors only did not change the values substantially.

Wind turbine	**Wind direction difference (with respect to SMHI station)**	**Wind direction difference (with respect to WTG04)**
WTG01	-3.7	-2.2
WTG02	2.2	4.4
WTG03	-4.8	-3.1
WTG04	-1.7	0
WTG05	7.3	9.7
WTG06	**14.9**	**17.8**
WTG07	-2.2	0.4
WTG09	**-25.7**	**-24.7**
WTG10	-4	-2.6
WTG11	4.3	6.8
WTG12	-8.3	-7
WTG13	**-10.5**	**-8.7**
WTG15	5.1	7.4
WTG18	2.4	4.3
WTG19	**12.6**	**15**
WTG20	6.9	9
WTG44	-8.6	-7.1

NA wind speeds did not reveal systematic differences to both SMHI mast and NA wind speeds from other turbines. Average NA wind speed differences between turbines were smaller than ±1 m/s, on average, for all turbines (not shown). Correlation of NA wind speeds from the individual turbines was very good (wake sectors excluded). Average bias seems to be mostly caused by terrain effects and to a lesser extent by different NTFs. Also, correlation of NA wind speeds to the SMHI mast was quite good (not shown).

Temperatures from nacelle thermometers showed excellent agreement in between the 17 wind turbines of the wind farm (not shown). Comparing temperatures of the individual turbines to nacelle temperatures from wind turbine WTG01 yielded biases between -0.7 and +0.5°C, on average. Standard deviations of the differences were around 0.5-0.6°C. Correlation coefficients of the temperature inter-comparison were above 0.995 for all wind turbines. This suggests that the temperatures from nacelle thermometers of this particular wind turbine have sufficient accuracy for use in power performance studies. Nevertheless, nacelle thermometers could be affected by heat produced in the nacelle through the generator, the gear box, etc. (Derneryd, 2017, personal communication).

10.6.3 Power curves from nacelle anemometers

In this study, wind turbine power is analysed using nacelle anemometers (NA) in conjunction with the improved Nacelle Transfer Functions (NTFs) suggested by Turkyilmaz et al. (2016).

For the older wind turbines of the wind farm, Turkyilmaz et al. (2016) found large differences between real winds measured by nacelle Lidars (Wind Iris) and winds obtained from NA using manufacturer nacelle transfer functions (NTFs). They suggest that manufacturer NTFs can be vastly improved using nacelle Lidars installed during short time periods. Also NTFs might be influenced by free-stream turbulence intensity and atmospheric stability (St. Martin et al., 2017).

Turkyilmaz et al. (2016) recommend corrections for two wind turbines of the older part of the wind farm (WTG02 and WTG03) where Wind Iris wind speeds could be compared to NA wind speeds. Linear correction functions of the form

$$U_{NA} = \mathrm{a} \cdot U_{WI} + \mathrm{c} \qquad (10\text{-}11)$$

where U_{NA} and U_{WI} are wind speeds measured by the NA and Wind Iris, respectively. Wind speeds measured by the Wind Iris were assumed to represent correct free flow wind speeds.

Constants a and c for WTG02 and WTG03 were obtained from two weeks and three months, respectively, of nacelle Lidar measurements. For WTG02 and WTG03, constants were a = 0.86 and 0.89 as well as c = 0.63 and 0.41, respectively. These constants were used for WTG02 and WTG03 in the analysis below. For WTG04, the mean value of the constants from WTG02 and WTG03 (i.e. a = 0.875 and c = 0.52) was used.

For the newer turbines of the wind farm, manufacturer NTFs were much more accurate (not shown). However, a slight "correction" was still necessary to obtain realistic free-flow hub height wind speeds. The "correction" was obtained by a trial and error approach in order to fit the obtained power curve with low NA TI (3% ≤ TI ≤ 8%) to the manufacturer power curve. The constants a=0.955 and c=0.2 were found to give the best match to the manufacturer power curve. These constants were used for correcting NA wind speeds from WTG10, WTG18, WTG20 and WTG44.

Power curves from three old turbines of the wind farm (WTG02, WTG03 and WTG04) and four new turbines of the wind farm (WTG10, WTG18, WTG20 and WTG44) were analysed. The manufacturer power curve is given in Table 8.19 in Turkyilmaz et al. (2016).

To compute air density at each turbine, air temperatures from either the nearby SMHI station (corrected with -0.65°C per 100 m increase in altitude) or nacelle thermometers were used in conjunction with sea level pressure from a nearby SMHI station. Hourly sea level pressure observations from the SMHI station were interpolated in time and reduced to the altitudes of the turbine hubs using either temperatures from the nearby SMHI station or nacelle temperatures. A temperature correction of -0.65°C per 100 m increase in altitude was applied.

Air density at each turbine was used in the density correction described in Equation (10-2). There was slightly less scatter in power curve scatter plots when temperatures from nacelle thermometers were used in comparison to the case when temperatures from the nearby SMHI station were used (not shown). Therefore temperatures from the nacelle thermometers were used in the analysis below.

10.6.4 Influence of turbulence on power curve

Nacelle anemometers (NA) were used to determine the influence of turbulence on the wind turbine power curve. The advantage of NA is that the measurement is taken at almost exactly the same position as the centre of the rotor, only a couple of meters downstream. (The length of the nacelle of the turbines studied herein is approximately 10 meters.)

This is in contrast to power performance masts where measurements are taken at a considerable distance (≈ 2.5 rotor diameters) away from the turbine. Hence, in general, scatter should be less in power curves obtained from NA compared to power curves obtained from power performance met masts. This was, for instance, shown by St. Martin et al. (2016, Fig. 7), where the scatter of the power curve was considerably less when NA was used in comparison to a power performance met mast. Largest scatter was found when evaluating power against Lidar data.

The disadvantage of using NA for power curve studies is that wind measurements are influenced by wake effects of the rotor. Therefore, NA have to be corrected in order to represent true upstream free-flow wind speeds (see section 10.6.3).

TI from NA is influenced by the additional turbulence produced by the rotor. Barthelmie et al. (2007), for instance, found that *TI* from NA is considerably higher than TI from a met mast at the same site. *TI* derived from power measurements, on the other hand, agreed better with the *TI* from met mast. This is something that has not been evaluated in this study. In the future, NTFs for *TI* could perhaps be constructed.

Power curves from three old turbines of the wind farm (WTG02, WTG03 and WTG04) and from four new turbines of the wind farm (WTG10, WTG18, WTG20 and WTG44) were analysed. The remaining turbines were neglected because they were either on very pronounced hill tops, influenced by wakes from almost all wind directions or had large deviations in wind directions (see Table 10-3).

Figure 10-9 shows wind turbine power production from the seven analysed turbines as a function of NA *TI*. High *TI* (> 20% or so) clearly leads to a strong decrease in production for wind speeds from, say, 9 – 16 m/s. At lower wind speeds high *TI* should lead to a slight increase in production. However, this cannot be seen in Figure 10-9.

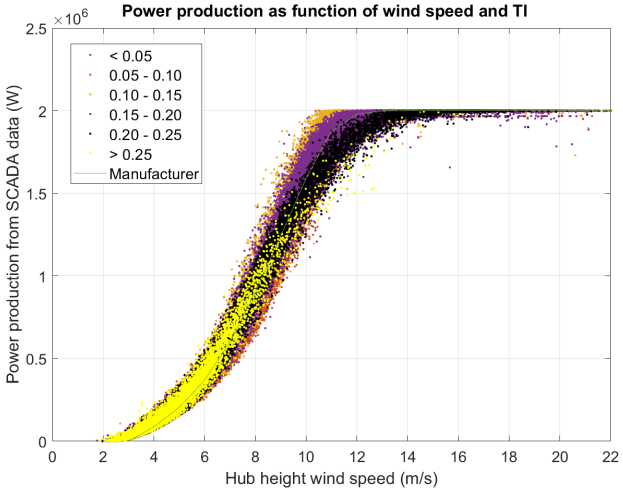

Figure 10-9. Scatter plot of produced power from seven wind turbines as function of nacelle anemometer (NA) wind speed. NA wind speeds were corrected using measured or "trial-and-error" nacelle transfer functions (NTFs). NA turbulence intensity (TI) was not corrected. There is a clear influence of NA TI on the power curve at wind speeds above 8 m/s or so. The manufacturer power curve is shown as a thin line.

Figure 10-10 shows the same as Figure 10-9, but binned averages as a function of *TI*. Bins of 1 m/s width were used and only bins with more than seven data points were taken into account. There is a clear influence of NA *TI* on the power curve at wind speeds above 8 m/s or so. However, at lower wind speeds no influence of NA *TI* on the power curve can be seen. The manufacturer power curve (black line) agrees with power curves for low NA *TI*. However, at wind speeds below 8 m/s or so, the manufacturer power curve is below all NA power curves. This, however, could be a result of slightly wrong NTFs.

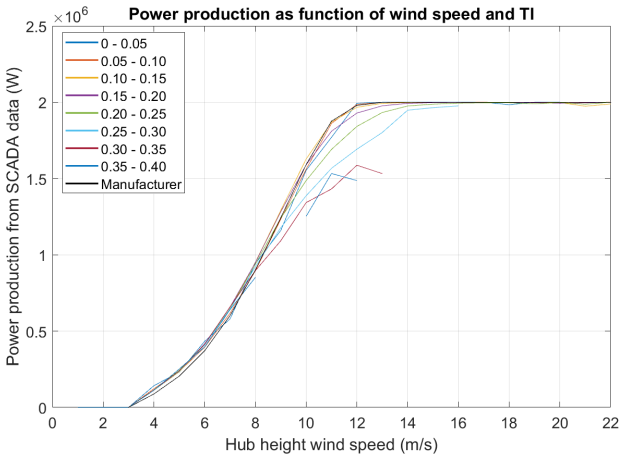

Figure 10-10. Same as in Fig. 10-9, but binned averages of produced power. Only bins with more than seven data points are shown. There is a clear influence of NA *TI* on the power curve at wind speeds above 8 m/s or so. The manufacturer power curve is shown in black.

10.7 IMPLICATIONS FOR FORESTS AND SWEDISH SITES

Forest is mainly affecting turbulence intensity and wind shear/veer (e.g. Wilkinson, 2014). Usually, forest is characterised by both high wind shear and high turbulence (e.g. Bernadett, 2013). Bernadett claimed that individually pitched blades could mitigate this problem, so performance would have to be determined for each turbine model. Considerable variations of shear and turbulence can be found within the standard 10 min measurement increment.

Stable conditions that are frequently occurring in Sweden are also characterised by high wind shear, however, with low turbulence. In these situations also directional shear (wind veer) is important.

For CFD models, Brady (2013) found that a detailed forest canopy model (see section 5.3 for description) significantly improves results over forest. Predicted *TI* and shear were found to be only 1% and 0.04 off, on average, for a selection of forested sites. Brady claimed that underperformance of wind turbines (compared to manufacturer power curves) is due to high turbulence and wind shear. The impact on energy yield could be assessed through multidimensional power curves.

Ribeiro (2014) mentioned the high frequency of stable atmosphere and substantially windy conditions in Scandinavia. Here, low TI could be seen as a proxy for stable atmospheric conditions. Caused by radiative cooling, there is a high frequency of stable and very stable atmospheric conditions at sites across the Nordic region. Ribeiro suggests using TI as a proxy for atmospheric stability, where

- Low *TI* (*TI* < 10%) suggests stable conditions
- High *TI* (*TI* > 10%) suggests unstable conditions

Ribeiro (2014) suggested a general low turbulence turbine underperformance in Scandinavia. Underperformance was found to be higher the lower the mean wind speed (around 2% for sites with annual mean wind speeds below 7 m/s). For annual mean wind speeds around and above 7 m/s no significant overall under- or over-performance should be expected.

Derrick & Oram (2014) mentioned that low hub heights, large rotors and tall trees are bad news. In such cases, hub height met mast measurements are probably inadequate to describe the situation, whereas full rotor height remote sensing measurements provide valuable insight.

Ormel (2015) suggests that there could be up to 3% change in AEP due to site-specific climatic conditions. For Havsnäs wind farm, it was found that REWS gave a slight increase (+0.8%) in annual energy yield (Stuart, 2013). Moreover, turbulence was found to give a slight increase (+0.2% or so). This summed up to an increase of roughly 1% in energy production for this specific site and turbine (Vestas V90-1.8MW and Vestas V90-2.0MW).

Stuart (2015) pointed out that, in stable stratification, there are buoyancy forces that act against the expansion of air required by wind power production (thereby inducing a loss). He suggested a new parameter to take this effect into account.

Mohr (personal communication) is currently exploring if mesoscale model results can be used to describe the effects of wind shear and veer as well as turbulence on the AEP. Otherwise remote sensing up to the rotor tip might be the only feasible option. However, Bernadett (2014) claims that the implementation of REWS would require a full year of wind data across the rotor disk.

10.8 SUMMARY AND CONCLUSIONS

Wind turbine energy production is (except for turbine hardware and software) dependent on wind speed, air density, vertical wind shear and veer as well as *TI* and inflow angle. Another factor is directional variation of the wind which, however, is correlated to *TI*. Hence, the Power Curve Working Group identified these 6 factors as main influencing factors on wind turbine power output. Several authors claim that in real life AEP is lower than estimated beforehand. This is something that should be investigated for Swedish wind farms in forests.

A problem is that measured power curves for wind turbines stem from coastal sites in Denmark, Germany or the Netherlands with little wind shear and turbulence. The averaging over 10 minutes creates additional issues with turbulence.

Wind shear and veer are included in the newly proposed REWS to be used instead of hub height wind speed (HHWS) (IEC 2017). However, for turbulence, correction methods are still not very good.

IEC now recommends to measure wind speed at hub height with a met mast including shear measurements at least for the lower half of the rotor. For complex terrain met masts covering heights up to hub height + 2/3 rotor diameter are suggested. Remote sensing devices have to be verified against met masts before use. Whilst there is broad agreement on existing correction methods (air density, REWS and turbulence renormalisation) there still are large deviations in the the low wind speed/low turbulence case (Stuart 2014b). Power curves should be referenced to either HHWS, REWS or both.

Conditions are divided into an inner and outer range where the manufacturer power curve is thought to be valid in the inner range, with under- or overperformance in the outer range. In the outer range corrections to the power curve (using REWS and *TI* correction) should be applied. For the four sites Hornamossen, Ryningsnäs, the Östergötland site and Havsnäs wind farm outer range conditions prevailed between 50 and 90% of the time. This, however, also depends on the definition of the inner/outer range. Approximately the same percentages apply for the energy produced.

REWS were calculated for Hornamossen, Ryningsnäs and the Östergötland site. REWS are very well correlated to hub height wind speeds. Using REWS in manufacturer power curves instead of HHWS resulted in AEP differences of less than ≈ ±1%.

The effect of *TI* on produced power was modelled by a simple Gaussian distribution model yielding to a frequency distribution for the turbulent wind speed deviations *U*' valid for the whole rotor area. Turbulence coherence models

could be used to estimate real distributions of *U'*. As a first guess 50% of the *U'* value computed from hub height *TI* was used. The model seems to adequately describe *TI* effects on the power curve. However, a laminar power curve (which has to be estimated or modelled) has to be used as input.

Power output from a wind farm in a forest in southern Sweden was analysed using SCADA data only. After correction nacelle transfer functions (NTFs) power curves agreed well with the manufacturer power curve. There was a clear effect of *TI* (approximated by nacelle anemometer *TI*) on the power curve. High *TI* (> 20% or so) was found to lead to strong decreases in production for wind speeds between 9 and 16 m/s. At lower wind speeds high *TI* should lead to a slight increase in production. However, this could not be verified.

It is still unclear what the impacts are for Swedish forests. Usually, forest is characterised by both high wind shear and high turbulence. However, in the Nordic regions often stable stratification with high shear and low turbulence can be found. The use of REWS is believed to yield differences in AEP of less than ±1%. The same is true for turbulence effects, which are thought to amount to additional differences in AEP of maximum ±1%. In the worst case this could add up to ±2% difference in AEP at maximum as compared to using manufacturer power curves in conjunction with HHWS.

11 Load simulations

11.1 SCALING OF A BENCHMARK TURBINE MODEL FOR THE SCANDINAVIAN INLAND

When investigating the consequences off different strategies for site specific load analysis, or when studying the sensitivity to various inflow modelling options, it is of great value to have an aeroelastic simulation model representing a turbine as close to the target as possible. Within the international R&D communities, several benchmark turbines have been developed and shared over the past 15 years. However, the main focus has been on the development of offshore turbines with rated power in the range 5-20 MW and IEC wind class I. For studies targeting conditions representing the Scandinavian inland, the available benchmark models are not suitable due to the very different site conditions and overall requirements. The lower wind speeds allow for a slimmer design, and the challenging road transports will further push the size/weight optimization for most components.

For the reasons described above, it was decided in the present study to work out a turbine configuration that will fit typical onshore sites described by forestry and moderate terrain variations. The main challenge when outlining/designing a modern wind turbine is obviously the rotor design. Wind turbine blades have become very advanced, mainly du to the use of optimized composite materials and several steps of development in the manufacturing process.

It was here decided to aim at a design close to IEC class IIB, a rotor size ~130 m, and a max tip height of ~180 m. The moderate height was mainly chosen to facilitate a standard soft-stiff tower design, since a tall and soft tower would here add to many additional design steps. As a starting point the rotor design presented in Resor (2013) (126 m class IB) was here chosen, due to the availability of a detailed design description, including material layup as well as a full load envelop. The corresponding turbine design was originally presented in Jonkman et.al (2009), but there the main blade characteristics were defined without performing a full design study.

When moving from IEC wind class I to class II the 50 year reference wind speed drops from 50 m/s to 42 m/s. Since the original class IB blade was partly design by shell buckling in the inner parts, it can be assumed that the corresponding design load scales with the wind speed squared. Using the scaling laws for slender structures outlined in Sieros et.al (2012), assuming preserved thickness ratio, a new set of blade characteristics can be derived (see e.g. Figure 11-1).

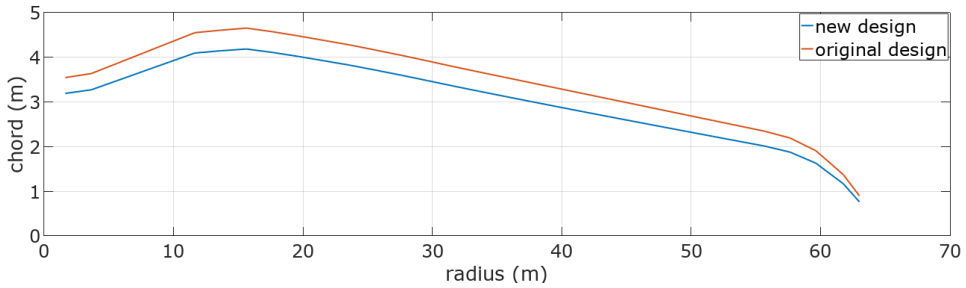

Figure 11-1. Chord distribution for the scaled blade design.

Using standard aerodynamic design based on Blade Element Momentum (BEM) theory, a new optimal twist layout was finally applied and a power coefficient vs. tip-speed-ratio relation could be established as presented in Figure 11-2.

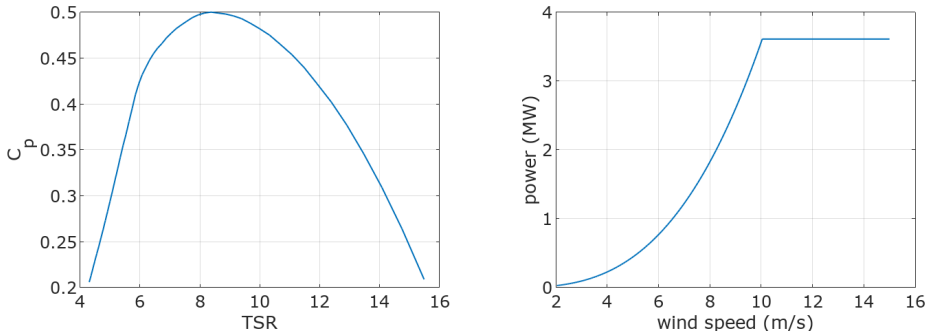

Figure 11-2. Power coefficient vs. tip-speed-ratio and corresponding design power curve (including electrical losses) for the new rotor design.

Following Jonkman et.al. (2009) the generator characteristics were here outlined similar to the IB design, keeping the basic layout but increasing the gear ratio to 100 while assuming a smaller generator inertia of ~400 kgm^2. The original pitch-speed controller was modified to the new rotor characteristics, and the resulting torque-speed schedule together with a summary of derived values for essential controller parameters, is presented in Figure 11-3.

Weights of nacelle and hub were defined to be 140 and 30 tonnes respectively. A new 117 m tower was designed and verified according to IEC-61400-1 class IIB (IEC 2005) for relevant load cases within load categories Ultimate and Fatigue.

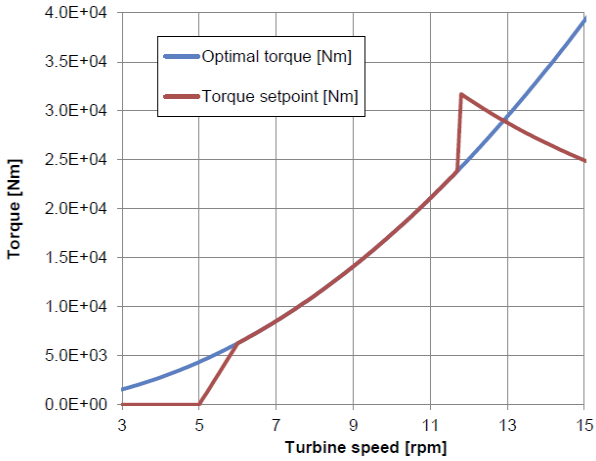

Controller input file parameters		
501	0.0080683	PC_KI
502	0.1099965	PC_KK
503	0.0188268	PC_KP
504	1.5707960	PC_MaxPit
505	0.140	PC_MaxRat
506	0.015	PC_MinPit
507	122.9096	PC_RefSpd
508	52.35988	VS_CtInSp
509	15000.0	VS_MaxRat
510	35078.15	VS_MaxTq
511	1.588363	VS_Rgn2K
512	62.83185	VS_Rgn2Sp
513	0.0174533	VS_Rgn3MP
514	121.68048	VS_RtGnSp
515	3919491.5	VS_RtPwr
516	10.0	VS_SlPc
517	0.02618	PC_MaxRatSt
518	100	CornerFreq

Figure 11-3. Torque-speed design for the new class IIB rotor, aiming at a rated wind speed just above 10 m/s. The table contain parameter values for the classic pitch-speed controller originally developed in Jonkman et.al. (2009).

11.2 SENSITIVITY OF INFLOW MODEL ASSUMPTIONS ON LOAD RESULTS

In chapter 8, the turbulence structure evaluated in the 180 m met mast in Hornamossen was analysed in detail, and several deviations from standard model parameter values and property profiles were found. An initial investigation of the importance of these findings was thus defined here. The wind turbine model developed in section 11.1 was then implemented in the aeroelastic simulation tool Vidyn, a software developed by Teknikgruppen AB that has been extensively used for wind turbine design as well as within European R&D projects. The software has been verified in international framework benchmark projects described in Grol and Bulder (1993), Arias and Soria (1996), Shepers (2001), and theory and implementation is presented in Ganander (2003).

An initial parameter study performed for wind speeds 6, 10 and 14 m/s was set up to identify the most important modifications of the standard turbulence models to better align with the measured characteristics:

A) shorter length scales of turbulence during night
B) inclusion of a realistic phase profile for the longitudinal wind component
C) lower 2-point correlation over the size of a large rotor.

A proven implementation of the simulation method outlined in section 8.5 was here modified to include the adapted coherence model (Equation 8-15) and the proposed phase profile (Equation 8-16).

An overview of a set of 120 ten minute-aeroelastic simulations is outlined in table 11-1.

Table 11-1. Initial set of 120 aeroelastic simulations using the turbine model outlined in 11.1

Mean wind speed	**6 , 10 , 14 m/s**
Coherence decay exponent	1.00 , 1.24
Governing turbulent length scale	340 m , 204 m
Phase profile added for u-component	On , Off
Realizations	5 random seeds

The study clearly pointed out the modified coherence formulation as having the largest influence on main load components in terms of fatigue load ranges. In figure 11-4 it is seen for 6 m/s that the standard coherence model results in significantly higher sensitivity to thrust variations due to *low frequency gusts* than the one fitted to Hornamossen data.

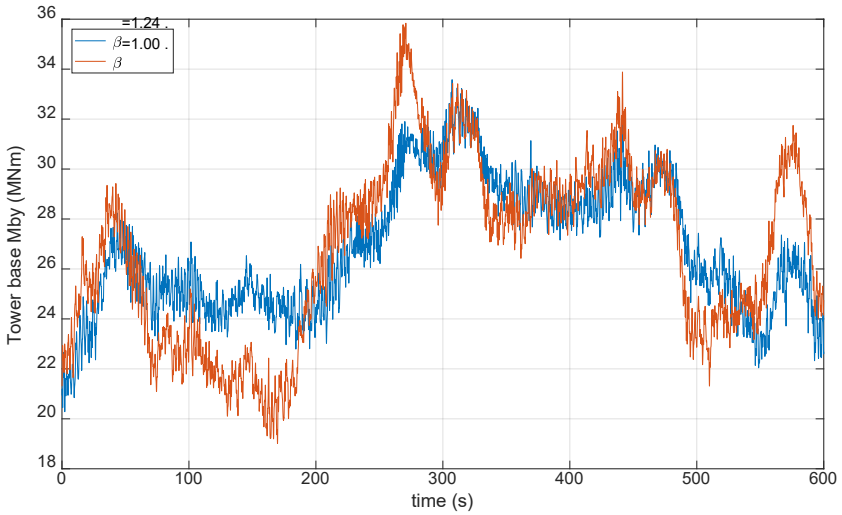

Figure 11-4. Simulated for-aft bending moment in tower base at 6 m/s mean wind speed and turbulence intensity 15%. Original coherence formulation (red) vs. modified (blue).

It should be noted here that the modification to the standard coherence model was implemented for vertical as well as lateral separations. Since the high mast at Hornamossen measures across several different *layers* (i.e. *roughness sublayer, surface layer, mixed layer*), there is a reason to assume that the lateral two-point correlation is stronger for separations within the size of a large rotor. One way to further investigate this could be to analyse detailed LES simulations over a forest canopy.

11.3 SUMMARY AND CONCLUSIONS

A modern-size class IIB wind turbine model with 126 m rotor diameter, 117 m hub height and rated power of 3.6 MW, was developed by scaling an existing class IB design. The resulting turbine design is believed to be of relevant type and scale for wind farm projects in the Scandinavian inland. A model for two-point correlation in the turbulent rotor inflow proposed in chapter 8 was here implemented in procedures for aeroelastic load simulations. Initial results show that the modified formulation has a significant influence on calculated tower base for-aft bending moment.

12 Executive summary and conclusions

Within project Forestwind, Wind power in forests II, researchers from Uppsala University, WeatherTech Scandinavia, the Royal Institute of Technology (KTH), Chalmers University of Technology and Teknikgruppen have been cooperating. Atmospheric turbulence measurements with very high vertical resolution have been carried out, in order to develop better theoretical descriptions of the observed properties. Several mesoscale and LES models have also been used to model the winds and turbulence above forests. A new linearised wind flow model with a dedicated forest module was developed. Synthetic turbulence descriptions were improved and compared with measurements. Airborne laser data from Swedish forest was analysed over the site. Forest effects on wind turbine energy production were studied. Finally, load simulations were carried out with aeroelastic wind turbine simulations using the new/improved model for synthetic turbulence.

Some important results are:

Wind resource at very high heights - Section 2

Wind profiles at very high heights (up to 150-250 m height depending on the site) were studied using measurements from three tall masts (Hornamossen, Ryningsnäs and a site in Östergötland) as well as two Sodars (Luleå and Ronneby airport) and one Lidar (Havsnäs wind farm). For wind speed, a logarithmic, linear and log-linear wind profile was tested in conjunction with the power law. For wind direction, a linear profile was used. Both 10-minute averages as well as wind direction sector averages were studied. The log-linear profile outperformed, on average, both for 10-minute averaged as well as for sector-averaged wind profiles. The Power law slightly outperformed the logarithmic wind law, except for Hornamossen where both performed approximately equally well. At Luleå, a linear wind profile slightly outperformed the power law, on average. Indeed, it was found that, quite often, the 10-minute average wind profile is linear, rather than following a logarithmic/power law.

For Ryningsnäs and the Östergötland site, wind shear, on average, decreased slightly with height from the lower half of the profiles to the upper half of the profiles. At Luleå, Ronneby and Havsnäs wind shear increased slightly with height. At Hornamossen, on the other hand, wind shear decreased strongly (by about 10%) with height. There is a lot of variation in 10-minute average wind shear exponents due to stability effects. Above a wind speed of 12 m/s or so, neutral stratification can be assumed and wind shear exponents are almost constant.

Wind shear exponents from the lower half of the profiles correlate well with wind shear exponents of the full profiles, indicating that measuring wind shear over the lower half of the rotor only could be enough. Wind shear exponents derived from two heights only agree excellently with wind shear exponents from curve fitting using multiple heights.

Wind direction profiles follow a linear expression very well. Most of the time wind direction (in degrees) increases with height. Wind direction changes with height were on average roughly 5°, 13° and 15° per 100 m height difference at

Hornamossen, Ryningsnäs and the Östergötland site. At Ronneby, Luleå and Havsnäs, this was 4°, 6° and 5° respectively, per 100 m height difference.

Turbulence and wind measurements - Section 3

Wind profiles and turbulence was measured at Hornamossen with 10 cup and 8 sonic anemometers. Also, temperature profiles (9 levels) were measured. Airborne laser scans from the site to characterize the forest show that the forest around the site has a patchwork character, i.e. is far from homogeneous. Measurements taken within the project, as well as those from the New European Wind Atlas program are described.

Sonic anemometers were corrected for wind speed magnitude and wind direction, which was necessary due to inadequate calibration and mounting precision. Wind and turbulence profile measurements from 6 measurement systems concurrently for one month show good agreement in terms of mean wind speed. However, turbulence profiles from the same systems differ hugely. The reasons for the different turbulence magnitudes are instrument response times for the cups and measurement volumes for the remote sensing instruments.

Analysis of turbulence data – Section 4

An analysis of turbulence measurements from Hornamossen and Ryningsnäs, split into different bins of atmospheric stratification as well as daytime and night conditions, shows that the average long-term wind profile is biased to stable stratification (neutral conditions are not a good approximation). There is a large difference between day and night and the wind veer is considerable at night times and in stable stratification.

Second-order turbulence moments (variances and covariances) decrease more rapidly with height at Hornamossen than at Ryningsnäs but the qualitative behavior with stratification is the same (also for skewness). Standard deviations follow roughly $\sigma_u \approx 2u_*$, $\sigma_v \approx 1.6u_*$ and $\sigma_w \approx 1.4u_*$ for both sites. Turbulence intensity is generally much larger during the day than during the night, apart from during the very highest wind speeds. The long term averaged turbulence intensity did not follow the IEC standard but instead showed lower than expected values below rated wind speed and higher than expected values above rated wind speed. In strictly neutral conditions turbulence intensity is constant with respect to wind speed.

Turbulence intermittence during otherwise calm (nearly laminar) periods was found to be common occurring roughly 20-25 % of the time. During such conditions sudden bursts of turbulence were found to be quite common occurring about 100 times a year. Median lengths of these bursts were around 20 minutes. This is usually not taken into account and could have considerable influence on operation and loads of wind turbines.

New linear wind-flow model ORFEUS – Section 5

A new linearised wind-flow model with a dedicated forest module (ORFEUS) was developed. The model was compared to Open-FOAM and to data from Hornamossen and Ryningsnäs. The new model is an improvement to other wind flow models that only use surface roughness and zeroplane displacement as input in terms that it uses vertical profiles of forest-density as input.

Mesoscale model simulations – Section 6

Model simulations with the WRF model and the MIUU model were carried out with different surface roughness fields as input as well as with different turbulence schemes. There are large differences in mean wind profiles for different roughness and turbulence parameterisations.

The MIUU-model was used together with the MIUU-method to estimate the wind resource at Ryningsnäs and Hornamossen. Different sources for roughness length and zero-plane displacement were tested. Generally roughness lengths estimated from laser scanning data are higher than what is estimated from land use data following generally used relations. Also, this yields better model performance. At Ryningsnäs, however, the use of laser scanning data did not give any difference in modelled mean wind profile as compared to the use of land-use databases.

LES model simulations – Section 7

Chalmers LES-model was run with input from WRF. In addition, WRF-LES was run.

A method was developed to specify inflow boundary conditions to Chalmers LES-model from WRF-data. Two methods were tested to introduce turbulent winds (vortices) at the lateral boundaries of the LES model domain: Statistical perturbation using synthetic turbulence and a so-called pre-cursor run with the same LES-model, but with periodic boundary conditions. For WRF-LES another perturbation method was tested.

The results are inconclusive and more research is needed as to what perturbation method should be used.

Synthetic turbulence – Section 8

It has been shown how high-resolution site data can be used to describe the turbulence characteristics over the rotor in detail. Improved site-specific wind descriptions will in many cases mean better possibilities for site optimization, and help to reduce uncertainties in the suitability assessment. It was demonstrated how spectral models given in the international standard IEC 61400-1 can be adjusted to reach reasonable correspondence with measured turbulence data. The problem with the IEC 61400-1 turbulence model is a lack of effects of atmospheric stratification. The IEC turbulence model fits neutral and daytime data rather well, but disagrees during nights. An improved version of the IEC turbulence model (the Segalini & Arnqvist 2015 model) where the effects of stratification are included is used. In the IEC turbulence model, vertical two point coherence is overestimated

compared to measurements. A modification of the coherence in the IEC turbulence model is suggested based upon measurements.

Analysis of airborne laser data – Section 9

Three (including one newly developed) methods were used to derive forest densities from airborne laser scans (ALS). Several methods of converting forest densities into roughness lengths and displacement height have been described. Two of the formulations are new. It was found that roughness sublayer effects are important to find estimates that agree with the measured wind profiles from Ryningsnäs and Hornamossen. The method of Raupach (1994) seems to work best when the estimation of roughness and displacement is made on a fine grid and subsequently averaged, while for the other methods it was better to first average the forest densities and then compute the roughness and displacement from the average forest density.

When using WAsP, ALS improved the estimation compared to standard surface data sets and minimized the risk of making large prediction errors. Roughness length was calculated as 0.1h and displacement as 0.75h, which seemed to give reasonable estimates, but omits the effect forest density has on the parameters.

Forest heights and PAI from ALS, using the newly developed model, were compared to official estimates of forest tree height and biomass from Skogsstyrelsen, showing good agreement. It was suggested that using Skogsstyrelsen data might be a good idea as it is continuously updated for clear-cuts etc.

Forest effects on power production - Section 10

Wind shear and veer are included in the newly proposed Rotor Equivalent Wind Speed (REWS) to be used instead of hub height wind speed (HHWS) in power curves (IEC 2017). However, no good turbulence correction method exists at present. REWS for Hornamossen, Ryningsnäs and the Östergötland site were very well correlated to hub height wind speeds. Using REWS in manufacturer power curves instead of HHWS resulted in AEP differences of less than ≈ ±1%.

The effect of turbulence on produced power was modelled by a simple Gaussian distribution model yielding a frequency distribution for the turbulent wind speed deviation U′ valid for the whole rotor area. The model seems to adequately describe TI effects on the power curve. However, a laminar power curve (which has to be estimated or modelled) has to be used as input.

Power output from a wind farm in a forest in southern Sweden was analysed using SCADA data only. After correction nacelle transfer functions (NTFs) power curves agreed well with the manufacturer power curve. There was a clear effect of TI (approximated by nacelle anemometer TI) on the power curve.

The use of REWS is believed to yield differences in AEP of less than ±1%. The same is true for turbulence effects, which are thought to amount to additional differences in AEP of maximum ±1%. In the worst case this could add up to ±2% difference in AEP.

Load simulations – Section 11

A generic open-source wind turbine was developed from several open-source wind turbines. The new open-source turbine was used for load studies in conjunction with the newly developed modifications of the IEC synthetic turbulence model. The low vertical turbulence coherence across the rotor (based upon measurements from Hornamossen and Ryningsnäs) yields lower loads compared to the original IEC turbulence model. Other characteristics of Swedish forest wind conditions, such as short turbulent length scales during night or highly sheared gusts, were found to be less important for wind turbine loads.

13 Discussion

In the project “Forestwind - Wind power in forests II”, research has continued following project “V312 – Wind power in forests”. Research has gone along several paths with the main goal to better understand the mean wind and turbulence properties in the boundary layer above forest.

An ultimate goal would be to be able to describe winds across the whole rotor diameter at every second during an entire year or so. This, however, will probably never be possible. Part of that, however, can be achieved by either LES modelling or synthetic turbulence combined with a mean air flow. For that reason both of these areas were included in the project.

The project has shown that LES models can be used to gain valuable knowledge on turbulent flows in the wind farm area. One issue with running LES models for real weather conditions, however, is that turbulent wind fields at the inflow boundaries have to be introduced. This can be done using several methods. Here, a pre-cursor method was suggested. Synthetic turbulence is another possibility. A third possibility that was used in WRF-LES are potential temperature perturbations. More research is needed to solve this problem.

Wind conditions at very high heights were studied with both measurements and mesoscale modelling. The atmospheric measurements have resulted in a large number of high quality wind and turbulence data up to 180 m height. The project also acquired data from another 150 m high mast with high quality measurements. In addition to that, Sodar and Lidar data was studied. Wind profile relationships were studied and it was found that the power law that is very frequently used in the industry compares slightly better to measurements than the logarithmic law. This is valid for both 10-minute averages and sector-wise average profiles. Shear exponents for a hypothetical full rotor were found to be well correlated to those from the lower half of the hypothetical rotor. Shear exponents seem to be approximately constant with height over forest except for sites with considerable topographical speed-up such as Hornamossen. Wind direction was found to vary linearly with height to a good degree.

Turbulence was studied with both measurements from masts and remote sensing devices. Remote sensing devices, however, seem to show varying results. Turbulence statistics were computed and compared to our previous mast in Southern Sweden (Ryningsnäs). Of special interest here is how turbulence intensity varies with height as well as how coherent turbulent winds are across a wind turbine rotor. A large number of turbulence statistics have been presented using the atmospheric data from Ryningsnäs and Hornamossen. Also it is interesting to see if the IEC turbulence class for wind turbines (class A, B and C) is complied with. Another subject studied is intermittent turbulence, i.e. a sudden spike in turbulence during otherwise calm (near-laminar) conditions. This was found to occur quite frequently during nighttime and stable conditions. If this is important for wind turbine loads has yet to be shown.

A new linearised model with a dedicated forest module was developed. The model seems to be better with respect to forest compared to WAsP and windPRO in that respect that it includes forest density profiles and not only surface roughness and displacement height.

Although measurements, which commonly are just available at single sites, may form the main basic knowledge about the wind conditions, models are needed in order to transfer this knowledge to other sites where wind power might be developed. Therefore, mesoscale models have been used and compared to the measured wind profiles at Hornamossen and Ryningsnäs. The results indicate that mesoscale models sometimes overestimate winds over forest in other cases wind speed predictions were spot on. Therefore, the sensitivity to surface roughness and in the case of WRF also the turbulence scheme was studied. Default values are usually not a good choice.

Airborne laser scans (ALS) of forests yield much more accurate knowledge over the forest canopy. This however has to be translated into surface roughness, displacement height and forest density profiles. There exist several methods for doing this. However, another question is how this should be spatially averaged if the grid size of the model is of the order of 1 km^2 or so. The project has looked at all these issues. Clearly, more research is needed to get definite conclusions.

The project also studied and improved the description of synthetic turbulence by the IEC-standard for wind turbine design (the Mann model). An improvement of the synthetic turbulence model was developed for stable atmospheric conditions that occur very often in Sweden. The new model was validated against measurements. In addition, turbulence coherence functions and phase profiles were improved.

The advantage of using atmospheric data compared to synthetic turbulence is that it is collected in an environment where wind turbines actually are supposed to work. A drawback, however, is that atmospheric turbulence data is very expensive to obtain.

The new synthetic turbulence model, proposed herein, yields less correlation of turbulent winds across the rotor yielding lower loads. This was shown through aero-elastic wind turbine simulation. By developing a generic open-source wind turbine model for typical Swedish sites from several available open source turbines, loads can be studied further, also including controller settings that usually are confidential.

The predecessor project “V312 – Wind power in forest” recommended carrying out research about winds and turbulence higher up in the boundary layer (up to about 250 m height). This was done in the current project. However, our knowledge for wind power sites in northern Sweden is still limited. Also research on LES modelling and forest modelling should be continued.

14 References

Albers, A., 2012: Modelling Impact of Non-Standard Conditions. Proceedings of Power Curve Working Group, 1st meeting, 4 December 2012, London, UK. [Available at http://www.pcwg.org/proceedings/2012-12-04/WTWG-04Dec2012-06-AA-WG-Power_Curve_Modelling_WindGuard.pdf]

Arias, F., and Soria E., 1996: Strength and fatigue testing of large size wind turbine rotors. Vol. II: Fullsize natural vibration and static strength test, a reference case. Technical report, CIEMAT-816, 1996

Arnqvist, J., 2015: Mean wind and turbulence conditions in the boundary layer above forests, PhD thesis, Acta Universitatis Upsaliensis, Uppsala University. http://urn.kb.se/resolve?urn=urn:nbn:se:uu:diva-237764

Arnqvist, J., Segalini, A., Dellwik, E. et al., 2015: Wind Statistics from a Forested Landscape. *Boundary-Layer Meteorol*., **156**:53. https://doi.org/10.1007/s10546-015-0016-x

Atkinson, N., S. Baylis, M. Colls, P. Marek, 2015: Turbine performance prediction. Proceedings from EWEA workshop Resource Assessment, 2-3 June 2015, Helsinki, Finland. [Available on http://www.ewea.org/events/workshops/past-workshops/resource-assessment-2015/proceedings-oral-presentations/]

Barthelmie, R. J., S. T. Frandsen, M. N. Nielsen, S. C. Pryor, P.-E. Rethore and H. E. Jørgensen, 2007: Modelling and Measurements of Power Losses and Turbulence Intensity in Wind Turbine Wakes at Middelgrunden Offshore Wind Farm. *Wind Energy* 2007; **10**:517–528.

Baylis, S., M. Colls, P. Marek and A. Head, 2014: Parameterised turbine performance. Proceedings 9th meeting of the Power Curve Working Group, 16 December 2014, Glasgow, Scotland. [Available at http://www.pcwg.org/]

Belcher SE, Jerram N, Hunt JCR. 2003 Adjustment of a turbulent boundary layer to a canopy of roughness elements. *J. Fluid Mech.* **488**, 369–398. (doi:10.1017/S0022112003005019)

Bergström, H., 2002: Boundary-layer modelling for wind climate estimates. *Wind Engineering* **25**(5): 289-299.

Bergström, H., and Söderberg, S., 2009: Wind mapping of Sweden – Summary of results and methods used. Elforsk Report 09:04, 84 pp.

Bergström, H., and Söderberg, S., 2011: Beräkning av vindklimatet i Sverige med 0,25 km^2 upplöösning med hjälp av MIUU-modellen. WeatherTech Scandinavia AB, 18 pp. https://www.energimyndigheten.se/globalassets/fornybart/framjande-av-vindkraft/vindkartering/slutrapport-uppdatering-av-vindkarteringen.pdf

Bergström, H., Alfredsson, H. Arnqvist, J., Carlén, I., Dellwik, E., Fransson, J., Ganander, H., Mohr, M. Segalini, A., and Söderberg, S., 2013: Wind power in forests, Winds and effects on loads. Elforsk rapport 13:09, 167 pp.

Bernadett, D. W., 2013: Use of 5 Distinct Power Curves As a Function of Shear and Turbulence In Time-Series Energy Capture Calculations. Proceedings from 2nd meeting of the Power Curve Working Group, 12 March 2013, Remisen Brande, Denmark. [Available at http://www.pcwg.org/]

Bernadett, D. W. (2014): Calculating site specific power curve loss estimates. Proceedings from Power Curve Working Group, 6th meeting, 1 April 2014, Risø Campus, Roskilde, Denmark. [Available at http://www.pcwg.org/]

Bernadett, D., 2016: Power curve loss adjustments at AWS Truepower: a 2016 update. Proceedings from 20th meeting of the Power Curve Working Group, 29 September 2016, Minneapolis, US. [Available at http://www.pcwg.org/]

Boudreault, L-E., Bechmann, A, Taryainen, L, Klemedtsson, L, Shendryk, L and Dellwik, E, 2015: A LiDAR method of canopy structure retrieval for wind modeling of heterogeneous forests Agricultural and Forest Meteorology, Vol. 201, 2015, p. 86-97.

Brady, O., 2013: How can CFD models complement measurements? Proceedings from Power Curve Working Group, 4th meeting, 19 September 2013, Aarhus, Denmark. [Available at http://www.pcwg.org/proceedings/2013-09-19/07a-The-role-CFD-Modelling-Oisin-Brady-Natural-Power.pdf]

Byrkjedal, Ø. and E. Åkervik, 2009: Vindkart for Norge, NVE rapport nr 9/2009, 34 s.

Chougule, A. S., Mann, J., & Kelly, M. C., 2013: Infulence of atmospheric stability on the spatial structure of turbulence. Kgs. Lyngby: Technical University of Denmark (DTU).

Chougule, A., J. Mann, M. Kelly, and G.C. Larsen, 2017: Modeling Atmospheric Turbulence via Rapid Distortion Theory: Spectral Tensor of Velocity and Buoyancy. *J. Atmos. Sci.*, 74, 949–974, https://doi.org/10.1175/JAS-D-16-0215.1

Chougule, A., Mann, J., Kelly, M. and G.C. Larsen, 2018: Simplification and Validation of a Spectral-Tensor Model for Turbulence Including Atmospheric Stability. *Boundary-Layer Meteorol.* **167**:371. https://doi.org/10.1007/s10546-018-0332-z

Clerc, A., 2013: PCWG Validation Analysis. Proceedings from Power Curve Working Group, 5th meeting, 4 December 2013, Glasgow, UK. [Available at http://www.pcwg.org/proceedings/2013-12-04/04-Validation-Analysis-Alex-Clerc-RES.pdf]

Clifton, A., 2013: Using Machine Learning To Create Turbine Performance Models. Proceedings of Power Curve Working Group, 2nd meeting, 12 March 2013, Remisen Brande, Denmark. [Available at http://www.nrel.gov/docs/fy13osti/58314.pdf]

Dahlberg, J.-Å., 2009: Vattenfall Vindkraft AB - Mätningar i Ryningsnäs. Proceedings *Nationella Vindkraftskonferensen 2009*. 7-8 May 2009, Kalmar, Sweden.

Davidson, L. and Peng, S.-H. (2003), Hybrid LES-RANS: A one-equation SGS Model combined with a k-omega for predicting recirculating flows, International Journal for Numerical Methods in Fluids, Vol. 43, Number 9,, pp. 1003-1018.

Derrick, A., N. Atkinson, I. Campbell, A. Clerc, J. Cronin, A. Ely, S. Feeney, G. Hutton, M. Lannic, M. MacDonald, A. Oram, 2013: *Havsnäs – Pilot project report on cold climate and high hub height*, Renewable Energy Systems Ltd/NV Nordisk Vindkraft AB, Gothenburg, Sweden.

Derrick, A. and A. Oram, 2014: Illustrating the Importance of Site Specific PC. Proceedings from Power Curve Working Group, 6th meeting, 1 April 2014, Risø Campus, Roskilde, Denmark. [Available at http://www.pcwg.org/]

Donlon, C. J., M. Martin, J. D. Stark, J. Roberts-Jones, E. Fiedler and W. Wimmer, 2011: The Operational Sea Surface Temperature and Sea Ice analysis (OSTIA). *Remote Sensing of the Environment.* doi: 10.1016/j.rse.2010.10.017

Ebenhoch, R., Muro, B., Dahlberg, J.-Å., Berkesten Hägglund, P., and Segalini, A., 2016: A linearised numerical model of wind farm flows. *Wind Energy, 20*, 859–875.

Emeis, S., 2013: *Wind Energy Meteorology, Atmospheric Physics for Wind Power Generation*, Springer, 198 pp.

Etling, D., 2008: *Theoretische Meteorologie*. Springer, Berlin, 3. edition.

Fiedler, F., Panofsky, H. A., 1972: The geostrophic drag coefficient and the 'effective' roughness length. *Quart. J. Roy. Met. Soc.*, **98** (415), 213-220, https://doi.org/10.1002/qj.49709841519.

Floors, R., Enevoldsen, P., Davis, N., Arnqvist, J., and Dellwik, E. 2018: From lidar scans to roughness maps for wind resource modelling in forested areas, *Wind Energ. Sci.*, **3**, 353-370, https://doi.org/10.5194/wes-3-353-2018, 2018.

Freier, J., 2017: Approaches to characterise forest structures for wind resource assessment using airborne laser scan data, 111 pp. Kassel University, Master Thesis.

Ganander H., 2003: The use of a code generating system for the derivation of the equations for wind turbine dynamics. *Wind Energy* , 2003; **6:4** 333-345.

Geer, T., 2015: ENERGY. An Advanced Understanding of the Impact of Deviations in Turbine Performance. Proceedings from EWEA workshop Resource Assessment, 2-3 June 2015, Helsinki, Finland. [Available on http://www.ewea.org/events/workshops/past-workshops/resource-assessment-2015/proceedings-oral-presentations/]

Göçmen, T. and G. Giebel, 2016: Estimation of turbulence intensity using rotor effective wind speed in Lillgrund and Horns Rev-I offshore wind farms. *Renewable Energy*, **99**, 524-532.

Grol, H.J. van, Bulder, B.H., 1993: Procedures to determine the fatigue life for large size wind turbines. Technical report ECN-RX--93-030, 1993.

Gryning, S.-E., E. Batchvarova, B. Brümmer, H. Jørgensen, and S. Larsen, 2007: On the extension of the wind profile over homogeneous terrain beyond the surface boundary layer. Bound.-Layer Meteor., **124**, 251–268.

Harman, I. N. and J. J. Finnigan, 2007: A simple unified theory for flow in the canopy and roughness sublayer. *Boundary-Layer Meteorol.* **123**:339–363.

Hopkinson C, Chasmer L., 2007: Modelling canopy gap fraction from lidar intensity. *Proceedings of ISPRS Workshop on Laser Scanning 2007 and SilviLaser 2007*, Espoo, Finland.

Högström, U. 1996: Review of some basic characteristics of the atmospheric surface layer, *Boundary-Layer Meteorol* 78: 215. https://doi.org/10.1007/BF00120937

Højstrup, J., 2014: The influence of inflow angle on the power curve, *Proceedings 8th meeting of the Power Curve Working Group*, 6 October 2014, Vaisala, Louisville, Colorado. [Available at http://www.pcwg.org/]

IEC, 2005: *Wind turbines - Part 1: Design requirements*. IEC 61400-1, Third edition, 2005-08.

IEC, 2017: Wind energy generation systems – Part 12-1: *Power performance measurements of electricity producing wind turbines*. IEC 61400-12-1, Edition 2.0.

Inoue, E. 1963: On the structure of airflow within crop canopies J. met. Soc. Japan (Ser. II), 41 (1963), pp. 317-326

Jackson, P.S., 1981: On the displacement height in the logarithmic velocity profile. *J Fluid Mech* 111:15–25.

Jacobsen, H. S., 2014: Wind shear exponents, Frequently asked Questions, WASP. Available at http://www.wasp.dk/support-and-services/faq#general__wind-shear-exponents

Jarvis, P.G., 1976: The Interpretation of Variations in Leaf Water Potential and Stomatal Conductance Found in Canopies in the Field, *Philosophical Transactions of the Royal Society of London, Series B, Biological Sciences*, **273**, 93--610. doi:10.1098/rstb.1976.0035

Jonkman, J., Butterfield, S., Musial, W., and Scott, G., 2009: Definition of a 5-MW Reference Wind Turbine for Offshore System Development. *National Renewable Energy Laboratory Technical Report*, NREL/TP-500-38060, Golden, CO.

Kelly, M., 2014: Probabilistic Atmospheric characterization: relevant Shear and Turbulence Intensity statistics. Towards effective specification for power curves, loads, ... Proceedings from *Power Curve Working Group*, 6th meeting, 1 April 2014, Risø Campus, Roskilde, Denmark. [Available at http://www.pcwg.org/]

Khatab, A. M., 2017: Performance analysis of operating wind farms. *Master thesis*. Uppsala University, 70 p. [Available at http://www.diva-portal.org/smash/get/diva2:1150284/FULLTEXT01.pdf]

Konow, H. M., 2015,: Tall Wind Profiles in Heterogeneous Terrain. *Dissertation from University of Hamburg*, 103 p. [Available at https://d-nb.info/1068316713/34]

Landberg, L., 2015,: *Meteorology for Wind Energy: An Introduction*, Wiley, 224 pp.

Lantmäteriet, 2018 : Produktbeskrivning: Laserdata NH. Document version 2.4. *Technical report*, Lantmäteriet, Sweden [Available at https://www.lantmateriet.se/globalassets/kartor-och-geografisk-information/hojddata/laserdata_nh.pdf

Lezaun Mas, I., 2014: REWS EWEA Power Curve Working Group. Proceedings from *Power Curve Working Group*, 6th meeting, 1 April 2014, Risø Campus, Roskilde, Denmark. [Available at http://www.pcwg.org/]

Liu, B., 2011: Wind turbine power performance verification by anemometer on the nacelle. *Nowitech Wind Power R&D Seminar 2011*, Trondheim, Norway. https://www.sintef.no/globalassets/project/nowitech/poster-phd-2011/bing-liu_postera4-1_jan2011.pdf

Liu, Y., Warner, T., Liu, Y.. Vincent, C. L., Wu, W., Mahoney, B., Swerdlin, S., Parks, K., Boehnert, J., 2011: Simultaneous nested modeling from the synoptic scale to the LES scale for wind energy applications. *J. Wind Eng. Ind. Aerodyn.* **99**:308–319. https://doi.org/10.1016/j.jweia.2011.01.013

Lopes, A.S., Palma, J.M.L.M. & Piomelli, U. 2015: On the Determination of Effective Aerodynamic Roughness of Surfaces with Vegetation Patches. *Boundary-Layer Meteorol* **156**:113. https://doi.org/10.1007/s10546-015-0022-z

Mann, J. (1994): The spatial structure of neutral atmospheric surface-layer turbulence. *Journal of fluid mechanics*, 273, 141-168.

Mann, J., 1998: Wind field simulation. *Probabilistic engineering mechanics* **13**(4), 269-282.

Mirocha et al., 2014: Large eddy simulation of wind turbine wake dynamics in the stable boundary layer using the Weather Research and Forecasting Model. Journal of *Renewable and Sustainable Energy* **6**(3):033137, DOI: 10.1063/1.4885111.

Mohr, M., 2018: *Analysis of Sodar Data from Swedish Defence*. Internal report available on request.

Mohr, M., 2018: *Power Curve Summary Report*. Internal report available on request.

Monsi, M., Saeki, T., 1953: Über den Lichtfaktor in den Pflanzengesellschaften and seine Bedeutung für die Stoffproduktion, *Jpn. J. Bot.*, **14**, 22-53.

Moriarty, P., 2012: Power Curve Working Group. Proceedings of Power Curve Working Group, 1st meeting, 4 December 2012, London, UK. [Available at http://www.pcwg.org/proceedings/2012-12-04/WTWG-04Dec2012-09a-PM-NREL-Discussion-Points.pdf]

Muñoz-Esparza, D. et al., 2015. A stochastic perturbation method to generate inflow turbulence in large-eddy simulation models: Application to neutrally stratified atmospheric boundary layers. *Physics of Fluids*, 27(3). doi: http://dx.doi.org/10.1063/1.4913572.

Nebenführ, B. and Davidson, L., 2014: Influence of a forest canopy on the neutral atmospheric boundary layer - a LES study. *Proceedings of 10th International ERCOFTAC Symposium on Engineering Turbulence Modeling and Measurements (ETMM10)*, Marbella, Spain, 17-19 September.

Nebenführ, B. and Davidson, L., 2015: Large-Eddy Simulation Study of Thermally Stratified Canopy Flow, *Boundary-Layer Meteorol.*, **156**:2, 253-276, doi=10.1007/s10546-015-0025-9.

Ormel, F., 2015: Presentation of Power Curve Uncertainty to PCWG. *Proceedings from Power Curve Working Group*, 11th meeting, 8 May 2015, Glasgow, Scotland. [Available at http://www.pcwg.org/]

Peña, A., S.-E. Gryning, and C. Hasager, 2010: Comparing mixing-length models of the diabatic wind profile over homogeneous terrain. *Theor. Appl. Climatol.*, **100**, 325–335.

Peña, A., R. Floors, A. Sathe, S.-E. Gryning, R. Wagner, M. S. Courtney, X. G. Larsén, A. Hahmann, C. B. Hasager, 2016: Ten Years of Boundary-Layer and Wind-Power Meteorology at Høvsøre, Denmark. *Boundary-Layer Meteorol*. **158**:1-26. DOI 10.1007/s10546-015-0079-8

Raupach, M.R., 1994: Simplified expressions for vegetation roughness length and zero-plane displacement as functions of canopy height and area index, *Boundary-Layer Meteorol*. **71**: 211. https://doi.org/10.1007/BF00709229.

Resor, B.R., 2013: Definition of a 5 MW/61.5 m Wind Turbine Blade Reference Model. *Technical Report SAND2013-2569*, Sandia National Laboratories: Albuquerque, NM, USA, 2013.

Ribeiro, C., 2014: A Study of Turbine performance under cold weather driven stable atmospheric conditions in Scandinavia (PDF). *Proceedings from Power Curve Working Group*, 6th meeting, 1 April 2014, Risø Campus, Roskilde, Denmark. [Available at http://www.pcwg.org/]

Rivera Lamata, R. and D. Pollack, 2014: Turbulence Intensity measurements offshore for power curve verification and wind resource assessment. *Proceedings from Power Curve Working Group*, 8th meeting, 6 October 2014, Vaisala, Louisville, Colorado. [Available at http://www.pcwg.org/]

Schepers J.G., 2001: VEWTDC: Verification of European Wind Turbine Design Codes - Final Report for JOR3-CT98-0267 Joule III project, ECN-C-01-055, 2001.

Segalini, A., Arnqvist, J., 2015: A spectral model for stably stratified turbulence. *Journal of FluidMechanics*, **781**, 330-352, doi=10.1017/jfm.2015.502.

Segalini, A., Nakamura, T., and Fukagata, K., 2016: A linearised k-ε model of forest canopies and clearings. *Bound.-Lay. Meteorol., 161*, 439–460.

Segalini, A., 2017: Linearised simulation of the flow over wind farms and complex terrains, *Phil. Trans. R. Soc. A, 375*, 20160099.

Shaw, R. H., and Patton, E. G., 2003: Canopy element influences on resolved-and subgrid-scale energy within a large-eddy simulation. *Agric For Meteorol* **115**:1, 5-17.

Shinozuka, M. and Jan, C. M., 1972: Digital simulation of random processes and its applications. *J. Sound Vib.*, 1972; **25**:111–128.

Sieros, G.; Chaviaropoulos, P., Sørensen, J.D., Bulder, B.H., Jamieson, P., 2012: Upscaling Wind Turbines: Theoretical and Practical Aspects and Their Impact on the Cost of Energy. *Wind Energy* 2012; **15**:3–17.

Skamarock, W. C., J. B. Klemp, J. Dudhia, D. M. Gill, M. Duda, X.-Y. Huang, W. Wang, and J. G. Powers, 2008: A Description of the Advanced Research WRF Version 3. *NCAR Technical Note*.

Skibin, D. and J. A. Businger, 1985: The vertical extent of the log-linear wind profile under stable stratification. *Atmospheric Environment* **19**:1, 27-30.

Stangroom, P., 2004: CFD modelling of wind flow over terrain. *PhD thesis*, University of Nottingham. [Available at http://eprints.nottingham.ac.uk/10112/1/Stangroom.pdf]

St. Martin, C. M., J. K. Lundquist, A. Clifton, G. S. Poulos, and S. J. Schreck, 2016: Wind turbine power production and annual energy production depend on atmospheric stability and turbulence. *Wind Energ. Sci.*, 1, 221–236.

St. Martin, C. M., J. K. Lundquist, A. Clifton, G. S. Poulos, and S. J. Schreck, 2017: Atmospheric turbulence affects wind turbine nacelle transfer functions. *Wind Energ. Sci.*, **2**, 295-306. https://doi.org/10.5194/wes-2-295-2017

Stevens, D., 2013: Power Curve Working Group #5: Potential validation dataset. *Proceedings from Power Curve Working Group*, 5th meeting, 4 December 2013, Glasgow, UK. [Available at http://www.pcwg.org/proceedings/2013-12-04/06a-Potential-validation-dataset-Daniel-Stevens-SSE.pdf]

Stuart, P., 2013: Introduction to the Power Curve Working Group. Proceedings from *EWEA workshop Resource Assessment*, 25-26 June 2013, Dublin, Ireland. [Available at http://www.ewea.org/events/workshops/wp-content/uploads/2013/06/EWEA-RA2013-Dublin-3-1-Peter-Stuart-RES.pdf]

Stuart, P., 2014a: 6th Meeting Minutes, Wednesday 1st April 2014, DTU Risø Campus, Roskilde, Denmark. *Proceedings from Power Curve Working Group*, 6th meeting, 1 April 2014, Roskilde, Denmark. [Available at http://www.pcwg.org/proceedings/2014-04-01/14-01-April-2014-MoM.pdf]

Stuart, P., 2014b: Overview of the Power Curve Working Group. *Proceedings from Power Curve Working Group*, 8th meeting, 6 October 2014, Vaisala, Louisville, Colorado. [Available at http://www.pcwg.org/]

Stuart, P., 2015: A New Theoretical Basis for Describing Low Turbulence Wind Turbine Performance. *Proceedings from Power Curve Working Group*, 13th meeting, 15 September 2015, New Orleans, United States. [Available at http://www.pcwg.org/]

Stull, R., 1988: *An Introduction to Boundary Layer Meteorology*, Springer, 670 pp.

Talbot, Charles Talbot, Elie Bou-Zeid, and Jim Smith, 2012: Nested Mesoscale Large-Eddy Simulations with WRF: Performance in Real Test Cases. *J. of Hydrometeorology*, 1421-1441. https://doi.org/10.1175/JHM-D-11-048.1

Tindal, A., 2013b: Turbine Performance in "Non-Standard" Wind Conditions Wind Energy Working Group -Review of Previous Meetings. Proceedings from *Power Curve Working Group*, 3rd meeting, 30 May 2013, Hamburg, Germany. [Available at http://www.pcwg.org/proceedings/2013-05-30/02-Review-of-Previous-Meetings-Andrew-Tindal-GLGH.pdf]

Turkyilmaz, U., J. Hansson and O. Undheim, 2016: Use of remote sensing for performance optimization of wind farms - Assessment and optimization of the energy production of operational wind farms: Part 2. *Energiforsk report* **2016:298**, 72 pp.

Tüxen, E., 2014: Type B Effects. *Proceedings from Power Curve Working Group*, 6th meeting, 1 April 2014, Roskilde, Denmark. [Available at http://www.pcwg.org/]

Van de Wiel, B.J., R.J. Ronda, A.F. Moene, H.A. De Bruin, and A.A. Holtslag, 2002: Intermittent Turbulence and Oscillations in the Stable Boundary Layer over Land. Part I: A Bulk Model. *J. Atmos. Sci.*, 59, 942–958, https://doi.org/10.1175/1520-0469(2002)059<0942:ITAOIT>2.0.CO;2

Vanderwende, B. J. and J. K. Lundquist, 2012: The modification of wind turbine performance by statistically distinct atmospheric regimes. *Environ. Res. Lett.*, **7,** 034035.

Veers, P. S., 1988: Three-Dimensional Wind Simulation. *Technical report SAND88-0152*, Sandia National Laboratories, March 1988.

Whiting, R. 2014b: Modelling type B effects in the 4th Quadrant using BLADED. *Proceedings 9th meeting of the Power Curve Working Group*, 16 December 2014, Glasgow, Scotland. [Available at http://www.pcwg.org/]

Wilkinson, M., 2014: Long-term Performance of Wind Farms. *Proceedings EWEA workshop Analysis of Operating Wind Farms*, 9-10 December 2014, Malmö, Sweden. [Available on http://www.ewea.org/events/workshops/past-workshops/operational-assessment-2014/]

Winkelaar, D., 1991: Fast three-dimensional wind simulation of stochastic blade loads. *Proceedings of the 10th ASME Wind Energy Symposium*, 20–24.

15 Publications and presentations

15.1 DISSERTATIONS

Arnqvist, J. (2015): Mean Wind and Turbulence Conditions in the Boundary Layer above Forests. Digital Comprehensive Summaries of Uppsala Dissertations from the Facilty of Science and Technology 1212. See http://www.diva-portal.org/smash/get/diva2:698598/FULLTEXT01.pdf

Nebenführ, B. (2015): Turbulence-resolving simulations for engineering applications. *Doktorsavhandlingar vid Chalmers tekniska högskola*. Ny serie nr. 3935. Se http://publications.lib.chalmers.se/records/fulltext/220828/220828.pdf

15.2 CONFERENCE PRESENTATIONS

Arnqvist, J. and Bergström H, 2016: Characterization of turbulence intermittency in the SABL through observations. Proceedings *EUROMECH Colloquium 576 "Wind Farms in Complex Terrains"*, Stockholm, June 8-10, 2016.

Arnqvist, J. and Segalini, A. 2015: Linear stability analysis of canopy flows. *The International Conference on Jets, Wakes and Separated Flows (ICJWSF)*, KTH, Stockholm, Sweden 15-17 Jun 2015.

Dellwik, E., Arnqvist, J., Cavar, D., Enevoldsen, P., and van der Laan, P. 2016: Aerial LIDAR scans for validation of CFD models in complex forested terrain. Abstract from *WindEurope Summit, Hamburg, Germany*

Dellwik, E., Papetta, A., Arnqvist, J., Nielsen, M., & Larsen, T. J. (2017). Inflow conditions and wake effects for wind turbines in forested terrain. *Abstract from WindFarms 2017, Lyngby, Copenhagen, Denmark.*

M. Mohr, J. Arnqvist and H. Bergström, 2016: Wind Energy Resource Assessment Is wind speed at hub height enough or are other meteorological parameters needed as well? *30th Nordic Meteorological Meeting*, 22-24 August 2016, Stockholm, Sweden.

Mohr, M. Arnqvist, J and Bergström, H. 2016: Influence of turbulence on wind turbine power curves. Proceedings *EUROMECH Colloquium 576 "Wind Farms in Complex Terrains"*, Stockholm, June 8-10, 2016.

Mohr, M. J. Arnqvist and H. Bergström, 2015: Wind resource, turbulence and electricity production in forests. Proceedings *Vindkraftsforskning i focus 2015*, Uppsala 6-7th of October. https://standupforwind.se/konferenser-med-samband-med-standup/vindkraftsforskning+i+fokus+2015/conference-presentations/

Mohr, M., Jayawardena, W., Arnqvist, J and Bergström H. 2014: Wind energy estimation over forest canopies using WRF mesoscale model, *Proceedings of EWEA Annual Event, Barcelona, Spanie*n, 10-13 March 2014.

15.3 SCIENTIFIC PAPERS

Alfredsson, P. H. and A. Segalini (2017), Wind farms in complex terrains: an introduction, *Phil. Trans. R. Soc. A* 375, 20160096.

Arnqvist, J. and Bergström, H. (2015). Flux-profile relation with roughness sublayer correction. *Quarterly Journal of the Royal Meteorological Society, 141(689), 1191-1197*.

Arnqvist, J., Bergrström, H. and Nappo, C. (2016). Examination of the mechanism behind observed canopy waves. *Agricultural and Forest Meteorology*, 218, 196-203.

Arnqvist, J., Dellwik, E., Segalini, A. & Bergström, H. (2015). Wind statistics from a forested landscape. *Boundary-layer Meteorology*, 156(1), 53-71.

Chougule, A., Mann J., Segalini A., Dellwik E , (2014):Spectral tensor parameters for wind turbine load modeling from forested and agricultural landscapes , *Wind Energy*, Wiley Online Library DOI: 10.1002/we.1709.

Ebenhoch, R. Muro, B, Dahlberg, J-Å Berkesten Hägglund P. and Segalini, A. (2016), A linearised numerical model of wind-farm flows, *Wind Energy* 20, 859-875. doi: 10.1002/we.2067 https://onlinelibrary.wiley.com/doi/epdf/10.1002/we.2067

Floors, R., Enevoldsen, P., Davis, N., Arnqvist, J., and Dellwik, E. 2018: From lidar scans to roughness maps for wind resource modelling in forested areas, *Wind Energ. Sci.*, 3, 353-370, https://doi.org/10.5194/wes-3-353-2018, 2018.

Hyvärinen, A. and A. Segalini (2017), Effects from complex terrain on wind-turbine performance, *J. Energy Resour. Technol.* 139, September 2017.

Mann, J. N., Angelou, J. Arnqvist, D. Callies, E. Cantero, R. Chávez Arroyo, M. Courtney, J. Cuxart, E. Dellwik, J. Gottschall, S. Ivanell, P. Kühn, G. Lea, J. C. Matos, J. M. L. M. Palma, L. Pauscher, A. Peña, J. Sanz Rodrigo, S. Söderberg, N. Vasiljevic and C. Veiga Rodrigues: Complex terrain experiments in the New European Wind Atlas, *Phil. Trans. R. Soc.* A 375, 20160101.

Nebenführ, B. and L. Davidson (2015): Large-Eddy Simulation Study of Thermally Stratified Canopy Flow. *Boundary-Layer Meteorology*, Vol. 156, no. 2, 253-276. https://research.chalmers.se/publication/219896

Nebenführ, B. and L. Davidsson (2016): Prediction of wind-turbine fatigue loads in forest regions based on turbulent LES inflow fields. *Wind Energ*. **20**:1003–1015, doi: 10.10 02/we.2076 [Available at https://research.chalmers.se/publication/250452]

Segalini, A. (2017), Linearised simulation of the flow over wind farms and complex terrains, *Phil. Trans. R. Soc. A* 375, 20160099.

Segalini, A. & Arnqvist, J. (2015). A spectral model for stably stratified turbulence. Journal of Fluid Mechanics, 781, 330-352.

Segalini, A., Nakamura, T. and Fukagata, K. (2016): A linearised k − ϵ model of forest canopies and clearings. *Boundary-Layer Meteorol*. **161**: 439. https://doi.org/10.1007/s10546-016-0190-5

15.4 PEER REVIEWED CONFERENCE PROCEEDINGS

Dellwik, E., J. Arnqvist, H. Bergström, M. Mohr, S. Söderberg and A. Hahmann, 2014: Meso-scale modeling of a forested landscape. *J. Phys.: Conf. Ser.* **524** 012121

Medici, D. Segalini, A and Dellwik, E. (2014), On the determination of stability conditions over forested areas from velocity measurements, *EWEA conference*, Barcelona, Spain, 10-13 March 2014

Odemark, Y and Segalini, A. (2014), The effects of a model forest canopy on the outputs of a wind turbine model, *J. Phys.: Conf. Ser*. 555 012079 doi:10.1088/1742- 6596/555/1/012079

Segalini A. & Castellani F. (2017) Wind-farm simulation over moderately complex terrain, *J. Phys.: Conf. Ser*. 854 012042

Segalini A. (2015) Experimental and analytical investigation of forest clearings. *Proceedings of the International Conference on Jets, Wakes and Separated Flows* 2015, 15-18 June 2015, Stockholm, Sweden

Segalini, A. Arnqvist, J. Carlén, I. Bergström, H. and Alfredsson, P.H. (2015) A spectral model of stably stratified surface-layer turbulence. *Wake Conference*, 9-11 June 2015,

Visby, Gotland, Sweden. J. Phys.: Conf. Ser. 625 012003 doi:10.1088/1742-6596/625/1/012003

15.5 OTHER PUBLICATIONS OF INTEREST

Nakamura, T. (2014): Effects of a Forest Clearing: Experimental and Numerical Assessment. Master Thesis. School of Science for Open and Environmental Systems, Graduate School of Science and Tecnology, Keio University, Japan.

Dahl, E. AQ510 Wind Finder full classification according to IEC 61400-12-1: 2017, AQ System Internal Report No. AQS 510-007-008-04, Issue B, Status Release 2, Issue Date 2017-04-12. [Available on request from info@aqs.se]

Dahl, E., AQ510 - 3 Month 180m Comparison of Atmospheric Stability and Turbulence Intensity. AQ System broschyr [Available on request from info@aqs.se] (160324_broschyr_AQ510_180M_mast_3-months.pdf)

Freier, J. Approaches to characterise forest structures for wind resource assessment using airborne laser scan data, 2017, 111 pp. Kassel, Univ., Master Thesis, 2017

16 Appendix

16.1 STATISTICAL MEASURES FOR MODEL COMPARISON

$$bias = \frac{1}{N}\sum_{i=1}^{N} x_i - y_i$$

Mean Absolute Error:

$$MAE = \frac{1}{N}\sum_{i=1}^{N} |x_i - y_i|$$

Root Mean Square Error:

$$RMSE = \sqrt{\frac{1}{N}\sum_{i=1}^{N} (x_i - y_i)^2}$$

Standard deviation:

$$Std = \sqrt{\frac{1}{N}\sum_{i=1}^{N} \left(x_i - \bar{x}\right)^2}$$

Correlation coefficient:

$$R = \frac{\frac{1}{N}\sum_{i=1}^{N} \left(x_i - \bar{x}\right)\left(y_i - \bar{y}\right)}{Std(x)\,Std(y)}$$

WIND POWER IN FORESTS II

Sverige har goda förutsättningar för vindkraft. Men cirka 70 procent av landets yta är täckt av skog som kan bromsa vinden och som orsakar turbulens vilket inte gynnar vindkraften. Men flera vindkarteringar har visat att skogsområden i Norden kan vara lämpliga.

Det finns en stor osäkerhet kring hur vindförhållandena över skog är på mycket höga höjder. Hur påverkas elproduktionen av den ökade turbulensen? Stämmer modellerna som används för resurskartering? Hur kommer vindkraftverk i skog att producera och vilka laster utsätts vindkraftverken för i skogen? Här har alla dessa frågor undersökts och för att studera vind och turbulens över skog mer i detalj har modellsimuleringar gjorts med både mesoskaliga modeller och med LES-modellen för både homogen och icke-homogen skog.

Resultaten innebär att det går att göra bättre beräkningar av vind över skog, vilket är viktigt för att bedöma turbinlaster och energiproduktion. Mycket av vindkraftutbyggnaden sker i skogsmiljö och kunskap om vindarna i den här miljön är därför viktig för att kunna minska osäkerheterna vid projektering och upphandling av vindkraftverk.

Energiforsk is the Swedish Energy Research Centre – an industrially owned body dedicated to meeting the common energy challenges faced by industries, authorities and society. Our vision is to be hub of Swedish energy research and our mission is to make the world of energy smarter! Vindforsk is operated in cooperation with the Swedish Energy Agency.

Energiforsk

Energimyndigheten